Scuola Internazionale Superiore di Studi Avanzati

Cross-correlating Gravitational Waves with Large Scale Structure: from Cosmology to Astrophysics

Author:
Giulio Scelfo

Supervisors:
Prof. Matteo Viel
Prof. Andrea Lapi

A thesis submitted in fulfillment of the requirements
for the degree of Philosophiæ Doctor in
Astrophysics & Cosmology

December 2022

Jennifer Parker: "Dr. Brown, I brought this note back from the future and - now it's erased."

Doc: "Of course it's erased!"

Jennifer Parker: "But what does that mean?"

Doc: "It means your future hasn't been written yet. No one's has. Your future is whatever you make it. So make it a good one."

[*"Back to the future - pt. III"*]

Acknowledgements

As many know, PhD life is quite like a roller coaster, full of ups and downs, which eventually bring you to the final desired destination. This process would not have been the same without several people who took part during the whole or fraction of this process and I'll try to articulate some of the gratitude I want to express in the lines below.

Firstly, I want to thank my supervisors: Matteo Viel and Andrea Lapi. Thank you for being so great on a human and personal level, and for being always so easily approachable and easy going. I want to thank you also for the trust you always had in me, and for the freedom of thinking you always granted me. I am also grateful for the amount of physics I learnt thanks to you and, even more, for the art of critical thinking while doing science. This will always be part of me.

Secondly, I would like to thank the external referees of my PhD thesis dissertation: Enzo Branchini and Ely Kovetz. I really appreciated your commitment in reading my thesis and the detailed feedback I received from both of you. It was a honor to discuss science with you during my defense.

Thirdly, I wish to thank all the other scientists and colleagues I had the pleasure to work with during these years. From those connections who stayed active from the past (especially Alvise Raccanelli and Nicola Bellomo), to the new ones that have emerged during the PhD times (especially Marta Spinelli, Maria Berti, Lumen Boco, Riccardo Murgia and Gabriele Parimbelli).

At this point, I feel the need to open a small parenthesis. I urge the whole academic scientific environment to severely work towards changing the way the job system works here. Offering profound instability, both on the employment and on the geographical side, to the people who consider the option of building their work life into this sector is

the most efficient way to lose a huge number of good brains that would develop cutting edge science, but simply choose to move where their efforts are more valorized and where they can build their life on stable conditions. And this, let me say, leaves quite a bitter taste.

Science and academia apart, my deepest gratitude must be expressed towards my parents: you always believed in me, whatever my life choices, and always supported me in every decision I made, profoundly trusting me. The faith you always had in me was some of the strongest support I have ever received.

I also want to fondly thank my cousin Simona: you are one of my greatest sources of inspiration and, of course, a wonderful friend I can always count on.

Furthermore, I want to express profound gratitude to all of my friends, without whom my life would have been only partially full. I need to thank my historic friends, which stayed by my side over the course of the years no matter what: you really made me understand how beautiful it is to have such close and sincere human relationships, and how important they are. Moreover, I am deeply grateful for the new friends I had the privilege to find during my PhD and even in the latest months: you made me realize how life can always surprise you with the most amazing people, and that quite often a stranger is just a friend you have not met yet.

Finally, thank you to whom stayed by my side and showed me the deepest love for a big bulk of this journey. Although you could not ride with me until the end, it was a blast of a run and I will never forget it.

A new life chapter is now about to begin. I don't know how it'll go and where it will lead, but I want to conclude this section with one sentence I discovered and made mine just recently: seek discomfort. Because life's greatest moments and deepest connections are outside your comfort zone.

Giulio

Contents

Abstract **x**

List of publications **xii**

List of abbreviations **xiv**

1 Introduction **1**

1.1 Description of the Universe 1

1.1.1 Robertson-Walker metric 3

1.1.2 Evolution equations 4

1.1.3 Distance measurements 6

1.1.4 Power spectrum 8

1.2 Gravitational waves 9

1.2.1 Theoretical introduction 9

1.2.2 Detection instruments and experiments 12

1.2.3 Signal to Noise Ratio 14

1.3 Cross-correlation of GWs with other LSS tracers 16

1.3.1 Number Counts Angular Power Spectrum 18

1.3.2 Intensity Mapping 23

1.4 Methodology: Fisher analysis 26

2 Exploring galaxies - gravitational waves cross-correlations as an astrophysical probe **29**

2.1 Chapter overview and motivation 29

2.2 Tracers 31

2.2.1 Galaxies 31

2.2.1.1 SFR functions 31

2.2.1.2 Galaxy bias 33

2.2.1.3 Galaxy magnification bias 34

2.2.2 Gravitational waves . . . 35
2.2.2.1 Merging rates . . . 35
2.2.2.2 Bias for GW events . . . 40
2.2.2.3 Magnification bias for GW events . . . 41
2.3 Galaxies - GWs cross-correlations and Signal-to-Noises . . . 42
2.3.1 Tomographic case . . . 44
2.3.2 Non-tomographic case . . . 50
2.4 Cross-correlations as astrophysical probe . . . 50
2.4.1 Compared astrophysical models . . . 52
2.4.2 Theoretical forecasts . . . 53
2.5 Summary . . . 55

3 Gravitational waves × HI intensity mapping: cosmological and astrophysical applications 59
3.1 Chapter overview and motivation . . . 59
3.2 Methodology . . . 61
3.2.1 Fisher analysis . . . 61
3.3 Observables . . . 62
3.3.1 Gravitational Waves . . . 62
3.3.2 HI Intensity Mapping . . . 65
3.3.2.1 From resolved sources to IM . . . 65
3.3.2.2 Noise sources . . . 66
3.4 Gravitational waves statistical redshift distribution . . . 69
3.5 Cosmological constraints: dynamical dark energy . . . 73
3.6 Astrophysical vs. primordial origin of merging black hole binaries . . . 76
3.6.1 Progenitors . . . 78
3.6.1.1 Astrophysical scenario . . . 79
3.6.1.2 Primordial scenario: “early” binaries . . . 79
3.6.1.3 Primordial scenario: “late” binaries . . . 80
3.6.1.4 Primordial scenario: “mixed” binaries . . . 81
3.6.2 Forecasts . . . 81
3.7 Summary . . . 82

4 Testing gravity with gravitational waves × electromagnetic probes cross-correlations **87**
4.1 Chapter overview and motivation . . . 87
4.2 Methodology . . . 88
4.2.1 Observables: angular power spectra (in ΛCDM) . . . 88
4.2.2 Fisher analysis . . . 91
4.3 Tracers . . . 93
4.3.1 Gravitational Waves . . . 93
4.3.2 Neutral Hydrogen Intensity Mapping . . . 95
4.3.3 Galaxies . . . 97
4.4 Tested models . . . 98
4.4.1 Angular power spectra (in MG) and MG parameters . . . 103
4.5 Forecasts . . . 104
4.5.1 Results . . . 105
4.6 Summary . . . 113

5 Conclusions **115**
5.1 Summary of the thesis . . . 115
5.2 Future perspectives . . . 118

Appendices **122**

A Relativistic number counts for angular power spectra **123**

B GW×IM - Astrophysical vs. primordial BBHs: "early" primordial scenario as fiducial **125**

C Lyman-α forest constraints on Primordial Black Holes **127**
C.1 Overview and motivation . . . 127
C.2 Poisson noise and impact on the matter power spectrum . . . 128
C.3 Extended Mass Distributions . . . 130
C.4 Data set and Methods . . . 133
C.5 Results and Discussion . . . 134
C.6 Summary . . . 139

D GW×EM - Constraints on $\{\mu_0, \eta_0\}$: plots **141**

Bibliography **141**

Abstract

Nowadays we can probe the Universe by means of different observables and through a large set of working or planned experiments. We can now rely on data coming from several ambitious experiments observing the Universe through the electromagnetic (EM) radiation emitted by celestial bodies and traveling through space. The Large Scale Structure (LSS) of the Universe has been mapped through various galaxy, weak lensing or intensity mapping surveys such as KiDS, DES or MeerKAT, and even a bigger amount of data will be provided by e.g., Euclid, SKAO, the Vera Rubin Observatory, the Nancy Grace Roman Space Telescope, EMU, SPHEREx and many others. In parallel, a load of information was delivered by looking at the Cosmic Microwave Background radiation (CMB), improving the knowledge on the history of the Universe by virtue of e.g., COBE, WMAP and Planck. The ΛCDM theoretical model is fitted very well by data, with its 6 main parameters being exquisitely constrained by Planck. Nonetheless, the quest for new physics is still open.

The amount of knowledge that could be extracted by such large amount of data coming from EM observations was often found to be even more powerful when different observables were studied in cross-correlation together. Indeed, the study of the cross-correlation between e.g., distinct galaxy types, intensity mapping (IM) of the 21 centimeter line or CMB either improved the constraining ability over the parameters or models that were being tested, helped in reducing systematics, or even opened new scientific paths that would not have been explorable with single-tracer experiments.

Furthermore, on September 2015 the way we observe and study the cosmos changed once again, after the first detection (made by the LIGO/Virgo collaboration) of a Gravitational Wave (GW) signal emitted from a Binary Black Hole (BBH) system, leading to the beginning of the so called Gravitational Wave astronomy. Among several other reasons, the striking importance of this event consists on the fact that the Universe was then probable through a completely different and new observation channel. Before that breakthrough, many different types of observations had relied on the same physical observable: EM signals. With GWs, it was finally possible to retrieve data and test physics in a completely novel manner. Several detections were made in the subsequent years, and many more are expected thanks to experiments such as e.g., KAGRA, the Einstein Telescope, Cosmic Explorer and LISA.

Due to the novelty of this alternative probe, multi-tracing analyses are expected to bring even more interesting and unexpected results, as some studies have started investigating, exploring the cross-correlation signal of GWs with observables based on EM signals, such as galaxies, line intensity mapping, CMB and so on.

This thesis is based on my original scientific publications, which have the aim of expanding the knowledge in the GW×LSS cross-correlations field, by investigating how to better quantify this relation, by means of which observables and, mainly, which progresses in both Cosmology and Astrophysics the GW×EM cross-correlations are likely to be provided by forthcoming experiments and theoretical modeling.
Chapter 1 of this thesis presents an overall introduction to fundamental topics for the description of the Universe, followed by some context of Gravitational Waves both under a theoretical and an experimental point of view. Finally, an overall introduction of GW×LSS cross-correlations is provided, along with the formal description of one of the most common tools to quantify it: the number counts angular power spectrum. This is followed by a sketched introduction to another observable often considered in this thesis: the intensity mapping of the 21 cm line. Finally, a presentation of the adopted Fisher formalism in provided.
Chapter 2 is mainly based on Scelfo et al. (2020). In this chapter we study the measurable cross-correlation signal of galaxies and GWs with a refined characterization of both these tracers. Regarding the first one, we make use of a solid statistics of actively star-forming galaxies, based on high redshift far-IR/sub-mm observations. Regarding GWs, we treat events originated from Compact Objects (COs) mergers in the stellar mass range, adopting prescriptions consistently derived from the galaxy ones. Firstly, we aim at forecasting the detectability of such cross-correlation signal. Secondly, we make use of a proof-of-concept scenario to investigate the exploit-ability of GW×LSS cross-correlations to explore their utility in constraining astrophysical models.
Chapter 3 is taken from Scelfo et al. (2022a). In this chapter we investigate, to our knowledge for the first time, several cosmological and astrophysical applications by exploring the cross-correlations of GWs with another relatively novel observable: the IM of the 21 cm line. The strongest advantage of the IM is given by the fact that this technique allows to perform a very well refined tomography, since the redshift information is known with great accuracy, unlike for GWs. We explore three main topics: *(i)* statistical inference of the observed redshift distribution of GWs events from BH-BH mergers; *(ii)* constraints on dynamical dark energy models as an example of cosmological studies; *(iii)* determination of the nature of the progenitors of merging binary black holes, distinguishing between primordial and astrophysical origin.
Chapter 4 is mainly based on Scelfo et al. (2022b). Here we study how the cross-correlation of GWs and EM sources (namely resolved galaxies and the 21 cm IM) can be indicative of possible signatures of Modified Gravity (MG) models, beyond General Relativity (GR). This investigation relies on the idea that, under a GR framework, GWs and EM signals are expected to behave in the same way under the effects of matter perturbations between the emitter and the observer. A different behaviour might be an imprint of alternative theories of gravity, which may be detectable with forthcoming experiments.
Finally, in chapter 5 we draw our conclusions and discuss future perspectives for the GW×LSS cross-correlations domain.

List of publications

This thesis is the result of the scientific research I carried out as a Ph.D. student in the Astrophysics & Cosmology sector at SISSA, Trieste (Italy), under the supervision of Prof. Matteo Viel and Prof. Andrea Lapi and in collaboration with several people both from SISSA and other institutions.

In particular, this thesis is mainly based upon the following publications:

- G. Scelfo, L. Boco, A. Lapi, M. Viel
  Exploring galaxies - gravitational waves cross-correlations as an astrophysical probe
  JCAP 10 (2020) 045, `arXiv:2007.08534`

- G. Scelfo, M. Spinelli, A. Raccanelli, L. Boco, A. Lapi, M. Viel
  Gravitational waves × HI intensity mapping: cosmological and astrophysical applications
  JCAP 01 (2022) 004, `arXiv:2106.09786`

- G. Scelfo, M. Berti, A. Silvestri, M. Viel
  Testing gravity with gravitational waves × electromagnetic probes cross-correlations
  Accepted for publication on JCAP, `arXiv:2210.02460`

All other personal scientific publications, upon some of which this thesis may be partially based (chronological order):

- G. Scelfo, N. Bellomo, A. Raccanelli, S. Matarrese, L. Verde
  GW×LSS: chasing the progenitors of merging binary black holes
  JCAP 09 (2018) 039, `arXiv:1809.0352`

- R. Murgia, G. Scelfo, M. Viel, A. Raccanelli
  Lyman-α Forest Constraints on Primordial Black Holes as Dark Matter
  Phys. Rev. Lett. 123 (2019) 7, 071102, `arXiv:1903.10509`

- N. Bellomo, J. L. Bernal, G. Scelfo, A. Raccanelli, L. Verde
  Beware of commonly used approximations. Part I. Errors in forecasts
  JCAP 10 (2020) 016, `arXiv:2005.10384`

- G. Capurri, A. Lapi, C. Baccigalupi, L. Boco, G. Scelfo, T. Ronconi
  Intensity and anisotropies of the stochastic gravitational wave background from merging compact binaries in galaxies
  JCAP 11 (2021) 032, arXiv:2103.12037

- G. Parimbelli, G. Scelfo, S. K. Giri, A, Schneider, M. Archidiacono, S. Camera, M. Viel
  Mixed dark matter: matter power spectrum and halo mass function
  JCAP 12 (2021) 044, arXiv:2106.04588

List of abbreviations

ΛCDM	Lambda Cold Dark Matter
BBH	Binary Black Hole
BH	Black Hole
CDM	Cold Dark Matter
CMB	Cosmic Microwave Background
CO	Compact Object
DE	Dark Energy
DM	Dark Matter
EM	Electromagnetic
ET	Einstein Telescope
GR	General Relativity
GW	Gravitational Wave
IGM	Inter Galactic Medium
IM	Intensity Mapping
LIGO	Laser Interferometer Gravitational waves Observatory
LIM	Line Intensity Mapping
LSS	Large Scale Structure
MG	Modified Gravity
NS	Neutron Star
PBH	Primordial Black Hole
SFR	Star Formation Rate
SFRF	Star Formation Rate Function
S/N	Signal-to-Noise ratio
SKAO	Square Kilometre Array Observatory

1 Introduction

This chapter aims at providing a general introduction to topics both at the bases of the description of the cosmos, both more tightly connected to the central topic of this thesis: the cross-correlation between Gravitational Waves and other LSS tracers. Section 1.1 provides an overview on introductory topics in Cosmology, namely the Robertson-Walker metric, evolution equations, ways to measure distances and the power spectrum. Section 1.2 presents Gravitational Waves, from a theoretical and an observational point of view. Section 1.3 provides an introduction to GW×LSS cross-correlations, characterizing also one of the most used physical observables in this field: the number counts angular power spectrum. It also provides a general introduction to another LSS tracer often considered in this work in correlation with GW events: the intensity mapping of the 21 cm line. Finally, section 1.4 presents the Fisher formalism, often adopted in this thesis.

1.1 Description of the Universe

One of the main bases of standard Cosmology is the so called Cosmological Principle, which states that the Universe is homogeneous and isotropic at large scales. Homogeneity and isotropy imply that there are no preferred locations or directions respectively, allowing every observer to measure on average the same properties of the Universe in every point of the space and looking in any direction. At small scales the Universe is inhomogeneous, but on larger scales the validity of the Cosmological Principle is

tested and confirmed by many experiments studying the Large Scale Structures (LSS) of the Universe and the Cosmic Microwave Background (CMB). The CMB is a black body radiation made up of photons with an average temperature of $T_{\rm CMB} \simeq 2.7K$ and is a relic of the first times of the Universe, when it was still opaque. At the time it became transparent (at hydrogen recombination, approximately 380000 years after the Big Bang), these photons could finally travel freely and are observed nowadays. The CMB relative temperature fluctuations are of the order of only $\delta T/T \simeq 10^{-5}$ in every direction of the sky, strongly supporting the hypothesis of isotropy and homogeneity.
At the moment, the model that best fits our cosmological observational data and is able to make robust predictions is the Λ-Cold Dark Matter model (ΛCDM). To our knowledge, the ingredients composing the content of matter-energy of the Universe are those listed below. The abundance of a certain species can be quantified using the density parameter $\Omega \equiv \rho/\rho_c$, where ρ indicates the density of the species and ρ_c the critical density, i.e. the density necessary to have a flat space. According to the ΛCDM model, our Universe today is made of (Aghanim et al. (2020)):

- *Baryonic Matter* ($\Omega_b \simeq 0.05$): ordinary matter made of electrons, protons and neutrons. They started forming the first atomic nuclei in the early Universe (during the Nucleosynthesis);

- *Cold Dark Matter* ($\Omega_{\rm cdm} \simeq 0.26$): we do not know yet the nature of this type of matter, which may be made of non-baryonic constituents. It is called "dark" because it does not interact with radiation. The term "cold", instead, stands for the fact that this specie decoupled from the other components when its particles were not relativistic;

- *Dark Energy* ($\Omega_\Lambda \simeq 0.71$): this energy component was introduced to justify the fact that the Universe is expanding in an accelerated way (which, for example, can be argued by observing Type Ia Supernovae). In the most common framework dark energy is the well known cosmological constant (Λ) introduced by Einstein, but some alternative theories have been hypothesized too;

- *Radiation* ($\Omega_r \simeq 10^{-5}$). this radiation component of the Universe (i.e. photons) contributes very little to the amount of total energy today, but was dominant in the early stages of the Universe, during the so called radiation dominated era.

To quantify the total matter abundance, the parameter

$$\Omega_{\rm m} = \Omega_{\rm cdm} + \Omega_b \tag{1.1}$$

is often used.
In the rest of this Section other background concepts about Cosmology are provided.

1.1.1 Robertson-Walker metric

The starting point to describe the properties of the Universe is to determine unequivocally the way to measure distances between two points in spacetime. To do so, one needs to establish a rule, which depends on the geometry of the space considered, described by the line element ds^2 from the assumed metric $g_{\mu\nu}$. The simplest type of metric that one could think of is the Minkowski one:

$$\eta_{\mu\nu} = diag(-1, 1, 1, 1), \tag{1.2}$$

where the corresponding line element ds^2 reads as

$$ds^2 = -(c\,dt)^2 + dx^2 + dy^2 + dz^2 \tag{1.3}$$

in Cartesian coordinates, and

$$ds^2 = -(c\,dt)^2 + dr^2 + r^2 d\theta^2 + r^2 \sin^2\theta d\phi^2 \tag{1.4}$$

in the polar coordinates

$$\begin{cases} x = r\sin\theta\cos\phi \\ y = r\sin\theta\sin\phi \\ z = r\cos\theta \end{cases} \tag{1.5}$$

where c is the speed of light.
Following the cosmological principle, H. Robertson and A. Walker derived the expression for the metric of a spatially homogeneous and isotropic Universe. This metric, called Robertson-Walker metric, can be written as (see e.g. Weinberg (2008)):

$$ds^2 = -dt^2 + a(t)^2\left[\frac{dr^2}{1-kr^2} + r^2 d\Omega^2\right], \tag{1.6}$$

where $d\Omega = d\theta^2 + \sin^2\theta d\phi^2$. The constant k depends on the curvature of the space-like hypersurfaces time: it is $k = 0$ for the case of flat space, $k > 0$ for a closed space and $k < 0$ for an open space. A variable rescaling is often applied, such that k can only assume the values $k = -1; 0; 1$. The variable t is the so called cosmological proper time: it is the time measured by a reference frame who sees the Universe expanding uniformly around itself. The spatial coordinates (r, θ, ϕ) are said to be comoving of a point in space: if the Universe is under a homogeneous and isotropic expansion,

these coordinates stay fixed over time. Finally, $a(t)$ is the scale factor, which relates comoving distances with physical ones as $d_{\text{physical}} = a(t)\, d_{\text{comoving}}$, with the standard normalization of $a(t) = 1$ today.
Note the the RW metric is appropriate only when describing the Universe on large scales: at small ones, instead, it is not homogeneous and another metric has to be taken into account.

1.1.2 Evolution equations

Let us now introduce the Einstein equations. They relate the geometry of spacetime with the matter-energy that shapes it as:

$$R_{\mu\nu} - \frac{1}{2} R g_{\mu\nu} = 8\pi G T_{\mu\nu} \tag{1.7}$$

where $R_{\mu\nu}$ (Ricci tensor) and $R = R^{\mu}_{\mu}$ (Ricci scalar) provide information about the geometry, while $T_{\mu\nu}$ is the energy-momentum tensor. G is the universal gravitational constant. In the case of a perfect fluid, the energy-momentum tensor assumes the following expression:

$$T^{\mu\nu} = (\rho + p) u^{\mu} u^{\nu} + p g^{\mu\nu} \tag{1.8}$$

where ρ, p, u^{μ} are the matter-energy density, the isotropic pressure and the 4-velocity of the fluid. For a reference frame at rest with the fluid it reduces to

$$T^{\mu\nu} = \text{diag}(\rho, p, p, p). \tag{1.9}$$

Assuming the cosmological fluid as perfect and considering that on large scales our Universe can be described by a RW metric, we can obtain the so called Friedmann equations by computing the Einstein equations:

$$\begin{cases} H^2 = \left(\dfrac{\dot{a}}{a}\right)^2 = \dfrac{8}{3}\pi G \rho - \dfrac{k c^2}{a^2} \\ \dfrac{\ddot{a}}{a} = -\dfrac{4}{3}\pi G \left(\rho + \dfrac{3p}{c^2}\right) \end{cases} \tag{1.10}$$

where time dependencies are omitted and $\cdot$ indicates a derivative with respect to t. These equations are essential in describing the background dynamics of our Universe, since they describe how the scale factor $a(t)$ varies with time.
From the first Friedmann equation we can derive an expression for the critical density ρ_c that would provide a flat Universe ($k = 0$):

$$\rho_c = \frac{3H^2}{8\pi G}. \tag{1.11}$$

Finally, we can introduce the parameter Ω_k which describes the geometry of the universe as:

$$\Omega_k + \Omega_m + \Omega_\Lambda + \Omega_r = 1, \tag{1.12}$$

such that:

- $\Omega_k = 0$ for a flat Universe;
- $\Omega_k < 0$ for a closed Universe;
- $\Omega_k > 0$ for an open Universe.

As of today, experiments tell us that $|\Omega_k| = 0.001 \pm 0.002$ (Aghanim et al. (2020)).

Another important equation is the continuity equation, which derives from the Bianchi identities (that yield $T^{\mu\nu}_{;\nu} = 0$) and describes the energy density evolution of the cosmic fluid in a Universe described by the RW metric. It states that

$$\dot{\rho} + 3H(\rho + p) = 0. \tag{1.13}$$

Another useful expression which relates p with ρ, providing us with the third of three independent equations in the unknowns $a,\ \rho, p$, is the equation of state:

$$p = w\rho \tag{1.14}$$

where w is a constant.
From the continuity equation we can obtain that $\rho \sim a^{-3(1+w)}$ which brings to

$$a(t) = t^{\frac{2}{3}(1+w)}. \tag{1.15}$$

For a radiation dominated Universe the equation of state is $w = 1/3$, from which

$$\rho \sim a^{-4} \quad ; \quad a(t) \sim t^{1/2}, \tag{1.16}$$

while for non-collisional matter domination we have that $w = 0$ and then

$$\rho \sim a^{-3} \quad ; \quad a(t) \sim t^{2/3}. \tag{1.17}$$

1.1.3 Distance measurements

Distance measurements in Cosmology can be performed in different ways. We shall describe them in this Section. Firstly, let us introduce the Hubble constant H_0. It describes the proportional relation between the recession speed v and the distance d of an object from the observer:

$$v = H_0 d. \tag{1.18}$$

The above expression, known as Hubble law, was first theoretically proposed by Lemaitre and then experimentally observed by Hubble (1929) measuring the redshift z of close galaxies. The redshift z was obtained by looking at the shift of galaxies spectral lines. It can be quantified as:

$$z = \frac{f_e}{f_o} - 1 = \sqrt{\frac{1 + v/c}{1 - v/c}} - 1 \approx \frac{v}{c}, \tag{1.19}$$

where f_e and f_o are the emitted and observed frequencies of the light emitted from the sources. Note that this expression is valid only for nearby objects ($v \ll c$), a general description of the redshift is in fact given by relativity. Some calculus can provide a relation between redshift and scale factor: $a(t) = (1 + z)^{-1}$.

It must be specified that the value H_0 is only valid today. In fact, generally one has to consider the Hubble parameter $H(t)$, which varies with time. Measurements of the Hubble constant by the Planck mission (Aghanim et al. (2020)) estimate the value of

$$H_0 = 67.4 \pm 0.5 \,\mathrm{km/s/Mpc}. \tag{1.20}$$

The parameter h, which is H_0 in units of $100\,\mathrm{km/s/Mpc}$, is often used too. It is worth mentioning that an issue regarding the value of this constant is still open, since local measurements of H_0 (e.g. based on standard candles) yield values typically higher than those based on non-local methods (e.g. observing the CMB), see for example Bennett et al. (2014).
From this constant it is possible to determine the so called Hubble time t_H:

$$t_H = \frac{c}{H_0} = 9.78 \cdot 10^9 \, h^{-1} \,\mathrm{yr}, \tag{1.21}$$

giving a rough estimate of the age of the Universe, and the Hubble distance d_H:

$$d_H \equiv \frac{c}{H_0} = 3000 \, h^{-1} \mathrm{Mpc}, \tag{1.22}$$

which represents the distance traveled by light in a Hubble time, setting the scale of the Universe.
Defining

$$E(z) = \sqrt{\Omega_m(1+z)^3 + \Omega_k(1+z)^2 + \Omega_\Lambda}, \tag{1.23}$$

the Hubble parameter can be written as $H(z) = H_0 E(z)$ and we can introduce the line-of-sight comoving distance $\chi(z)$:

$$\chi = d_H \int_0^z \frac{dz'}{E(z')}. \tag{1.24}$$

From this, it is possible to derive the comoving transverse distance d_M between two objects at the same redshift but located in different points on the sky. It reads as:

$$d_M \equiv \begin{cases} d_H \dfrac{1}{\sqrt{\Omega_k}} \sinh\left[\sqrt{\Omega_k}\chi/d_H\right] & \text{for } \Omega_\mathrm{k} > 0; \\ \chi & \text{for } \Omega_\mathrm{k} = 0; \\ d_H \dfrac{1}{\sqrt{\Omega_k}} \sin\left[\sqrt{\Omega_k}\chi/d_H\right] & \text{for } \Omega_\mathrm{k} < 0. \end{cases} \tag{1.25}$$

The angular diameter distance d_A, instead, is given by the ratio of the physical trans-

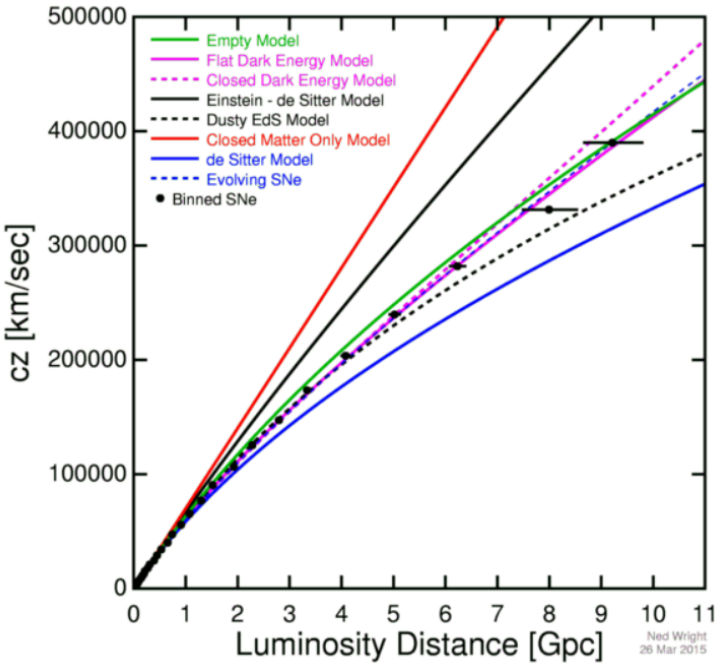

Figure 1.1: Luminosity distance - redshift relation for a variety of cosmological models. Data points from SNe Ia favour a flat universe with a DE component (Betoule et al. 2014).

verse dimension of on object and its and its angular size in radians. It can be expressed

as

$$d_A \equiv \frac{d_M}{1+z}. \tag{1.26}$$

Furthermore, we can define the luminosity distance d_L as

$$d_L \equiv \sqrt{\frac{L}{4\pi S}}, \tag{1.27}$$

where S is the bolometric flux of the object and L its bolometric luminosity. It can also be expressed as a function of the other distances:

$$d_L = (1+z)d_M = (1+z)^2 d_A. \tag{1.28}$$

The luminosity distance will be a key quantity for the work described in chapter 4, as we will see. Indeed, its redshift dependence is tightly correlated with the the assumed cosmological model and measurements of the $d_L - z$ relation through observations (such as Supernovae Ia, see e.g., figure 1.1) can be powerful in constraining cosmology.
Finally, the comoving volume gives the measure of a volume in which the number densities of non-evolving sources following the Hubble expansion are constant with redshift. For a redshift interval dz and a solid angle $d\Omega$ the comoving volume element reads as

$$dV_c = D_H \frac{(1+z)^2 D_A^2}{E(z)} d\Omega dz. \tag{1.29}$$

1.1.4 Power spectrum

Let us now consider a generic fluctuation $\delta(x,t)$ in a point of spacetime. For example, it can be the fluctuation of the density field. It is useful to introduce a statistical tool denominated two-point correlation function (see e.g. Weinberg (2008)):

$$\xi(r) = \langle \delta(x+r,t)\delta(x,t) \rangle, \tag{1.30}$$

which is an average value taken over the entire statistical ensemble. In Fourier space one can write

$$\delta(x,t) = \frac{1}{(2\pi)^3} \int d^3k e^{ik\,x} \delta_k(t) \tag{1.31}$$

and define the power spectrum $\mathcal{P}(k)$ of the fluctuation δ as:

$$\langle \delta_{k_1} \delta_{k_2} \rangle = (2\pi)^3 \mathcal{P}(k) \delta^{(3)}(k_1 + k_2). \tag{1.32}$$

The power spectrum is actually the Fourier transform of the two-point correlation function. Indeed, considering its expansion in plane waves one can write:

$$\begin{aligned}\xi(r) = \langle\delta(x+r)\delta(x)\rangle &= \left\langle \frac{1}{(2\pi)^3}\int d^3k e^{ik\,x}\delta_k \frac{1}{(2\pi)^3}\int d^3k' e^{ik'\,x}\delta'_k \right\rangle \\ = \int \frac{d^3k}{(2\pi)^3}\int \frac{d^3k'}{(2\pi)^3} e^{ik\,(x+r)} e^{ik'\,x}(2\pi)^3\mathcal{P}(k)\delta^{(3)}(k+k') &= \int d^3k(2\pi)^3\mathcal{P}(k)e^{ik\,r}.\end{aligned} \tag{1.33}$$

Finally, introducing the variance $\sigma^2 = \langle\delta^2(x)\rangle$, another way to express the power spectrum can be:

$$\Delta(k) = \frac{k^3}{2\pi^2}\mathcal{P}(k) \tag{1.34}$$

with

$$\sigma^2 = \int_0^\infty \frac{dk}{k}\Delta(k). \tag{1.35}$$

1.2 Gravitational waves

One of the newest observables is given by Gravitational Waves (GWs), whose study is expected to shed light over a vast array of sectors in both Astrophysics and Cosmology. In this section we give a general theoretical introduction to this observable, followed by an overall description of present and future instruments, to conclude with specifics over GWs detectability and Signal-to-Noise ratios.

1.2.1 Theoretical introduction

Gravitational waves are perturbations in the metric of spacetime which are produced by accelerated masses. They are transverse waves which move at the speed of light c. Poincaré firstly introduced this thematic in 1905, to be later analytically described in Einstein's General Relativity as wave solutions to the linearized field equations of gravity. Starting from these equations and considering the weak gravitational field case, the metric $g_{\mu\nu}$ in a point of spacetime can be written as

$$g_{\mu\nu}(x) = \eta_{\mu\nu} + h_{\mu\nu}(x) \tag{1.36}$$

where $h_{\mu\nu}$ is a small perturbation of the Minkowskian $\eta_{\mu\nu}$ (i.e. $|h_{\mu\nu}| \ll 1$). $h_{\mu\nu}$ being small, contributes of order higher than one can be neglected, such that we are left with the linearized version of General Relativity.
Starting from the Lorentz gauge condition

$$\frac{\partial\bar{h}^{\mu\nu}}{\partial x^\nu} = 0 \tag{1.37}$$

(where $\bar{h}^{\mu\nu} \equiv h_{\mu\nu} - \frac{1}{2}\eta_{\mu\nu}h$ and $h \equiv h^{\mu}_{\mu}$) a few mathematical calculations (see e.g. Hartle (2003)) lead to the linearized Einstein equations:

$$\Box\bar{h}^{\mu\nu} = -16\pi T_{\mu\nu}, \tag{1.38}$$

where $T_{\mu\nu}$ is the energy-momentum tensor (1.8) and $\Box$ is the d'Alembertian operator

$$\Box \equiv \eta^{\mu\nu}\partial_{\mu}\partial_{\nu} = -\frac{\partial^2}{\partial t^2} + \nabla^2. \tag{1.39}$$

Equation (1.38) shows that the components of $\bar{h}^{\mu\nu}$ obey a flat-space wave equation of the form

$$-\frac{\partial^2 f(x)}{\partial t^2} + \nabla^2 f(x) = j(x) \tag{1.40}$$

where $j(x)$ is the source. Solutions for this kind of problem are well known in physics. The above expression (outside the source) reduces to

$$-\frac{\partial^2 f(x)}{\partial t^2} + \nabla^2 f(x) = 0 \tag{1.41}$$

if we approximate $j(x)$ as a Dirac's delta (valid at large distance from the source).
Let us now call (x, y, z) three orthogonal axes defining directions in space. Given a plane wave propagating in the z direction, one can write the perturbed metric tensor $h_{\mu\nu}$ as

$$h_{\mu\nu} = \begin{pmatrix} 0 & 0 & 0 & 0 \\ 0 & 1 & 0 & 0 \\ 0 & 0 & -1 & 0 \\ 0 & 0 & 0 & 0 \end{pmatrix} f(t-z) \tag{1.42}$$

where $f(t-z) = A\sin(\omega t + \phi)$ describes a plane wave propagating along z with amplitude A, pulsation ω and phase ϕ. With this recipe, we can write the metric element ds^2 as

$$ds^2 = -dt^2 + [1 + f(t-z)]dx^2 + [1 - f(t-z)]dy^2 + dz^2. \tag{1.43}$$

Given a circular distribution of test particles in the (x,y) plane, from Equation (1.43) one can define the following coordinate system (assuming $\phi = 0$ for simplicity):

$$\begin{cases} X = x\left(1 + \frac{1}{2}A\sin(\omega t)\right) \\ Y = y\left(1 - \frac{1}{2}A\sin(\omega t)\right) \end{cases} \tag{1.44}$$

so that one can express the spatial metric element on the plane as

$$dS^2 = dX^2 + dY^2. \tag{1.45}$$

Since dX and dY in general are different while changing in time, the above Equation expresses an elliptical deformation: while time changes, firstly a deformation along one axes and then one along the other take place. The original circular shape is re-obtained for each multiple of the semi-period $T/2 = \pi/\omega$, for which $\frac{1}{2}Asin(\omega t) = -\frac{1}{2}Asin(\omega t)$. We have just described one independent polarization mode for gravitational waves. The second polarization mode can be portrayed by rotating the axes of an angle $\phi = \pi/4$:

$$\begin{cases} x' = x\cos\phi + y\sin\phi \\ y' = -x\sin\phi + y\cos\phi \end{cases} \tag{1.46}$$

which gives

$$\begin{cases} x = \dfrac{1}{\sqrt{2}}(x' + y') \\ x = \dfrac{1}{\sqrt{2}}(x' - y') \end{cases} \tag{1.47}$$

The perturbed metric tensor for this polarization mode is

$$h^{\times}_{\mu\nu} = \begin{pmatrix} 0 & 0 & 0 & 0 \\ 0 & 0 & 1 & 0 \\ 0 & 1 & 0 & 0 \\ 0 & 0 & 0 & 0 \end{pmatrix} f_{\times}(t-z). \tag{1.48}$$

Renaming the metric element in Equation (1.42) (which describes only the first polarization mode) as $h_{\mu\nu}$ (and $f(t-z)$ as $f_+(t-z)$) one can write in a general way:

$$h_{\mu\nu} = h^{\times}_{\mu\nu} + h^{+}_{\mu\nu} = \begin{pmatrix} 0 & 0 & 0 & 0 \\ 0 & f_+ & f_{\times} & 0 \\ 0 & f_{\times} & -f_+ & 0 \\ 0 & 0 & 0 & 0 \end{pmatrix}. \tag{1.49}$$

Figure 1.2 provides a schematic picture of the effects of the two polarization modes of GWs.

Gravitational waves are produced when the $T^{\mu\nu}$ tensor varies in time in such a manner that it has a quadrupole or higher pole component. It means that (for example) a mass moving in an accelerated non-isotropic motion can generate GWs, whereas a circular mass expanding or contracting in an isotropic way can not. Some examples of GWs sources are:

- inspiraling and/or merging binary systems;
- spinning neutron stars with deformities on surface;
- non spherically symmetric Supernovae explosions;

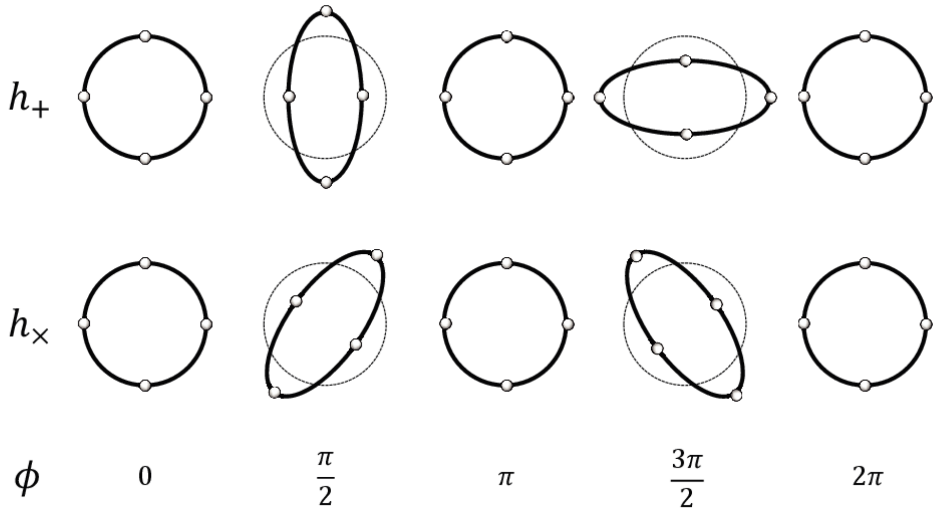

Figure 1.2: Polarization modes h_+ and $h_\times$ and their effects on a circular distribution of test particles, as function of the phase ϕ.

- non symmetric inflationary expansion from the early Universe.

In the manuscripts mainly building this thesis the attention is focused towards the case of GWs emitted by the merger of binary Compact Objects (COs) systems in the stellar mass range.

1.2.2 Detection instruments and experiments

The physics behind the Michelson and Morley interferometer is at the bases of the functioning of GWs detectors. This instrument splits light rays coming from an artificial laser source into two beams along different arms, to finally collect them to a detector after they have travelled given distances. The detector is able to collect a fringe pattern: the characteristics of this pattern depend on the difference of distances traveled by the two beams, allowing for a very precise measurement of such quantity. Given the fact that GWs are transverse waves perturbing the spacetime fabric, when a GW traveling into spacetime passes through an interferometer of this type, the two arms will contract/stretch in different ways, depending on the angular inclination of such wave. This induces a difference between the paths traveled by the two beams, consequently altering the interference fringe pattern. Detections of GWs can happen by observing changes in this pattern. Figure 1.3 provides a schematic portrait of this type of interferometers.
Let us now give a sketch of present and planned GWs detectors. The LIGO experiment (Abbott et al. (2009)) is composed by two ground based detectors, located in

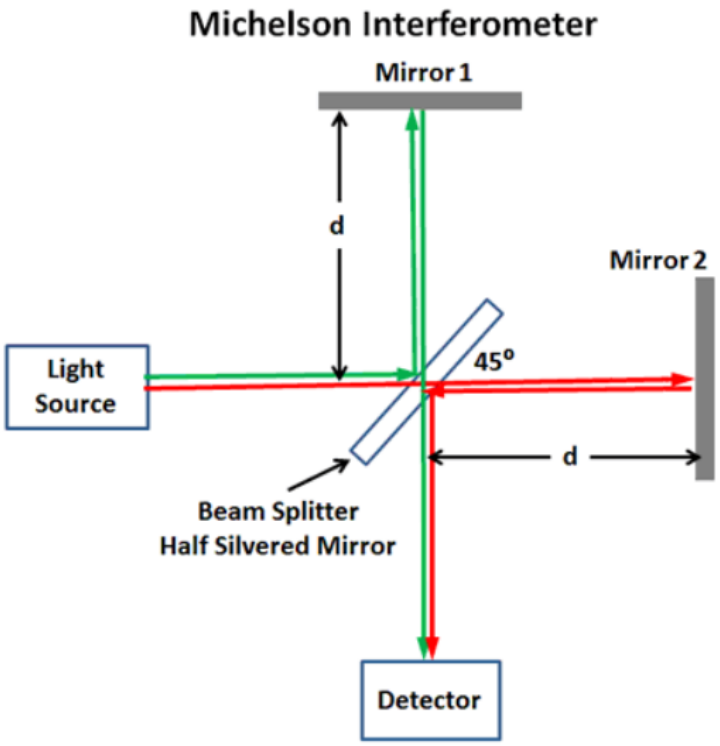

Figure 1.3: Schematic picture of a Michelson and Morley interferometer. The laser is split into the two arms (between the beam splitter and the mirrors) and then recollected at the detector, where interference fringe patterns are observed.

Livingston and Hanford (US), both of which have 4 km arms. In the most optimal conditions, a GW would alter the length of the arms by a factor of roughly 10^{-18} m, which should be detected by the instrument. Then, Virgo (Accadia et al. (2012)) is a 3 km interferometer near Pisa (Italy) and the Japanese Kamioka Gravitational Wave Detector (KAGRA, Aso et al. (2013)), 3 km arms, and the LIGO India (Fairhurst (2014)), 4 km arms are being developed. In addition, improvements to both LIGO (advanced LIGO, Abbott et al. (2016a)) and Virgo are developed to increase sensitivity. The Einstein Telescope (ET, Sathyaprakash et al. (2012a)) is still in the early design study phase, but it should be composed by three 10 km long underground arms forming a triangular shape, with two detectors. Finally, the Cosmic Explorer (CE, Reitze et al. (2019)) is also under planning, with an expected arms length of 40 km. Having multiple detectors in different locations gives a huge boost in performance: not only it allows to identify and get rid of instrumental and environmental sources of noise, it also allows to improve the sources localization.

Since for ground based detectors the noise contribution is strong, space instruments would provide a significant advantage. A space based observatory would also allow

much longer arms, consequently increasing the instrument sensibility. This is what the Laser Interferometer Space Antenna (LISA, Audley et al. (2017)) aims to achieve, with a triangular shape of 2.5 million km arms.
The LIGO experiment detected for the first time GWs coming from the coalescence event of a black hole binary system on September 14^{th} 2015, classified as GW150914 Abbott et al. (2016b). The colliding black holes had masses of $36^{+5}_{-4}M_{\odot}$ and $29^{+4}_{-4}M_{\odot}$, while the final black hole mass is $M_f = 62^{+4}_{-4}M_{\odot}$. It means that an energy amount of $3^{+0.5}_{-0.5}M_{\odot}c^2$ was radiated under the form of GWs. Pictures (1.4) and (1.5) provide details on the detection of GW150914. It is remarkable to note how well the observed strain amplitudes fit numerical relativity calculations outputs for a model with the parameters inferred for this event. Indeed, the significance of the event was estimated to be greater than 5.1σ, corresponding to a false alarm rate smaller than one event per 203000 years. As of today, the first part of the third observing run (Abbott et al. (2021)) of the LIGO/Virgo instruments (and previous runs, Abbott et al. (2019a)) have collected evidences of a total of 90 compact objects mergers. Figure 1.6 provides a collection of the GW events detected by the LIGO-Virgo-KAGRA collaboration up to present time.

1.2.3 Signal to Noise Ratio

The global output $s(t)$ of a GW detector can be written as a superposition of the noise $n(t)$ and the GW signal $h(t)$:

$$s(t) = n(t) + h(t). \tag{1.50}$$

The detectability of GWs passing through a detector depends on the so called Signal to Noise Ratio (SNR) ϱ, defined as (Moore et al. (2015))

$$\varrho^2 = \int_{f_{\min}}^{f_{\max}} df \frac{4|\hat{h}(f)|^2}{S_n(f)}, \tag{1.51}$$

where $f_{\min}$, $f_{\max}$ are the instrumental cut-off frequencies, f is the observed frequency, $\hat{h}(f)$ is the Fourier transform of the signal, defined according to the following convention

$$\hat{h}(f) = \int_{-\infty}^{+\infty} dt\ h(t)e^{2\pi i f t}, \quad h(t) = \int_{-\infty}^{+\infty} df\ \hat{h}(f)e^{-2\pi i f t}, \tag{1.52}$$

and S_n is the so called one-sided noise power spectral density. Assuming that the noise is stationary and Gaussian, it can be expressed as

$$\langle \tilde{n}(f)\tilde{n}^*(f')\rangle = \frac{1}{2}\delta(f - f')S_n(f), \tag{1.53}$$

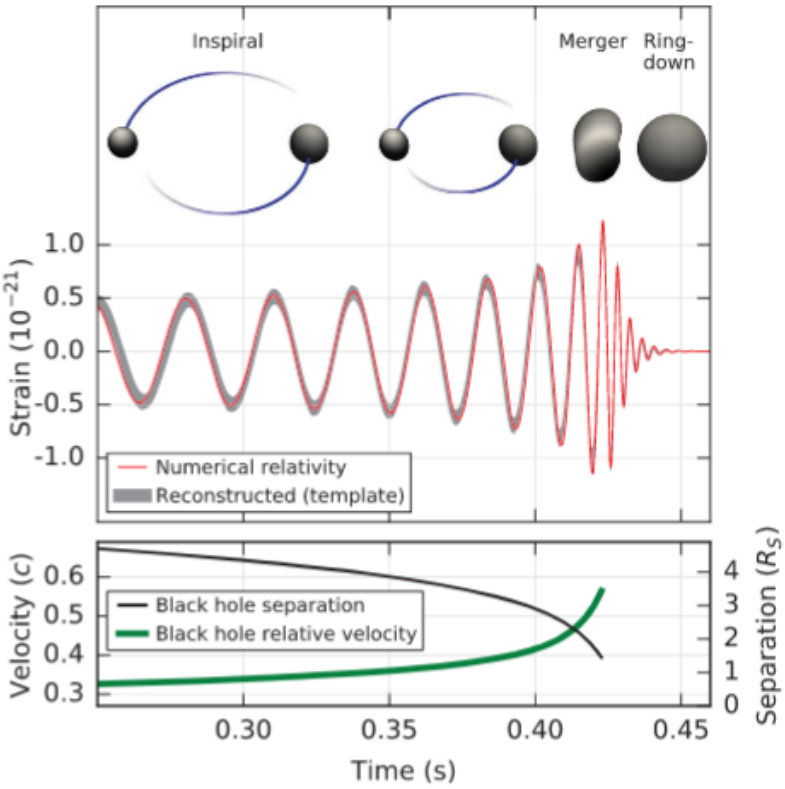

Figure 1.4: *Top panel:* numerical relativity predictions of GW strain amplitude and reconstructed template (Hanford detector). *Bottom panel:* black holes separation (in units of the Schwarzschild radius) and effective relative velocity as function of time (Abbott et al. (2016b)).

where the angle brackets indicate an ensemble average over many noise realizations. A value of $\varrho \sim 8$ is taken as minimum requirement to claim a GW event detection (Littenberg & Cornish (2010)).

In the case of an inspiraling signal we can have a detection even if the instantaneous amplitude of the signal is below the noise level, since the signal is integrated over many orbits. In this case what is used is the dimensionless characteristic strain

$$h_c^2(f) = 4f^2|\hat{h}(f)|^2 \tag{1.54}$$

and the SNR can be re-expressed as:

$$\varrho^2 = \int_{f_{\min}}^{f_{\max}} df \frac{h_c^2(f)}{f^2 S_n(f)}. \tag{1.55}$$

In reality the response of the detector does not depend only on the frequency of the gravitational wave, but also on the relative orientation with respect to the incoming wave, on the polarization of the wave and possibly on the orientation of the system.

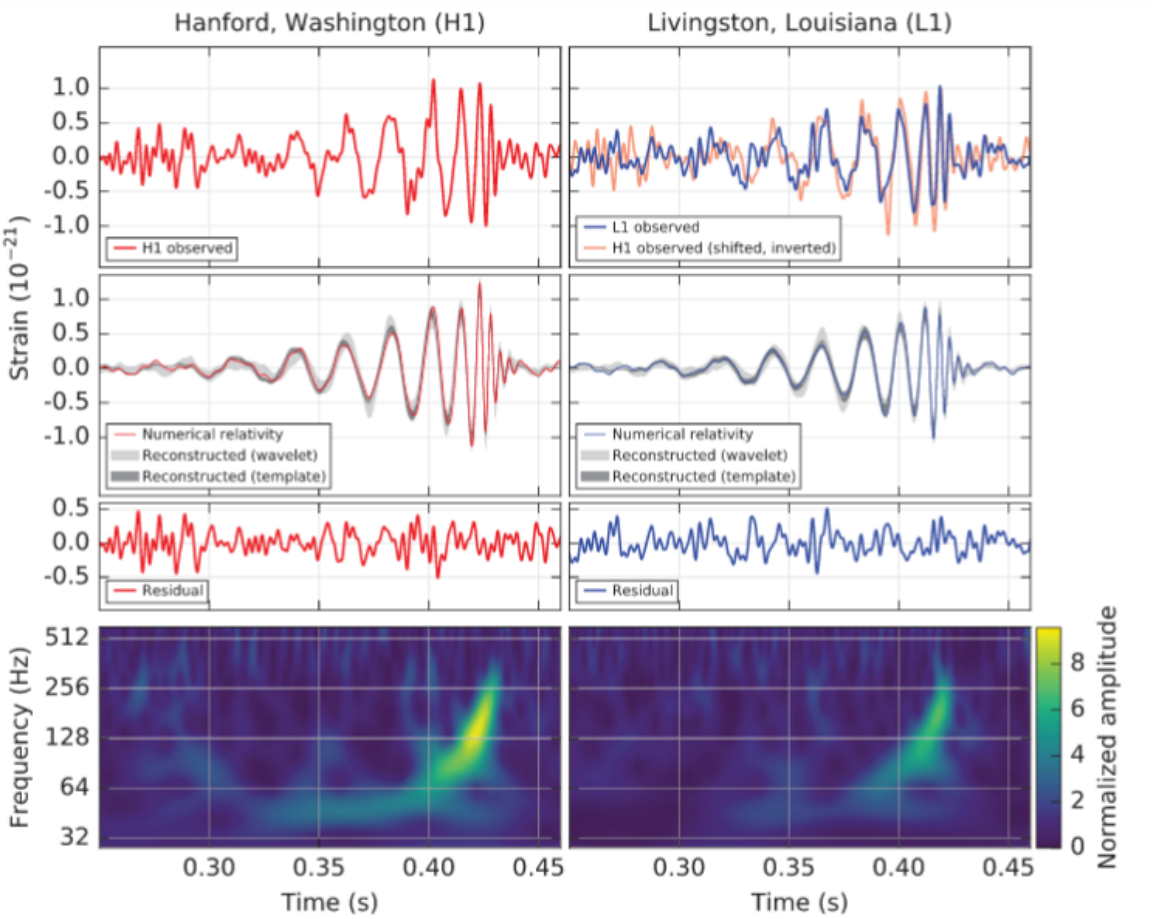

Figure 1.5: Detection of GW150914 by the LIGO Hanford (H1) and Livingston (L1) detectors. In the top row the observed GW strain amplitudes are provided. In the middle row the reconstructed waveforms are compared to the one predicted by numerical relativity calculations consistent with the system parameter attributed to GW150914 (and residuals). In the bottom row a time-frequency display of the strain data is provided. For specific details see Abbott et al. (2016b).

For this reason it is often used the orientation-averaged SNR (see e.g. Moore et al. (2015); Flanagan & Hughes (1998)):

$$\left\langle \varrho^2 \right\rangle = \frac{1}{5} \int_{f_{\rm min}}^{f_{\rm max}} df \frac{4|\hat{h}(f)|^2}{S_n(f)}. \tag{1.56}$$

The multiplicative factor actually slightly depends on the characteristics of the system considered, but it is usually near the value 1/5.

1.3 Cross-correlation of GWs with other LSS tracers

After the first detection of a GW signal was announced, originating from the merger of Binary Black Holes of a total mass $M_{\rm tot} \sim 60 M_\odot$ (Abbott et al. (2016b,c)), the

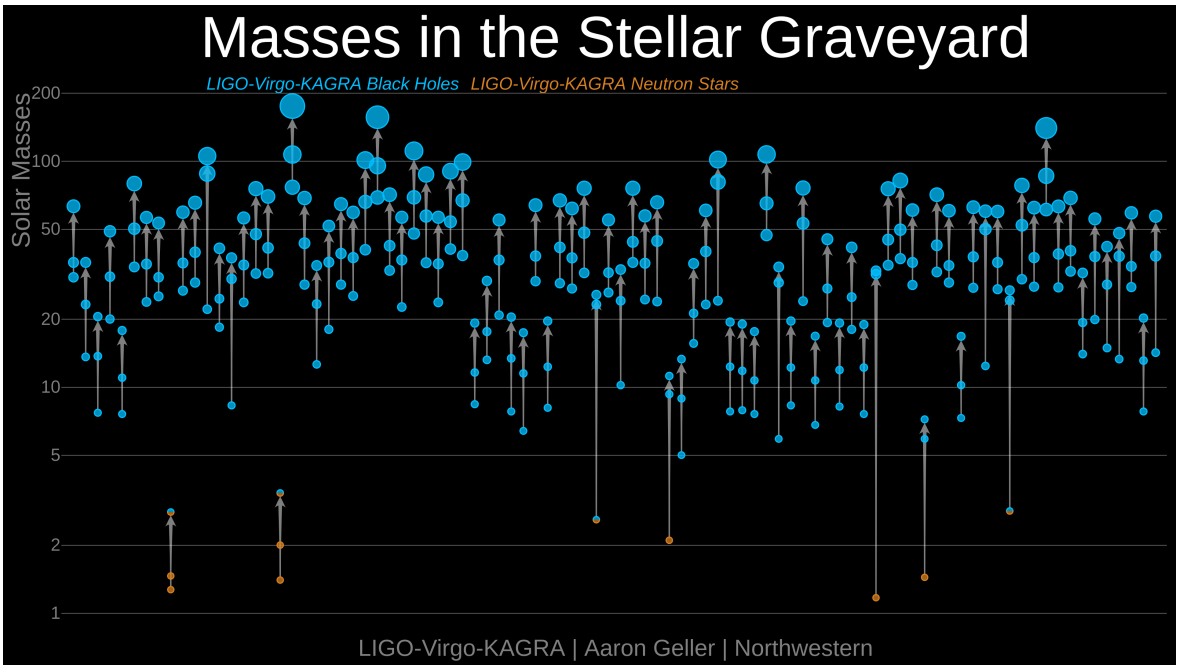

Figure 1.6: Collections of detected LIGO-Virgo-KAGRA compact objects binaries. Black holes are represented in blue and neutron stars in orange. The objects are arranged in order of discovery date (horizontal axis) and masses (vertical axis). Image credit: LIGO-Virgo/Aaron Geller/Northwestern.

era of GW astronomy began, with several detections made since then (Abbott et al. (2019a, 2021)). The groundbreaking importance of this new window comes from the fact that it opened a completely new way to observe the cosmos, using an observable that could not be exploited before. Among the newly opened directions, the birth of GW astronomy also led to new possibilities in the multimessenger field of tracers' cross-correlations.

The study of cross-correlations between distinct tracers is not new. Indeed, several studies regarding e.g., correlations between the Large Scale Structure (LSS) and the Cosmic Microwave Background (see e.g., Ho et al. (2008); Hirata et al. (2008); Bianchini et al. (2015); Bianchini & Lapi (2014); Bianchini et al. (2016); Mukherjee et al. (2020a)), neutrinos (see e.g., Fang et al. (2020)) or among different LSS tracers (see e.g., Martínez et al. (1999); Jain et al. (2003); Yang et al. (2005); Paech et al. (2017)) have been performed.

For what concerns the specific possibility to cross-correlate GW signals with LSS tracers, various works on different applications have been made, spanning a plethora of topics from both Cosmology and Astrophysics. For example, GW$\times$LSS cross-correlations have been exploited for the investigation of the origin of merging BBHs, in particularly

to detect the possible imprint left by a population of Primordial Black Holes (Raccanelli et al. (2016b); Scelfo et al. (2018, 2022a)), a topic also related to the investigation of the GW bias (e.g., Calore et al. (2020)). Furthermore, they have been exploited for the study of anisotropies of the number density and luminosity distances of compact binaries (e.g., Namikawa et al. (2016)) and of the stochastic GW background (e.g., Alonso et al. (2020)). Nonetheless, the possibility of alternatives to General Relativity can also be investigated with these tools, testing possible observational marks predicted by Modified Gravity (MG) theories (e.g., Camera & Nishizawa (2013); Mukherjee et al. (2020b, 2021a); Baker & Harrison (2021); Mukherjee et al. (2021b); Garoffolo et al. (2021); Scelfo et al. (2022b)). Additionally, GWs and their cross-correlations have been used to probe H_0 and other cosmological parameters through the $d_L - z$ relation (e.g., Oguri (2016); Bera et al. (2020); Mukherjee et al. (2022); Cigarrán Díaz & Mukherjee (2022). Moreover, cross-correlations can be addressed to learn about the nature of the Stochastic Gravitational Waves Background (e.g., Adshead et al. (2021); Braglia & Kuroyanagi (2021); Ricciardone et al. (2021); Capurri et al. (2022)) or to infer the clustering properties of GWs (e.g., Libanore et al. (2021, 2022); Cañas Herrera et al. (2020)). Finally, cross-correlations are well known for helping in reducing systematics limitations (e.g., Bonaldi et al. (2016)).
In the next section we introduce a statistical tool that can be used to quantitatively describe the cross-correlation of two different tracers: the number counts angular power spectrum. This is also the main tool adopted for the majority of the works presented in this thesis.

1.3.1 Number Counts Angular Power Spectrum

The most natural way to compute cross-correlations is by looking at the 3D angular power spectrum, C_ℓ, therefore calculating the correlation of distributions on concentric spheres. This formalism has a long history in cosmology and was initially developed by Peebles (1973, 1980), and subsequently applied to cosmological datasets by Regos & Szalay (1989); Scharf et al. (1992); Lahav et al. (1993); Fisher et al. (1994); more recently it has been used mostly for cross-correlations (e.g., Nolta et al. (2004)). The advantage of this formalism resides in the fact that it naturally includes effects coming from large angular separations, the curvature of the sky, and that it makes use of directly observable quantities such as angles and redshifts. The drawback of having to calculate a large number or auto- and cross-bin correlations in the case of many narrow redshift bins does not apply for GW waves as their maps are not accompanied by very good radial information. Moreover, recent theoretical developments allow us

to compute a large number of correlations in very short times (see e.g., Gebhardt & Jeong (2018); Assassi et al. (2017)).

In the harmonic space, the multipole number ℓ relates to the angular resolution θ as $\ell \sim 180^o/\theta$ (see e.g., Heavens & Taylor (1995); Szalay et al. (1998); Matsubara (2000); Pápai & Szapudi (2008); Raccanelli et al. (2010); Bertacca et al. (2012a); Raccanelli et al. (2013); Dai et al. (2012); Yoo & Desjacques (2013); Blake et al. (2018); Taruya et al. (2019) for works about giving up the flat sky approximation and the advantages of working in this space). As will be shown later on, this tool is also very well suited for performing tomographic analyses.

Let us now formally introduce the number counts angular power spectra. X and Y being two given tracers (e.g., Gravitational Waves resolved events, galaxies, etc.) one can write the relation between the *observed* angular power spectrum $\tilde{C}_\ell^{XY}(z_i, z_j)$ (obtained by cross-correlating tracer X in redshift bin z_i with tracer Y in bin z_j) and the harmonic coefficients $a_{\ell m}$ as:

$$\langle a^X_{\ell m}(z_i) a^{Y*}_{\ell' m'}(z_j)\rangle = \delta_{\ell\ell'}\delta_{mm'}\tilde{C}_\ell^{XY}(z_i, z_j), \tag{1.57}$$

where δ is the Kronecker delta. The observed harmonic coefficients $a^X_{\ell m}(z_i)$ are given by the sum of the partial wave coefficients of the signal and of the noise:

$$a^X_{\ell m}(z_i) = s^X_{\ell m}(z_i) + n^X_{\ell m}(z_i). \tag{1.58}$$

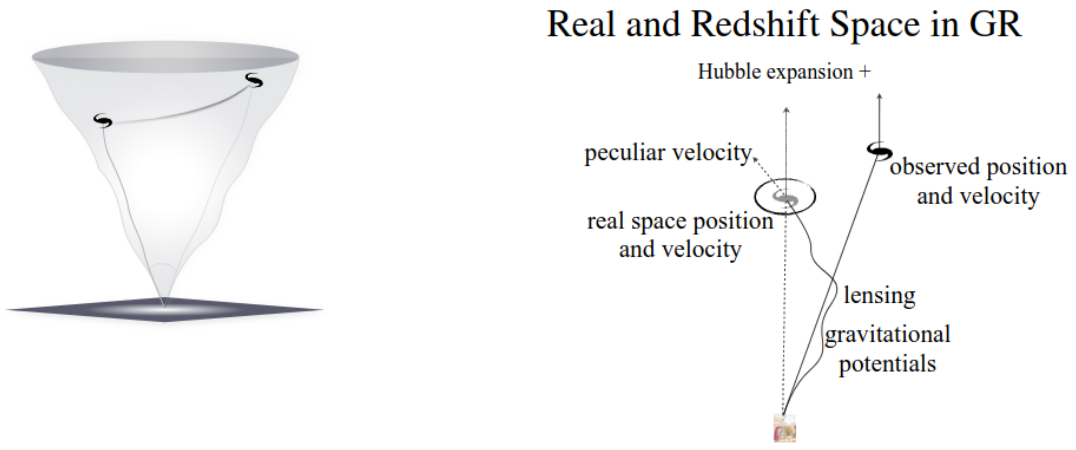

Figure 1.7: Illustrative picture (Raccanelli et al. 2016a) of the effects between the source and the observer on the apparent position of a galaxies: peculiar velocities, lensing and other GR effects alter the observed object position from the intrinsic one.

The observed angular power spectra read as

$$\tilde{C}_\ell^{XY}(z_i, z_j) = C_\ell^{XY}(z_i, z_j) + \delta_{XY}\delta_{ij}\mathcal{N}^X_\ell(z_i). \tag{1.59}$$

The angular power spectrum is directly obtained from the signal wave coefficients as (Raccanelli et al. (2008); Pullen et al. (2013))

$$\langle s^X_{\ell m}(z_i) s^{Y^*}_{\ell' m'}(z_j)\rangle = \delta_{\ell\ell'}\delta_{mm'} C^{XY}_\ell(z_i, z_j). \tag{1.60}$$

Usually, a noise angular power spectrum is constructed from the shot noise $\mathcal{N}^X_\ell(z_i)$ (inversely proportional to the number of sources per steradian), assuming no other sources of error and no correlation between noise terms of different experiments and z bins. In that case, the expectation value of the noise can then be written as

$$\langle n^X_{\ell m}(z_i) n^{Y^*}_{\ell' m'}(z_j)\rangle = \delta_{\ell\ell'}\delta_{mm'}\delta_{XY}\delta_{ij}\mathcal{N}^X_\ell(z_i). \tag{1.61}$$

Other noise sources will be explored throughout this thesis, especially in chapters 3 and 4. Assuming signal and noise as statistically independent, one can write

$$\langle s^X_{\ell m}(z_i) n^{Y^*}_{\ell' m'}(z_j)\rangle = 0. \tag{1.62}$$

Finally, the theoretical angular power spectrum $C^{XY}_\ell(z_i, z_j)$ for different tracers and different redshift bins can be written as

$$C^{XY}_\ell(z_i, z_j) = \frac{2}{\pi}\int \frac{dk}{k}\mathcal{P}(k)\Delta^{X,z_i}_\ell(k)\Delta^{Y,z_j}_\ell(k), \tag{1.63}$$

where $\mathcal{P}(k) = k^3 P(k)$ is the primordial power spectrum and

$$\Delta^{X,z_i}_\ell(k) = \int_{z_i-\Delta z}^{z_i+\Delta z} dz \frac{dN_X}{dz} W(z, z_i)\Delta^X_\ell(k, z), \tag{1.64}$$

where $\dfrac{dN_X}{dz}$ is the source number density per redshift interval, $W(z, z_i)$ is a window function centered at z_i with half-width Δz (with the integral of $W(z, z_i)\dfrac{dN_X}{dz}$ being normalized to unity). Note that equation (1.63) follows the notation of Bonvin & Durrer (2011), which reflects how the public code `CLASS` (Blas et al. (2011a); Di Dio et al. (2013)) is built. The $\Delta^X_\ell(k, z)$ is the angular number count fluctuation of the X tracer, which is determined by density (den), velocity (vel), lensing (len) and gravity (gr) effects (Bonvin & Durrer (2011); Challinor & Lewis (2011a)):

$$\Delta_\ell(k, z) = \Delta^{\rm den}_\ell(k, z) + \Delta^{\rm vel}_\ell(k, z) + \Delta^{\rm len}_\ell(k, z) + \Delta^{\rm gr}_\ell(k, z). \tag{1.65}$$

See also figure 1.7. The reader interested in the full expressions of the number counts fluctuations in equation (1.65) can find them in Appendix A. The relative importance between each of these terms depends on the specific configuration (redshift bins, window

functions, etc.) but some general statements can be made (see e.g., figure 1.8). The main contribution is usually given by the density term, whereas the gravity effects are subdominant (even by two orders of magnitude at $\ell \sim 50$), since it is relevant mostly at horizon scales. The lensing term is only slightly scale-dependent, while the velocity one can be comparable to it at smaller scales, while stronger than it at lower multipoles (even almost one order of magnitude at very low ℓ). This last statement holds especially for auto-bin correlations, while for power spectra among distant redshift bins the lensing term can overcome the velocity.

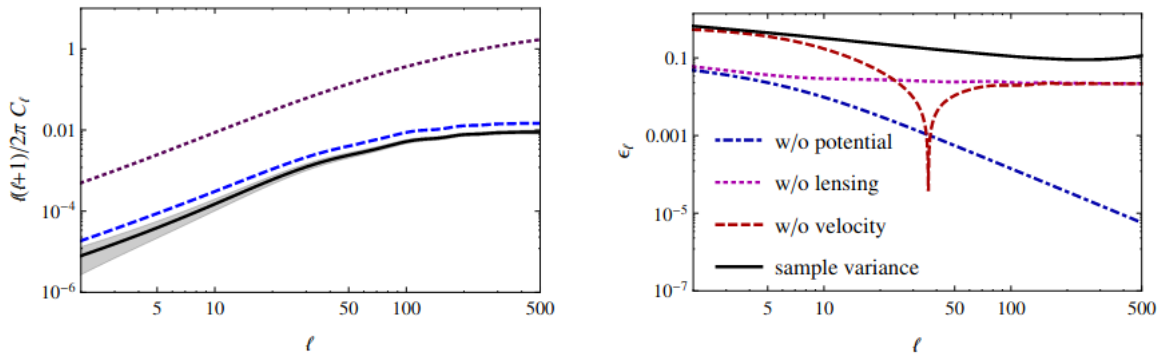

Figure 1.8: Angular power spectra and their dependence on window functions and projection effects, from Di Dio et al. (2013). Left panel: auto-correlation C_ℓs for DES-like galaxies, for a redshift bin centered around $z = 0.55$ and three different window functions: Gaussian with half-width $\Delta z = 0.1$ (solid, black), Top-Hat of half-width $\Delta z = 0.1$ (dashed, blue), and a Dirac delta (dotted, purple). The shaded band indicates the error σ_{C_ℓ}. Right panel: errors on the C_ℓs when neglecting gradually gravitational potential terms (dot-dashed, blue), lensing (dotted, purple) and velocity terms (Doppler and z-space distortions, dashed, red). The r.m.s. variance $\sigma_{C_\ell}/C_\ell^{\rm full}$ is also shown (solid, black). Results are computed for the Gaussian bin case.

One possible tool to compute the angular power spectra is `Multi_CLASS`, the modified version of `CLASS` presented by Bellomo et al. (2020); Bernal et al. (2020) which allows the user to compute cross-correlations between different tracers $X \neq Y$.
As can be seen by the above equations and Appendix A, there are four main ingredients that are needed to fully characterize one tracer X:

- *Redshift distribution* $\dfrac{dN_X}{dz}$: the source number density per redshift interval is characterized by a shape which is a fundamental ingredient in the angular power spectra computation (see equation (1.64)). Eventually, the number of sources in a specific redshift bin is also necessary to compute the shot noise that enters in the estimate of the observed $\tilde{C}_\ell$'s in equation (1.59).

- *Bias* b_X: it quantifies the mismatch between the distribution of matter and of the tracer X (see e.g., Kaiser (1984); Bardeen et al. (1986); Mo & White (1996); Matarrese et al. (1997); Dekel & Lahav (1999); Benson et al. (2000); Peacock & Smith (2000); Desjacques et al. (2018)). In the works on which this thesis is built on the linear bias formulation was adopted. Indicating the local contrasts of matter and tracer X at position x respectively by $\delta(x)$ and $\delta_X(x)$, one can write $\delta_X(x) \equiv \frac{n_X(x)-\bar{n}_X}{\bar{n}_X} = b_X\delta(x)$, where n_X is the comoving density of tracer X and $\bar{n}_X$ is its mean value. The bias appears as a linear factor in the density term of equation (1.65) (see the full expression in appendix A).

- *Magnification bias* $s_X(z)$: it quantifies the change in the observed surface density of sources of tracer X induced by gravitational lensing Turner et al. (1984). Two effects compete against each other: on one side the number of observed sources can increase due to a magnification of the received flux, which would make visible some sources right below the visibility threshold (luminosity or magnitude for galaxies and Signal-to-Noise ratio for GWs); on the other side an increase of the area reduces the observed number density of objects. The magnification bias mainly affects the lensing term of equation (1.65), but enters also in the velocity and gravity terms.

- *Evolution bias* $f_X^{\rm evo}$: it reflects the fact that the number of elements of a tracer X is not necessarily conserved in redshift due to the possible formation of new objects. The evolution bias can be written as (Challinor & Lewis (2011b); Jeong et al. (2012); Bertacca et al. (2012b)): $f_{\rm g}^{\rm evo}(z) = \frac{d\ln\left(a^3\frac{d^2N_{\rm g}}{dzd\Omega}\right)}{d\ln a}$, where a is the scale factor and $\frac{d^2N_{\rm X}}{dzd\Omega}$ is the absolute distribution of objects of tracer X, which can usually be substituted by the observed distribution with good approximation (Scelfo et al. (2018)). The evolution bias appears only in sub-leading contributions, since it is just present in the non-dominant part of the velocity term and in the gravity term (which has a smaller influence with respect to the others, see e.g., Di Dio et al. (2013)) of equation (1.65).

We complete this section by explicitly summarizing the dependence of the various contributions to the angular number count fluctuations on the three biases types presented

above (see appendix A for full expressions):

$$\begin{cases} \Delta_\ell^{\rm den} = \Delta_\ell^{\rm den}(b_X) \\ \Delta_\ell^{\rm vel} = \Delta_\ell^{\rm vel}(s_X, f_X^{\rm evo}) \\ \Delta_\ell^{\rm len} = \Delta_\ell^{\rm len}(s_X) \\ \Delta_\ell^{\rm gr} = \Delta_\ell^{\rm gr}(s_X, f_X^{\rm evo}) \end{cases} \tag{1.66}$$

where dependencies on k and z are implied.

1.3.2 Intensity Mapping

One key observable that we studied in cross-correlation with GWs is given by the Line Intensity Mapping (LIM, or simply IM) of the 21 cm line. Not only is IM a relatively new technique, but especially studies on the cross-correlation of GW×IM are only at their beginning, with works present in this thesis being at the forefront. In this paragraph we sketch an overview on IM, whereas we address the interested reader to Kovetz et al. (2017c); Bernal & Kovetz (2022) for comprehensive reviews.

IM is a novel technique consisting of the measurement of the integrated emission from spectral lines coming from unresolved galaxies and the diffuse inter-galactic medium (IGM). The IM technique allows probing large areas of the sky in a relatively small amount of time, since it does not aim at resolving single galaxies: it measures the intensity of a specific emission line in order to map the underlying matter distribution, treating it as a diffuse background. Since we exactly know the emission frequency of the line under study, the observed wavelength provides information on the radial position of the source, whereas its brightness temperature fluctuations describe how the underlying LSS is distributed. We refer the interested reader to Furlanetto et al. (2006); Morales & Wyithe (2010); Pritchard & Loeb (2011); Liu & Shaw (2020) for comprehensive reviews on the 21 cm line.
One of the advantages of performing IM is given by the high amount of available modes: IM (at a specific observed wavelength) provides maps similar to the CMB ones, but with the significant advantages of having accessibility to (potentially) very small scales due to the absence of Silk damping and the ability of performing a very refined tomography over large volumes. It is possible to calculate that the number of modes that would be reachable (in the ideal case without foregrounds and partial sky coverage) with IM could potentially be as high as 10^{16} (Loeb & Zaldarriaga 2004).
As Kovetz et al. (2017c) point out, the potential fields of application for IM cover a very wide area, ranging from astrophysics to cosmology. The main ones are:

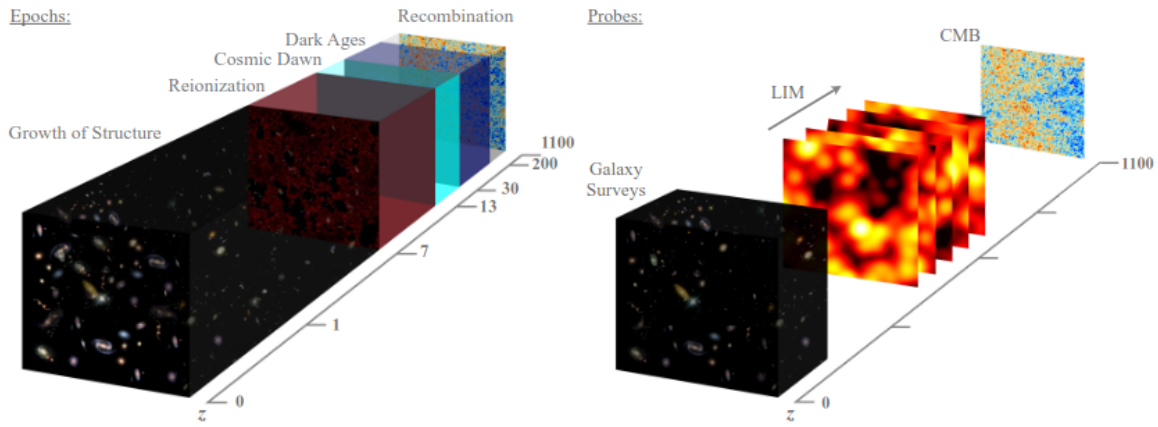

Figure 1.9: Illustrative picture of the large volume accessibility by IM (Kovetz et al. 2017c).

- **Galaxy Evolution**. The observation of large volumes, associated with a good sensitivity to faint objects and a very refined redshift information are great ingredients to answer questions on this topic. For example, IM can shed light on the cosmic star formation rate history thanks to the ability of providing a complete census of emitting gas that traces star formation across cosmic times. The interstellar medium and the IGM can also be investigated thanks to observations of multiple emission lines coming up to very high redshifts. See e.g., figure 1.10 (taken from Spinelli et al. (2020)) where the HI power spectrum is provided at different z and for different galaxy types.

- **Reionization**. During the reionization epoch, the first stars and galaxies were forming, emitting ultraviolet radiation which ionized the surrounding neutral hydrogen (HI). IM can be a powerful tool in this regard, since it can map both the star forming galaxies (origins of the ionizing photons) and the distribution of remaining neutral gas in the IGM.

- **Cosmology.** IM can be also used in cosmology to test theories both in and beyond the ΛCDM model. Since line emitters observed with IM trace the underlying dark matter distribution and can provide observables up to high redshifts, they can probe the LSS distribution and test, for example, DE models and Modified Gravity (MG) theories. Furthermore, decays or annihilations from DM particles would be detectable through IM, and IM measurements over large redshift volumes at large scales could help discern between single and multi-field models of inflation.

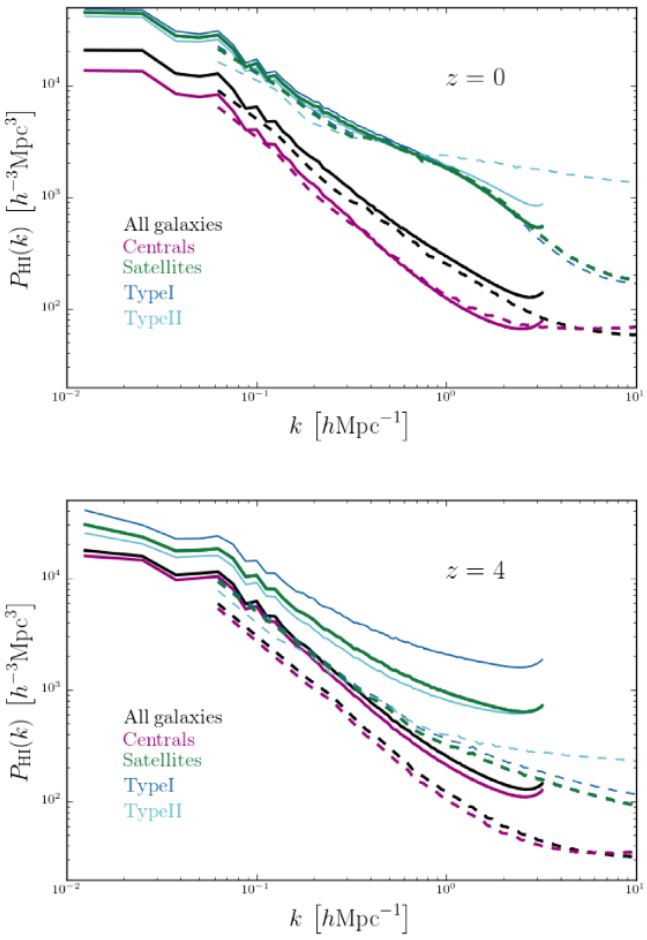

Figure 1.10: The power spectrum of HI selected galaxies at $z = 0, 4$ in the Millennium I (Springel (2005), solid) and Millennium II (Boylan-Kolchin et al. (2009), dashed lines) simulations, considering separately the contribution from centrals (magenta) and satellites (green). Satellite galaxies are further divided into Type I (dark blue) and Type II (light blue). The total HI power spectrum is shown in black. Figure from Spinelli et al. (2020).

The redshifted 21 cm line from the spin-flip transition of neutral hydrogen is one of the most promising targets for IM and several detections of the signal in cross-correlation with galaxy surveys have already been achieved (see e.g., Chang et al. (2010); Masui et al. (2013); Anderson et al. (2018); Wolz et al. (2021)), since this tool potentially allows us to trace the LSS over a vast range of redshifts, from the end of the reionization epoch ($z \sim 6$) to the present day (Villaescusa-Navarro et al. (2014)). IM surveys have been proposed for the forthcoming Square Kilometre Array Observatory (SKAO, Braun et al. (2015)) and are ongoing on its precursor MeerKAT (Santos et al. (2017); Wang et al. (2020)), potentially bringing exquisite constraints for Cosmology (Bacon et al. (2020); Maartens et al. (2015); Santos et al. (2015)). Other purpose-built experiments

are taking data or will be build in the near future e.g. CHIME (Bandura et al. (2014)), FAST (Hu et al. (2020)), BINGO (Battye et al. (2016)), Tianlai (Das et al. (2018)) and HIRAX (Newburgh et al. (2016)).
The IM technique has already been the subject of cross-correlation studies with other LSS tracers, such as e.g., Schmidt et al. (2013a); Alonso & Ferreira (2015a); Kovetz et al. (2017b); Alonso & Ferreira (2015b); Wolz et al. (2016); Pourtsidou et al. (2016); Pourtsidou (2016); Raccanelli et al. (2016a); Pourtsidou et al. (2017); Wolz et al. (2017); Alonso et al. (2017); Wolz et al. (2018); Cunnington et al. (2018).
One way to describe the HI distribution can be by means of the linear power spectrum

$$P_{\rm HI}(z,k,\mu) = \bar{T}_{\rm b}^2(z)\left[b_{\rm HI}(z) + f(z)\mu^2\right]^2 P_{\rm m}(z,k) \tag{1.67}$$

where $\bar{T}_b$ is the mean brightness temperature, $b_{\rm HI}$ is the HI bias, f is the growth rate, μ is the cosine of the angle between the wave-number and the line of sight and $P_{\rm m}(z,k)$ is the linear matter power spectrum. The second term of the sum describes redshift-space distortions. Figure 1.10 shows examples from HI power spectra from different sources. Several works (see e.g., Spinelli et al. (2020); Berti et al. (2022)) approach the modeling and study of the 21 cm line by means of this observable. An alternative approach, such as that adopted in the works presented in this thesis, is to describe the IM signal with the same angular power spectra formalism for the C_ℓs introduced in the previous section, with a few formalism adaptations.
Chapters 3 and 4 provide the GW×IM cross-correlation as a potential tool for both astrophysics and cosmology. We refer the reader to those chapters for the modeling of the angular power spectra in the case of un-resolved observables, such as the IM.

1.4 Methodology: Fisher analysis

In this section we sketch the cornerstones of the main statistical tool used in most of the works presented in this thesis: the Fisher matrix analysis. Fisher analysis is a useful and quick tool to predict how well a given designed experiment will be able to perform in constraining a set of parameters. This methodology is at the bases of the works presented in chapters 3 and 4. Since the main observables considered in this thesis are angular power spectra C_ℓs, this chapter also relies on those, but we stress that the general concepts presented here are valid for other observables too.

Assuming two tracers {X,Y} (e.g., GW events, IM, resolved galaxies), when performing tomography we can divide the total redshift interval surveyed in $N_{\rm bins}^{\rm X}$ bins, with amplitude $\Delta z^{\rm X}$ for tracer X, and in $N_{\rm bins}^{\rm Y}$ bins with amplitude $\Delta z^{\rm Y}$ for tracer Y.

Considering the observed power spectra $\tilde{C}_\ell$s and a generic set of parameters $\{\theta_n\}$ for the Fisher analysis, we can organize our data in the (symmetric) matrix $\mathcal{C}_\ell$ as

$$\mathcal{C}_\ell = \begin{bmatrix} \tilde{C}_\ell^{\,\mathrm{X\,X}}(z_1^{\mathrm{X}}, z_1^{\mathrm{X}}) & \dots & \tilde{C}_\ell^{\,\mathrm{X\,X}}(z_1^{\mathrm{X}}, z_N^{\mathrm{X}}) & \tilde{C}_\ell^{\,\mathrm{X\,Y}}(z_1^{\mathrm{X}}, z_1^{\mathrm{Y}}) & \dots & \tilde{C}_\ell^{\,\mathrm{X\,Y}}(z_1^{\mathrm{X}}, z_N^{\mathrm{Y}}) \\ & \dots & \tilde{C}_\ell^{\,\mathrm{X\,X}}(z_2^{\mathrm{X}}, z_N^{\mathrm{X}}) & \tilde{C}_\ell^{\,\mathrm{X\,Y}}(z_2^{\mathrm{X}}, z_1^{\mathrm{Y}}) & \dots & \tilde{C}_\ell^{\,\mathrm{X\,Y}}(z_2^{\mathrm{X}}, z_N^{\mathrm{Y}}) \\ & \dots & \vdots & \vdots & \dots & \vdots \\ & & \tilde{C}_\ell^{\,\mathrm{X\,X}}(z_N^{\mathrm{X}}, z_N^{\mathrm{X}}) & \tilde{C}_\ell^{\,\mathrm{X\,Y}}(z_N^{\mathrm{X}}, z_1^{\mathrm{Y}}) & \dots & \tilde{C}_\ell^{\,\mathrm{X\,Y}}(z_N^{\mathrm{X}}, z_N^{\mathrm{Y}}) \\ & & & \tilde{C}_\ell^{\,\mathrm{Y\,Y}}(z_1^{\mathrm{Y}}, z_1^{\mathrm{Y}}) & \dots & \tilde{C}_\ell^{\,\mathrm{Y\,Y}}(z_1^{\mathrm{Y}}, z_N^{\mathrm{Y}}) \\ & & & & \dots & \vdots \\ & & & & & \tilde{C}_\ell^{\,\mathrm{Y\,Y}}(z_N^{\mathrm{Y}}, z_N^{\mathrm{Y}}) \end{bmatrix}, \quad (1.68)$$

The matrix $\mathcal{C}_\ell$ has dimensions of $(N_{\mathrm{bins}}^{\mathrm{X}} + N_{\mathrm{bins}}^{\mathrm{Y}}) \times (N_{\mathrm{bins}}^{\mathrm{X}} + N_{\mathrm{bins}}^{\mathrm{Y}})$, and in general $z_i^{\mathrm{X}} \neq z_i^{\mathrm{Y}}$. The $\mathcal{C}_\ell$ matrix is then used to compute the Fisher matrix elements as

$$F_{\alpha\beta} = f_{\mathrm{sky}} \sum_\ell \frac{2\ell+1}{2} \mathrm{Tr}\left[\mathcal{C}_\ell^{-1}(\partial_\alpha \mathcal{C}_\ell)\mathcal{C}_\ell^{-1}(\partial_\beta \mathcal{C}_\ell)\right], \quad (1.69)$$

where ∂_α indicates the partial derivative with respect to the parameter θ_α and f_{sky} is the fraction of the sky covered by the intersection of the surveys for the two tracers. The sum over multipoles ℓ is performed up to a maximum value ℓ_{max}, which corresponds to the achievable angular resolution for the considered sources and instruments. All scales smaller than it are cut from the analysis.

Finally, the Fisher-estimated marginal error on the parameter θ_α is given by $\sqrt{(F^{-1})_{\alpha\alpha}}$. According to statistics and estimation theory, the so called Cramér-Rao bound provides the smallest error that one should expect to achieve in reality: errors on parameters deriving from "real-life" experiments are expected to be equal or higher than the Fisher estimated errors (Cramér-Rao inequality), where the equality stands only in the case of gaussian likelihood. Even though this is often an approximation and the Fisher approach may not always give precise results, it still remains an easy and quick method to provide forecasts for planned experiments. We refer the interested reader to Bellomo et al. (2020); Bernal et al. (2020) for further discussion about Fisher analysis and the impact of several approximations therein and in the observables considered. Figure 1.11 is taken from (Bellomo et al. 2020). It pictures how approximations in the observables can lead to altered Fisher forecasts. In that case, the ratio of the Fisher matrix elements for several cosmological parameters is provided, including and neglecting the lensing contribution to the angular power spectra C_ℓs in the case of uniform or Euclid-like galaxy distributions. Further details can be found in the related reference.

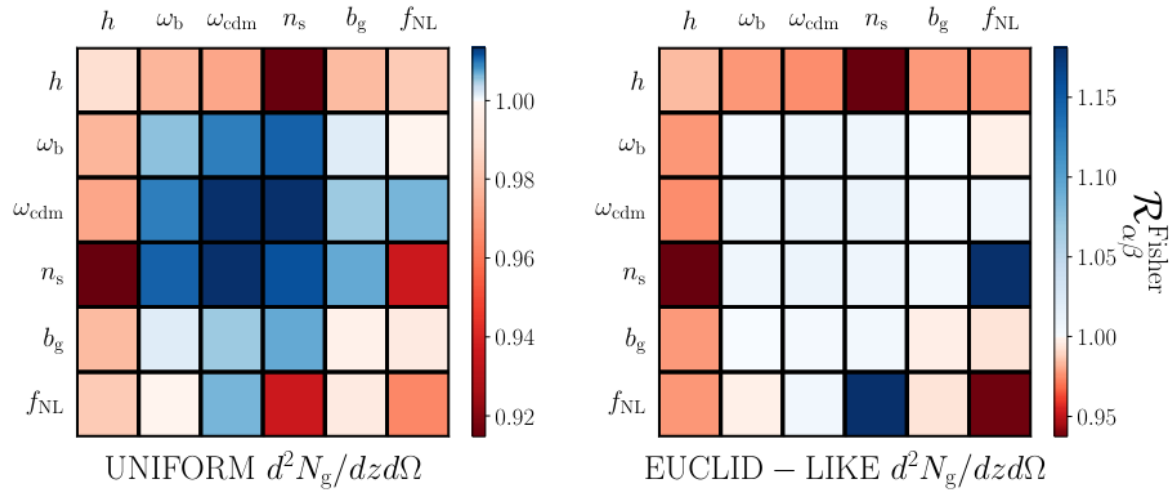

Figure 1.11: Ratio of the Fisher matrix elements (parameters as in figure) obtained including and neglecting the lensing contribution to the angular power spectra C_ℓs in the case of uniform or Euclid-like galaxy distributions, with a magnification bias $s = 0.6$ (Bellomo et al. 2020). Approximations in the observables can lead to altered Fisher forecasts.

2

Exploring galaxies - gravitational waves cross-correlations as an astrophysical probe

This chapter is based on the following manuscript:
G. Scelfo, L. Boco, A. Lapi, M. Viel
Exploring galaxies - gravitational waves cross-correlations as an astrophysical probe
JCAP 10 (2020) 045, `arXiv:2007.08534`.

2.1 Chapter overview and motivation

In this chapter we extend the work addressed by the community in the GW $\times$ LSS area studying the measurable cross-correlation signal with a refined description of both the LSS and GW tracers. Regarding the characterization of the LSS tracers we make use of actively star-forming galaxies. Observations of the last decade, with the advent of high redshift far-IR/sub-mm surveys, have helped in robustly characterizing the galaxies luminosity functions, from which the Star Formation Rate (SFR) ψ can be derived, allowing us to have a rather solid statistics of actively star-forming galaxies (for a more detailed discussion see section 2.2.1.1 and references therein). Therefore, we exploit the galaxy SFR to organize different galaxy types in different SFR bins. In this way we can look at the contribution to the cross-correlation signal coming from galaxies with different star formation activities.
On the other hand, we model the redshift distributions of the detected GW signals, coming from all types of merging COs (BH-BH, BH-NS, NS-NS), by convolving a de-

tector sensitivity curve with the intrinsic merging rates. We self-consistently derive the latter from the aforementioned galaxy distribution. Thus, the two tracers considered here are not coming from different and independent sources: we are looking at the same objects (galaxies) but through different messengers (light and GWs). However, we need to take into account that the GWs distribution does not only depend on the SFR of the galaxies. Both the number of merging compact objects and their chirp mass (affecting the GW signal detectability) can strongly depend also on the environmental conditions in which the binary forms and evolves. For these reasons, in this work we use a refined determination of the COs merging rates, following Boco et al. (2019), where a metallicity distribution is associated to each single galaxy through a chemical evolution model. Once the intrinsic merging CO distribution is computed, we convolve it with the sensitivity curve of the future third generation GW observatory ET (see e.g., Sathyaprakash et al. (2012b)) to get the detected GW events redshift distribution. These characterizations altogether lead to our forecast on the cross-correlation signal that can be obtained by realistically modeling these two types of tracers, especially awaiting the soon-to-come GWs detections from third generation observatories. We perform here both a tomographic and a non tomographic approach, working in the harmonic space and considering as observables the number counts angular power spectra C_ℓs defined in section 1.3.1.

As a possible application of this cross-correlation formalism, we explore the idea of testing different astrophysical scenarios, which predict different GWs distributions, clustering and other specifics. We consider an exemplifying proof-of-concept case, in which we test whether metallicity dependencies on the COs merging efficiency can be detected and distinguished with respect to a benchmark case with no metallicty dependence. Looking at the distribution and clustering of these two tracers can be a promising tool to discriminate between different features imprinted by several astrophysical mechanisms.

This chapter is structured as follows: in section 2.2 we describe the tracers considered and the theoretical background behind the physical quantities characterizing them; in section 2.3 we present estimates of the cross-correlation signals through Signal-to-Noise computations; in section 2.4 we describe how to potentially distinguish astrophysical features from different models and predict its viability using a test scenario; in section 2.5 we wrap the discussion up.

2.2 Tracers

In this section we describe how our two tracers (galaxies and GWs) are characterized, along with the theoretical frameworks used in their modeling. Since we deal with a statistical approach to count and describe the properties of galaxies and GWs, we use the notation $dp/d\Theta$ to express the probability distribution of a generic variable Θ.

2.2.1 Galaxies

Our first tracers are actively star-forming galaxies. We do not deal with any specific galaxy catalog: we count and distribute galaxies on the basis of the observationally determined star formation rate functions (SFRFs) at different redshifts (described in section 2.2.1.1). The SFR of a galaxy measures the stellar mass in solar units formed per year inside the galaxy. We briefly explain how it is measured in section 2.2.1.1. In this work we consider objects with three different SFR lower limits: $\psi \geq 10$, 100, 300 $M_\odot$/yr. The lower value of $10 M_\odot$/yr roughly corresponds to the limit below which uncertainties in the SFRFs are significant, especially at high redshift. The cut of $100 M_\odot$/yr is set to take into account the highly star forming dusty galaxies which constitute the bulk of the cosmic SFR. Finally, the highest limit of $300 M_\odot$/yr is set to take into account the most extreme star forming objects.

2.2.1.1 SFR functions

The star formation rate functions $\mathrm{SFRF} = d^2N/d\log_{10}\psi/dV$ correspond to the number density of galaxies per cosmological comoving volume per logarithmic bin of SFR at a given cosmic time t or redshift z. In the last years several observations (e.g., UV+far-IR/submillimeter/radio luminosity functions and stellar/gas/dust mass functions) have allowed to robustly estimate these functions. The SFR of a galaxy could in principle be estimated by its UV luminosity, since it is proportional to the quantity of young stars present in the galaxy. However, this estimation can be easily biased by the presence of dust. Indeed, even a modest amount of dust can significantly absorb the UV radiation and re-emit it in the far-IR/(sub)millimeter wavelengths. Standard UV slope corrections (e.g., Meurer et al. (1999); Calzetti et al. (2000); Bouwens et al. (2015)) can still be applied to galaxies with relatively low SFR $\psi \lesssim 30 - 50 M_\odot/yr$, since the dust attenuation for them is mild. Therefore, deep UV surveys in the rest frame UV band are enough to robustly determine the SFRF at the faint end. Instead, in highly star-forming galaxies with SFR $\psi \gtrsim 30 - 50 M_\odot$/yr dust obscuration is heavy and the corrections mentioned above are no more reliable (e.g., Silva et al. (1998);

Efstathiou et al. (2000); Coppin et al. (2015); Reddy et al. (2015); Fudamoto et al. (2017)). To soundly estimate their SFRF, it is necessary to use far-IR/(sub)millimeters observations. The latters have been exploited in many works over the recent years (e.g., Lapi et al. (2011); Gruppioni et al. (2013, 2015); Gruppioni & Pozzi (2019); Magnelli et al. (2013)) to reconstruct, in combination with UV data, the SFRF for the whole SFR range at redshift $z \lesssim 3$. At higher redshifts, given the sensitivity limits of wide-area far-IR surveys, the reconstruction of the SFRF, especially at the bright end, is more uncertain. Useful information have been obtained from far-IR/(sub)millimeter stacking (see Rowan-Robinson et al. (2016), Dunlop et al. (2017)) and super-deblending techniques (see Liu et al. (2018)), from targeted far-IR/(sub)millimeter observations (e.g., Riechers et al. (2017); Marrone et al. (2018); Zavala et al. (2018)) and from radio surveys (Novak et al. (2017)).

All the above datasets have been fitted through simple Schechter functions by Mancuso et al. (2016), obtaining:

$$\frac{d^2N}{d\log_{10}\psi\, dV}(\log_{10}\psi, z) = \mathcal{N}(z)\left(\frac{\psi}{\psi_c(z)}\right)^{1-\alpha(z)} e^{-\psi/\psi_c(z)}\,, \tag{2.1}$$

where the values of the redshift-dependent parameters $\mathcal{N}(z)$, $\psi_c(z)$ and $\alpha(z)$ can be found in table 1 of Mancuso et al. (2016) (see also figure 1 of Boco et al. (2019)). From the SFRF we can obtain the number density of galaxies per unit comoving volume at different cosmic times t and the cosmic star formation rate density as:

$$\frac{dN}{dV}(t) = \int d\log_{10}\psi\, \frac{d^2N}{d\log_{10}\psi\, dV}\,(\log_{10}\psi, t)\,, \tag{2.2}$$

$$\rho_\psi(t) = \int d\log_{10}\psi\; \psi\, \frac{d^2N}{d\log_{10}\psi\, dV}\,(\log_{10}\psi, t)\,. \tag{2.3}$$

Notice that the evolution of the cosmic star formation rate density with redshift, reconstructed in this way, is well in agreement with the available datasets (see Boco et al. (2019)). The number of galaxies per redshift bin dN/dz can be easily obtained multiplying equation 2.2 by the differential cosmological comoving volume dV/dz. The redshift distribution of our 3 galactic populations (galaxies with $\psi > 10,\ 100,\ 300\, M_\odot/\mathrm{yr}$) can be obtained integrating the SFRF excluding galaxies below a certain threshold $\bar{\psi}$:

$$\frac{dN_{\bar{\psi}}}{dz}(t, \psi \geq \bar{\psi}) = \frac{dV}{dz}\int_{\bar{\psi}} d\log_{10}\psi \frac{d^2N}{d\log_{10}\psi\, dV}. \tag{2.4}$$

In figure 2.1, left panel, the three $dN_{\bar{\psi}}/dz$ of the galactic populations considered in this work are plotted as a function of redshift.

From this quantity it is straightforward to compute the evolution bias for each galactic population as

$$f_{\rm g}^{\rm evo}(z) = \frac{d\ln\left(a^3 \frac{d^2 N_{\bar{\psi}}(z,\psi\geq\bar{\psi})}{dz d\Omega}\right)}{d\ln a}. \tag{2.5}$$

2.2.1.2 Galaxy bias

A fundamental ingredient entering the computation of the observed number counts fluctuations in equation (1.65) is the bias $b_X(z)$. Since our tracers are galaxies selected, counted and divided by their SFR, we should connect the bias to this quantity. We adopt the procedure of Aversa et al. (2015) associating the luminosity/SFR of the galaxy to the mass of the hosting dark matter halo through an abundance matching technique and then assigning to a galaxy with given SFR the bias of the corresponding halo. Abundance matching is a standard method to derive a monotonic relationship between the galaxy and the halo properties by matching the corresponding number densities in the following way:

$$\int_{\log_{10}\psi}^{\infty} d\log_{10}\psi' \frac{d^2N}{d\log_{10}\psi'\, dV} = \int_{-\infty}^{\infty} d\log_{10} M'_H \frac{d^2N}{d\log_{10} M'_H\, dV} \frac{1}{2} erfc\left\{\frac{\log_{10}\left(M_H(\psi)/M'_H\right)}{\sqrt{2}\tilde{\sigma}}\right\}, \tag{2.6}$$

where M'_H is the halo mass, $d^2N/d\log_{10} M'_H/dV$ is the galaxy halo mass function i.e. the mass function of halos hosting one individual galaxy (see Appendix A of Aversa et al. (2015)) and $M_H(\psi)$ is the relation we are looking for. Finally, $\tilde{\sigma} \equiv \sigma\, d\log_{10} M_H/d\log_{10}\psi$ is the scatter around that relation (we set $\sigma_{\log_{10}\psi} \simeq 0.15$ following Lapi et al. (2006); Lapi & Cavaliere (2011); Lapi et al. (2014)). Once $M_H(\psi)$ is determined we assign to each galaxy the bias corresponding to the halo associated to its SFR: $b(z,\psi) = b(z, M_H(z,\psi))$, where $b(z, M_H)$ is computed as in Sheth et al. (2001) and approximated by Lapi & Danese (2014). Note that this formulation for the bias is based on the excursion set approach. Other possible alternatives are present, such as the Effective Field Theory, Peak Theory, etc. (see e.g., Desjacques et al. (2018); Bernardeau et al. (2002) and references therein).

It is now easy to compute an effective bias for all the galaxies above a certain SFR threshold $\bar{\psi}$ weighting $b(z,\psi)$ by the corresponding galaxy distribution:

$$b_{\bar{\psi}}(z,\psi\geq\bar{\psi}) = \frac{\int_{\log_{10}\bar{\psi}}^{\infty} d\log_{10}\psi \frac{d^2N}{d\log_{10}\psi\, dV} b(z,\psi)}{\int_{\log_{10}\bar{\psi}}^{\infty} d\log_{10}\psi \frac{d^2N}{d\log_{10}\psi\, dV}}. \tag{2.7}$$

In figure 2.1, middle panel, we show the galaxy effective bias as a function of redshift for our galactic populations. We see, as expected, that it tends to increase with redshift

and it is, in general, lower for galaxies with lower SFRs, since these are typically associated to less massive halos.
Note that the bias computed in this section refers to star forming galaxies, which can be the progenitors of quenched massive objects at the present time. We stress that, in order to estimate the bias for these galaxies, we should not look at their current SFR, but at the SFR of their progenitor when most of the stellar mass was accumulated, which is directly linked to the mass of the host dark matter halo, via the abundance matching technique described in equation (2.6).

2.2.1.3 Galaxy magnification bias

The magnification bias is another important factor entering the angular power spectra computation. In fact, as we already described in section 1.3.1, the contribution to the angular number count fluctuations due to the lensing term of equation (1.65) can be comparable to that of the velocity term (or even higher, especially when correlating objects between distant redshift bins). As mentioned above, our galactic populations have SFR cuts $\bar{\psi} = 10,\, 100,\, 300\, M_\odot/\mathrm{yr}$. The magnification bias for each of them is proportional to the logarithmic slope of their dN_ψ/dz computed at $\psi = \bar{\psi}$:

$$s_{g,\bar{\psi}}(z) = -\frac{2}{5}\left.\frac{d\log_{10}\left(\frac{d^2N_\psi(z,>\psi)}{dzd\Omega}\right)}{d\log_{10}\psi}\right|_{\psi=\bar{\psi}} . \tag{2.8}$$

Using equation (2.4) we can show that the magnification bias can be directly related to the SFRF as:

$$s_{g,\bar{\psi}}(z) = \frac{2}{5\ln 10}\frac{\frac{d^2N}{d\log_{10}\psi\, dV}(z,\bar{\psi})}{dN_{\bar{\psi}}/dz}\frac{dV}{dz} . \tag{2.9}$$

Figure 2.1 (right panel) shows the magnification bias for our galactic populations as a function of redshift. We can see that, at small z, the magnification bias decreases rapidly, especially for the tracers with higher SFRs: this is due to the fact that at small redshifts we have less and less galaxies with high SFRs, therefore the function $d^2N(z,\psi\geq\bar{\psi})/dz/d\Omega$ strongly depends on the choice of the faint end in SFR. Moreover, the overall magnification bias for higher star forming galaxies is larger because they are less and a variation of the faint end SFR limit has a larger impact on their dN/dz. This is why, in general, the magnification bias shape tends to be specular to the one of the dN/dz.

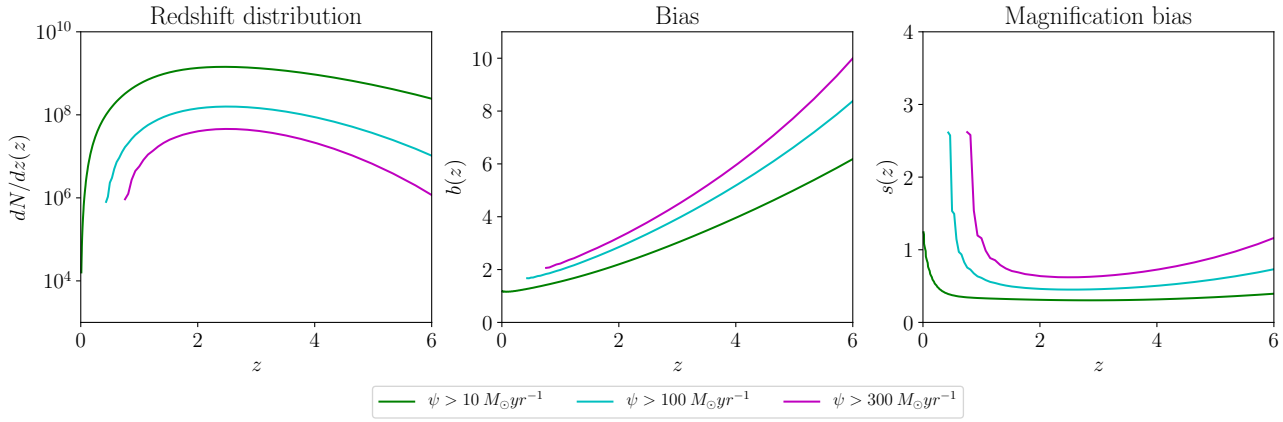

Figure 2.1: Full-sky redshift distributions (*left*), bias (*center*) and magnification bias (*right*) for all galactic populations. Quantities referred to galaxies with Star Formation Rate $\psi > 10 M_\odot/yr$, $\psi > 100 M_\odot/yr$, $\psi > 300 M_\odot/$yr are respectively in green, cyan and magenta lines.

2.2.2 Gravitational waves

The other class of tracers that we are considering are resolved GWs signals coming from the merging of BH-BH, NS-NS and BH-NS binaries. In the next subsections, as already done for the case of galaxies, we are going to illustrate how to compute their merging and detected rates, their bias and magnification bias.

2.2.2.1 Merging rates

The merging rate of compact binaries is the number of mergers per year per redshift bin $d\dot{N}/dz$[1]. Multiplying it by an observational time one gets the number of events per redshift bin in that period of time. Computing the merging and detected rates of compact binaries is a complex issue since it involves the necessity to understand and to correctly model many astrophysical processes occurring on different time and spatial scales: from stellar astrophysics, to galaxy formation and evolution, to GW physics. However, a number of studies have approached the problem combining population synthesis simulations (e.g., Dominik et al. (2013, 2015); de Mink et al. (2013); Spera et al. (2015); Spera & Mapelli (2017); Spera et al. (2019); Giacobbo & Mapelli (2018)) either with cosmological simulations (e.g., Mapelli et al. (2017); O'Shaughnessy et al. (2017); Lamberts et al. (2018); Mapelli & Giacobbo (2018); Artale et al. (2019)) or with recipes for the cosmic star formation rate density and metallicity distributions inferred from observations (e.g., Belczynski et al. (2010); Lamberts et al. (2016); Cao et al.

[1]The factor $d\dot{N}/dz$ is well defined since it stays put for typical observation times of the order of $\sim 10\,$yr.

(2018); Elbert et al. (2018); Li et al. (2018); Boco et al. (2019); Neijssel et al. (2019)). In this work we adopt the same approach of Boco et al. (2019), briefly re-sketched hereafter for completeness.

The three main ingredients to compute the merging rates of compact binaries are: *i)* an observational determination of the SFRF at different redshifts, *ii)* average chemical enrichment histories of individual galaxies and *iii)* outcomes from single stellar and binary evolution simulations.

The first ingredient has already been described in section 2.2.1.1 and provides the galaxy statistics. In the following subsections we are going to describe respectively the other two ingredients and the way to combine them to compute the merging rates of compact binaries.

Metallicity

The average chemical enrichment histories of individual galaxies is crucial since it allows to associate a metallicity Z to galaxies with different properties (SFR, mass, age or morphological type). Knowing the metallicity is fundamental because many binary evolutionary phenomena strongly depend on it: stellar winds, supernova kicks, direct collapse, common envelope effects, etc. (for a more detailed explanation of the main effects of metallicity on stellar and binary evolution see section 2.4.1 and references therein). In Boco et al. (2019) the chemical enrichment history of a galaxy with a given average SFR is reproduced with a simple model featuring a linear increase of the metallicity in the early stages of the galaxy life up to a saturation value dependent on the SFR. This model is an approximation of the more elaborated chemical evolution model of Pantoni et al. (2019) and Lapi et al. (2020) and well reproduces observations of both elliptical and disk galaxies (see e.g., Arrigoni et al. (2010); Spolaor et al. (2010); Gallazzi et al. (2014); Andrews & Martini (2013); Zahid et al. (2014); de la Rosa et al. (2016); Onodera et al. (2016)). The authors of Boco et al. (2019) generate a metallicity distribution at given cosmic time t and SFR $dp/d\log_{10} Z\,(\log_{10} Z|t,\psi)$ taking into account the time spent by a galaxy with given SFR in each bin of metallicity. Their final expression to compute the metallicity distribution is:

$$\frac{dp}{d\log_{10} Z}(\log_{10} Z|t,\psi) = \Delta\times\frac{Z}{Z_{sat}}\ln(10)\Theta_H(Z-Z_{sat})+(1-\Delta)\times\delta_D(\log_{10} Z-\log_{10} Z_{sat})\,, \tag{2.10}$$

where $Z_{sat}(t,\psi)$ and $\Delta(t,\psi)$ are parameters depending on the cosmic time and the SFR of the single galaxy. Z_{sat} represents the saturation value of the metallicity and its typical values are in the range $\sim 0.3-1.5Z_{\odot}$, $\Delta\sim 0.1-0.3$ specifies how quickly the

metallicity saturates to such values as a consequence of the interplay between cooling, dilution and feedback processes.

Stellar and binary evolution

The outcomes of single stellar and binary evolution simulations can provide three important factors: the remnant mass $m_\bullet(m_\star, Z)$ as a function of the zero age main sequence (ZAMS) star mass $m_\star$ and metallicity Z, a time delay distribution between the formation of the binary and the merging dp/dt_d and a mass ratio distribution dp/dq, where q is the ratio between the less and the more massive compact remnant.
For the mass distribution of compact remnants we take as a reference the $m_\bullet(m_\star, Z)$ relation given in Spera & Mapelli (2017), and we generate a probability distribution function just applying a logarithmic gaussian scatter ($\sigma = 0.1$dex) around the $m_\bullet(m_\star, Z)$ value to take into account possible uncertainties coming from stellar evolutionary processes as in Boco et al. (2019):

$$\frac{dp}{d\log_{10} m_\bullet}(m_\bullet|m_\star, Z) = \frac{1}{\sqrt{2\pi}\sigma} \exp\left[-(\log_{10} m_\bullet - \log_{10} m_\bullet(m_\star, Z))^2/2\sigma^2\right]. \quad (2.11)$$

To get rid of the dependence on the initial stellar mass it is sufficient to select an initial mass function (IMF) $\phi(m_\star)$ (in this work we used the one by Chabrier (2003)[2]) and integrate over the initial stellar masses weighting the integral with the IMF:

$$\frac{dp}{d\log_{10} m_\bullet}(m_\bullet|Z) = \int_{\bar{m}_\star} dm_\star \phi(m_\star) \frac{dp}{d\log_{10} m_\bullet}(m_\bullet|m_\star, Z), \quad (2.12)$$

where $\bar{m}_\star \sim 7M_\odot$ is the ZAMS star mass limit originating a NS remnant[3]. However, since the amplitude of the gravitational wave events is determined by the chirp mass $\mathcal{M}_{\bullet\bullet} \equiv m_\bullet q^{3/5}/(1+q)^{1/5}$, rather than by the primary mass $m_\bullet$ [4], we should make use of the mass ratio distribution to change variable and determine the probability distribution function for a given chirp mass in the following way:

$$\frac{dp}{d\mathcal{M}_{\bullet\bullet}}(\mathcal{M}_{\bullet\bullet}|Z) = \int dq \frac{dp}{dq} \frac{dp}{dm_\bullet}(m_\bullet(\mathcal{M}_{\bullet\bullet}, q)|Z) \frac{dm_\bullet}{d\mathcal{M}_{\bullet\bullet}}(q), \quad (2.13)$$

[2]In principle the IMF could be different and also dependent on the galaxy properties as SFR or metallicity. However the authors of Boco et al. (2019) showed that its choice has only a mild impact on the detected GWs rate.

[3]Note that in equation (2.12), the integral should contain the quantity $\phi(m_\star)/\int dm_\star \phi(m_\star) m_\star$. However, in the literature the denominator is usually left implicit because of the IMF normalization condition $\int dm_\star \phi(m_\star) m_\star = 1M_\odot$, though the reader should keep track of the measurement units (i.e. the factor computed in equation (2.12) is a distribution of remnant masses per unit of star formed mass).

[4]The primary mass $m_\bullet$ is the mass of the most massive compact remnant of the binary.

where $m_\bullet(\mathcal{M}_{\bullet\bullet}, q) = \mathcal{M}_{\bullet\bullet}(1+q)^{1/5}/q^{3/5}$, $dm_\bullet/d\mathcal{M}_{\bullet\bullet} = (1+q)^{1/5}/q^{3/5}$ and the distribution dp/dq is taken from binary evolution simulations. In particular, the mass ratio distribution for BH-BH mergers scales linearly with q: $dp/dq \propto q$ (see e.g., de Mink et al. (2013); Belczynski et al. (2010); Kovetz et al. (2017a)), instead, for NS-NS or BH-NS merging, the mass ratio distribution tends to be flatter (see Dominik et al. (2012, 2015); de Mink & Belczynski (2015); Chruslinska et al. (2019); Mapelli & Giacobbo (2018)). We set the q distributions ranges for the three types of merging events on the basis of the allowed masses for each CO type. The authors of Boco et al. (2019) have checked that the merging rate depends very little on the chosen q distribution.
The last ingredient provided by observations and simulations is the probability distribution function for the time delay between the formation of the binary and its merging: $dp/dt_d \propto t_d^{-1}$ Dominik et al. (2012); Giacobbo & Mapelli (2018), normalized to unity between a minimum value of $t_{d,min} \sim 50$Myr and the age of the universe.

Computing merging and detected rates

After this brief overview of the main ingredients, we can compute the cosmic merging rates of compact remnant binaries per redshift and chirp mass interval in the following way:

$$\begin{aligned}\frac{d^2\dot{N}_{merge}}{dz\, d\mathcal{M}_{\bullet\bullet}}(t, \mathcal{M}_{\bullet\bullet}) =& f_{\rm eff}\frac{dV}{dz\,(1+z)}\int dt_d \frac{dp}{dt_d}\int d\log_{10}\psi \frac{d^2N(\log_{10}\psi, t-t_d)}{d\log_{10}\psi\, dV}\psi\times \\ &\times \int d\log_{10} Z \frac{dp}{d\log_{10} Z}(\log_{10} Z|t-t_d,\psi)\frac{dp}{d\mathcal{M}_{\bullet\bullet}}(\mathcal{M}_{\bullet\bullet}|Z)\,.\end{aligned} \tag{2.14}$$

To grasp the meaning of this cumbersome expression let us look first at the innermost integral: it represents the probability of formation of a compact remnant with chirp mass $\mathcal{M}_{\bullet\bullet}$ in a galaxy with SFR ψ. This quantity is then integrated over all the galaxies weighted with the galaxy statistics (the SFRF). Since we are computing the merging rates at the cosmic time t, the quantities related to the formation of the binary should be computed at $t - t_d$, with t_d being the time delay between the formation and the merging of the binary. The outermost integral over the time delay is finally performed to account for all the time delays. The factor dV/dz is just the differential comoving volume, while the $(1+z)$ factor in the denominator keeps into account the cosmological time dilation. Finally, the factor $f_{\rm eff}$ is defined as the fraction of primary compact remnants hosted in binary systems with characteristics apt to allow merging within a Hubble time.

The factor $f_{\rm eff}$ is the result of many different and complex physical processes related to stellar and dynamical evolution (binary fraction, common envelope development/survival, SN kicks, mass transfers, etc.), so it could in principle depend on metallicity and binary type. In stellar and binary evolution simulations (e.g., O'Shaughnessy et al. (2010); Dominik et al. (2015); Belczynski et al. (2010); Spera & Mapelli (2017); Giacobbo & Mapelli (2018); Chruslinska et al. (2018); Neijssel et al. (2019)) this quantity is naturally obtained, but largely dependent on model assumptions. This is why, at this stage, as already done in other works (e.g. Cao et al. (2018), Li et al. (2018), Calore et al. (2020)), we set it empirically by normalizing the local BH-BH, BH-NS and NS-NS merger rates to the logarithmic average values of the 90% confidence interval measured by the LIGO/Virgo collaboration after the O1 and O2 runs (see Abbott et al. (2019a)): $30\,{\rm Gpc}^{-3}/{\rm yr}$ for BH-BH, $650\,{\rm Gpc}^{-3}/{\rm yr}$ for NS-NS and $25\,{\rm Gpc}^{-3}/{\rm yr}$ for BH-NS (this last choice is less certain since the BH-NS local merging rate is limited only by an upper value). We stress that in doing so the factor $f_{\rm eff}$ loses all the possible metallicity dependence, which, however, is highly uncertain and model dependent (we will come back to its metallicity behaviour in section 2.4). Therefore, this factor acts only on the normalization of the merging rates and can be changed when a more accurate determination of the local rates will be done after further GWs observations. Thus, the difference in the merging rates normalization between the three types of merging events is given by the different $f_{\rm eff}$ factors, while the difference in shape is given by the distribution $dp/d\mathcal{M}_{\bullet\bullet}(\mathcal{M}_{\bullet\bullet}|Z)$ in equation (2.13), depending on the stellar and binary evolution prescriptions.

Once the merging rates per chirp mass bin are computed, it is easy to derive the detected rates by a specific GW detector. As already mentioned, we consider the ET instrument. The rates per unit redshift, chirp mass and signal to noise ratio (SNR) can be computed as:

$$\frac{d^3\dot{N}_{merge}}{dz\,d\mathcal{M}_{\bullet\bullet}\,d\rho}(\rho|z,\mathcal{M}_{\bullet\bullet}) = \frac{d^2\dot{N}_{merge}}{dz\,d\mathcal{M}_{\bullet\bullet}}\frac{dp}{d\rho}(\rho|z,\mathcal{M}_{\bullet\bullet}) \tag{2.15}$$

where $dp/d\rho$ is the probability distribution of SNR dependent on redshift, chirp mass and on the sensitivity curve of the detector (for a full treatment of the $dp/d\rho$ see Taylor & Gair (2012); Li et al. (2018); Boco et al. (2019, 2020)). Therefore, the rates with SNR $\rho > \bar{\rho}$ can be computed as:

$$\frac{d\dot{N}_{\bar{\rho}}}{dz}(z,\rho\geq\bar{\rho}) = \int_{\bar{\rho}} d\rho \frac{d^2\dot{N}}{dz\,d\rho}(\rho,z) = \int_{\bar{\rho}} d\rho \int d\mathcal{M}_{\bullet\bullet}\frac{d^3\dot{N}}{dz\,d\mathcal{M}_{\bullet\bullet}\,d\rho}(\mathcal{M}_{\bullet\bullet}|z,\rho)\,. \tag{2.16}$$

We consider the GW event detected when the SNR is higher than $\bar{\rho} = 8$. The detected rates by ET for BH-BH, NS-NS and BH-NS are shown in figure 2.2 (left panel).

Eventually, the rate for GWs events above a given SNR can be used to compute the evolution bias:

$$f_{\rm GW}^{\rm evo}(z) = \frac{d\ln\left(a^3 \frac{d^2\dot{N}_{\bar{\rho}}(z,\rho\geq\bar{\rho})}{dzd\Omega}\right)}{d\ln a}. \tag{2.17}$$

2.2.2.2 Bias for GW events

Since we consider GWs produced by the merging of COs of stellar origin, their signals originate from galaxies and trace their distribution, so that they trace the underlying total matter distribution the same way their host galaxies do. For this reason, GWs events can be characterized by the same bias of their hosts. Since the CO mergers take place in all galaxy types with different rates, the correct estimate of their bias needs to take into account which galaxy types are contributing most/less to the detected mergers, giving proportioned weight to their bias values when estimating that of all GWs events.

In order to assign a redshift dependent bias to the GW events, we make use of the bias $b(z,\psi)$, computed in section 2.2.1.2, associated with a galaxy at a given redshift with given SFR and we weight it through the quantity $d^3\dot{N}_{merge}/dz/d\rho/d\log_{10}\psi$ which keeps into account the contribution of the different SFRs (i.e. of different galaxies) to the total merging rates at a given redshift and SNR. This differential merging rate can be computed from equation (2.14) and (2.15) not integrating over the SFR. Therefore, to compute the bias for gravitational waves we use the following expression:

$$b_{GW}(z,\rho) = \frac{\int d\log_{10}\psi \frac{d^3\dot{N}}{dz\,d\rho\,d\log_{10}\psi} b(z,\psi)}{\int d\log_{10}\psi \frac{d^3\dot{N}}{dz\,d\rho\,d\log_{10}\psi}}\,. \tag{2.18}$$

The effective bias, i.e. the bias for GWs with a SNR above a certain threshold $\bar{\rho}$, is now easy to compute:

$$b_{GW,\bar{\rho}}(z,>\bar{\rho}) = \frac{\int_{\bar{\rho}} d\rho \frac{d^2\dot{N}}{dz\,d\rho} b(z,\rho)}{\int_{\bar{\rho}} d\rho \frac{d^2\dot{N}}{dz\,d\rho}}\,. \tag{2.19}$$

The bias for the detected events ($\bar{\rho}=8$) is shown in figure 2.2 (middle panel). The interpretation of the shape of the GW bias is not trivial and explained in the following. At low redshift its value is ~ 1 since the only galaxies that contribute to the GW signals have low SFR and consequently a smaller bias. The following rapid increase with redshift is due to two factors: the first is just the standard growth with redshift of the galaxy bias, the second is that, increasing the redshift, there are more and more highly star forming galaxies that contribute to the GW events. These galaxies, as shown in figure 2.1, are more biased. At redshift $z\sim 5$ the GW bias flattens. Again,

this is due to different astrophysical effects. In particular, the redshift increase of the galaxies bias is compensated by the fact that at high redshift the detected GW events receive a larger contribution by less star forming and, thus, less biased galaxies. This is due to two facts: firstly, the number of highly star forming galaxies tends to decrease at redshift $z \gtrsim 3-4$; secondly, in galaxies with high SFR the metallicity is also high and, consequently, the compact remnants produced are less massive. This means that galaxies with larger SFRs tend to produce GW events with lower chirp mass (see section 2.4.1). However, at high redshift the detector starts not to see anymore these low chirp mass events and, due to this selection effect, the GW events detected at higher and higher redshifts come from galaxies with lower SFR and are, consequently, less biased.

2.2.2.3 Magnification bias for GW events

Similarly to the galaxy case and as done by Scelfo et al. (2018), the magnification bias for GW events with $\rho > \bar{\rho}$ is the logarithmic slope of their $dN_\rho/dz\,(z, > \rho)$ computed at $\rho = \bar{\rho}$:

$$s_{GW,\bar{\rho}}(z) = -\left.\frac{d\log_{10}\left(\frac{d^2\dot{N}_\rho(z,>\rho)}{dz\,d\Omega}\right)}{d\rho}\right|_{\rho=\bar{\rho}}, \tag{2.20}$$

which, after some algebraic manipulation, can be rewritten as:

$$s_{GW,\bar{\rho}}(z) = \bar{\rho}\frac{\frac{d^2\dot{N}(z,\bar{\rho})}{dz\,d\rho}}{d\dot{N}_{\bar{\rho}}/dz}\,. \tag{2.21}$$

We show in figure 2.2 (right panel) the magnification bias for detected mergers ($\bar{\rho} = 8$). It can be seen that the magnification bias for NS-NS events features a fast growth with redshift because the NS-NS distribution in SNR is peaked at lower values of ρ with respect to BH-BH or BH-NS events (see figure 2.3). So, as the redshift increases, the peak of such distribution shifts toward values $\rho \lesssim 8$: the choice of the faint end of SNR then has a huge effect on NS-NS events. Instead, for BH-BH and BH-NS events, the distribution in SNR ratio is much broader, even at high redshifts: the choice of the faint end of SNR has not a large impact on the number of detections. For this reason the magnification bias for those events always remains at moderate values.
In figure 2.3 we show the SNR probability distribution functions for BH-BH, BH-NS and NS-NS events at redshift $z = 0.5$ left panel, $z = 1$ middle panel and $z = 2$ right panel.
A useful thing to notice is that changing the cosmological parameters values affects the description of the tracers (both galaxies and GWs) only as a volume term dV/dz

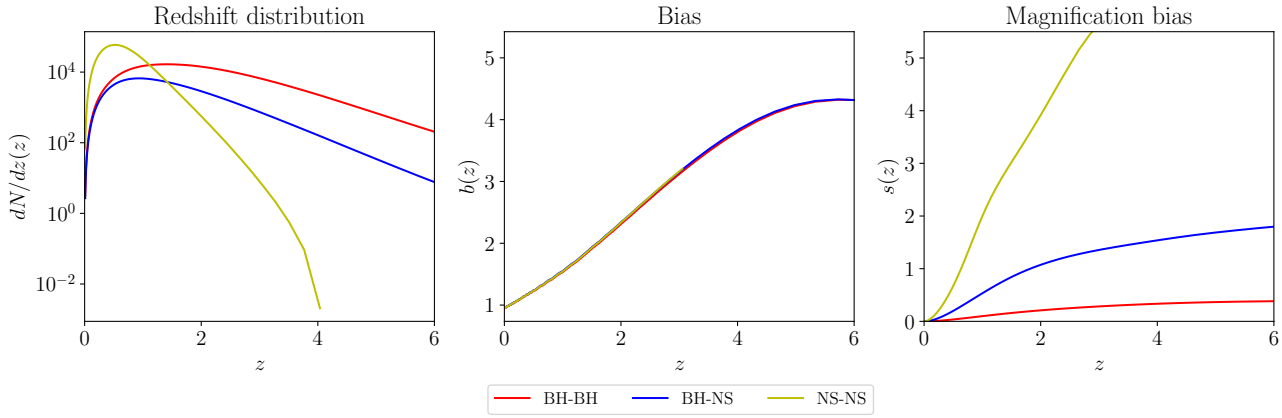

Figure 2.2: Full-sky redshift distributions for an observation time $T_{\rm obs} = 1$yr (*left*), bias (*center*) and magnification bias (*right*) for all GWs tracers, as detected by ET. Quantities referred to BH-BH, BH-NS, NS-NS mergers are respectively in red, blue and yellow lines.

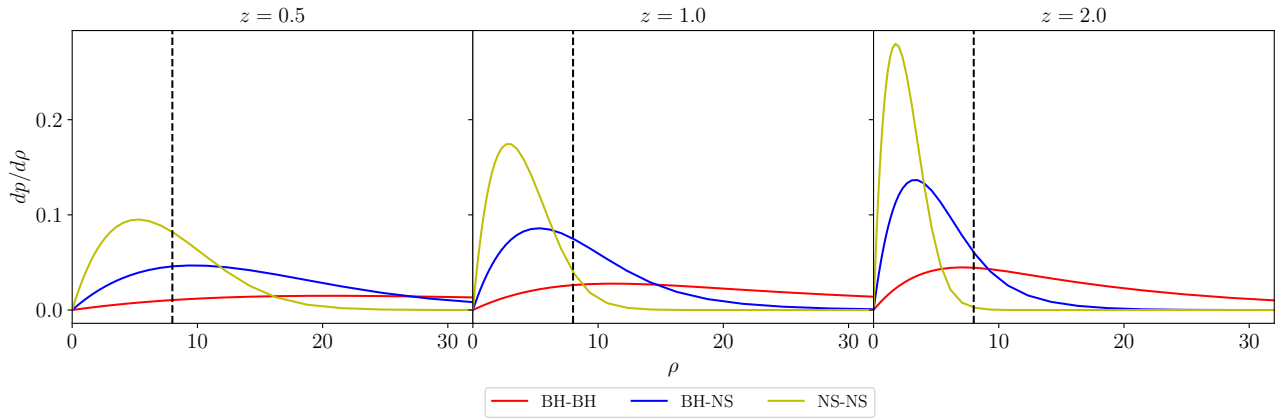

Figure 2.3: SNR ρ normalized distributions at redshifts $z = 0.5$ (*left*), $z = 1.0$ (*center*) and $z = 2.0$ (*right*) for all GWs tracers. Distributions for BH-BH, BH-NS, NS-NS are respectively in red, blue and yellow lines. The black dashed vertical lines correspond to the limit of $\rho = 8$.

in the computation of the redshift distributions, as can be seen in equations (2.4) (for galaxies) and (2.14) (for GWs). This implies that, changing the cosmological parameter values, all the redshift distributions will vary in the same way, making it difficult to constrain them.

2.3 Galaxies - GWs cross-correlations and Signal-to-Noises

Making use of the formalism presented in section 1.3.1 we compute the cross-correlation angular power spectra C_ℓ's between the tracers presented in section 2.2. Note that the GWs events considered in the cross-correlation are computed from the whole galaxy distribution, not just from galaxies with the specified SFR cuts, in order to realistically

take into account all the GWs signals that can be detected by a specific instrument (ET in our case). We considered both tomographic and non tomographic approaches, whose details and results are provided in sections 2.3.1 and 2.3.2 respectively.
Following Scelfo et al. (2018), we can organize the angular power spectra from different tracers and redshift bin couples in a data vector $\mathbf{C}_\ell$ ordered as

$$\mathbf{C}_\ell = \begin{pmatrix} C_\ell^{\mathrm{gg}}(z_1, z_1) \\ \vdots \\ C_\ell^{\mathrm{gGW}}(z_1, z_1) \\ \vdots \\ C_\ell^{\mathrm{GWGW}}(z_1, z_1) \\ \vdots \end{pmatrix} \tag{2.22}$$

where g and GW respectively refer to our galaxy and gravitational wave tracers. Given N_{bin} redshift bins, the $\mathbf{C}_\ell$ is a N_{bin}^2 dimensional data vector, where its I^{th} element can be associated to two indices (I_1, I_2), corresponding to the two tracers and redshift bins of the angular power spectra in that specific entry. As an example, the first $(I = 1)$ entry is associated to the couple of indices $[I_1 = \mathrm{g}_{z_1}, I_2 = \mathrm{g}_{z_1}]$. From this, one can write the covariance matrix $(\mathrm{Cov}_\ell)_{IJ}$, whose elements are given by

$$(\mathrm{Cov}_\ell)_{IJ} = \tilde{C}_\ell^{I_1 J_1} \tilde{C}_\ell^{I_2 J_2} + \tilde{C}_\ell^{I_1 J_2} \tilde{C}_\ell^{I_2 J_1}, \tag{2.23}$$

where the $\tilde{C}_\ell$ are the angular power spectra of equation (1.59).
In order to characterize the magnitude of the signal that could be extracted by the cross-correlations and determine whether it could be discerned from the noise, it is useful to compute a Signal-to-Noise ratio (S/N). With this purpose, we compute two types of S/N.
The first one is an estimate of the S/N of the C_ℓ's for each combination of redshift bins (at fixed tracers couple). This provides a total of $N_{\mathrm{bin}} \times N_{\mathrm{bin}}$ S/N values. While on the one hand they do not take into account correlations with the other redshift bins (which can be non negligible, especially due to lensing effects), on the other hand they provide an unpacked information about which bin combinations are the most powerful in terms of signal. At fixed multipole ℓ, the S/N computed in this way can be written as:

$$\left(\frac{S}{N}\right)^2_{[I_1,I_2]}(\ell) = f_{\mathrm{sky}}(2\ell+1)\frac{\left(\tilde{C}_\ell^{[I_1,I_2]}\right)^2}{\sigma^2_{[I_1,I_2]}(\ell)} = f_{\mathrm{sky}}(2\ell+1)\frac{\left(\tilde{C}_\ell^{[I_1,I_2]}\right)^2}{\left[\tilde{C}_\ell^{[I_1,I_1]}\tilde{C}_\ell^{[I_2,I_2]} + \left(\tilde{C}_\ell^{[I_1,I_2]}\right)^2\right]} \tag{2.24}$$

where $\sigma^2_{[I_1,I_2]}(\ell)$ is obtained imposing $I = J$ in equation (2.23).
The second method for the computation of the S/N provides (still at fixed tracers couple) one single S/N estimate for the whole probe, taking into account also the covariance between the C_ℓ's of different redshift bins. It is computed as:

$$\left(\frac{S}{N}\right)^2_{\rm TOT}(\ell) = f_{\rm sky}(2\ell+1)\cdot \mathbf{C}_\ell^{\rm T}\cdot {\rm Cov}_\ell^{-1}\cdot \mathbf{C}_\ell \tag{2.25}$$

Note that, in order to compute the S/N of the cross-correlation, we do not make use of the auto-correlation C_ℓ's appearing in the vector of equation (2.22). In this way we compute the S/N related only to the cross-correlation part, avoiding the contribution from auto-correlations which is likely to increase the S/N, if the auto-correlations are free of systematic effects. The rationale behind this treatment is to be conservative and assume that the cross-correlation signal is less prone to systematic effects compared to the auto-correlations, as it is indeed the case for other Large Scale Structure tracers.
More often, a cumulative Signal-to-Noise ratio $\left(\frac{S}{N}\right)(\ell < \ell_{\rm max})$ is considered. In both cases it is defined as

$$\left(\frac{S}{N}\right)(\ell < \ell_{\rm max}) = \sqrt{\sum_{\ell'=\ell_{\rm min}}^{\ell_{\rm max}} \left(\frac{S}{N}\right)^2(\ell')}. \tag{2.26}$$

In sections 2.3.1 and 2.3.2 we show the results for the two S/N calculations. Note that in the non tomographic case, characterized by one single redshift bin, the two estimates coincide.

2.3.1 Tomographic case

We cross-correlate all the considered galaxy tracers (i.e. galaxies with the SFR cuts $\psi > 10,\ 100,\ 300\, M_\odot/{\rm yr}$) with all the GWs tracers (i.e. BH-BH, BH-NS, NS-NS) along three or four redshift bins $z_{i,j}$. The number of bins and their ranges differ from case to case due to the different redshift ranges in which these tracers can be defined (see section 2.2). In table 2.1 we provide the redshift binning considered for each probe. In this section we provide results for the exemplifying case of $f_{\rm sky} = 0.7$ and up to a maximum multipole of $\ell_{\rm max} = 100$, corresponding to the best angular resolution reachable by ET (see e.g., Klimenko et al. (2011)).
In figures 2.4, 2.5, 2.6 we provide the cumulative S/N computed from the first method (i.e. applying equation (2.26) to (2.24)) for all combinations of tracers and redshift bins. Each subplot shows the estimates for one specific galactic tracer, with every

		GW		
		BH-BH	BH-NS	NS-NS
g	$\psi > 10 M_\odot/\mathrm{yr}$	$0 \leq z_1 \leq 1$ $1 \leq z_2 \leq 2$ $2 \leq z_3 \leq 3$ $3 \leq z_4 \leq 6$	$0 \leq z_1 \leq 1$ $1 \leq z_2 \leq 2$ $2 \leq z_3 \leq 3$ $3 \leq z_4 \leq 6$	$0 \leq z_1 \leq 1$ $1 \leq z_2 \leq 2$ $2 \leq z_3 \leq 3$
	$\psi > 100 M_\odot/\mathrm{yr}$	$0.5 \leq z_1 \leq 1$ $1 \leq z_2 \leq 2$ $2 \leq z_3 \leq 3$ $3 \leq z_4 \leq 6$	$0.5 \leq z_1 \leq 1$ $1 \leq z_2 \leq 2$ $2 \leq z_3 \leq 3$ $3 \leq z_4 \leq 6$	$0.5 \leq z_1 \leq 1$ $1 \leq z_2 \leq 2$ $2 \leq z_3 \leq 3$
	$\psi > 300 M_\odot/\mathrm{yr}$	$1 \leq z_1 \leq 2$ $2 \leq z_2 \leq 3$ $3 \leq z_3 \leq 6$	$1 \leq z_1 \leq 2$ $2 \leq z_2 \leq 3$ $3 \leq z_3 \leq 6$	$1 \leq z_1 \leq 2$ $2 \leq z_2 \leq 3$

Table 2.1: Redshift binning for the tomographic case.

GW tracer. The following notation regarding the redshift binning is adopted: given a g×GW couple, the notation $z_i - z_j$ means that we are cross-correlating galaxies in bin z_i with GWs in bin z_j. Note that each subplot refers to cross-correlations between redshift bins $z_i - z_j$, but each $z_{i,j}$ can actually be different between different tracers according to table 2.1. For this reason, curves with different colors should not be directly compared to one another, since they refer to different ranges.

As for the S/N values, it can be seen that in several cases $\mathrm{S/N}(< \ell_{\max}) > 1$. In particular: *i)* for all galaxy tracers, the highest $\mathrm{S/N}(< \ell_{\max})$ are found for correlations among the same redshift bins; *ii)* cross-correlations between distant redshift bins are those providing a lower $\mathrm{S/N}(< \ell_{\max})$: even though effects such as lensing can induce even a strong correlation between distant objects, in many of the cases considered here it is not enough to strengthen the S/N; *iii)* considering correlations among the same bins, the $\mathrm{S/N}(< \ell_{\max})$ are strongly sensitive to the amount of detected sources: for large redshift values (bins $z_{2,3,4}$) they are always higher in the BH-BH case, followed by BH-NS and eventually by NS-NS. Indeed, the BH-BH case corresponds to a higher number of merging events (as can be seen by looking at its redshift distribution of the left panel of figure 2.2). This provides a smaller amount of shot noise, which contributes to making the S/N of equation (2.24) higher. On the other hand, at low redshift (bin z_1) the redshift distribution of NS-NS mergers is significantly higher than the others, which is reflected in a $\mathrm{S/N}(< \ell_{\max})$ which is often bigger; *iv)* in analogy with the previous point, at fixed GW tracer the higher is the cut in SFR, the lower is the S/N, reflecting the smaller number of galaxies considered.

The cumulative S/N for the whole probe, computed applying equation (2.26) to (2.25),

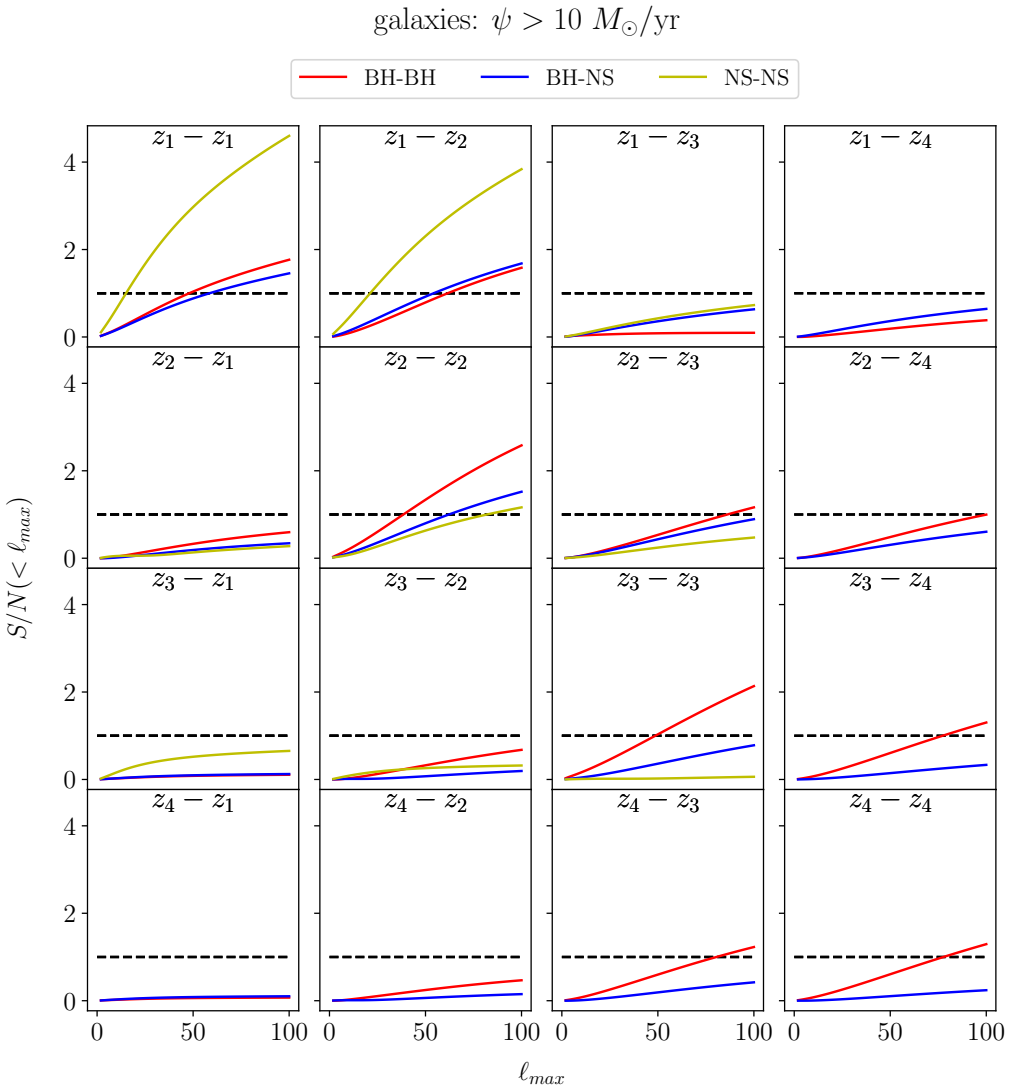

Figure 2.4: Cumulative Signal-to-Noises S/N($< \ell_{\rm max}$) (equations (2.24) and (2.26)) for the cross-correlations cases between galaxies with $\psi > 10 M_\odot$/yr with all three types of GWs signals (BH-BH in red, BH-NS in blue, NS-NS in yellow). Horizontal dashed lines correspond to S/N($< \ell_{\rm max}$) = 1. The plot refers to $T_{\rm obs} = 1$yr and $f_{\rm sky} = 0.7$.

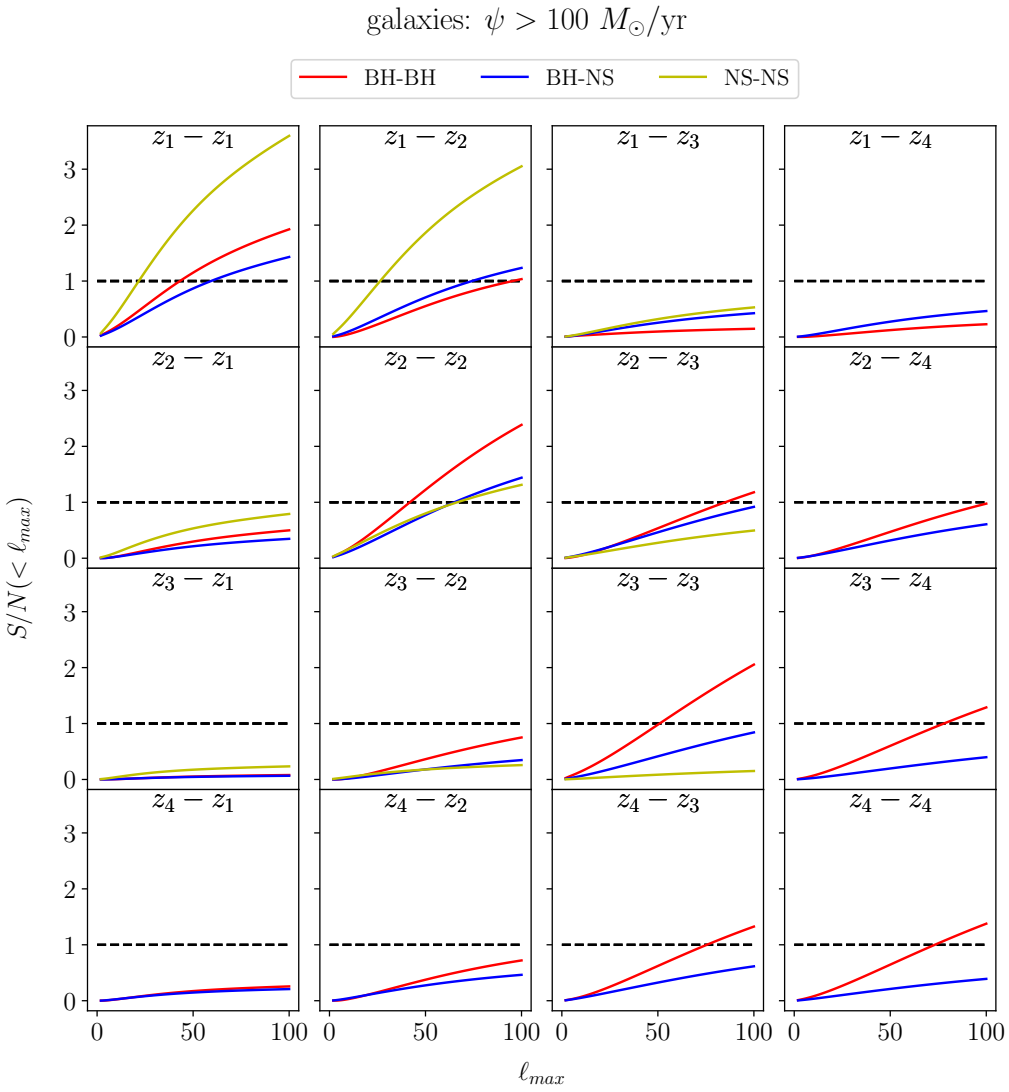

Figure 2.5: Cumulative Signal-to-Noises S/N($< \ell_{\mathrm{max}}$) (equations (2.24) and (2.26)) for the cross-correlations cases between galaxies with $\psi > 100 M_\odot/\mathrm{yr}$ with all three types of GWs signals (BH-BH in red, BH-NS in blue, NS-NS in yellow). Horizontal dashed lines correspond to S/N($< \ell_{\mathrm{max}}$) = 1. The plot refers to $T_{\mathrm{obs}} = 1\mathrm{yr}$ and $f_{\mathrm{sky}} = 0.7$.

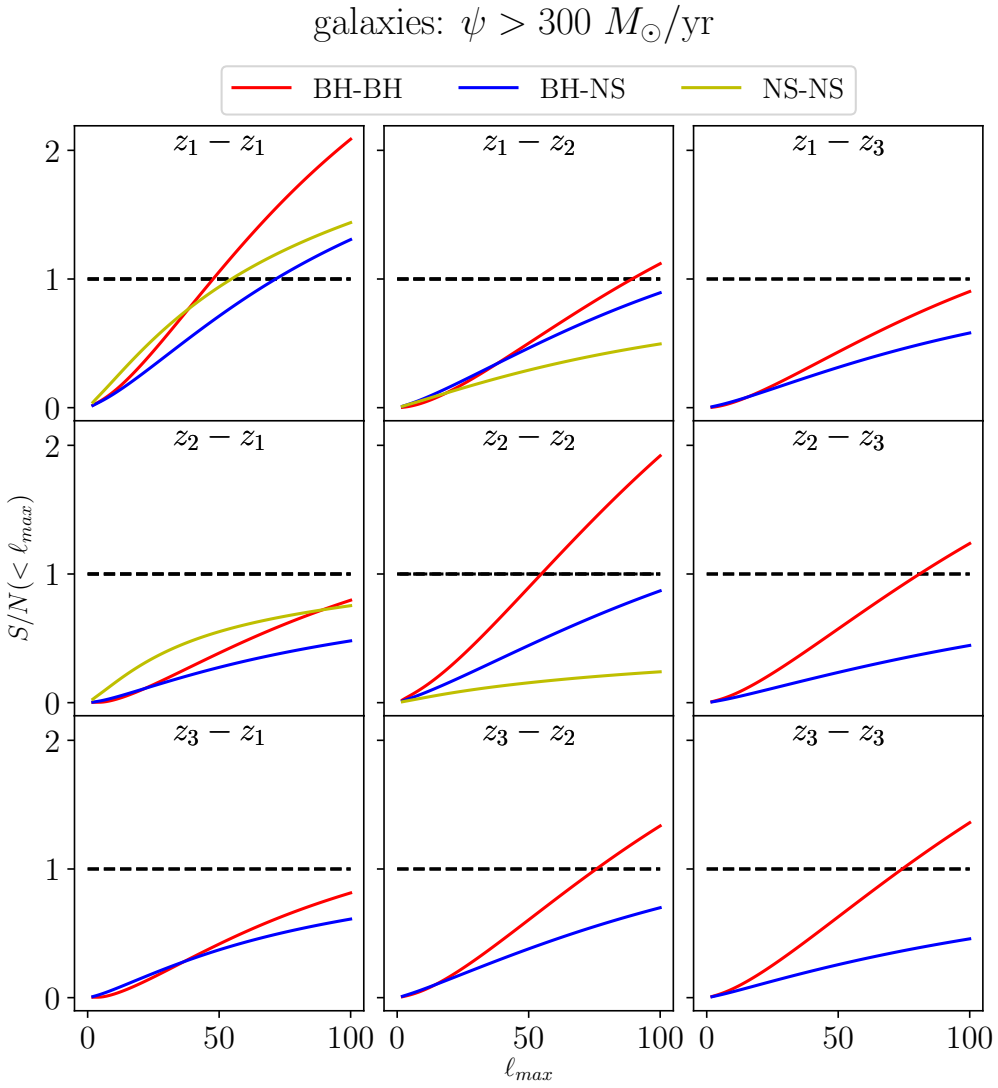

Figure 2.6: Cumulative Signal-to-Noises S/N($< \ell_{\mathrm{max}}$) (equations (2.24) and (2.26)) for the cross-correlations cases between galaxies with $\psi > 300 M_\odot/\mathrm{yr}$ with all three types of GWs signals (BH-BH in red, BH-NS in blue, NS-NS in yellow). Horizontal dashed lines correspond to S/N($< \ell_{\mathrm{max}}$) = 1. The plot refers to $T_{\mathrm{obs}} = 1\mathrm{yr}$ and $f_{\mathrm{sky}} = 0.7$.

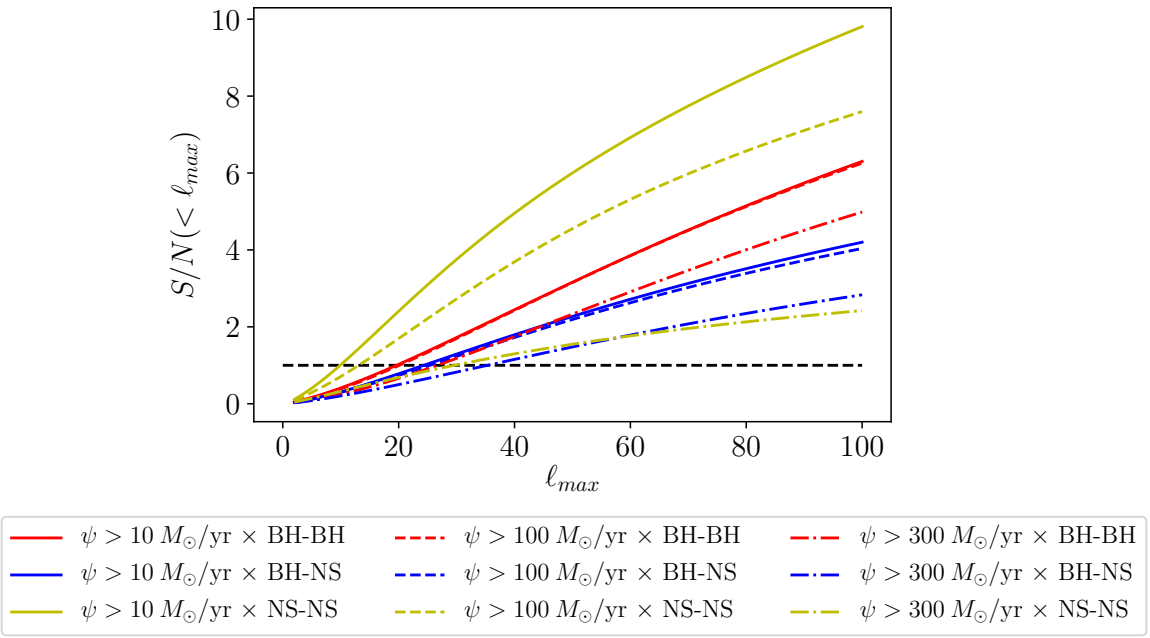

Figure 2.7: Cumulative Signal-to-Noises S/N($< \ell_{\rm max}$) for all cross-correlation cases (equations (2.25) and (2.26)). The horizontal dashed line corresponds to S/N($< \ell_{\rm max}$) = 1. Line-styles refer to galaxies ($\psi > 10 M_\odot$/yr in full line, $\psi > 100 M_\odot$/yr in dashed line, $\psi > 300 M_\odot$/yr in dotted-dashed line) while colors refer to gravitational waves (BH-BH in red, BH-NS in blue, NS-NS in yellow). The plot refers to $T_{\rm obs} = 1$yr and $f_{\rm sky} = 0.7$.

is shown in figure 2.7. The line-styles refer to a specific galaxy tracer, while the colors distinguish between GW types (as indicated in the legend). It can be seen that generally it reaches values above unity for all the tracers combinations. Note that the cross-correlation signal overcomes the noise already for relatively low multipoles, at around $\ell_{\rm max} \sim 10 - 40$. The S/N is particularly high especially for the $\psi > 10 M_\odot$/yr× NS-NS case, where it reaches a value of ~ 10. The NS-NS case is also the most dependent on the chosen SFR cut, because the peak of the detected NS-NS distribution is at rather low redshift ($z \leq 1$), where the distribution of highly star forming galaxies tends to fall down (see figures 2.1 and 2.2, left panels). We stress again that the different cases should not be directly compared since they refer to different redshift ranges, depending on the tracers characteristic intervals. All in all, cross-correlations between the treated tracers, adopting a tomographic approach, can be informative given the rather high S/N ratio values.

		GW		
		BH-BH	BH-NS	NS-NS
g	$\psi > 10 M_\odot/\mathrm{yr}$	$0 \leq z \leq 6$	$0 \leq z \leq 6$	$0 \leq z \leq 3$
	$\psi > 100 M_\odot/\mathrm{yr}$	$0.5 \leq z \leq 6$	$0.5 \leq z \leq 6$	$0.5 \leq z \leq 3$
	$\psi > 300 M_\odot/\mathrm{yr}$	$1 \leq z \leq 6$	$1 \leq z \leq 6$	$1 \leq z \leq 3$

Table 2.2: Redshift binning for the non-tomographic case.

2.3.2 Non-tomographic case

In this subsection we compute the cross-correlations between our tracers without a tomographic approach. This is done to see how the measured cross-correlation signal can differ when squeezing all the detected sources into one single bin, without a sliced tomographic approach. As for the previous case, the redshift ranges of all the tracers combinations differ for each combination. In table 2.2 we provide the redshift ranges considered for each probe.
In figure 2.8 (left panel) we show the angular power spectra for all combinations of tracers. As in figure 2.7, line-styles/colors refer to galaxies/GWs. It can be seen that the power spectra are higher when galaxies with a higher SFR are considered, as logically expected, since a higher SFR leads to a larger absolute number of remnants, and so to a larger amount of merging pairs.
In figure 2.8 (right panel) we provide the cumulative $\mathrm{S/N}(< \ell_{\mathrm{max}})$ for each probe. We stress again that the S/N, computed applying equation (2.26) to equations (2.24) and (2.25), are in this case coincident. It can be seen that for an ℓ_{max} large enough a $\mathrm{S/N}(< \ell_{\mathrm{max}}) > 1$ is always reached for any tracer combination. The cross-correlation signal overcomes the noise at around $\ell_{\mathrm{max}} \sim 20 - 40$. The NS-NS contribution in this case is lower with respect to the tomographic approach because, even if their shot noise is small, their C_ℓ's values are also small, due to the fact that NS-NS mergers are mostly seen at low redshifts making their distribution rather different with respect to the galaxies one.
By comparing figure 2.7 and figure 2.8 (right panel) it is possible to gauge the fact that assuming a tomographic approach is indeed an advantage, since the extra (radial) information provided contributes to build a stronger S/N.

2.4 Cross-correlations as astrophysical probe

In this section we are going to discuss the possibility to exploit GW $\times$ LSS cross-correlations to compare and test the validity of different astrophysical scenarios con-

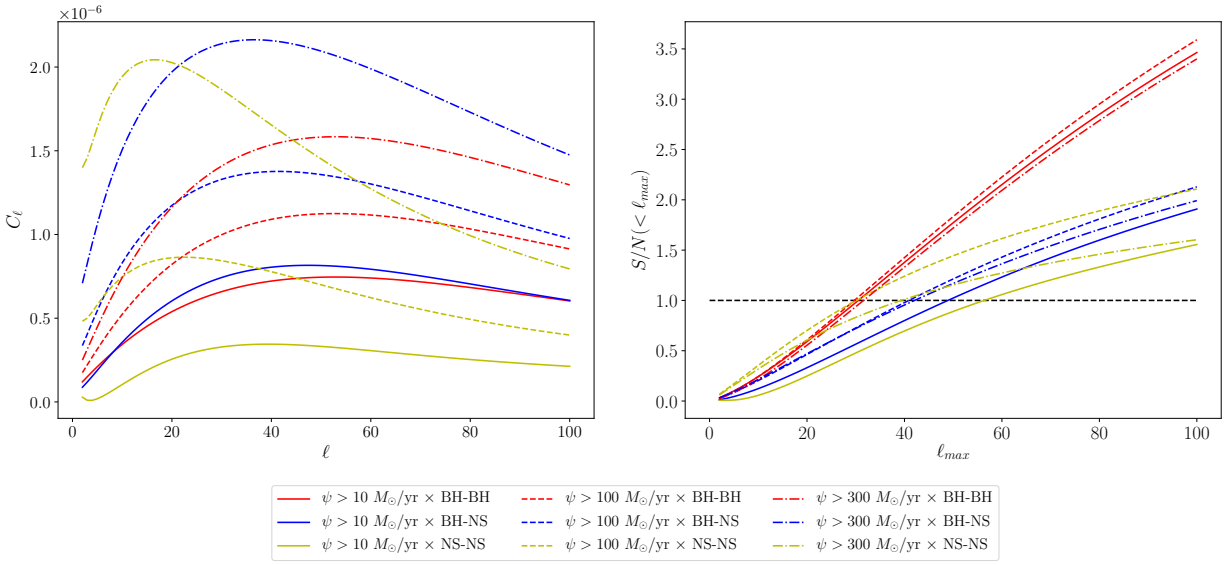

Figure 2.8: *Left:* angular power spectra C_ℓ's for all cross-correlations cases. *Right:* cumulative Signal-to-Noises S/N($< \ell_{\rm max}$) for all cross-correlations cases. The horizontal dashed line corresponds to S/N($< \ell_{\rm max}$) = 1. Line-styles refer to galaxies ($\psi > 10 M_\odot$/yr in full line, $\psi > 100 M_\odot$/yr in dashed line, $\psi > 300 M_\odot$/yr in dotted-dashed line) while colors refer to gravitational waves (BH-BH in red, BH-NS in blue, NS-NS in yellow). The plot refers to $T_{\rm obs} = 1$yr and $f_{\rm sky} = 0.7$.

cerning the formation, evolution and merging of COs binaries. Given the uncertainties in the astrophysics and the enormous modeling possibilities, it is at the moment unlikely to be able to unequivocally determine the validity of one specific combination of prescriptions with respect to any possible other. For this reason, our approach does not aim at excluding or validating specific models, whereas it looks at the possibility to apply this methodology to some general proof-of-concept cases, leaving the chance to use this formalism to whom is interested in applying it for specific tests. In fact, it is worth stressing again that the application we presented in this section is not the only possible one. Any other astrophysical formulation and modeling that influences the estimate of redshift distributions and/or biases of the considered tracers can in principle be addressed. This can cover a wide range of possibilities, from the stellar modeling (especially regarding the estimation of the CO mass and the constrain of all those processes influencing it) to galaxy evolution and SFRs calculation methods.
To compare two models (which we describe in section 2.4.1) and investigate the possibility to discern them, we make use of a $\Delta\chi^2$ statistics, whose formalism and results are presented in section 2.4.2.

2.4.1 Compared astrophysical models

The two cases that we compare in this study differ in the treatment of the effect of the galaxy metallicity on binary evolution. The metallicity value of the ZAMS stars constituting the binary, as already mentioned in section 2.2.2.1, is fundamental in order to determine the subsequent binary evolution. The value of metallicty has a strong impact both on the COs mass and on the number of COs merging per unit of star forming mass. In particular the higher is the metallicity the lower is the chirp mass and the number of merging binaries per unit of star forming mass. The physical reasons of these dependencies are well explained in e.g., Belczynski et al. (2010), Dominik et al. (2012), Chruslinska et al. (2018).

In section 2.2.2.1 and throughout this paper we accounted for the differences in the compact remnant masses due to the different metallicities present in galaxies through the factor $dp/d\log_{10}\mathcal{M}_{\bullet\bullet}\,(\mathcal{M}_{\bullet\bullet}|Z)$ in equation (2.14). However, as explained in section 2.2.2.1, we did not consider the possible dependence on metallicity of the merging efficiency due to binary evolution effects. This is translated in the fact that we have chosen a factor $f_{\rm eff}$ independent on metallicity, whose value was determined by normalizing the merging rates to the local value constrained by the LIGO/Virgo team.

In this specific section we change approach, aiming to address the issue of the possibility to distinguish, through GW $\times$ LSS cross-correlations, between different astrophysical models of stellar and binary evolution. Therefore, we compare our precedent results obtained with a constant $f_{\rm eff}$ (we refer to it as "benchmark case") with one of the models with a metallicity dependent $f_{\rm eff}\,(Z)$. As an example we choose the reference model presented in Chruslinska et al. (2018). The metallicity dependence of the number of merging events per unit star forming mass of such a model is shown in figure 1 of Chruslinska et al. (2019), thin lines (we refer to it as "Z-dependent case"). However, the reader should keep in mind that we are considering only the shape of this factor as a function of metallicity, the normalization is still fixed by the local merging rate given by the LIGO/Virgo teams. The equation to compute the merging rates now becomes:

$$\begin{aligned}\frac{d^2\dot{N}_{merge}}{dz\,d\mathcal{M}_{\bullet\bullet}}(t,\mathcal{M}_{\bullet\bullet}) =&\tilde{a}\frac{dV}{dz\,(1+z)}\int dt_d \frac{dp}{dt_d}\int \log_{10}\psi \frac{d^2N(\log_{10}\psi|t-t_d)}{d\log_{10}\psi\,dV}\psi\times\\ &\times\int d\log_{10}Z\frac{dp}{d\log_{10}Z}(\log_{10}Z|t-t_d,\psi)\,f_{\rm eff}(Z)\,\frac{dp}{d\mathcal{M}_{\bullet\bullet}}(\mathcal{M}_{\bullet\bullet}|Z)\,,\end{aligned} \tag{2.27}$$

which is identical to equation (2.14), except for the metallicity dependent $f_{\rm eff}$ factor, which now takes part in the integration. The factor $\tilde{a}$ instead guarantees the normalization to the LIGO/Virgo local values mentioned above.

Thus, we are comparing a simple case (the benchmark one), where the dependence on metallicity enters only in the remnant mass distribution, but not in the number of merging binaries per unit of star forming mass, with a more realistic model (the Z-dependent case) where this latter dependence is included. The differences in the shape of the merging rates between the two cases enters in the computation of the C_ℓ's allowing the possibility to distinguish between them. On the other hand differences in the absolute number of sources affects the shot noise of the two cases, in particular the number of merging events of the benchmark case tends to be, on average, higher with respect to the Z-dependent case, resulting in a lower shot noise.
Clearly this is a case study to check whether it is possible to detect this metallicity imprinting through GW $\times$ LSS cross correlations, but this technique could be in principle pursued in more refined studies to test different astrophysical models. One of the reasons of exploiting the cross-correlation formalism to test these two cases is given by the fact that, since SFR and metallicity are interconnected parameters, a dependence on the metallicity of the efficiency with which COs binaries merge will (non-trivially) be expressed also as a dependence on the SFR, causing GWs mergers to correlate differently with galaxies of different SFR values. We finally remark that we are going to compare these two models only for the BH-BH merging case for two main reasons: the first one is that the metallicity dependence of the number of merging events is stronger for the BH-BH case (see Chruslinska et al. (2019)), the second one is that BH-BH events are much more frequent with respect to the other types of merging: this, as already seen, reduces the shot noise enhancing the S/N of the cross-correlation.

2.4.2 Theoretical forecasts

In this section we provide the forecasts for discerning the benchmark scenario from the metallicity dependent one. We make use of a $\Delta\chi^2$ statistics to evaluate a S/N, whose value (above/below unity) can provide information on how different the two models (one called as Fiducial and the other as Alternative) are. Following the same approach of Scelfo et al. (2018) we define a S/N as:

$$\left(\frac{S}{N}\right)^2 \sim \Delta\chi^2 := f_{\rm sky}\sum_{2}^{\ell_{\rm max}}(2\ell+1)(\mathbf{C}_\ell^{\rm Alternative}-\mathbf{C}_\ell^{\rm Fiducial})^T{\rm Cov}_\ell^{-1}(\mathbf{C}_\ell^{\rm Alternative}-\mathbf{C}_\ell^{\rm Fiducial}), \tag{2.28}$$

where $\mathbf{C}_\ell^{\rm Fiducial/Alternative}$ is a vector containing the C_ℓ'S from the Fiducial/Alternative model, organized with the same logic of equation (2.22) and where the ${\rm Cov}_\ell$ is the covariance matrix as in equation (2.23), built with the C_ℓ's of the fiducial model. Since

the entries of the covariance matrix depend on which model is assumed as fiducial, the final forecasts also depend on this choice. For this reason, we computed S/N in both cases and compared them.

In figure 2.9 we provide the S/N obtained considering galaxies with SFR cuts $\psi > 10, 100, 300 M_\odot/\mathrm{yr}$. We show results for different observed sky-fractions f_{sky}, observation times T_{obs} and for both models assumed as fiducial. More precisely, our results are expressed not only as a function of T_{obs} (on the horizontal axis) but, instead, of the product $r \cdot T_{\mathrm{obs}}$. The quantity r is a multiplicative fudge factor to the merging rate of GWs introduced to take into account any possible uncertainty in the modeling of this quantity. Note that r and T_{obs} are degenerate: for example, observing for $T_{\mathrm{obs}} = 1\,\mathrm{yr}$ with a factor $r = 2$ yields the same result as observing for $T_{\mathrm{obs}} = 2\,\mathrm{yr}$ with a factor $r = 1$. The case of $r = 1$ corresponds to the scenario in which the models used here are the "true" ones. It is worth noticing that the r factor has the same effect of the $\tilde{a}$ factor that quantifies the normalization to the local observed rate introduced in equation 2.27, since they both are multiplicative factors to the merger rate. For this reason, the r factor can also be seen as absorbing the uncertainties on the local merging rates estimates.

First of all, it can be seen that when the benchmark model is assumed as fiducial, the forecasts are significantly better compared to the opposite (for fixed f_{sky} and T_{obs}): this is due to the fact that this model predicts a higher number of GWs mergers, providing a smaller shot noise contribution. For analogous reasons, when comparing the panels in figure 2.9, it can be seen that results are more optimistic when considering galaxies with $\psi > 10 M_\odot/\mathrm{yr}$: the higher the number of sources (galaxies in this case) the better the results. This is also reflected on the fact that the case with galaxies of $\psi > 300 M_\odot/\mathrm{yr}$ is the most pessimistic.

Looking in detail at each of the figures, we can see that in the $\psi > 10 M_\odot/\mathrm{yr}$ case a S/N above unity can be reached in a relatively short time: even for small observed fractions of the sky (e.g., $f_{\mathrm{sky}} = 0.3$) not more than 3 years of observation would be required to marginally distinguish the two scenarios. Looking instead at the most pessimistic case, in which only galaxies with $\psi > 300 M_\odot/\mathrm{yr}$ are considered, approximately 5 to 10 years of observation would be required to reach S/N ~ 1 in the case of benchmark model assumed as fiducial. A much higher observation time (at least above 10 years) is required when assuming the Z-dependent scenario as fiducial. The case of $\psi > 100 M_\odot/\mathrm{yr}$ lies in between, with a still fairly optimistic prediction.

All in all our results are rather promising, especially when considering galaxies with $\psi > 10\,\mathrm{M}_\odot/\mathrm{yr}$ and $\psi > 100\,\mathrm{M}_\odot/\mathrm{yr}$: if the benchmark case is the fiducial one, deviations

from it can be detected after just 2 yr of observational time. If the Z-dependent case is the fiducial, we should be able to detect variations from it in $\lesssim 5$ yr of observations. For highly star forming galaxies with $\psi > 300\,\mathrm{M}_\odot/\mathrm{yr}$ instead, some more time is required to distinguish the two models. Still an observational time $\lesssim 10$ yr is enough if the benchmark case is considered as fiducial.

Finally, we stress again that this forecast does not aim at testing or excluding any of the two models considered here. It aims instead at showing how different astrophysical prescriptions (such as a Z dependence on the f_{eff} factor) could in principle be distinguished through the cross-correlation formalism, contributing in tackling different astrophysical issues.

2.5 Summary

In this chapter we have expanded the investigation in the field of the cross-correlations between resolved GWs signals and LSS tracers. We worked in the harmonic space with the number counts angular power spectra. The two categories of tracers we considered consist of resolved GWs events from BH-BH, BH-NS, NS-NS mergers detectable by the Einstein Telescope and actively star-forming galaxies with SFR cuts of $\psi > 10,\ 100,\ 300\,M_\odot/\mathrm{yr}$. We characterized them with their redshift distributions, bias and magnification bias values, presenting a detailed description of the computation of these quantities. We stress again that both the SFRF and the GWs distributions derive from the same type of sources (galaxies) but trace them in a different way, since GW signals depend not only on the galaxy SFR, but also on the galaxy metallicity and on stellar and binary evolution prescriptions. For this reasons we kept into account all the aforementioned elements in this work. Cross-correlating the same sources via two different messengers can help not only in alleviating systematics but also in enhancing the amount of astrophysical information encoded in the signal.

In our analysis we took into account all lensing and all general relativistic contributions in the computation of the observed number counts fluctuations and we extended the basis for future works regarding the GW $\times$ LSS cross-correlations with a more robust theoretical astrophysical background.

After computing the number counts angular power spectra for all the combinations of our GW $\times$ LSS tracers, we estimated Signal-to-Noise ratios in order to forecast the detectability of the cross-correlation signal. We have considered both tomographic and non-tomographic approaches. Our results show that in several scenarios it is possible to reach a Signal-to-Noise ratio higher than unity, whereas it is not always the case

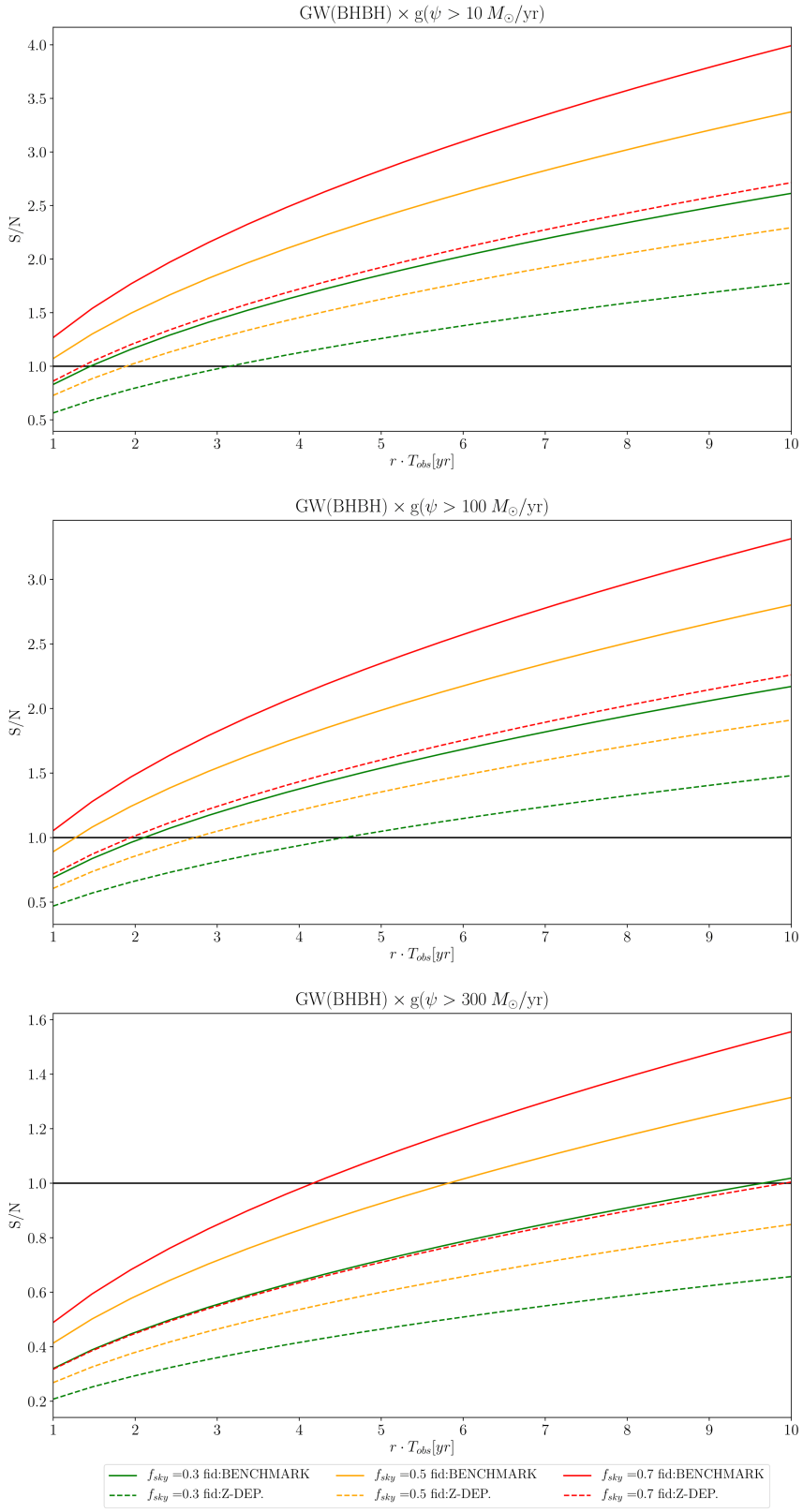

Figure 2.9: S/N from $\Delta\chi^2$ analysis (equation (2.28)) for discerning the two considered astrophysical scenarios. Galaxies with $\psi > 10, 100, 300 M_\odot$/yr are considered (top, central and bottom panel respectively). Continuous/dashed lines refer to the benchmark/Z-dependent model assumed as fiducial. Colors refer to different values of $f_{\rm sky}$ as shown in legend.

for cross-correlations between distant redshift bins (in the tomographic case) or with a low number of observed objects. In addition, the total cumulative Signal-to-Noise ratios for each of the probes considered in this work are in turn quite optimistic. Even though each of the many considerable surveys (such as ALMA (Wootten & Thompson (2009)), JWST (Gardner et al. (2006)), EMU (Norris et al. (2011)), SKAO (Maartens et al. (2015)) and many others) will have its own specifics, this work still provides a general possibility to gauge the cross-correlations efficacy.

Finally, we have investigated the possibility of exploiting the GW $\times$ LSS formalism to compare and test possible scenarios in the astrophysical modeling of GWs events. In particular we considered a proof-of-concept case in which we made use of a $\Delta\chi^2$ statistics to compare the cross-correlation signal obtained by modeling the COs merging efficiency with a specific metallicity dependency with respect to a benchmark signal obtained neglecting this dependency. We have showed that in principle, given enough individual objects observed (i.e. enough observation time, observed fraction of the sky, etc.) a metallicity dependency feature could be discerned from the flat benchmark case. This is another step in the promising multi-tracers field and towards its astrophysical applications for future works to come.

3

Gravitational waves × HI intensity mapping: cosmological and astrophysical applications

This chapter is based on the following manuscript:
G. Scelfo, M. Spinelli, A. Raccanelli, L. Boco, A. Lapi, M. Viel
Gravitational waves × HI intensity mapping: cosmological and astrophysical applications
JCAP 01 (2022) 004, arXiv:2106.09786.

3.1 Chapter overview and motivation

Beside GWs, another observable that has recently emerged as extremely promising is the measurement of the integrated emission from spectral lines coming from unresolved galaxies and the diffuse intergalactic medium, the so-called Intensity Mapping (IM - see e.g., Kovetz et al. (2017c); Bernal & Kovetz (2022) for comprehensive reviews). The IM technique allows probing large areas of the sky in a relatively small amount of time, since it does not aim at resolving single galaxies: it measures the intensity of a specific emission line in order to map the underlying matter distribution, treating it as a diffuse background. Since we exactly know the emission frequency of the line under study, the observed wavelength provides information on the radial position of the source, whereas its brightness temperature fluctuations describe how the underlying

Large Scale Structure (LSS) is distributed. As described in section 1.3.2, the redshifted 21 cm line of neutral hydrogen is one of the most promising targets for IM and several detections of the signal in cross-correlation with galaxy surveys and other LSS tracers have already been performed. The advantage of considering maps of emission line intensity as observables is not limited to the fact that they provide another LSS tracer. Intensity mapping measurements allow performing a very refined tomography: knowing the expected emission wavelength of the line under study allows for a precise and fine redshift distribution determination. In addition, IM is able to cover large cosmological volumes with respect to resolved galaxy surveys, in a relatively fast and inexpensive way.

Given the rapidly growing interest in both GW and IM, it is natural to investigate the synergies and the scientific output that can be obtained through their combination. In this chapter we aim at characterizing the cross-correlation signal between the two, focusing on the IM of the neutral hydrogen (HI) from the proposed 21cm IM survey with the SKAO and on resolved GW events from the merger of BBHs as detected by the Einstein Telescope. A cross-correlation signal is expected because both HI and GWs trace the cosmic density field. Crucially, as we will see, they do so in different ways depending on some underlying assumptions on both astrophysics and cosmology. We then present a few possible applications by studying astrophysical and cosmological tests that can be performed through the GW $\times$ IM cross-correlation and forecast their potential when considering expected data from the SKAO and the ET.

Firstly, we investigate the possibility of calibrating the statistical redshift distribution of GW events thanks to the cross-correlation with IM. This idea relies on the fact that, while GWs are affected by a large redshift uncertainty (in case an electromagnetic counterpart is not available, such as for BBHs), the IM provides uniquely refined tomographic information on the observed signal. Since the HI is a good tracer of the LSS, by assuming that the BBH have astrophysical origin, we would expect them to highly cross-correlate with the LSS and, consequently, with the HI IM signal. This is a generally valid technique applicable when considering two tracers, one of which is characterized by much smaller redshift errors than the other; this was already addressed is several works in the literature (see e.g., Newman (2008); Benjamin et al. (2010); Matthews & Newman (2010); Schmidt et al. (2013b); Ménard et al. (2013); McQuinn & White (2013); Choi et al. (2016); Scottez et al. (2016); Rahman et al. (2016); Johnson et al. (2016); Alonso et al. (2017); van Daalen & White (2018); Cunnington et al. (2018); Alonso et al. (2021)). Here we investigate, to our knowledge for the first time,

its potential as a method to obtain statistical redshift distributions for GW catalogs, which will provide a great improvement in dark sirens and cross-correlation studies.
Secondly, we study how this observable could help constraining cosmological models. As an example application, we focus on limits that will be possible to obtain for parameters describing the time evolution of the dark energy equation of state.
Thirdly, we tackle the issue of understanding the nature of the progenitors of the merging BBHs: evidences of the presence of Primordial Black Holes (PBHs) among the detected mergers can be found by looking at how GWs trace the underlying matter distribution (and, consequently, the HI IM signal) since different formation scenarios provide different predictions (Raccanelli et al. (2016b); Scelfo et al. (2018)).
This chapter is structured as follows: in section 3.2 we present the methodology used, introducing the mathematical formalism for the Fisher matrix we use for our analyses; in section 3.3 we characterize our GW and HI tracers; in section 3.4 we describe the GW statistical redshift distribution calibration application; in section 3.5 we address the dynamical DE topic; in section 3.6 we tackle the determination of the BBHs progenitors and in section 3.7 we wrap the discussion up.

3.2 Methodology

The observable physical quantities considered throughout this chapter are the angular power spectra C_ℓ introduced in section 1.3.1. The already described formalism for resolved events applies for GW events. In section 3.3.2 we describe how this formalism can easily be extended to non-resolved tracers such as HI from intensity mapping. In section 3.2.1 we describe the methodology adopted for obtaining our results, namely the Fisher matrix formalism.

3.2.1 Fisher analysis

In this work we make use of the Fisher analysis methodology, which we have introduced in chapter 1.4. We summarize here again, for completeness, the formalism adopted for this analysis.
Assuming GWs and IM signals as the two tracers, we divide the total redshift interval surveyed by considered GW experiments in $N_{\rm bins}^{\rm GW}$ bins, with amplitude $\Delta z^{\rm GW}$, and the signal from intensity mapping distributed among $N_{\rm bins}^{\rm IM}$ redshift bins with amplitude $\Delta z^{\rm IM}$.

Given the observed power spectra $\tilde{C}_\ell$s and our set of parameters $\{\theta_n\}$ for the Fisher analysis, we can organize the data in the (symmetric) matrix $\mathcal{C}_\ell$ as

$$\mathcal{C}_\ell = \begin{bmatrix} \tilde{C}_\ell^{\,\mathrm{IM\,IM}}(z_1^{\mathrm{IM}}, z_1^{\mathrm{IM}}) & \dots & \tilde{C}_\ell^{\,\mathrm{IM\,IM}}(z_1^{\mathrm{IM}}, z_N^{\mathrm{IM}}) & \tilde{C}_\ell^{\,\mathrm{IM\,GW}}(z_1^{\mathrm{IM}}, z_1^{\mathrm{GW}}) & \dots & \tilde{C}_\ell^{\,\mathrm{IM\,GW}}(z_1^{\mathrm{IM}}, z_N^{\mathrm{GW}}) \\ & \dots & \tilde{C}_\ell^{\,\mathrm{IM\,IM}}(z_2^{\mathrm{IM}}, z_N^{\mathrm{IM}}) & \tilde{C}_\ell^{\,\mathrm{IM\,GW}}(z_2^{\mathrm{IM}}, z_1^{\mathrm{GW}}) & \dots & \tilde{C}_\ell^{\,\mathrm{IM\,GW}}(z_2^{\mathrm{IM}}, z_N^{\mathrm{GW}}) \\ & \dots & \vdots & \vdots & \dots & \vdots \\ & & \tilde{C}_\ell^{\,\mathrm{IM\,IM}}(z_N^{\mathrm{IM}}, z_N^{\mathrm{IM}}) & \tilde{C}_\ell^{\,\mathrm{IM\,GW}}(z_N^{\mathrm{IM}}, z_1^{\mathrm{GW}}) & \dots & \tilde{C}_\ell^{\,\mathrm{IM\,GW}}(z_N^{\mathrm{IM}}, z_N^{\mathrm{GW}}) \\ & & & \tilde{C}_\ell^{\,\mathrm{GW\,GW}}(z_1^{\mathrm{GW}}, z_1^{\mathrm{GW}}) & \dots & \tilde{C}_\ell^{\,\mathrm{GW\,GW}}(z_1^{\mathrm{GW}}, z_N^{\mathrm{GW}}) \\ & & & & \dots & \vdots \\ & & & & & \tilde{C}_\ell^{\,\mathrm{GW\,GW}}(z_N^{\mathrm{GW}}, z_N^{\mathrm{GW}}) \end{bmatrix}, \tag{3.1}$$

The $\mathcal{C}_\ell$ matrix has dimensions of $(N_{\mathrm{bins}}^{\mathrm{IM}} + N_{\mathrm{bins}}^{\mathrm{GW}}) \times (N_{\mathrm{bins}}^{\mathrm{IM}} + N_{\mathrm{bins}}^{\mathrm{GW}})$. We remind the reader that the tilde symbol stands for *observed* C_ℓs.

From $\mathcal{C}_\ell$ matrix we can compute the Fisher matrix elements as

$$F_{\alpha\beta} = f_{\mathrm{sky}} \sum_\ell \frac{2\ell+1}{2} \mathrm{Tr}\left[\mathcal{C}_\ell^{-1}(\partial_\alpha \mathcal{C}_\ell)\mathcal{C}_\ell^{-1}(\partial_\beta \mathcal{C}_\ell)\right], \tag{3.2}$$

where ∂_α indicates the partial derivative with respect to the parameter θ_α and f_{sky} is the fraction of the sky covered by the intersection of IM and GW surveys. The sum over multipoles ℓ is performed up to a maximum value ℓ_{max}, which corresponds to the achievable angular resolution for the considered sources and instruments. For GW events an accurate estimate of ℓ_{max} would depend on (not limited to) redshift, SNR of the events and other source properties such as mass and spin. Since a rigorous analysis for the estimation of this parameter goes beyond the scope of this work, we use the constant threshold of $\ell_{\mathrm{max}} = 100$, which provides a general plausible value for ET (as also performed in other studies, see e.g., Raccanelli et al. (2016b); Scelfo et al. (2018, 2020)). All scales smaller than it are conservatively cut from the analysis.

The Fisher-estimated marginal error on the parameter θ_α is eventually given by $\sqrt{(F^{-1})_{\alpha\alpha}}$.

3.3 Observables

In this section we characterize the considered tracers: resolved GWs from BBH mergers and the HI signal from intensity mapping experiments. In table 3.1 we summarize the redshift distributions for our tracers, as mentioned in sections 3.3.1 and 3.3.2.

3.3.1 Gravitational Waves

As first tracer we consider GWs from resolved mergers of BBHs, as detected by the Einstein Telescope (ET) experiment, as currently planned in Sathyaprakash et al. (2012b).

Tracer	GW (ET)	IM (SKAO)
z range	[0.5-3.5]	
$N_{\rm bins}$	3	30
Δz	1.0	0.1

Table 3.1: Chosen redshift specifics and experiments for the two tracers considered in this work. Note that the redshift ranges do not necessarily correspond to the best achievable from the indicated surveys.

We study this tracer for $N_{\rm bins}^{\rm GW} = 3$ redshift bins with width $\Delta z^{\rm GW} = 1.0$ in the redshift range $[0.5-3.5]$. Even though the ET instrument would be able to detect BBH mergers outside this redshift range, we limit our analysis to it because it is the most optimal redshift range for the SKA-Mid IM survey (Bacon et al. (2020)), i.e., the survey we consider for our HI tracer). Considering GWs events beyond this limit would not help our analysis because we would not have any HI signal to cross-correlate them with.
It is worth noting that the ET is not the only planned third-generation GW detector. Another promising experiment is given by the Cosmic Explorer (CE) (Reitze et al. (2019)). We anticipate here that, within our framework, results for ET and CE are quite similar, although slightly optimistic for the latter. We thus concentrate on the more conservative ET for the rest of the paper.
Note that we consider such large bins in order to take into account any possible luminosity distance uncertainty on the observed GWs events, also maintaining an approach as independent as possible on cosmological parameters. Indeed, the bin width $\Delta_z^{\rm GW} = 1.0$ is larger than any redshift uncertainty estimated for LIGO/Virgo sources (see e.g., Table 6 of Abbott et al. (2021)), which will be even smaller for third-generation observatories. As a matter of fact, measurements of BBH mergers are associated to an uncertainty on the luminosity distance, which can be connected to a redshift uncertainty only by assuming a specific cosmology. An error on the assumed cosmology leads to a wrong assumption on the redshift of the event (and on its error). Since we are making use of a statistical tomographic approach, the main important element here is that the containing redshift bin for each observed event is the appropriate one. Assuming large bins for GWs makes this assumption safer, i.e., even when making errors on the assumed cosmology, the event-bin mapping would not be biased for most of the events. On the other hand, assuming smaller bins for GWs might provide more information and more optimistic forecasts, but it could lead to biased results if the wrong cosmology is assumed when actually performing these applications with real future data We have tested the impact on our results on the bin width choice. As way of example, we found that by reducing $\Delta_z^{\rm GW}$ from 1.0 to 0.5 (doubling the number of GW bins)

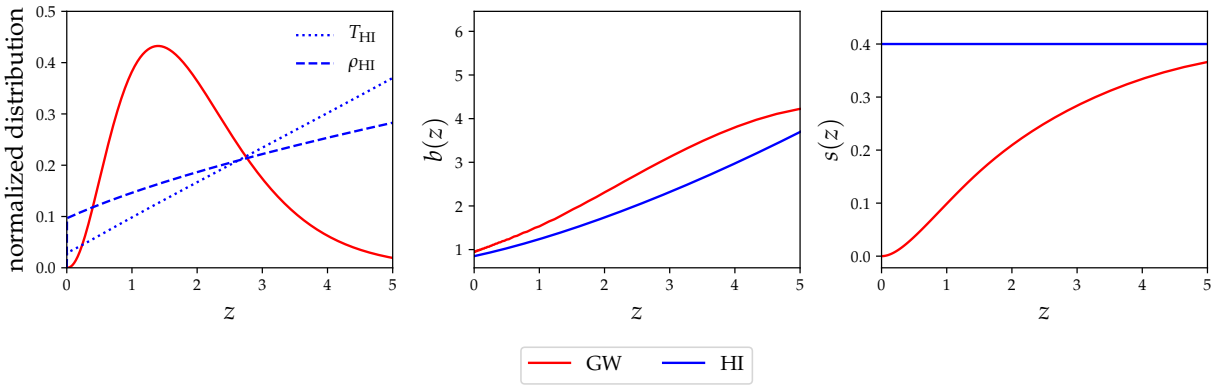

Figure 3.1: Specifics for the astrophysical GW and HI tracers considered in this work. *Left:* normalized redshfit dependence (dN/dz for GWs; $T_{\rm b}(z)$ and $\rho_{\rm HI}(z)$ for HI). *Center:* bias $b(z)$. *Right:* magnification bias $s(z)$.

the forecasts on the bias parameter $\bar{b}_{\rm GW}$ are 40% more optimistic, since a more refined tomographic information is being exploited. Nonetheless, this shows that results could be even more promising than those reported in this paper, but we preferred to choose a more conservative approach by adopting larger GW redshift bins, safely getting rid of any possible bias due to redshift or cosmology related errors. This makes the forecasts presented in this manuscript almost "cosmology-agnostic" and independent on reasonable errors on the single sources redshifts.
Regarding the redshift distribution and the biases, which are fundamental quantities in estimating the C_ℓs (as discussed in section 1.3.1), we characterize this tracer following prescriptions from Boco et al. (2019); Scelfo et al. (2020), which are already summarized in chapter 2 (section 2.2.2). In figure 3.1 we provide redshift distribution and biases values for our GW tracer of astrophysical origin, together with the same quantities characterizing the HI from IM.

Noise sources

We characterize the considered GWs events with a shot-noise component as the only noise source to the angular power spectra:

$$C_\ell^{\rm N,GW}(z_i, z_j) = C_\ell^{\rm shot}(z_i, z_j) = \frac{\delta_{ij}}{\bar{n}(z_i)} \tag{3.3}$$

where δ_{ij} is the Kronecker delta and $\bar{n}(z_i)$ is the mean number density of sources in the i^{th} redshift bin. It affects the $C_\ell(z_i, z_i)^{\rm GW,GW}$ entries (i.e. only cross-correlations between the same GW tracer among the same redshift bin).

3.3.2 HI Intensity Mapping

In this section we characterize our second tracer: the forecasted measure of the HI distribution by a SKAO-Mid intensity mapping survey (Bacon et al. (2020); Dewdney et al. (2009); Maartens et al. (2015)). In the following sections we describe how the resolved sources formalism for the angular power spectra can be easily translated to be applied to the unresolved HI IM case, and we characterize the specifics for this observable.
Throughout this work we consider the HI tracer in the redshift range $[0.5-3.5]$, divided in bins of width $\Delta z^{\rm IM} = 0.1$, for a total of $N^{\rm IM}_{\rm bins} = 30$ redshift bins. This is expected to be around the optimal redshift range for the SKAO-Mid.

3.3.2.1 From resolved sources to IM

As provided in section 1.3.1, the cross-correlation formalism for resolved sources of different tracers is well defined and comprehensive of relativistic effects. When working with the IM signal of any line (the HI in our case), we do not deal with number counts, since we are looking at the ensemble of unresolved sources. However, the unresolved tracer case can be treated adapting the same formalism (e.g., Alonso & Ferreira (2015a); Hall et al. (2013)). The following points are specifically referred to the HI, but are valid for any other line. In particular:

- *Redshift distribution:* while we characterize resolved sources with a redshift distribution of their number counts dN_X/dz, for the HI intensity mapping case we shall consider the HI comoving density distribution defined in Crighton et al. (2015) as $\rho_{\rm HI}(z) = \Omega_{\rm HI}(z)\rho_{\rm crit,0}$ and the mean brightness temperature $T_b(z)$. Their explicit expressions are (see e.g., Crighton et al. (2015); Battye et al. (2013)):

$$\rho_{\rm HI}(z) = 4(1+z)^{0.6}10^{-4} \cdot \rho_{\rm crit,0} \tag{3.4}$$

$$T_b(z) = 44\mu{\rm K}\left(\frac{\Omega_{\rm HI}(z)h}{2.45\times10^{-4}}\right)\frac{(1+z)^2}{E(z)}, \tag{3.5}$$

  where $\rho_{\rm crit,0}$ is the critical density today and $E(z) = H(z)/H_0$. Since the density $\rho_{\rm HI}$ provides the redshift dependence of the *absolute* redshift distribution of HI atoms, whereas the mean brightness temperature T_b is a directly *observed* physical quantity through IM, we make use of T_b in place of the observed redshift distribution of equation (1.64) and of $\rho_{\rm HI}$ to compute the evolution bias term $f_{\rm evo}(z)$. Both $\rho_{\rm HI}(z)$ and T_b redshift dependencies are plotted in the left panel of figure 3.1.

- *Bias:* we can treat the bias analogously as it is done for the resolved sources case. In this work we use the following analytic expression obtained fitting results from Spinelli et al. (2020):

$$b_{\rm HI}(z) = a(1+z)^b + c, \tag{3.6}$$

with $a = 0.22$, $b = 1.47$ and $c = 0.63$. This quantity is plotted in the central panel of figure 3.1. This prescription originates from the outputs of a semi-analytical model for galaxy formation that include an explicit treatment of neutral hydrogen and are in agreement with the findings of Villaescusa-Navarro et al. (2018) based on Illustris TNG hydro-dynamical simulations. The bias is expected to be around unity at low z (e.g. ~ 0.85 at $z \sim 0.06$ Martin et al. (2010)), where the HI is strongly present in young galaxies with high Star Formation Rates (Anderson et al. (2018)). In order to make sure that uncertainties on the HI bias at higher z do not affect the conclusions of our work, we have checked that performing the same analysis with the extreme hypothesis of a constant unitary value of $b_{\rm HI}(z)$ leads to a change on the Fisher estimated errors for cosmological parameters below 15%.

- *Magnification bias:* when treating any IM experiment, the magnification bias assumes the value

$$s_{\rm HI}(z) = 0.4, \tag{3.7}$$

which corresponds to the absence of lensing effects. This is due to the fact that the observed physical quantity is a surface brightness (instead of number counts) which is not altered by this type of phenomena (see e.g., Hall et al. (2013) and references therein).

- *Evolution bias:* as mentioned above, this quantity is obtained analogously to the resolved sources case, substituting the redshift distribution for resolved sources with the density distribution:

$$f_{\rm HI}^{\rm evo}(z) = \frac{d\ln\rho_{\rm HI}(z)}{d\ln a} \tag{3.8}$$

with a being the scale factor.

3.3.2.2 Noise sources

When considering C_ℓs including the IM component (both IM $\times$ IM and GW $\times$ IM cases) we express the relation between theoretical C_ℓ^{XY} (computed with `Multi_CLASS`)

and the observed $\tilde{C}_\ell^{XY}$ as:

$$\tilde{C}_\ell^{\mathrm{IM,IM}}(z_i, z_j) = \mathcal{B}(z_i)\mathcal{B}(z_j)C_\ell^{\mathrm{IM,IM}}(z_i, z_j) + C_\ell^{\mathrm{N,IM}} \tag{3.9}$$

and

$$\tilde{C}_\ell^{\mathrm{IM,GW}}(z_i, z_j) = \mathcal{B}(z_i)C_\ell^{\mathrm{IM,GW}}(z_i, z_j) \tag{3.10}$$

where the $\mathcal{B}^X(z_i)$ encodes the signal suppression at scales smaller of the FWHM of the beam θ_B. In single-dish configuration $\theta_B \sim 1.22\lambda/D_d$, thus implying a more severe suppression of the signal at lower frequencies:

$$\mathcal{B}(z_i) = \exp[-\ell(\ell+1)(\theta_B(z_i)/\sqrt{16\ln 2})^2]. \tag{3.11}$$

In equation (3.9), the term $C_\ell^{\mathrm{N,IM}}$ indicates noise sources (see also equation (1.59)). For the HI case we consider the intrinsic noise of the instrument C_ℓ^{instr} and the residual error due to the procedure of cleaning the cosmic IM signal from the bright foreground emission C_ℓ^{fg}:

$$C_\ell^{\mathrm{N,IM}} = C_\ell^{\mathrm{instr}} + C_\ell^{\mathrm{fg}}, \tag{3.12}$$

whereas the shot-noise is instead a very subdominant component (see e.g., Castorina & Villaescusa-Navarro (2017); Villaescusa-Navarro et al. (2018)). In the following paragraphs we describe how these noise sources are treated.

Instrumental noise

The experiment setup considered in this work is IM performed in single dish (Bacon et al. (2020); Santos et al. (2017)) mode and with a collection of N_d dishes. The noise angular power spectrum for this case is given by (see e.g., Bull et al. (2015); Santos et al. (2015, 2017)):

$$C_\ell^{\mathrm{instr}} = \sigma_T^2\theta_B^2. \tag{3.13}$$

The single-dish rms noise temperature σ_T writes as

$$\sigma_T \approx \frac{T_{\mathrm{sys}}}{\sqrt{n_{\mathrm{pol}}Bt_{\mathrm{obs}}}}\frac{\lambda^2}{\theta_{\mathrm{B}}^2 A_e}\sqrt{S_{\mathrm{area}}/\theta_{\mathrm{B}}^2}\sqrt{\frac{1}{N_{\mathrm{d}}}}. \tag{3.14}$$

Since the beam FWHM of a single dish is $\theta_B \sim 1.22\lambda/D_d$, one gets $\lambda^2/A_e \sim \lambda^2/D_d^2 \sim \theta_B^2$, where D_d is the diameter of a single dish, A_e is the effective collecting area of the dish and $\lambda = \lambda(z)$ is the observed wavelenght of the redshifted 21cm signal emitted at at z: $\lambda(z) = \lambda_{21cm}(1+z)$. From this, one can write:

$$C_\ell^{\mathrm{instr}}(z_i) \approx \left(\frac{T_{\mathrm{sys}}}{T_b(z_i)\sqrt{n_{\mathrm{pol}}Bt_{\mathrm{obs}}N_d}}\sqrt{\frac{S_{\mathrm{area}}}{\theta_{\mathrm{B}}^2}}\frac{1}{T_b(z_i)}\right)^2\theta_B^2. \tag{3.15}$$

Following SKAO-Mid prescriptions, we have the following parameters values: $T_{\rm sys} = 28K$ for the system temperature, $B = 20 \cdot 10^6 Hz$ for the bandwidth, $t_0 = 5000h = 1.8 \cdot 10^7 s$ for the observation time, $N_d = 254$ for the total number of dishes, $S_{\rm area} = 20000 deg^2$ for the total surveyed area, $A_e = 140m^2$ and $D_d = 15m$. Notice the normalization to the mean brightness temperature at the center of the redshift bin $T_b(z_i)$, needed to retrieve a dimensionless power spectrum to be added to the theoretical dimensionless one in order to estimate the observed C_ℓs, according to equation (1.59) . Numerical values are taken from table 2 of Santos et al. (2015). Even though $S_{\rm area} = 20000\, deg^2 \sim f_{\rm sky} = 0.5$ is the official expected value of sky coverage, for the purpose of this work we consider also different values of $f_{\rm sky}$.
Finally, we remark that the $C_\ell^{\rm instr}(z_i)$ noise component is expressed as function of one single redshift because we assume that it is de-correlated among different bins, affecting only auto-correlations.

Foregrounds

The presence of strong foregrounds is one of the central challenges of IM, currently preventing a detection in auto-correlation of the signal (see e.g., references Switzer et al. (2013); Wolz et al. (2021)). Such detection should instead be possible for an IM survey with SKAO telescope due to improvements in the signal-to-noise, to a larger scanned sky patch and to the larger frequency band. Nevertheless, the cleaning procedure will not be perfect and the recovery of the pristine HI signal will still be partially complicated by the foreground emission. This effect has been studied with simulations with various degrees of complexity (Alonso et al. (2014); Carucci et al. (2020); Cunnington et al. (2021); Matshawule et al. (2021); Soares et al. (2021)). For the purposes of this work, we quantify the residual error that could be expected after a foregrounds removal procedure adding a noise term $C_\ell^{\rm fg}$ to the theoretical C_ℓs, for the IM $\times$ IM components and for any redshift bins combination. Note that, since we focus on the angular power spectrum, we do not model the well known foreground cleaning effect of removing too much power at large scales along the line-of-sight. Our noise term is only a residual systematic accounting for the difficulties in cleaning large spatial scales. We model the $C_\ell^{\rm fg}$ term as

$$C_\ell^{\rm fg} = K^{\rm fg} \cdot F(\ell), \tag{3.16}$$

where $K^{\rm fg}$ is a normalization constant determining the overall amplitude of the residual foregrounds related errors and $F(\ell)$ encodes the scale-dependency. We write this term

as

$$F(\ell) = \frac{1}{f_{\rm sky}} A e^{b\ell^c}, \tag{3.17}$$

accounting for a larger effect of the cleaning of the signal at larger scales and simply fitting this expression to results of Alonso et al. (2014) (middle-left panel of their figure 3), obtaining $A \sim 0.129$, $b \sim -0.081$, $c \sim 0.581$. This procedure introduces an error of around 12% at $\ell \sim 2$ and 4% at $\ell \sim 100$ (for $f_{\rm sky} = 1.0$). It is also possible to define the variance of this systematic error (see e.g., Camera et al. (2016)):

$$\sigma^2_{\rm sys} = \int \frac{{\rm d}\ln\ell}{2\pi} \ell(\ell+1) \left| C_\ell^{\rm fg} \right|. \tag{3.18}$$

Setting the value of the overall normalization factor $K^{\rm fg}$ to an average value of all the $C_\ell^{\rm IM,IM}(z_i, z_j)$ components:

$$K^{\rm fg} = \left\langle C_\ell^{\rm IM,IM}(z_i, z_j) \right\rangle, \tag{3.19}$$

and considering our redshift binning, we obtain a fiducial value of

$$K^{\rm fg} \simeq 6 \cdot 10^{-7}. \tag{3.20}$$

This leads to a variance of $\sigma^2_{\rm sys} \simeq 3 \cdot 10^{-7}$, in agreement with what assumed in Camera et al. (2016).

In figure 3.2 we compare the resulting $C_\ell^{\rm fg}$ for different amplitudes $K^{\rm fg}$ to the contribution from instrumental noise (at $z = 2.5$ by way of example). The contamination term from foreground removal is always dominant and stronger at low multipoles. We report in the figure also an example of the auto angular power spectrum of the HI signal and a cross power spectrum between two different bins.

We have repeated our analysis using different forms for (3.17) and with different amplitudes, and found a change in the Fisher estimated errors always below $\sim 10 - 15\%$. Therefore, this would not alter the conclusions reached. Note that our residual foreground contribution is neither frequency dependent nor considers possible coupling between the different scales. These should be secondary effects, especially assuming a full sky survey and a blind approach to cleaning (Alonso et al. (2014); Spinelli et al. (2021)).

3.4 Gravitational waves statistical redshift distribution

The first application of the GW × IM cross-correlation we present in this work is the possibility to obtain a statistical determination of the redshift distribution of GWs detected by laser interferometers. Those detections in fact provide information only

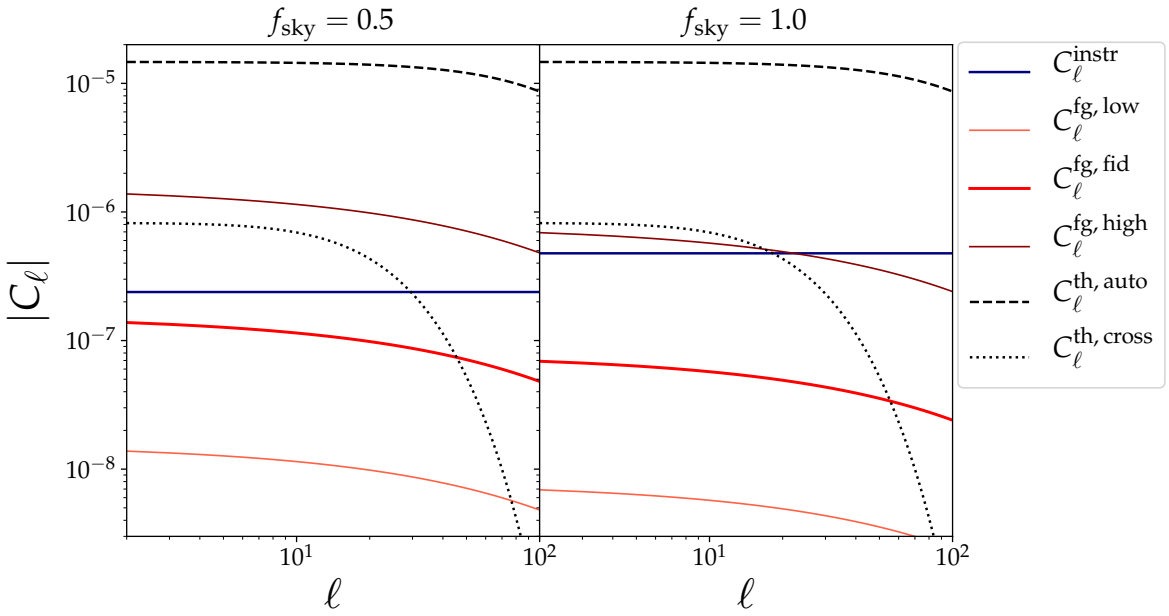

Figure 3.2: Comparison between HI angular power spectra C_ℓs. In black: theoretical power spectra $C_\ell^{\rm th}$ from `Multi_CLASS` for the IM $\times$ IM case, auto-correlating the $20^{\rm th}$ redshift bin ($2.4 < z < 2.5$) with itself (dashed line) and cross-correlating the $15^{\rm th}$ redshift bin ($1.9 < z < 2.0$) with the $20^{\rm th}$ (dotted line), as exemplificative case. In blue: instrumental noise power spectrum for SKAO-Mid survey at redshift $z_{\rm mean} = 2.5$. In different shades of red: foreground cleaning noise power spectra, with amplitudes equal to $K^{\rm fg}$ ($C_\ell^{\rm fg,\,fid}$), $0.1 \cdot K^{\rm fg}$ ($C_\ell^{\rm fg,\,low}$) and $10 \cdot K^{\rm fg}$ ($C_\ell^{\rm fg,\,high}$). Left(right) panel corresponds to $f_{\rm sky} = 0.5(1.0)$.

on the chrip mass of the system and the (GW) luminosity distance, therefore redshift information is only a derived quantity, based on astrophysical and cosmological assumptions (Schutz (1986); Bertacca et al. (2018)). We rely on the idea that a given tracer whose redshift distribution is well defined can help in calibrating that of a second tracer through studying the cross-correlation of the two. This was already done in several works with techniques such as correlations or the so-called Clustering Based Redshift estimation (see e.g., Newman (2008); Benjamin et al. (2010); Matthews & Newman (2010); Schmidt et al. (2013b); Ménard et al. (2013); McQuinn & White (2013); Kovetz et al. (2017b); Choi et al. (2016); Scottez et al. (2016); Rahman et al. (2016); Johnson et al. (2016); Alonso et al. (2017); van Daalen & White (2018); Cunnington et al. (2018); Alonso et al. (2021); Mukherjee et al. (2021a,b)). We mainly follow the methodology of Alonso et al. (2017), in which the authors perform a redshift calibration of a photometric sample of galaxies through cross-correlation with a spectroscopic sample.

Our case is equivalent, but we make use of the IM of the HI to calibrate GWs events. In fact, GW detected events are characterized by a big uncertainty on their localization due to poor angular resolution, whereas IM provides a refined sliced redshift information about the line under study. Assuming the progenitors of the merging BBHs have astrophysical origin, they are expected to trace very well the underlying distribution of the LSS, which is also well traced by the HI distribution. Combining these two tracers together is expected to improve the redshift localization of the poorly known one (GW) thanks to the refined information coming from other, much better localized (IM). We stress the fact that performing this analysis with resolved photometric galaxy samples instead of IM would not be feasible, due to their lower redshift resolution.

Let us stress again that this methodology aims at calibrating the statistical distribution of a tracer which is poorly localized: this is why we only consider BHBH mergers without taking into account also Neutron Stars (NS) binaries or BHNS systems. Indeed, these latter types of systems can likely be matched to an electromagnetic counterpart, allowing for a well precise localization of the binaries, much more competitively than what the method explored in this section can accomplish.

Given our fiducial redshift distribution for GWs (as described in section 3.3.1), we re-model it as a piecewise (PW) function. Each piece has width equal to the IM bin width $\Delta z^{\rm IM}$, so that the total number of pieces is equal to $N_{\rm bins}^{\rm IM} = 30$ and each of them perfectly overlaps with a specific IM redshift bin. The overall amplitude of the PW function in the i^{th} bin is indicated as A_i.

Following the formalism described in section 3.2.1, we perform a Fisher matrix analysis considering the following set of Fisher parameters: the 30 amplitudes $\{A_i\}$ of the GWs PW redshift distribution and $\{\ln 10^{10} A_s, n_s, \bar{b}_{\rm GW}, \bar{b}_{\rm HI}, K^{\rm fg}\}$ (for a total of 35 parameters)[1]. The spectral index and amplitude n_s and A_s are introduced in the pipeline in order to account for a possible cosmology dependence of our results. A fully cosmology based pipeline (including also the dark energy parameters $\{w_0, w_a\}$) will be explored in section 3.5. We set Planck priors on $\{\ln 10^{10} A_s, n_s\}$ (Planck Collaboration et al. (2016)).

Note that there is a disadvantage in performing GW $\times$ IM instead of LSS $\times$ IM (such as by Alonso et al. (2017)) and constraining the GWs redshift distribution is more difficult than that of photometric galaxy samples. Firstly, the sum over multipoles of equation 3.2 stops at $\ell_{max} = 100$ (for ET), while galaxy surveys provide a much higher angular resolution (e.g., $\ell_{max} \sim 2000$ in Alonso et al. (2017)). Also, less objects are detected when considering GWs signals from BHBH mergers, inducing a more relevant shot noise contribution, which is translated into higher error bars.

From the Fisher estimated error $\sigma_{\rm A_i}$ on the amplitudes A_i one can directly compute a relative error given by the fraction between the error and the fiducial value A_i:

$$e^{\rm rel}_{\rm A_i} = \sigma_{\rm A_i}/A_i. \tag{3.21}$$

In figure 3.3 we show the error bars on the 30 GW redshift distribution amplitudes A_i with absolute errors (left panels) and relative errors (right panels) for various combinations of $T^{\rm GW}_{\rm obs}$ and $f_{\rm sky}$. We recall that the $f_{\rm sky} = 0.5$ value is the fiducial scenario for SKAO-Mid, whereas cases for lower values of $f_{\rm sky}$ can be considered conservative, and higher values can be thought as a limiting case for future experiments. It is possible to see that for enough high values of $T^{\rm GW}_{\rm obs}$ and $f_{\rm sky}$ the error-bars are relatively small and the relative error is below unity. This takes place mainly at lower redshifts, whereas increasing z the error size becomes large and the relative error is raised above unity. Overall, it is possible to see that redshift calibration of GWs events is quite effective in the low-medium redshift range, whereas at higher redshift very high values of $T^{\rm GW}_{\rm obs}$ and $f_{\rm sky}$ would be required, when possible.

[1]The fiducial parameters values we use in this pipeline are: $\{\ln 10^{10} A_s, n_s, \bar{b}_{\rm GW}, \bar{b}_{\rm HI}, K^{\rm fg}\} = \{3.098, 0.9619, 2.166, 1.851, 6 \cdot 10^{-7}\}$. The cosmology parameters values are taken from (Planck Collaboration et al. (2016)), the biases values are obtained by weighting the bias expressions for the tracers redshift distribution in the considered redshift range $[0.5, 3.5]$ and the $K^{\rm fg}$ value derives from equation (3.20). Finally, the fiducial values for the amplitudes $\{A_i\}$ are given by the amplitudes of the full GWs redshift distribution at the corresponding redshifts.

We conclude noting one fundamental peculiarity of our approach, which is basically "cosmology-agnostic", in the sense that it solely relies on the cross-correlations between GWs (in large z bins, to account for redshift localization uncertainties) and IM (in appropriately small bins). It is independent from the underlying "true" cosmology, since we have only assumed fiducial cosmological parameters to perform our Fisher forecasts, but no assumptions in this regards will be needed when working with actual data (thanks to the large width of the considered GWs redshift bins). In addition, note also that in our Fisher analysis we allow for variation of the 30 amplitudes on the GWs redshift distribution: this essentially corresponds to not imposing any prior on the shape of this distribution, taking out any astrophysical assumption that would have imprints on the distribution shape. Forecasts obtained in this way are more pessimistic than other works in current literature (see e.g., Ng et al. (2021)) and this is due to the fact that a very general approach is being taken here, without any cosmology/astrophysics priors. Finally, let us stress again that the aim of this application is to calibrate the *statistical* distribution of GWs sources, i.e., improving the knowledge on the disposition along redshift of the whole ensemble. We do not aim at better localizing each single event. For this reason, we do not need to take into account the redshift error of each source, as long as the GW redshift binning is large enough the compensate any possible uncertainty in this regard.

3.5 Cosmological constraints: dynamical dark energy

The GW $\times$ LSS cross-correlation, as a tracer of the matter density field, can provide information on a variety of cosmological parameters. Regarding the GW $\times$ IM observable, given the specific redshift range and peculiarities of the expected signal, there might be some particular model or parameter that will be optimally tested by it.
In this section we present an example of one of such measurements, which is the possibility of constraining dark energy parameters; in particular, we will focus on parameters describing the redshift evolution of its equation of state.
Starting from the Einstein field equations, which describe how gravity behaves due to the presence of mass-energy (and how this moves given the space-time curvature), one can write

$$G_{\mu\nu} = T_{\mu\nu}\,, \tag{3.22}$$

with the appropriate choice of conventions. Here $G_{\mu\nu}$ and $T_{\mu\nu}$ are the so called Einstein tensor and stress-energy tensor respectively. In order to account for the observed accelerated expansion of the Universe, in a General Relativistic framework, equations

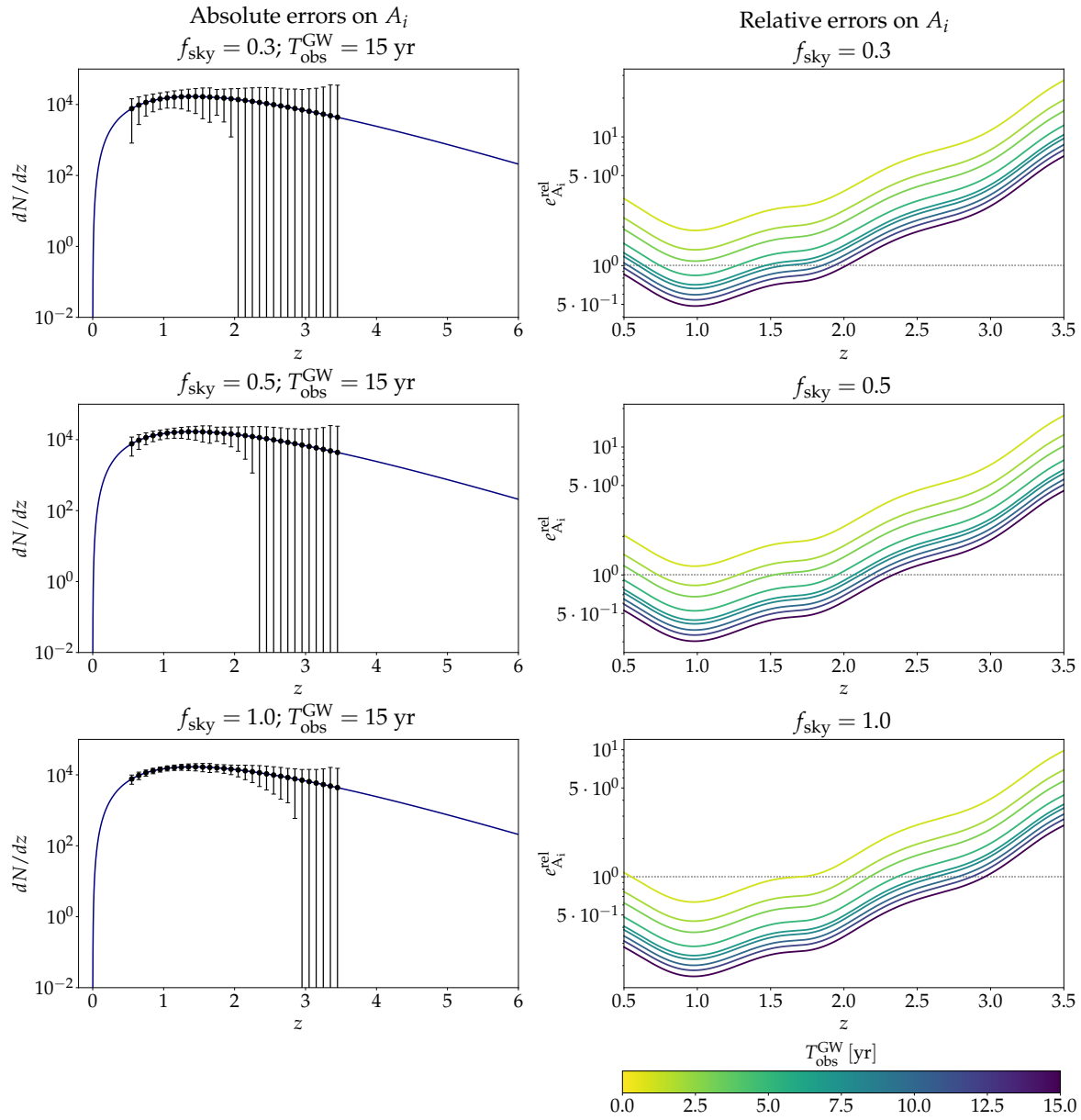

Figure 3.3: *Left:* GW fiducial redshift distribution (in blue) with error-bars on the amplitude parameters A_i. *Right:* Fisher estimated relative errors $e_{\rm A_i}^{\rm rel}$ on the amplitude parameters A_i. Different values of $T_{\rm obs}^{\rm GW}$ (from 1 yr to 15 yr) and $f_{\rm sky}$ ($f_{\rm sky} = 0.3$, 0.5, 1.0) are provided.

(3.22) have to be modified substituting $T_{\mu\nu}$ with $T'_{\mu\nu} = T_{\mu\nu} + T^{\rm DE}_{\mu\nu}$, where $T^{\rm DE}_{\mu\nu} = -\Lambda g_{\mu\nu}$ (with $g_{\mu\nu}$ the metric tensor) and DE stays for dark energy. This can be in the form of a cosmological constant or an additional field. Among the many possible proposed models and deviations from the cosmological constant (originally inspired by vacuum energy), a possibility is to investigate deviations from its equation of state (eos) being constant with redshift. The eos is defined as $w = \dfrac{p}{\rho}$ (where p and ρ are respectively the pressure and energy densities of the fluid). If the DE behaviour is described by a cosmological constant, then $w = -1$, whereas the relation

$$w(a) = w_0 + w_a(1 - a) \tag{3.23}$$

generally describes the case of time evolution. Current measurements from CMB and galaxy clustering are consistent with a cosmological constant (Planck Collaboration et al. (2018); Ross et al. (2017)), but many models predict small departures from the cc case (see e.g., Giudice et al. (2021); Heisenberg et al. (2018)), therefore this remains an important part in the efforts toward a better understanding of the cosmological model.

Here we investigate how well the DE parameters $\{w_0, w_a\}$ can be constrained through GW $\times$ IM cross-correlations. We include in our Fisher analysis pipeline summarized in section 3.2.1 the following parameters: $\{w_0, w_a, \omega_{\rm cdm}, \omega_{\rm b}, 100\theta_s, \ln 10^{10} A_s, n_s, \bar{b}_{\rm GW}, \bar{b}_{\rm HI}, K^{\rm fg}\}$ (for a total of 10 parameters)[2]. The differences with respect to the analysis of section 3.4 consist in the usage of the full GWs redshift distribution (in place of its piece-wise approximation) and the addition of other cosmology related Fisher parameters: w_0, w_a, the cold dark matter physical density $\omega_{\rm cdm} = \Omega_{\rm cdm} h^2$, the baryon physical density $\omega_{\rm b} = \Omega_{\rm b} h^2$ and the angular scale of the sound horizon at decoupling $100\theta_s$. We set a Planck prior on the $\{\omega_{\rm cdm}, \omega_{\rm b}, 100\theta_s, \ln 10^{10} A_s, n_s\}$ parameters, unless where stated otherwise.

In figure 3.4 we provide forecasts for the constraining power on the dark energy parameters $\{w_0, w_a\}$ for the experiments considered in this work, including or not Planck priors and for different values of $f_{\rm sky}$. On the right panel we can see the improvement that would come by increasing the fraction of the sky surveyed. Overall, we can notice that the predicted constraints are qualitatively in agreement with other studies, such

[2]The fiducial parameters values we use in this pipeline are: $\{w_0, w_a, \omega_{\rm cdm}, \omega_{\rm b}, 100\theta_s, \ln 10^{10} A_s, n_s, \bar{b}_{\rm GW}, \bar{b}_{\rm HI},$
$K^{\rm fg}\} = \{-1.0, 0.0, 0.12038, 0.022032, 1.042143, 3.098, 0.9619, 2.166, 1.851, 6 \cdot 10^{-7}\}$. As in the previous section, the cosmology parameters values are taken from Planck Planck Collaboration et al. (2016), the biases values are obtained weighting the bias functions for the respective redshift distributions in the considered redshift range $[0.5, 3.5]$ and the $K^{\rm fg}$ value derives from equation (3.20).

as e.g., Raccanelli (2017) in which a study of the cross-correlation between GWs and radio galaxy surveys is performed or Bull et al. (2015) in which forecasts are obtained for HI intensity mapping experiments.
We can also see that constraints are approximately comparable to the BOSS+Planck results available in the literature (see e.g., Ross et al. (2017)) for what concerns the errors on the $\{w_0, w_a\}$ parameters, with w_0 constraints slightly weaker. Comparing our results with those from the Euclid collaboration, we can see that (see e.g., Euclid Collaboration et al. (2019)) our constraints are approximately comparable or slightly less competitive when considering combinations of all probes tested by Euclid (weak lensing and spectroscopic/photometric galaxy clustering), but more stringent with respect to Euclid forecasts obtained through one single probe. A similar comparison can be done when looking at forecasts for the Vera Rubin Observatory (LSST, see e.g., Ivezić et al. (2019)): our forecasts are more optimistic than those from the LSST (up to 50%) when considering just the single isolated probes testable by the survey, but become less competitive when their combination in the LSST is exploited. All in all, although the forecasts we obtain with this methodology are not competitive with the maximum potential that other surveys (such as those mentioned above) can achieve, they can still provide an alternative way to test these scenarios. Cross-correlations are well known for helping in reducing systematics (see e.g., Bonaldi et al. (2016)). For this reason, these measurements will provide a very useful cross-check to available results, as they will come from cross-correlating two very different datasets and will be affected by much less and different systematics.

3.6 Astrophysical vs. primordial origin of merging black hole binaries

In this section we tackle the issue of using GW $\times$ IM for determining the origin of the progenitors of merging BBHs, distinguishing between the possibility that they originate from the end-point of stellar evolution, or that they are Primordial Black Holes (PBHs) generated in the early universe.
PBHs were first theorized a few decades ago (Hawking (1971); Carr & Hawking (1974)) when it was proposed that some over-dense regions in the primordial universe could reach the threshold for gravitational collapse and, in some regions, form black holes. Several formation mechanism have been proposed in literature, such as the collapse of cosmic string loops or domain walls (Polnarev & Zembowicz (1991); Hawking (1989); Wichoski et al. (1998); Berezin et al. (1983); Ipser & Sikivie (1984)), the collapse of

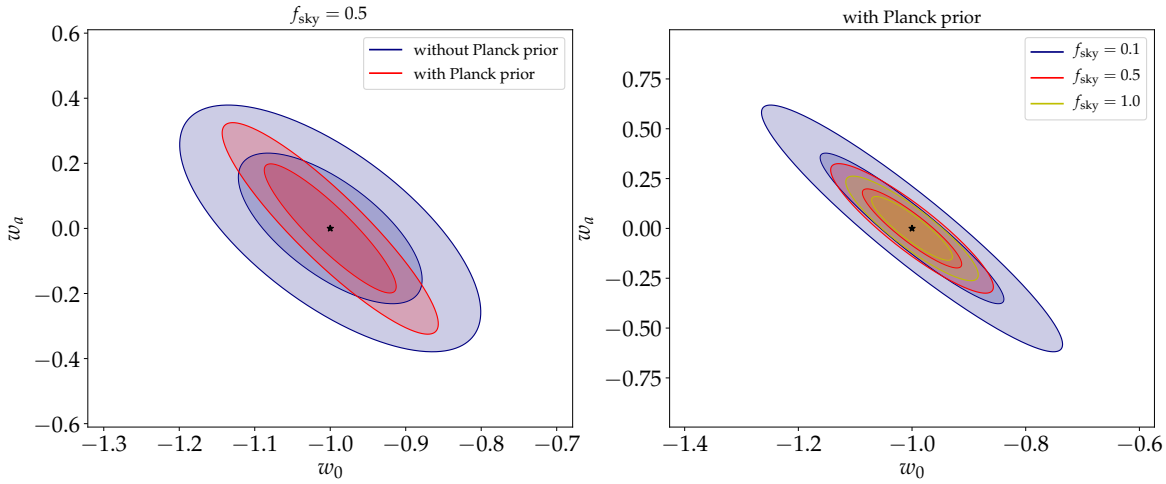

Figure 3.4: Contour plots for the DE parameters $\{w_0, w_a\}$ at 1σ and 2σ confidence levels, for fixed $T_{\rm obs}^{\rm GW} = 10$yr. *Left:* forecasts for fixed $f_{\rm sky} = 0.5$. With and without applying a Planck prior on other cosmology parameters. *Right:* forecasts for different values of $f_{\rm sky}$ (as legend). A Planck prior on all other cosmology parameters is applied.

large fluctuations at inflation (Ivanov et al. (1994); García-Bellido et al. (1996); Ivanov (1998)), bubble collisions (Crawford & Schramm (1982); La & Steinhardt (1989)), but the mainstream hypothesis is that they originate from large perturbations in the primordial curvature power spectrum (that went outside of the horizon during inflation) right after horizon re-entry; there has been an intense activity in the community in the last few years on the relation between the primordial power spectrum and PBHs (see e.g., Musco et al. (2005); Cole & Byrnes (2018); Kalaja et al. (2019); Musco (2019); Young et al. (2019); Byrnes et al. (2019); Sato-Polito et al. (2019); Muñoz et al. (2017); Motohashi & Hu (2017); Gow et al. (2022); Musco et al. (2021); Byrnes et al. (2012); Inomata et al. (2021)).

The interest towards this type of compact objects revived after the first detection of GWs from the merger of two massive black holes (Abbott et al. (2016b,c)), when it was proposed that their progenitors might have primordial origin and even constitute a non negligible fraction of the dark matter, reviving the "PBHs as dark matter" hypothesis (e.g., Bird et al. (2016); Clesse & García-Bellido (2017)). There is still no conclusive agreement on the possibility that stellar-mass PBHs exist in sufficient abundance to make up for a considerable part of the dark matter (see e.g., Brandt (2016); Muñoz et al. (2016); Green (2016); Zumalacarregui & Seljak (2018); Murgia et al. (2019); Ali-Haïmoud et al. (2017); De Luca et al. (2021); Mukherjee & Silk (2021) for some studies and constraints in this mass range), but confirmation (or exclusion) of their sheer existence would represent a big step in our understanding of the Universe. In

fact, detecting even one PBH would provide invaluable information on the physics of the early Universe on scales otherwise inaccessible to standard cosmological measurements; moreover, it was recently shown that PBHs and WIMP DM are incompatible (Adamek et al. (2019)), so that the observation of one PBH would rule out the main DM candidate model.

Therefore, it will be extremely important to add another probe for the possible detection of the presence of PBHs and to understand their formation channels and merger rates. Measurements of GW $\times$ IM will then add further information on this issue, on redshift ranges and with data sets complementary to what is and will be available otherwise. We refer the reader to PBH reviews such as e.g., Carr et al. (2016a); Sasaki et al. (2018); Carr & Silk (2018); Carr & Kühnel (2020); Green & Kavanagh (2021) for more details.

Nonetheless, we refer the reader to appendix C for a work on constraining PBHs abundance by looking at the Lyman-α forest.

The idea on top of which we build for our study follows the same logic of Raccanelli et al. (2016b); Scelfo et al. (2018): approaching the problem in a statistical way, we know that GWs from merging BBHs trace the underlying matter distribution in ways that depend on their origin (see later for more details) and consequently would correlate with the LSS - and the HI distribution, which is a tracer of the LSS - in different ways. The relation between observables and the underlying matter distribution is encapsulated in the bias parameter introduced in section 1.3.1. Crucially, it has been shown (Bird et al. (2016); Ali-Haïmoud et al. (2017)) that PBH mergers trace halos and the stellar distributions in ways that are different from endpoint of stellar evolution BHs, and in different ways depending on the PBH binary formation mechanism. This will then assign a different preferred bias $\bar{b}_{\rm GW}$ for the GWs, which will be the discriminant we can use for our study. The main features of the scenarios we aim to distinguish through GW $\times$ IM are sketched in the following section.

3.6.1 Progenitors

In this section we briefly characterize the scenarios (astrophysical and different primordial ones) that we compare. To do so, we introduce the $\Gamma_{\rm pbh}$ parameter, which indicates the fraction of detected merging BBHs with primordial origin (over the total number of observed BBH mergers). Assuming the detection of $\mathcal{N}_{\rm tot}$ mergers, of which $\mathcal{N}_{\rm astro}$ have astrophysical origin and $\mathcal{N}_{\rm pbh}$ have primordial origin ($\mathcal{N}_{\rm tot} = \mathcal{N}_{\rm astro} + \mathcal{N}_{\rm pbh}$),

the $\Gamma_{\rm pbh}$ parameter is defined as:

$$\Gamma_{\rm pbh} = \mathcal{N}_{\rm pbh}/\mathcal{N}_{\rm tot} \tag{3.24}$$

and spans from $\Gamma_{\rm pbh} = 0$ (i.e., only astrophysical BBH mergers are detected) to $\Gamma_{\rm pbh} = 1$ (i.e., only primordial BBHs mergers are detected).

3.6.1.1 Astrophysical scenario

In this case, the progenitors of merging BBHs are formed at the end-point of stellar evolution. All the features of the detected GW events originated from their mergers are already discussed in section 3.3.1. GWs from mergers of astrophysical BHs will then highly correlate with large, luminous halos that contain the majority of stars, and, consequently, they would highly correlate with the HI IM signal. The average bias (obtained weighting the bias function for the redshift distribution, in the redshift range considered here) is

$$\bar{b}_{\rm GW}^{\rm ASTRO} \sim 2.17. \tag{3.25}$$

Finally, by definition this scenario is characterized by a value of $\Gamma_{\rm pbh} = 0$.

3.6.1.2 Primordial scenario: "early" binaries

We start our analysis of the GW $\times$ IM that will be measured if $\Gamma_{\rm pbh} \neq 0$ with the scenario in which the vast majority of primordial black holes binary formation took place in the early universe (see e.g., Ali-Haïmoud et al. (2017); Raidal et al. (2019)), while late time formed PBH binaries are assumed to give a negligible contribution.
In analogy to the correlation of GW with galaxies, the HI distribution is expected to correlate with PBHs mergers from early binaries with a different bias. This is due to the fact that these binaries would form in correspondence of the DM distribution, tracing very well the underlying matter distribution, instead of just tracing locations with massive and luminous halos. Assuming $\Gamma_{\rm pbh} = 1.0$, GWs should have an associated bias of

$$\bar{b}_{\rm GW}^{\rm PBH} \sim 1.0 \tag{3.26}$$

since they would trace very effectively the underlying matter distribution. We provide in Figure 3.5 the specifics characterizing GWs events produced in this scenario. See appendix B for further explanations.

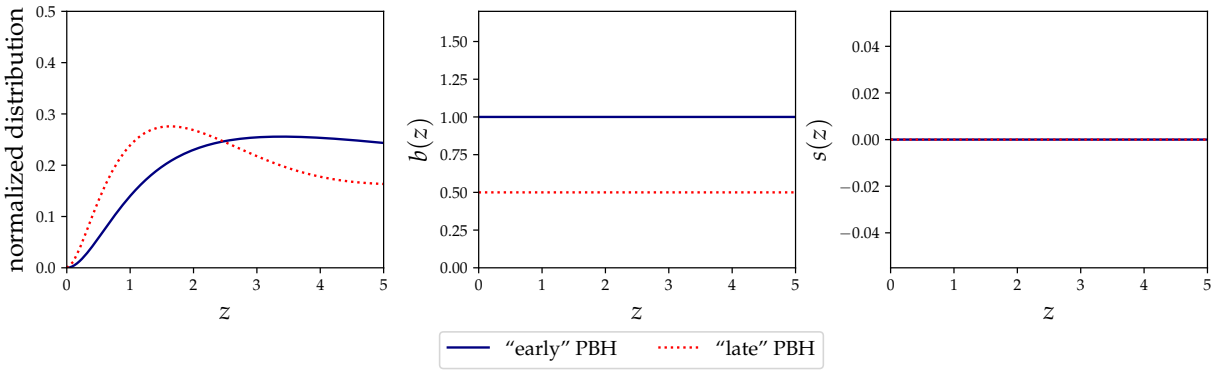

Figure 3.5: Specifics for the GW tracer in the "early" and "late" primordial scenarios. *Left:* normalized redshfit distribution. *Center:* bias $b(z)$. *Right:* magnification bias $s(z)$. Magnification bias assumed to be zero for both scenarios (see appendix B for further discussions).

3.6.1.3 Primordial scenario: "late" binaries

Under this scenario we again assume that the progenitors of the merging BBHs have primordial origin, but the formation of the binary system itself takes place in the late Universe through a gravitational bremsstrahlung process (Bird et al. (2016)).
We assume binary formation happens when two PBHs have a close encounter and their relative velocities are low enough that capture can take place and allows the binary formation. Given that the velocity dispersion is on average lower within small mass halos, which can not form large quantities of stars and are characterized by low values of the bias parameter, GWs in this case would be anti-correlated with luminous galaxies and (if $\Gamma_{\rm pbh} = 1.0$) GWs would be expected to poorly trace luminous, highly star-forming massive halos and would be characterized by a bias value of

$$\bar{b}^{\rm PBH}_{\rm GW} \sim 0.5, \tag{3.27}$$

which is typical of the dark, low-mass halos in which this PBHs late binary formation effect would take place (Bird et al. (2016)). It is worth mentioning that if a bias redshift evolution was to be taken into account, it would have a standard increasing behaviour with the redshift, likely increasing the average bias value of above. Nonetheless, given the several uncertainties in the PBHs physics modeling, we can safely stick to a 0.5 value without compromising the generality of our results.
In Figure 3.5 we show the specifics characterizing GWs events under this scenario. See appendix B for further explanations.

3.6.1.4 Primordial scenario: "mixed" binaries

Finally, we consider a case in which we assume that the progenitors of the merging BBHs have primordial origin, with PBH binary formation taking place through both channels described by the "early" and "late" scenarios.
The bias parameter value of this model is given by the weighted average of the two values of equations (3.26) and (3.27). In particular, as an example case, we assume that around 70% of the PBHs mergers come from early binaries, whereas around the 30% is given by mergers of late binaries. This rough estimate comes from taking the lower and upper bounds of the LIGO/Virgo local merger rate estimates and associating them to the "late" and "early" scenarios respectively. In fact, even though according to part of the current literature the "early" scenario might be the dominant one, the issue is not settled yet. In this case we aim at taking into account both PBHs binary formation channels, considering a non-negligible contribution to the total PBHs merger rate from either mechanism. Assuming $\Gamma_{\rm pbh} = 1.0$, this scenario is then characterized by:

$$\bar{b}_{\rm GW}^{\rm PBH} \sim 0.85. \tag{3.28}$$

3.6.2 Forecasts

We calculate the Signal-to-Noise ratio S/N to quantify how well a fiducial model (astrophysical or primordial) can be distinguished from an alternative one, by looking at the $\bar{b}_{\rm GW}$ value predicted by the two models:

$$\left(\frac{S}{N}\right)^2 = \frac{\left(\bar{b}_{\rm GW}^{\rm Alternative} - \bar{b}_{\rm GW}^{\rm Fiducial}\right)^2}{\sigma^2_{\bar{b}_{\rm GW}^{\rm Fiducial}}}\,, \tag{3.29}$$

where $\sigma_{\bar{b}_{\rm GW}^{\rm Fiducial}}$ is the Fisher estimated error on $\bar{b}_{\rm GW}$ in the fiducial scenario. The biases values $\bar{b}_{\rm GW}^{\rm Alternative}$ and $\bar{b}_{\rm GW}^{\rm Fiducial}$ are those characterizing the models presented in section 3.6.1, depending on which of them is assumed as alternative or fiducial. We obtain $\sigma_{\bar{b}_{\rm GW}^{\rm Fiducial}}$ by making use of the same Fisher pipeline (parameters and fiducial values) of the analysis of section 3.5: $\{K^{\rm fg}, ln10^{10}A_s, n_s, \omega_{\rm cdm}, \omega_{\rm b}, 100\theta_s, w_0, w_a, \bar{b}_{\rm GW}, \bar{b}_{\rm HI}\}$ for a total of 10 parameters. We set Planck priors on $\{ln10^{10}A_s, n_s, \omega_{\rm cdm}, \omega_{\rm b}, 100\theta_s\}$ (Planck Collaboration et al. (2016)).
We provide forecasts assuming the astrophysical model as fiducial, characterized by $\Gamma_{\rm pbh}^{\rm FID} = 0.0$. Regarding the alternative models to compare with, we consider a series of mixed astrophysical-primordial scenarios with $\Gamma_{\rm pbh}^{\rm ALT} \in [0.0, 1.0]$, with a bias given by

$$\bar{b}_{\rm GW}^{\rm ALT} = \bar{b}_{\rm GW}^{\rm ASTRO}(1 - \Gamma_{\rm pbh}^{\rm ALT}) + \bar{b}_{\rm GW}^{\rm PBH}\Gamma_{\rm pbh}^{\rm ALT}\,. \tag{3.30}$$

It is worth noting that this kind of approach may lead to possible degeneracies for some mixed scenarios, i.e., different scenarios combinations might yield the same $\bar{b}_{\rm GW}$. In this eventuality, comparing the bias in specific redshift sub-samples would be enough to break the degeneracy, given that its predicted redshift dependence is different among distinct cases.

We provide in figure 3.6 SNR estimates from equation (3.29) for a series of values of $f_{\rm sky}$ and $T_{\rm obs}^{\rm GW}$ assuming the astrophysical scenario as fiducial and comparing it with the three different primordial scenarios ("early", "late" and "mixed") described in section 3.6.1. On the left panel we show the SNR as a function of $\Gamma_{\rm pbh}^{\rm ALT}$, where the color code indicates the fraction of the sky observed. On the right panels we present the SNR obtainable (color coded) as a function of both the observation time and the fraction of primordial BBHs in the alternative model. In both columns, from top to bottom results for the three scenarios presented above are provided.

It can be seen that for large enough fractions of the sky and observation times, results are very promising, providing a S/N well above unity. In fact, it would be possible to distinguish, at a few sigma, a purely astrophysical model from an alternative model made up of similar relative abundances between astrophysical and primordial BBHs ($\Gamma_{\rm pbh}^{\rm ALT} \sim 0.5$) with a few years of observations and $f_{\rm sky} \sim 0.5$. In addition, an alternative model with low values of $\Gamma_{\rm pbh}^{\rm ALT}$ (i.e., mostly made of astrophysical BHs) such as $\Gamma_{\rm pbh}^{\rm ALT} \sim 0.2$, could be detected within 10 years of observation for $f_{\rm sky} = 0.5$, that we stress once again being the fiducial value for the considered SKAO-Mid survey. We have also tested mixed scenarios with different relative abundances of early/late-type PBHs to astrophysical BHs, finding as expected no extremely different qualitative behaviours when changing these quantities.

Finally, analogous conclusions can be reached when the assumed fiducial model is a primordial scenario: for completeness, we provide forecasts for the example case of "early" primordial scenario assumed as fiducial in appendix B.

3.7 Summary

In this chapter, we investigated the cross-correlation signal between gravitational wave catalogs and HI intensity maps that could be potentially measured with future experiments such as the Einstein Telescope and the SKA Observatory. We extended the range of applications of the publicly available code `Multi_CLASS`, by including signal from the IM unresolved HI sources and compute their angular power spectra C_ℓs, including all projection effects over a variety of redshift ranges.

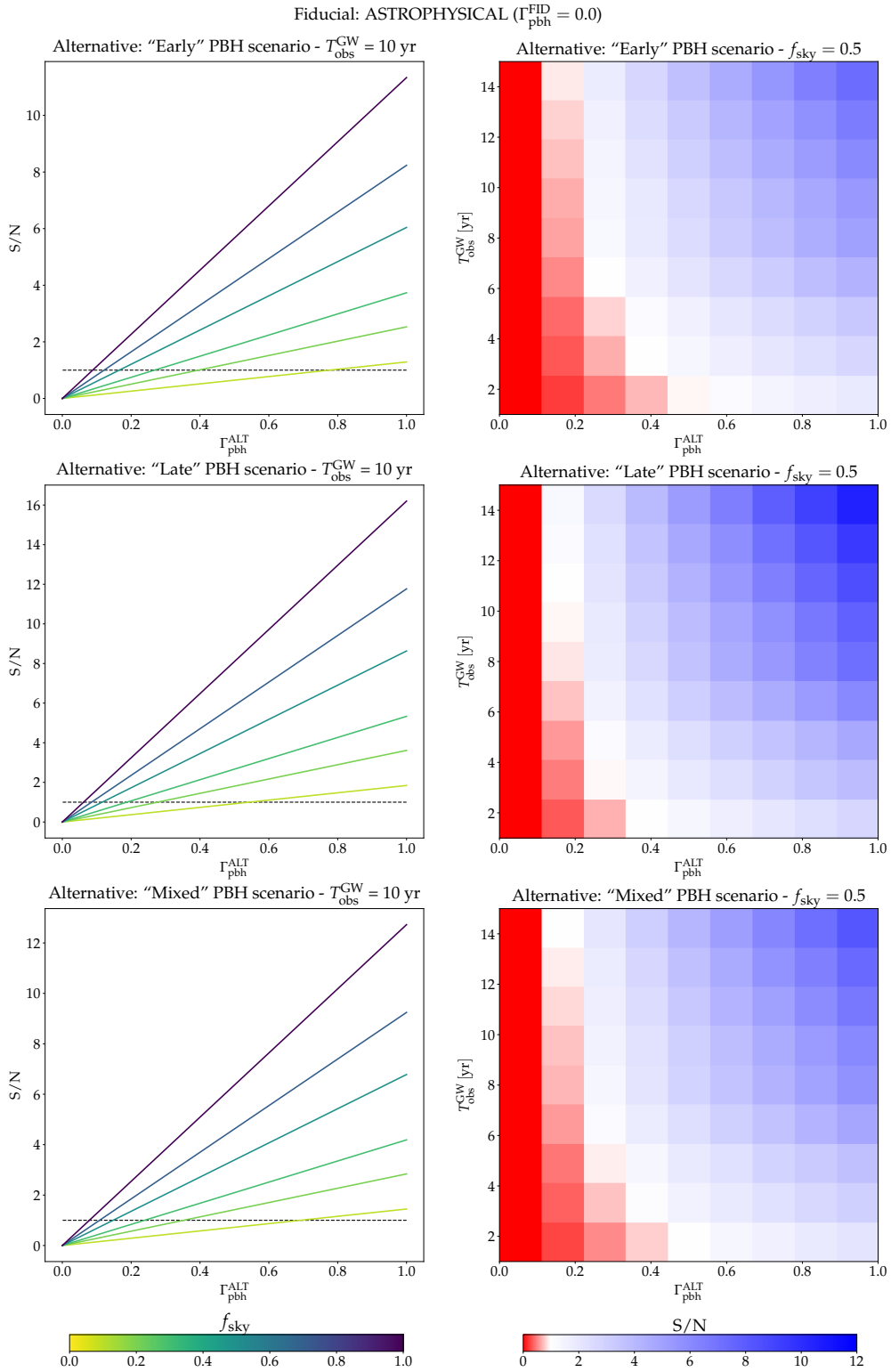

Figure 3.6: SNR for different values of $T_{\rm obs}^{\rm GW}$ (from 1 yr to 15 yr), $f_{\rm sky}$ (from 0.1 to 1.0) and $\Gamma_{\rm pbh}^{\rm ALT}$ (from 0.0 to 1.0), assuming the astrophysical model as fiducial. The alternative model assumed is the "Early", "Late" and "Mixed" primordial scenario in the top, center and bottom panel, respectively. The colorbar of the right-side plots is normalized to white at $S/N = 1$.

We presented three cosmological and astrophysical applications we believe will be particularly exciting for the future.

First, we investigated how well the GW $\times$ IM cross-correlation can provide model independent and agnostic information on the redshift distribution of resolved binary black hole mergers. Our results show that we will be able to obtain good precision in the inferred statistical redshift distribution of BBH merger number counts. With the experiments considered, we will be able to obtain a precision of order a few tens of % for redshifts up to $z \approx 1.5$, potentially providing ways to discriminate between different astrophysical models of the binary formation, evolution and mergers.

We stress that our methodology does not make use of any astrophysical model, including BH population, mass function, etc, and is free from assumptions on the values of the cosmological parameters. It will be of particular interest to compare results from our methodology with other approaches that either assume the knowledge of a cosmological model, set priors on the BH population distributions or exploit machine learning techniques (see e.g., Mukherjee et al. (2021a); Ng et al. (2021); Cañas-Herrera et al. (2021)). The combinations of these methods could lead to an improvement of constraints or, if some inconsistencies will emerge, could provide hints of inaccuracies in standard assumptions.

Measurements of power spectra of tracers of the matter distribution over cosmic epochs will naturally provide also cosmological information; as an example showcasing the potential of the GW $\times$ IM observable, we forecast constraints on dynamical dark energy parameters. Our results show that the GW $\times$ IM cross-correlations will provide a fundamental validation of IM-only results, as this latter could be a measurement affected by unknown systematic errors.

As a final application for GW $\times$ IM, we studied how we can use this correlation to detect a primordial component in the BBHs detected through GW from their mergers. We follow the approach of Raccanelli et al. (2016b); Scelfo et al. (2018) and extend it to HI IM maps, at the same time updating merger rate estimates and binary formation channels with the latest results available in literature. Compared to the case of the correlation with star forming galaxies, using IM allows us to reach higher redshifts and have a very fine tomographic binning. Our results show that with GW $\times$ IM from the ET and SKAO we will be able to detect the presence of a PBH component down to about 30% of detected mergers at high Signal-to-Noise ratios.

To conclude, we presented the first study of the cross-correlation between gravitational waves from resolved binary black hole mergers and the HI intensity mapping signal, and investigated some possible interesting applications with predictions from the future

Einstein Telescope and SKAO experiments. We believe that this first investigation can open up a plethora of new measurements and possibilities for the scientific community, potentially including also the observation of other emission lines other than the 21 cm. Moreover, it will be of particular interest to combine our suggested approach with other ones such as additional GWxLSS correlations. This chapter can be seen as part of the ongoing effort to develop multi-tracer approaches, which has an enormous potential in both cosmology and astrophysics, as it allows to test models in ways that would not be possible by looking at single tracers separately.

4

Testing gravity with gravitational waves × electromagnetic probes cross-correlations

This chapter is based on the following manuscript:
G. Scelfo, M. Berti, A. Silvestri, M. Viel
Testing gravity with gravitational waves × electromagnetic probes cross-correlations
Submitted to JCAP, `arXiv:2210.02460`

4.1 Chapter overview and motivation

In a General Relativistic framework, Gravitational Waves and Electromagnetic (EM) waves are expected to respond in the same way to the effects of matter perturbations between the emitter and the observer. A different behaviour might be a signature of alternative theories of gravity.
In this chapter, we explore the cross-correlation between GW events from resolved Compact Objects mergers and electromagnetic signals coming from luminous tracers, such as the IM of the 21 cm line and resolved galaxies. We consider the ET instrument for the first observable, and SKAO for the latter ones. We exploit these different probes with the aim of testing the possibility of gravity theories alternative to General Relativity. Indeed, once a GW or an EM signal is emitted from a source, cosmic structures between the origin and the observer interfere through distortion effects under the form of magnifications (or de-magnifications). In a standard GR framework, these effects are expected to act in the same way on GW and EM waves, whereas different imprints

may be a signal of deviations from GR, indicating the need for Modified Gravity (MG) theories. Consequently, cross-correlations between these distortion effects on these probes should highlight potential MG behaviours and help set constraints on related physical parameters. Thus, our main observable is the lensing power spectrum (both in auto and cross-tracers correlations). Subsequently, we also combine it with data from angular clustering power spectra, in order to test the improvement brought by the merger of different observational probes. This avenue of cross-correlating GW and EM signals to test gravity was already explored in the literature (see e.g., Mukherjee et al. (2020b, 2021a); Baker & Harrison (2021); Mukherjee et al. (2021b)). We expand on previous works by considering a larger variety of tracers (GWs, resolved galaxies and IM, eventually simultaneously) and different probes combinations (lensing, angular clustering and their cross-correlation).
This chapter is structured as follows: in section 4.2 we describe our methodology, presenting the treated probes (weak lensing, angular clustering, and their cross-term) in section 4.2.1 and the adopted Fisher analysis formalism in section 4.2.2; in section 4.3 we introduce and characterize the considered tracers (GWs, IM and resolved galaxies); in section 4.4 we introduce the tested MG parametrization; in section 4.5 we present our forecasts on the relevant MG parameters and in section 4.6 we wrap the discussion up.

4.2 Methodology

In this section we describe the observables considered and the adopted methodology. In section 4.2.1 we characterize our observables: the angular power spectra for weak lensing and angular clustering (and their cross term). In section 4.2.2 we describe some details on the Fisher formalism on which we rely.

4.2.1 Observables: angular power spectra (in ΛCDM)

The observables we consider are the angular power spectra C_ℓs for two different probes: weak lensing (denoted as L) and angular clustering (denoted as C), with the addition of the cross-term (L × C). Given two tracers {X,Y} (e.g., GW events, galaxies, IM) associated to two different redshift bins $\{z_i, z_j\}$, we define the power spectra of their cross-correlation as $C_{\Gamma\Theta}^{\mathrm{X_i,Y_j}}(\ell)$, with Γ, Θ indicating the considered probe (e.g., L or C). We make use of the flat-sky and Limber approximations, which are accurate at 10% for $\ell = 4$, 1% for $\ell = 14$, and less than 0.1% for $\ell > 45$ Kilbinger et al. (2017). In the following, we characterize the power spectra for the considered probes.

- **Weak lensing (L)**. The characterization and physical meaning of this observable depends on the tracer that we take into account. For what concerns resolved galaxies, it describes the physical effect of distortion of their shape due to the inhomogeneous distribution of matter between the objects and the observer. It is often referred to as *cosmic shear* (see e.g. Bartelmann & Schneider (2001); Hoekstra & Jain (2008)). It is given by the sum of three different terms: the proper cosmological signal ($\gamma\gamma$ term) and the two intrinsic alignment terms (γI and II terms). The latter ones consider that observed galaxies are usually already characterized by an intrinsic ellipticity, which should be taken into account when estimating the shear due to weak lensing only. The three terms can be written as:

$$C_{\gamma\gamma}^{\mathrm{X_i Y_j}}(\ell) = \int_0^\infty \frac{dz\ c}{H(z)} \frac{W_\gamma^{\mathrm{X_i}}(z)\ W_\gamma^{\mathrm{Y_j}}(z)}{\chi^2(z)}\ P_{\mathrm{mm}}\left(\frac{\ell}{\chi(z)}, z\right) \tag{4.1}$$

$$C_{\gamma\mathrm{I}}^{\mathrm{X_i Y_j}}(\ell) = \int_0^\infty \frac{dz\ c}{H(z)} \frac{W_\gamma^{\mathrm{X_i}}(z)\ W_{\mathrm{IA}}^{\mathrm{Y_j}}(z) + W_{\mathrm{IA}}^{\mathrm{X_i}}(z)\ W_\gamma^{\mathrm{Y_j}}(z)}{\chi^2(z)} \times \\ \times\ \mathcal{F}_{\mathrm{IA}}(z)\ P_{\mathrm{mm}}\left(\frac{\ell}{\chi(z)}, z\right) \tag{4.2}$$

$$C_{\mathrm{II}}^{\mathrm{X_i Y_j}}(\ell) = \int_0^\infty \frac{dz\ c}{H(z)} \frac{W_{\mathrm{IA}}^{\mathrm{X_i}}(z)\ W_{\mathrm{IA}}^{\mathrm{Y_j}}(z)}{\chi^2(z)}\ \mathcal{F}_{\mathrm{IA}}^2(z)\ P_{\mathrm{mm}}\left(\frac{\ell}{\chi(z)}, z\right), \tag{4.3}$$

where c is the speed of light, $H(z)$ is the Hubble parameter, $\chi(z)$ is the comoving distance, P_{mm} is the matter power spectrum and the window functions are given by:

$$W_\gamma^{\mathrm{X_i}}(z) = \frac{3}{2}\Omega_{\mathrm{m}}\ \frac{H_0^2}{c^2}\chi(z)(1+z) \int_z^\infty dx\ n_{\mathrm{X_i}}(x)\ \frac{\chi(x)-\chi(z)}{\chi(x)} \tag{4.4}$$

$$W_{\mathrm{IA}}^{\mathrm{X_i}}(z) = n_{\mathrm{X_i}}(z)\ \frac{H(z)}{c}, \tag{4.5}$$

where $n_{\mathrm{X_i}}$ is the redshift distribution of the considered tracer and the intrinsic alignment kernel $\mathcal{F}_{\mathrm{IA}}$ is modeled through the extended non-linear alignment model:

$$\mathcal{F}_{\mathrm{IA}}(z) = -\frac{A_{\mathrm{IA}}\mathcal{C}_1\Omega_{\mathrm{m}}}{D_1(z)}(1+z)^{\eta_{\mathrm{IA}}} \left(\frac{\langle L\rangle(z)}{L_*(z)}\right)^{\beta_{\mathrm{IA}}}, \tag{4.6}$$

with $\mathcal{C}_1 = 0.0134$, $D_1(z)$ is the linear growth factor and the intrinsic alignment parameters have fiducial values $\{A_{\mathrm{IA}}, \eta_{\mathrm{IA}}, \beta_{\mathrm{IA}}\} = \{1.72, -0.41, 2.17\}$. Finally, $\frac{\langle L\rangle(z)}{L_*(z)}$ is the mean luminosity of the sample in units of the typical luminosity at a given redshift. Here, we use the same specification used for Euclid (Euclid Collaboration et al. (2019)), both for ease of comparison with similar studies and also

under the assumption that the galaxies observed by SKAO will display a similar redshift evolution of their luminosity. However, we note that this assumption must be explicitly checked, by performing an analysis on actual observations, as in Joachimi et al. (2011).

Equations 4.1 - 4.3 can be summed up to give the lensing power spectrum

$$C_{\rm LL}^{\rm X_i Y_j}(\ell) = \int_0^\infty \frac{dz\ c}{H(z)}\ \frac{W_{\rm L}^{\rm X_i}(z)\ W_{\rm L}^{\rm Y_j}(z)}{\chi^2(z)}\ P_{\rm mm}\left(\frac{\ell}{\chi(z)}, z\right), \tag{4.7}$$

where

$$W_{\rm L}^{\rm X_i}(z) = W_\gamma^{\rm X_i}(z) + \mathcal{F}_{\rm IA}(z)\ W_{\rm IA}^{\rm X_i}(k, z). \tag{4.8}$$

In the case of GW events we do not have an intrinsic shape that undergoes cosmic shear, so the intrinsic alignment term is not present. Indeed, in this case, the propagation of the gravitational wave in the presence of a matter distribution leads to magnification in the strain signal $h\,(f)$:

$$h\,(f) = \mathcal{Q}(\alpha)\sqrt{\frac{5}{24}}\frac{G^{5/6}\mathcal{M}^2\,(f\mathcal{M})^{-7/6}}{c^{3/2}\pi^{2/3}d_L}e^{i\phi}, \tag{4.9}$$

where f is the frequency, $\mathcal{Q}(\alpha)$ is a function of the angles describing the position and orientation of the binary, $\mathcal{M}$ is the chirp mass of the binary system, d_L is the luminosity distance of the source and G is the gravitational constant. What one can measure is an alteration in the measured GW strain $\tilde{h}\,(\hat{r}, f) = h\,(f)\,[1 + \kappa(\hat{r})]$, where $\hat{r}$ describes the position of the source and $\kappa(\hat{r})$ is the lensing convergence, related to the angular power spectra as $C_{\rm LL}(\ell) = \langle\kappa_{\ell m}\kappa_{\ell' m'}\rangle\delta_{\ell\ell'}\delta_{mm'}$. We refer the interested reader to e.g., Takahashi (2006); Laguna et al. (2010); Cutler & Holz (2009); Camera & Nishizawa (2013); Congedo & Taylor (2019); Bertacca et al. (2018); Mukherjee et al. (2020a,b); Mpetha et al. (2022) for further details.

Finally, although IM (by definition) is a probe that does not provide resolved galaxies, we can still describe the effects of weak lensing as a magnification received by the observer (see e.g., Pourtsidou & Metcalf (2014, 2015) for additional details). As one would expect, also in this case the IA term is not present ($\mathcal{F}_{\rm IA}^{\rm IM}(z) = 0$).

- **Angular clustering (C)**. Our tracers can also be used to estimate the clustering as a function of the separation angle (or equivalently the multipoles):

$$C_{\rm CC}^{\rm X_i Y_j}(\ell) = \int_0^\infty \frac{dz\ c}{H(z)}\ \frac{W_{\rm C}^{\rm X_i}\left(\frac{\ell}{\chi(z)}, z\right)\ W_{\rm C}^{\rm Y_j}\left(\frac{\ell}{\chi(z)}, z\right)}{\chi^2(z)}\ P_{\rm mm}\left(\frac{\ell}{\chi(z)}, z\right), \tag{4.10}$$

where the window function for clustering is given by

$$W_{\rm C}^{\rm X_i}(k,z) = b_{\rm X}(k,z)\; n_{\rm X_i}(z)\frac{H(z)}{c} \tag{4.11}$$

and $b_{\rm X}(k,z)$ is the bias parameter for tracer X, describing the relation between the tracer and the underlying matter distribution. We apply this formalism to all tracers considered in this work.

- **Lensing $\times$ Clustering** (L $\times$ C). Finally, the cross-correlation L $\times$ C between weak lensing and angular clustering of two tracers can be expressed as

$$C_{\rm CL}^{\rm X_i Y_j}(\ell) = \int_0^\infty \frac{dz\; c}{H(z)}\; \frac{W_{\rm C}^{\rm X_i}\left(\frac{\ell}{\chi(z)}, z\right)\; W_{\rm L}^{\rm Y_j}(z)}{\chi^2(z)}\; P_{\rm mm}\left(\frac{\ell}{\chi(z)}, z\right). \tag{4.12}$$

Essentially, it is given by the combination of a Lensing window function with a Clustering one.

4.2.2 Fisher analysis

In this chapter, analogously to what was done in chapter 3, we make use of the Fisher matrix analysis. Again, we do not go through all the details already provided in section 1.4, but we sketch here the main points (along with newer specifics needed for this chapter) for practicality.

Assuming again two tracers {X,Y} (e.g., GW events, galaxies, IM), we divide the total redshift interval surveyed in $N_{\rm bins}^{\rm X}$ bins, with amplitude $\Delta z^{\rm X}$ for tracer X, and in $N_{\rm bins}^{\rm Y}$ redshift bins with amplitude $\Delta z^{\rm Y}$ for tracer Y.

Considering the observed power spectra $\tilde{C}_\ell$s for a specific probe (L only, C only or L $\times$ C, which we do not explicitate throughout this section) and a generic set of parameters $\{\theta_n\}$ for the Fisher analysis, we can organize our data in the (symmetric) matrix $\mathcal{C}_\ell$ as

$$\mathcal{C}_\ell = \begin{bmatrix} \tilde{C}_\ell^{\,\rm XX}(z_1^{\rm X}, z_1^{\rm X}) & \dots & \tilde{C}_\ell^{\,\rm XX}(z_1^{\rm X}, z_N^{\rm X}) & \tilde{C}_\ell^{\,\rm XY}(z_1^{\rm X}, z_1^{\rm Y}) & \dots & \tilde{C}_\ell^{\,\rm XY}(z_1^{\rm X}, z_N^{\rm Y}) \\ & \dots & \tilde{C}_\ell^{\,\rm XX}(z_2^{\rm X}, z_N^{\rm X}) & \tilde{C}_\ell^{\,\rm XY}(z_2^{\rm X}, z_1^{\rm Y}) & \dots & \tilde{C}_\ell^{\,\rm XY}(z_2^{\rm X}, z_N^{\rm Y}) \\ & \dots & \vdots & \vdots & \dots & \vdots \\ & & \tilde{C}_\ell^{\,\rm XX}(z_N^{\rm X}, z_N^{\rm X}) & \tilde{C}_\ell^{\,\rm XY}(z_N^{\rm X}, z_1^{\rm Y}) & \dots & \tilde{C}_\ell^{\,\rm XY}(z_N^{\rm X}, z_N^{\rm Y}) \\ & & & \tilde{C}_\ell^{\,\rm YY}(z_1^{\rm Y}, z_1^{\rm Y}) & \dots & \tilde{C}_\ell^{\,\rm YY}(z_1^{\rm Y}, z_N^{\rm Y}) \\ & & & & \dots & \vdots \\ & & & & & \tilde{C}_\ell^{\,\rm YY}(z_N^{\rm Y}, z_N^{\rm Y}) \end{bmatrix}, \tag{4.13}$$

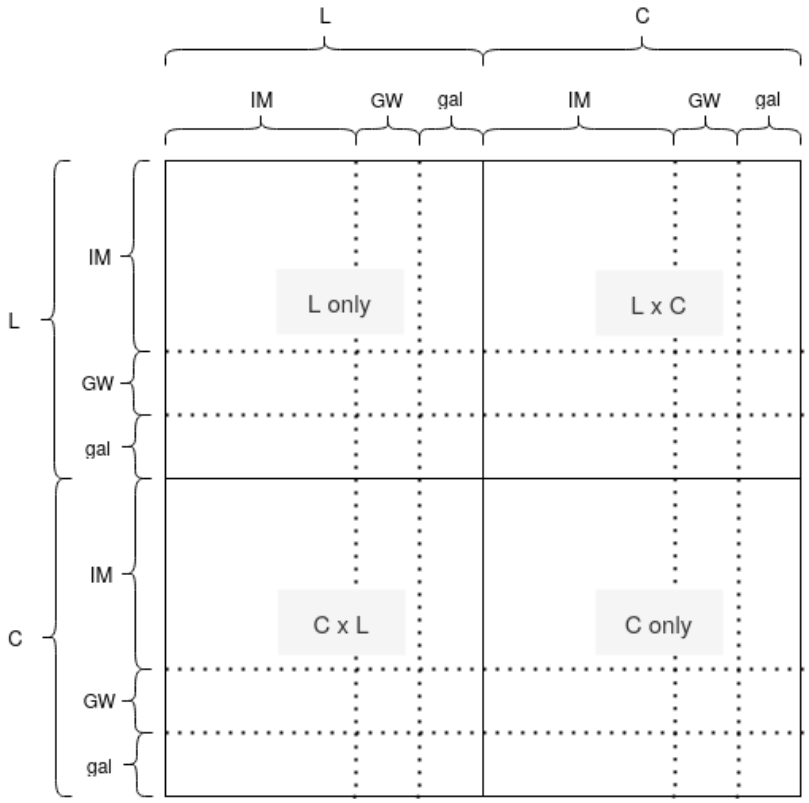

Figure 4.1: Sketch for the $\mathcal{C}_\ell$ matrix in the case of all probes (L only, C only, and L $\times$ C) and three tracers (GW, IM, gal) considered simultaneously.

The matrix $\mathcal{C}_\ell$ has dimensions of $(N^{\rm X}_{\rm bins}+N^{\rm Y}_{\rm bins})\times(N^{\rm X}_{\rm bins}+N^{\rm Y}_{\rm bins})$, and in general $z^{\rm X}_i \neq z^{\rm Y}_i$. It is trivial to expand the above matrix to the case in which a third tracer Z is considered at the same time. In this case, the matrix would be accordingly expanded with all XZ, YZ and ZZ correlations and would have dimensions of $(N^{\rm X}_{\rm bins} + N^{\rm Y}_{\rm bins} + N^{\rm Z}_{\rm bins}) \times (N^{\rm X}_{\rm bins} + N^{\rm Y}_{\rm bins} + N^{\rm Z}_{\rm bins})$. The three tracers case is also explored in this chapter (see sections 4.3 and 4.5). Equation (4.13) refers to the case in which just one probe is taken into account (L only, C only, or L $\times$ C). When all three probes are considered simultaneously for a forecast, the global $\mathcal{C}_\ell$ matrix will be made of 4 different sub-matrices like the one in equation (4.13): one for L only, one for C only, and two for L $\times$ C. We provide in figure 4.1 a sketch of the global $\mathcal{C}_\ell$ matrix in the case of all probes and three tracers (GW, IM, gal as described in section 4.3). Its dimensions are $2(N^{\rm IM}_{\rm bins} + N^{\rm GW}_{\rm bins} + N^{\rm gal}_{\rm bins}) \times 2(N^{\rm IM}_{\rm bins} + N^{\rm GW}_{\rm bins} + N^{\rm gal}_{\rm bins})$.
The $\mathcal{C}_\ell$ matrix is then used to compute the Fisher matrix elements as usual:

$$F_{\alpha\beta} = f_{\rm sky} \sum_\ell \frac{2\ell+1}{2} {\rm Tr}\left[\mathcal{C}_\ell^{-1}(\partial_\alpha \mathcal{C}_\ell)\mathcal{C}_\ell^{-1}(\partial_\beta \mathcal{C}_\ell)\right], \tag{4.14}$$

Tracer	$\mathrm{GW}^{\mathrm{bright}}$ (ET)	$\mathrm{GW}^{\mathrm{dark}}$ (ET) & gal (SKAO)	IM (SKAO)
z range	[0.5-2.5]	[0.5-3.5]	
$\mathbf{N_{bins}}$	8	3	30
$\mathbf{\Delta z}$	0.25	1.0	0.1

Table 4.1: Specifics for the considered tracers: redshift range, number of redshift bins N_{bins} and bin width Δz.

where ∂_α indicates the partial derivative with respect to the parameter θ_α and f_{sky} is the fraction of the sky covered by the intersection of the considered surveys. The Fisher-estimated marginal error on the parameter θ_α is given by $\sqrt{(F^{-1})_{\alpha\alpha}}$.

4.3 Tracers

In this section, we characterize the considered tracers. In table 4.1 we summarize their redshift dependent specifics (binning, redshift range, etc.).

4.3.1 Gravitational Waves

We consider GW events from compact objects resolved mergers (BHBH, BHNS, and NSNS) detected by the Einstein Telescope (ET) experiment, as planned in Sathyaprakash et al. (2012b). We treat two categories of GW events, depending on whether they can be associated with an EM counterpart:

- **Dark sirens**: they are not accompanied by an EM follow-up. We treat BHBH and BHNS mergers as dark sirens and consider $N_{\mathrm{bins}}^{\mathrm{GW^{dark}}} = 3$ redshift bins with width $\Delta z^{\mathrm{GW^{dark}}} = 1.0$ in the redshift range $[0.5 - 3.5]$. We choose large redshift bins to take into account the poor redshift localization of this kind of sources. Given the lack of an EM counterpart, their angular resolution is limited by the capabilities of the considered GW instrument, which we set to $\ell_{\mathrm{max}} = 100$ (Sathyaprakash et al. (2012b)).

- **Bright sirens**: the GW emission is associated with an EM counterpart. This helps not only in improving the angular localization of the emitting source but provides also extra information in the MG context, due to the fact that GWs and EM waves might behave differently depending on the MG model under consideration (see section 4.4 for further details). We treat NSNS mergers as bright sirens and consider $N_{\mathrm{bins}}^{\mathrm{GW^{bright}}} = 8$ redshift bins with width $\Delta z^{\mathrm{GW^{bright}}} = 0.25$ in the redshift range $[0.5 - 2.5]$. This is motivated by the z-uncertainty behaviour

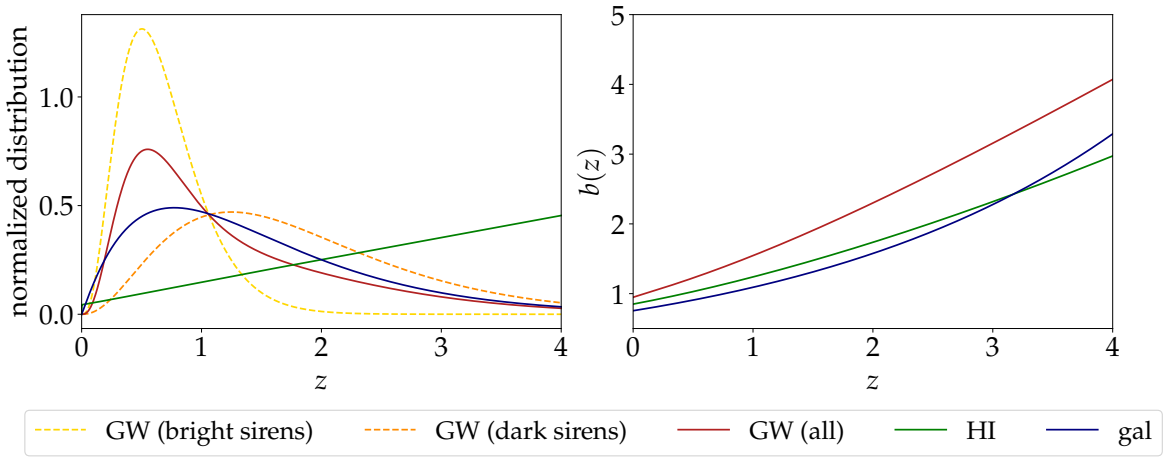

Figure 4.2: Specifics for the considered tracers: HI (green), resolved SKAO galaxies (blue), detected GW events from ET for dark sirens (orange), bright sirens (yellow), and both combined (dark red). *Left panel*: normalized redshift distributions (number counts for GWs and resolved galaxies, mean brightness temperature $T_b(z)$ for HI). *Right panel*: biases.

for NSNS binaries $\delta z/z \approx 0.1\ z$ (Safarzadeh et al. (2019)), making our choice quite conservative at lower redshifts. Since the detection of an EM follow-up can help in significantly improving the angular localization of the sources, it allows us to push our analysis to a higher $\ell_{\rm max}$. We set $\ell_{\rm max} = 300$ for bright sirens, which appears to be a conservative estimate for this type of experiments (see e.g. Mukherjee et al. (2020a,b); Balaudo et al. (2022)), furthermore allowing us to avoid non-linearities in the power spectra modeling. We comment on the impact of the choice of $\ell_{\rm max}$ in section 4.5.

Prescriptions to describe the redshift evolution of the GW tracers and their bias parameter are taken from Boco et al. (2019); Scelfo et al. (2020) and were already described in chapter 2. They are provided in figure 4.2 for practicality. These specifics predict a detection of $\sim 2.2 \cdot 10^4$ BHBH+BHNS mergers and $\sim 1.4 \cdot 10^4$ NSNS mergers in the corresponding redshift intervals (for $T_{\rm obs}^{\rm GW} = 1$yr and $f_{\rm sky} = 0.5$). The GW events bias is evaluated through an abundance matching technique (see e.g., Aversa et al. (2015)), linking the luminosity/SFR of each host galaxy to the mass of the hosting dark matter halo, eventually matching the bias of the associated halo to a galaxy with given SFR. Lastly, characterizing COs mergers with the same bias of their host galaxies, the final bias expression is estimated by taking into account which galaxy types give the biggest contribution to the observed merger rate proportionally. For further details on the GW bias estimate procedure we refer the interested reader to Boco et al. (2019); Scelfo et al. (2020) and references therein.

Given a theoretical predicted value for the C_ℓs under study (computed with `COLIBRI`[1], which we modified to extend it to the multi-tracing case), the observed power spectra $\tilde{C}_\ell$s are characterized by the presence of extra noise terms: $\tilde{C}_\ell^{\mathrm{GW,X}}(z_i, z_j) = C_\ell^{\mathrm{GW,X}}(z_i, z_j) + C_\ell^{\mathrm{N,GW}}(z_i)$. In the case of GWs-related power spectra, following e.g. Mukherjee et al. (2020b), we assume that:

$$C_\ell^{\mathrm{N,GW}}(z_i) = \frac{1}{n_{\mathrm{GW}}} e_{d_L}^2 \exp \frac{\ell^2 \theta_{\mathrm{min}}^2}{8 \ln 2}, \tag{4.15}$$

where n_{GW} is the number density of sources in the considered redshift bin z_i, θ_{min} is the sky localization area of the gravitational wave sources, and $e_{d_L} \sim 3/\mathrm{SNR}$ is the relative error on the luminosity distance estimation (see e.g. Pozzo (2014); Calore et al. (2020)), where the average value of the Signal-to-Noise ratio (SNR) estimate for detected GWs events is derived by results from Scelfo et al. (2020) and takes the values of SNR=8.4 (15.4) for bright (dark) sirens. We assume that this shot-noise/beam noise term affects all the probes considered in this work (i.e., L, C, L×C).

4.3.2 Neutral Hydrogen Intensity Mapping

We consider the forecasted HI distribution given by the SKA-Mid intensity mapping survey (Bacon et al. (2020); Dewdney et al. (2009); Maartens et al. (2015)). We consider the redshift range $[0.5 - 3.5]$, divided in bins of width $\Delta z^{\mathrm{IM}} = 0.1$, for a total of $N_{\mathrm{bins}}^{\mathrm{IM}} = 30$ redshift bins. This is expected to be around the optimal redshift range for the SKA-Mid survey (Bacon et al. (2020)). The HI mean brightness temperature redshift evolution and the bias are taken from Battye et al. (2013); Spinelli et al. (2020) and provided in figure 4.2 (they are the same described in chapter 3). The HI bias prescription derives from the outputs of a semi-analytical model for galaxy formation explicitly incorporating a treatment of neutral hydrogen and are in agreement with results of Villaescusa-Navarro et al. (2018) based on Illustris TNG hydro-dynamical simulations.
Noise sources for IM are the result of contributions from different elements, described as follows:

- **Beam effects**: in analogy to what considered in chapter 3, the relation between theoretical C_ℓ^{XY} and the observed $\tilde{C}_\ell^{XY}$ is:

$$\tilde{C}_\ell^{\mathrm{IM,IM}}(z_i, z_j) = \mathcal{B}(z_i)\mathcal{B}(z_j) C_\ell^{\mathrm{IM,IM}}(z_i, z_j) + C_\ell^{\mathrm{N,IM}} \tag{4.16}$$

[1]See `https://github.com/GabrieleParimbelli/COLIBRI`.

and

$$\tilde{C}_\ell^{\mathrm{IM,X}}(z_i, z_j) = \mathcal{B}(z_i) C_\ell^{\mathrm{IM,X}}(z_i, z_j) \tag{4.17}$$

where the $\mathcal{B}^X(z_i)$ describes the suppression of the signal at scales smaller than the FWHM of the beam θ_B. In single-dish configuration $\theta_B \sim 1.22\lambda/D_d$, implying a stronger suppression of the signal at lower frequencies:

$$\mathcal{B}(z_i) = \exp[-\ell(\ell+1)(\theta_B(z_i)/\sqrt{16\ln 2})^2]. \tag{4.18}$$

The beam term affects all probes considered (L, C, L×C).

- **Foreground noise**: we model this noise term following prescriptions from chapter 3, where the way we tackled the foreground issue was thoroughly described in section 3.3.2 (following Scelfo et al. (2022a)). Nonetheless, we briefly sketch here the main components.

  We model the foreground-cleaning related noise term as

  $$C_\ell^{\mathrm{fg}} = K^{\mathrm{fg}} \cdot F(\ell), \tag{4.19}$$

  where K^{fg} is an overall normalization constant determined by:

  $$K^{\mathrm{fg}} = \left\langle C_\ell^{\mathrm{IM,IM}}(z_i, z_j) \right\rangle. \tag{4.20}$$

  The function $F(\ell)$ encodes the scale-dependence, described by

  $$F(\ell) = \frac{1}{f_{\mathrm{sky}}} A e^{b\ell^c}, \tag{4.21}$$

  with a stronger error at larger scales. This term affects all probes (L, C, L×C), but only IM × IM terms (for all redshift bins combinations).

- **Instrumental noise**: this noise term also relies on prescriptions from chapter 3 (section 3.3.2). To sum it up for completeness, the noise angular power spectrum for the experiment setup of single dish mode (Bacon et al. (2020); Santos et al. (2017)) with an ensemble of N_d dishes writes as (see e.g., Bull et al. (2015); Santos et al. (2015, 2017)):

  $$C_\ell^{\mathrm{instr}}(z_i) = \sigma_T^2 \theta_B^2 \approx \left(\frac{T_{\mathrm{sys}}}{T_b(z_i)\sqrt{n_{\mathrm{pol}} B t_{\mathrm{obs}} N_d}} \sqrt{\frac{S_{\mathrm{area}}}{\theta_{\mathrm{B}}^2}} \frac{1}{T_b(z_i)} \right)^2 \theta_B^2, \tag{4.22}$$

  where the single-dish rms noise temperature σ_T is given by

  $$\sigma_T \approx \frac{T_{\mathrm{sys}}}{\sqrt{n_{\mathrm{pol}} B t_{\mathrm{obs}}}} \frac{\lambda^2}{\theta_{\mathrm{B}}^2 A_e} \sqrt{S_{\mathrm{area}}/\theta_{\mathrm{B}}^2} \sqrt{\frac{1}{N_{\mathrm{d}}}} \tag{4.23}$$

and the other parameters involved are defined in section 3.3.2. This noise component affects all the probes considered in this work (L, C, L×C) but it is decorrelated among different bins, affecting only IM auto-correlations.

- **Lensing reconstruction error**: references such as Pourtsidou & Metcalf (2014, 2015) model an extra scale independent noise contribution, due to inaccuracies in the reconstruction of the signal. Since it should affect scales smaller than our $\ell = \mathcal{O}(100)$ cut-off, we opt for not taking it into account. For sake of completeness, we checked that artificially introducing a noise term overcoming the observed signal at around 2/3 of the explored angular range, would worsen our forecasts by $\sim 15-20\%$ or less. Still, let us stress again that the actual scales at which this noise is supposed to dominate start from around $\ell \sim \mathcal{O}(100)$, safely allowing us to neglect this term.

4.3.3 Galaxies

We consider SKAO radio-galaxies distributed following the T-RECS catalog (Bonaldi et al. (2018)) for SKAO (radio continuum survey with $5\mu JY$ detection threshold for $z < 5$). We consider $N^{\rm g}_{\rm bins} = 3$ redshift bins with width $\Delta z^{\rm g} = 1.0$ in the redshift range $[0.5-3.5]$. Their redshift distribution and bias are provided in figure 4.2 (see e.g., Scelfo et al. (2018) for further details). The galaxy bias formulation relies on outputs from the S^3 simulation (Wilman et al. 2008). We model noise sources for SKAO radio galaxies as follows:

- **Shot noise**: the shot noise term affects only the Clustering probe and reads as

$$C_\ell^{\rm N,g} = C_\ell^{\rm shot,g} = \frac{1}{n_g}, \tag{4.24}$$

  where n_g is the source number density in the considered redshift bin. This term affects only $\mathrm{g(z_i)} \times \mathrm{g(z_i)}$ terms (same tracer and same z bin).

- **Shape noise**: this term affects only the Lensing probe and it encodes the intrinsic ellipticity of observed galaxies, which may bias results if not taken into account. It reads as

$$C_\ell^{\rm N,g} = C_\ell^{\rm shape,g} = \frac{\gamma^2}{n_g} \tag{4.25}$$

  where $\gamma = 0.3$ is the intrinsic shear term (Sprenger et al. (2019)). This term affects only $\mathrm{g(z_i)} \times \mathrm{g(z_i)}$ terms (same tracer and same z bin).

Parameter	$\ln 10^{10} A_s$	n_s	w_0	w_a	E_{11}	E_{22}
Fiducial value	3.098	0.9619	-1.00	0.00	0.18	0.80

Table 4.2: Assumed fiducial cosmology (Planck Collaboration et al. 2018). MG parameters are from Planck 2018 TT, TE, EE + lowE. Fiducial values for the E_{ii} parameters lead to fiducial values on $\{\mu_0, \eta_0, \Sigma_0\} = \{1.12, 1.55, 1.43\}$

- **Shot $\times$ shape noise**: being the $L \times C$ probe term made of the contribution of both Lensing and Clustering, we model its noise contribution as a mixture of the shot and shape noises affecting Clustering and Lensing respectively. It reads as

$$C_\ell^{\mathrm{N,g}} = \sqrt{\left(C_\ell^{\mathrm{shot,g}}\right)^2 + \left(C_\ell^{\mathrm{shape,g}}\right)^2} = \frac{\sqrt{1+\gamma^2}}{n_g}. \tag{4.26}$$

4.4 Tested models

Future GWs observations are expected to contribute significantly to probing gravity (Belgacem et al. 2019). Forecasts on the cross-correlation of the GWs signal with other probes suggest that the multi-messenger approach could be a powerful tool to exploit GWs observations to constrain models beyond ΛCDM (Mukherjee et al. 2020b,a; Balaudo et al. 2022; Casas et al. 2022). The GWs luminosity distance, for bright events, could provide a new probe to test gravity. In this work we discuss if future GWs observations combined with LSS probes could add new information on MG theories. We parametrize the effects of MG in a phenomenological way by adopting a general prescription suited to probe small departures from GR. In this section, we give a brief overview of the formalism we adopt and the models we investigate.
Starting from the LSS sector, we focus on scalar perturbations to the metric in the conformal Newtonian gauges, with the line element given by

$$\mathrm{d}s^2 = a^2 \left[-(1+2\Psi)\mathrm{d}\tau^2 + (1-2\Phi)\mathrm{d}x^2\right], \tag{4.27}$$

where a is the scale factor, τ is the conformal time, and the time and scale-dependent functions Ψ and Φ describe the scalar perturbations of the metric: the Newtonian potential and spatial curvature inhomogeneities, respectively. Modifications of gravity impact the growth of structure and the evolution of the gravitational potentials, see e.g. Silvestri & Trodden (2009); Joyce et al. (2015). Interestingly, these effects, on linear scales, can be fully captured by two functions of time and scale, e.g. Bertschinger (2006); Amendola et al. (2008); Pogosian & Silvestri (2008); Zhao et al. (2009); Zhang et al. (2007)

$$k^2\Psi \equiv -4\pi G a^2 \mu(k,z)\rho\Delta\,, \tag{4.28}$$

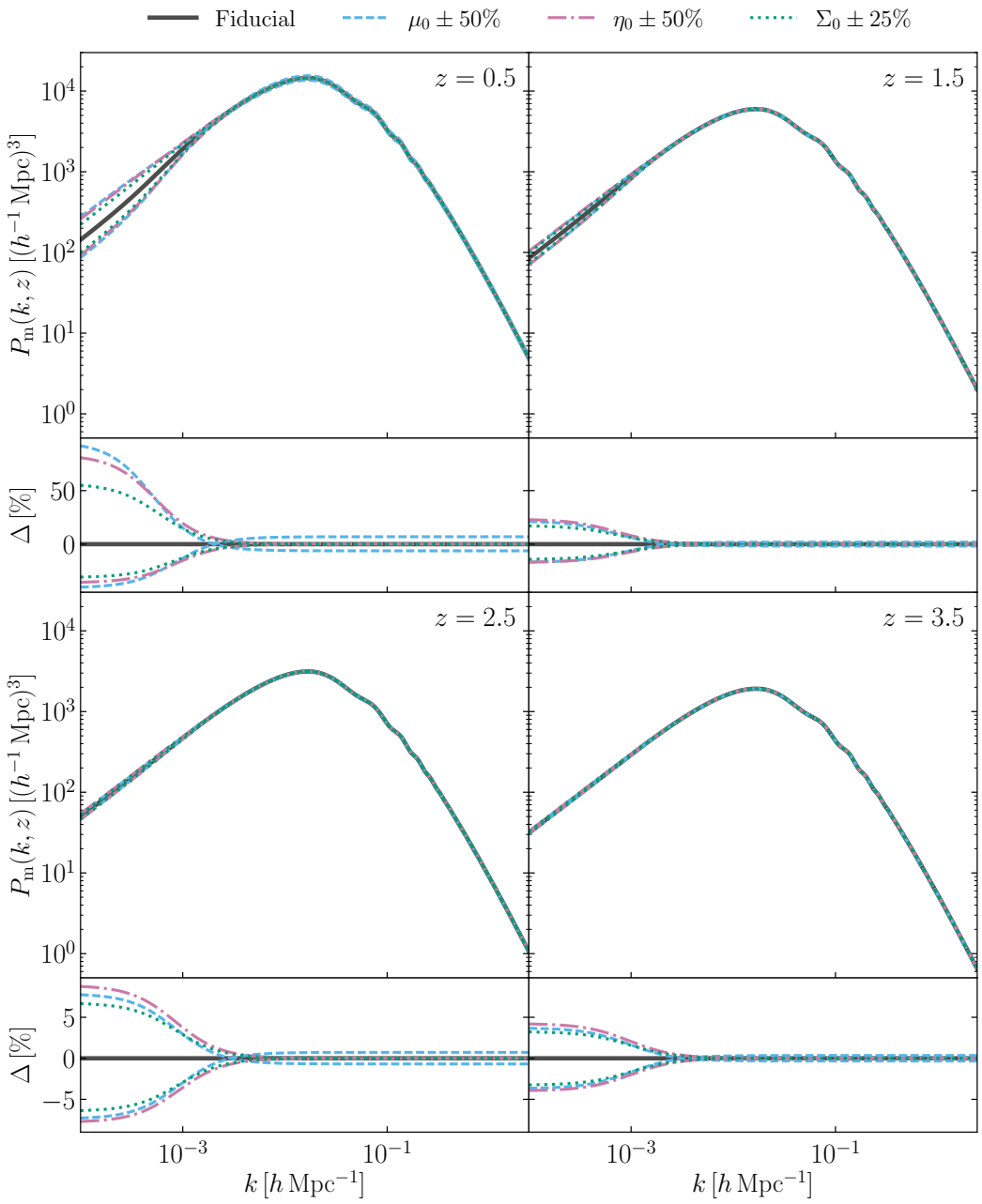

Figure 4.3: *Upper panels*: predicted matter power spectrum for different values of the MG parameters at redshifts $z = \{0.5, 1.5, 2.5, 3.5\}$. We show $P_{\rm m}(k, z)$ for the assumed fiducial cosmology (solid black lines, see table 4.2) and for variations of μ_0 (dashed light blue lines), η_0 (dashed-dotted pink lines) and Σ_0 (dotted green lines). When varying Σ_0, we keep μ_0 fixed. *Lower panels*: percentage variations with respect to the fiducial cosmology.

and

$$\Phi/\Psi \equiv \eta(k, z)\,, \tag{4.29}$$

where $\rho\Delta = \rho_{\rm m}\Delta_{\rm m} + \rho_{\rm r}\Delta_{\rm r}$, i.e., the sum of the matter (m) and radiation (r) contri-

butions. One can also define the function $\Sigma(k, z)$, that quantifies modifications to the lensing potential, as

$$k^2(\Phi + \Psi) \equiv -8\pi G a^2 \Sigma(k, z)\rho\Delta. \tag{4.30}$$

The three phenomenological functions $\mu(k, z)$, $\eta(k, z)$ and $\Sigma(k, z)$ are not independent. One should consider two of them at the time, e.g., the pair (μ, η) or (μ, Σ). It is possible to express $\Sigma(k, z)$ as a function of $\mu(k, z)$ and $\eta(k, z)$ as

$$\Sigma(k, z) = \frac{\mu(k, z)}{2}(1 + \eta(k, z)). \tag{4.31}$$

Deviations from ΛCDM are encoded in $(\mu(k, z),\ \eta(k, z))$ or $(\mu(k, z),\ \Sigma(k, z))$, with the ΛCDM case corresponding to $\mu(k, z) = 1$, $\eta(k, z) = 1$, $\Sigma(k, z) = 1$. To give a more intuitive interpretation of the physical meaning of the involved quantities, let us specify that the Σ function acts on relativistic particles, affecting mainly the lensing observable, whereas μ controls gravity effects on massive particles, controlling the growth of matter perturbations and affecting clustering. Finally, η, usually referred to as the gravitational slip parameter, cannot be directly connected to a constraining observable as the previous two functions. However, given that it quantifies differences between the two gravitational potential, its behaviour may be indicative of a breaking of the equivalence principle.

Several parametrizations of the phenomenological functions have been explored and constrained, see e.g. (Ishak 2019) for a review on recent results. In this work, we follow the approach of the Planck 2015 paper on dark energy and modified gravity (Ade et al. 2016a). We choose a time-dependent only parametrization for the evolution of $\mu(k, z)$ and $\eta(k, z)$, the so-called late-time parametrization

$$\begin{aligned} \mu(z) &= 1 + E_{11}\Omega_{\rm DE}(z) \\ \eta(z) &= 1 + E_{22}\Omega_{\rm DE}(z). \end{aligned} \tag{4.32}$$

The evolution is set by the value of the parameters E_{11} and E_{22}, while the background is kept fixed. This choice of parametrization simplifies the analysis and allows a direct comparison with the results of (Ade et al. 2016a). But there are also good reasons for not expecting any scale-dependence of the model to show up within the range of scales covered by the data that we consider. In fact, in order to satisfy local tests of gravity, these theories need to have a working screening mechanism, which suppresses any deviation from GR through environmental effects. Well known examples are the Chameleon and Vainshtein mechanism, see e.g. Brax (2021). In both cases, the requirements for a successful screening effectively pushes the characteristic length scale

of the model either into the small, non-linear scales (Chameleon case) or to very large, horizon-size scales (Vainshtein case). Let us point out that even while not working with a specific model, there are some assumptions that we make at the basis of our choice of parametrization. One such assumption is that modifications of gravity are relevant at late times; in this sense, we are linking them possibly to the source of cosmic acceleration, but more broadly to tests of gravity with large scale structure. Or, said in other words, we aim for this parametrization to broadly represent Horndeski models of gravity with luminal speed of sound, which is the theoretical framework on which our analysis is built.

We consider both the ($\mu(z)$, $\eta(z)$) and the ($\mu(z)$, $\Sigma(z)$) pair. In the latter case, $\Sigma(z)$ as a function of E_{11} and E_{22} is computed using equation (4.31). When performing the Fisher analysis, we vary E_{11} and E_{22} and derive the predicted constraints on the parameters (μ_0, η_0) and (μ_0, Σ_0), where $\mu_0 \equiv \mu(z=0)$, $\eta_0 \equiv \eta(z=0)$, $\Sigma_0 \equiv \Sigma(z=0)$. We compute the theoretical matter power spectrum with the code `MGCAMB`[2] Zhao et al. (2009); Hojjati et al. (2011); Zucca et al. (2019), the modified version of the Einstein-Boltzmann solver `CAMB`[3] (Lewis et al. 2000), extended to study modified gravity models within the phenomenological parametrization framework. In figure 4.3, we show the linear matter spectrum for the assumed fiducial cosmology (see table 4.2) and for different values of the MG parameters (μ_0, η_0) and (μ_0, Σ_0). This is the power spectrum used to compute the C_ℓs introduced in section 4.2.1. We observe that the most significant modifications occur at large scales. Varying the parameters η_0 or Σ_0 affects only the larger scales, while μ_0 has an impact on smaller scales too. The modifications become milder at higher redshifts, according to how the parametrization we chose performs.

The late-time parametrization has been studied in the literature in several contexts (Ade et al. 2016a; Planck Collaboration et al. 2018; Casas et al. 2017; Abbott et al. 2019b; Lee et al. 2021; Abbott et al. 2022) and current data sets do not show a significant preference for models beyond ΛCDM. Recently, a non-parametric Bayesian reconstruction of μ, Σ, along with the dark energy density, from all available LSS and CMB data was performed in Pogosian et al. (2021); Raveri et al. (2021); while the outcome is consistent with ΛCDM within 2σ, some interesting features in Σ were identified as an imprint of cosmological tensions.

The phenomenological functions μ, Σ and η parametrize modifications of the dynamics of perturbations within the scalar sector. When including GWs, one should consider that tensor perturbations are generally also affected by modifications of gravity. For the

[2]See `https://github.com/sfu-cosmo/MGCAMB`.

[3]See `https://camb.info/`.

observables of interest in this work, the effects of modified gravity on GWs propagating on the FLRW background, can be encoded in the difference between the electromagnetic luminosity distance $d_{\rm L}^{\rm EM}(z)$ and the GW one $d_{\rm L}^{\rm GW}(z)$. The phenomenological function $\Xi(z)$, defined as

$$\Xi(z) \equiv \frac{d_{\rm L}^{\rm GW}(z)}{d_{\rm L}^{\rm EM}(z)}, \tag{4.33}$$

quantifies the effect for bright sirens. The EM luminosity distance can be expressed as $d_{\rm L}^{\rm EM}(z) = \sqrt{L/4\pi S}$, where L and S are the bolometric luminosity and the bolometric flux for the observed object, respectively. This quantity can also be expressed as a function of the comoving distance χ as (for $\Omega_k = 0$): $d_{\rm L}^{\rm EM}(z) = (1+z)\chi = (1+z)d_H \int_0^z dz'/E(z')$, with $E(z) = \sqrt{\Omega_m(1+z)^3 + \Omega_k(1+z)^2 + \Omega_\Lambda}$ and $d_H = c/H_0$. The GW luminosity distance $d_{\rm L}^{\rm GW}(z)$ is estimated in a way not dependent on a distance ladder, and relies on the extraction of information enclosed in the GW waveform such as the strain and the frequency. A univocal analytic expression for the $d_L^{GW}(z)$ is non trivial to obtain, as it is also highly dependent on the assumed gravity model. In Belgacem et al. (2019), the authors performed an extensive study of Ξ both in terms of parametrizations and of specific form it takes in given models of MG. In the latter case, Ξ is in general related to operators of the Lagrangian that affect also scalar perturbations; for instance, in Horndeski gravity it is a function of the non-minimal coupling, which is a key contributor to μ and Σ as well. Therefore, in a theoretical embedding, Ξ is not completely independent of μ and Σ.

The expressions we used for GW lensing in the auto- and cross-correlation rely on calculations of the relativistic corrections to the luminosity distance of GW in Horndeski and DHOST theories with the speed of sound $c_T^2 = 1$ (Tasinato et al. 2021). In this case, it is not straightforward to find an explicit expression for $\Xi(z)$ in terms of μ, Σ and/or η which is valid on all linear scales. For $c_T^2 = 1$, in the quasi-static regime and on scales above the mass scale of the model, the running of the Planck mass is the main contributor to both μ, implying that the relation between Ξ and μ tends towards the simple form

$$\Xi(z) = \sqrt{1 + \frac{1}{\mu(z)}}. \tag{4.34}$$

However, on smaller scales, the relation becomes more complicated, as discussed in Pogosian & Silvestri (2016), and the expression for Ξ would acquire another term, dependent on the other MG functions at play. For the parametrization of μ and η that we employ in this work, based on Ade et al. (2016a), the exact form of this additional term, which

should depend on η, is complex to work out without loosing generality. For this reason, we decide to parametrize the Ξ function as follows

$$\Xi(z) = \sqrt{1 + \frac{1}{\mu(z)} + \frac{a_1}{\eta(z)^{a_2}}}, \tag{4.35}$$

where a_1 and a_2 are varied along with the other parameters in the Fisher analysis and regarded as nuisances. With this parametrization of Ξ we can reproduce the main features of the results found for several models (Belgacem et al. 2019). We fix the fiducial values of a_1 and a_2 in order to obtain a variation of Ξ in redshift comparable to the results for DHOST models in Belgacem et al. (2019).
Let us stress that our method for GW lensing builds on the expressions for the luminosity distance of GWs and its relativistic corrections; the latter are explicitly known only for the class of Horndeski models with luminal speed of tensors. This is therefore the context in which we perform our analysis. In this framework, the Ξ function is not independent of the μ, η or μ, Σ functions. In other words, they all depend, solely or partially, on the non-minimal coupling of the theory. A more general framework may not encode this dependence; forecasts in such case would be expected to be less constraining. In order to correctly quantify the degrading, we would need to go beyond the theoretical framework on which we have built our analysis; this is certainly an interesting direction for future work.
In the following section we discuss how the observables that we consider in this work are modified in light of the MG phenomenological functions.

4.4.1 Angular power spectra (in MG) and MG parameters

Above, we commented on how the MG parameters affect the linear matter power spectrum (see figure 4.3). In this section, we outline their impact on the observables that we consider in this work, presented in section 4.2.1.
On the one hand, all the angular power spectra are computed with the linear matter power spectrum $P_{\rm mm}(k, z)$. In our analysis the modified $P_{\rm mm}(k, z)$ is computed numerically by means of the code `MGCAMB`, as discussed above. As can be noticed in figure 4.3, the MG functions affect the matter power spectrum $P_{\rm mm}(k)$. The effect of μ is quite direct and the most notable, given that μ changes the rate of clustering of matter. The functions η and Σ have a less direct impact on $P_{\rm mm}(k)$, but still affect it. In particular, Σ impacts the C spectrum via the magnification bias. On the other hand, the MG models we consider modify the lensing potential. In the scalar sector, modifications to the lensing potential are encoded by the MG function $\Sigma(z)$, through eq. (4.30). This

means that an extra factor $\Sigma(z)$ appears for each time the term $(\Phi+\Psi)$ appears. Thus, the lensing angular power spectra of eq. (4.7) become Casas et al. (2017)

$$C_{\rm LL}^{\rm X_i Y_j}(\ell) = \int_0^\infty \frac{dz\ c}{H(z)}\ \frac{W_{\rm L}^{\rm X_i}(z)\ W_{\rm L}^{\rm Y_j}(z)}{\chi^2(z)}\ \Sigma^2(z)\ P_{\rm mm}\left(\frac{\ell}{\chi(z)}, z\right), \tag{4.36}$$

while the cross-correlation spectra between lensing and clustering will be

$$C_{\rm CL}^{\rm X_i Y_j}(\ell) = \int_0^\infty \frac{dz\ c}{H(z)}\ \frac{W_{\rm C}^{\rm X_i}\left(\frac{\ell}{\chi(z)}, z\right)\ W_{\rm L}^{\rm Y_j}(z)}{\chi^2(z)}\ \Sigma(z) P_{\rm mm}\left(\frac{\ell}{\chi(z)}, z\right). \tag{4.37}$$

Following Balaudo et al. (2022), the $\Xi(z)$ function is going to appear in the Lensing observables related to bright GW sirens. This is because for bright sirens the estimator of the convergence depends on the ratio $d_{\rm L}^{\rm GW}/d_{\rm L}^{\rm EM}$. Explicitly, this results into

$$C_{\rm LL}^{\rm GW_i^{bright} GW_j^{bright}}(\ell) \simeq \Xi^2(z) \int_0^\infty \frac{dz'\ c}{H(z')}\ \frac{W_{\rm L}^{\rm X_i}(z')\ W_{\rm L}^{\rm Y_j}(z')}{\chi^2(z')}\ \Sigma^2(z')\ P_{\rm mm}\left(\frac{\ell}{\chi(z')}, z'\right), \tag{4.38}$$

while the cross-correlation spectra between lensing and clustering will be

$$C_{\rm L\Theta}^{\rm GW_i^{bright} Y_j}(\ell) = \Xi(z) \int_0^\infty \frac{dz'\ c}{H(z')}\ \frac{W_{\rm L}^{\rm GW_i^{bright} Y_j}\left(\frac{\ell}{\chi(z')}, z'\right)\ W_{\rm L}^{\rm Y_j}(z')}{\chi^2(z')}\ \Sigma(z') P_{\rm mm}\left(\frac{\ell}{\chi(z')}, z'\right). \tag{4.39}$$

Following Balaudo et al. (2022), it is worth clarifying that the approximately equal symbol in the above two equations is due to the linearization at first order of the convergence estimator, in the parameters describing it which are introduced in equation (3.8) of Balaudo et al. (2022). We refer the interested reader to Balaudo et al. (2022) for further details.

4.5 Forecasts

In accordance to what described in section 4.2.2, we perform a Fisher analysis on the following parameters: $\{E_{11}, E_{22}, w_0, w_a, \ln 10^{10} A_s, n_s, K^{\rm fg}, a_1, a_2\}$ (for a total of 9 parameters). The fiducial values we use in this pipeline (mainly taken from Planck results Planck Collaboration et al. (2018)) are summarized in table 4.2.[4] Where explicitly stated, the $\{w_0, w_a\}$ parameters are kept fixed instead. Given errors on $\{E_{11}, E_{22}\}$, we derive constraints on the $\{\mu_0, \eta_0, \Sigma_0\}$ parameters. We perform Fisher analysis for the following different cases:

[4]The fiducial value of $K^{\rm fg}$ depends on the case considered (z binning and probe): we adopt $K^{\rm fg} = 5.72{\cdot}10^{-8}$ ($9.64{\cdot}10^{-6}$) for the redshift binning chosen in the dark sirens case for the Lensing (Clustering) probe and $K^{\rm fg} = 4.49 \cdot 10^{-8}$ ($1.05 \cdot 10^{-5}$) for the redshift binning chosen in the bright sirens case for the Lensing (Clustering) probe. The fiducial values for $\{a_1, a_2\}$ are respectively -0.95 and 0.14. We omit these values from table 4.2 for the sake of simplicity.

	σ_{μ_0}	σ_{η_0}	σ_{Σ_0}	σ_{w_0}	σ_{w_a}	σ_{μ_0}	σ_{η_0}	σ_{Σ_0}	σ_{w_0}	σ_{w_a}
	darkGW×IM					**brightGW×IM**				
LENSING	15.62	38.92	2.09	2.78	8.66	24.45	61.86	3.73	4.59	16.18
CLUSTERING	1.20	1.84	0.99	0.53	1.43	1.12	1.84	1.00	0.47	1.34
L + C	0.10	0.24	0.04	0.11	0.23	0.08	0.20	0.06	0.05	0.15
	darkGW×IM×gal					**brightGW×IM×gal**				
LENSING	1.96	4.48	0.09	0.45	1.41	2.78	6.66	0.24	0.96	3.62
CLUSTERING	0.80	1.39	0.82	0.32	0.92	0.30	1.25	0.68	0.12	0.35
L + C	0.05	0.11	0.01	0.04	0.08	0.06	0.10	0.02	0.03	0.09

Table 4.3: Fisher estimated errors on the $\mu_0, \eta_0, \Sigma_0,\ w_0, w_a$ parameters for different tracers and probes combinations.

- Different probes: L only, C only, and L + C;
- Different tracers combinations: GW × IM and GW × IM × gal;
- GW are either treated as dark (BHBH and BHNS mergers) or bright (NSNS) sirens.

The next section provides results for all the cases listed above.

4.5.1 Results

We provide Fisher estimated constraints on the μ_0, η_0, Σ_0 parameters (and w_0, w_a where relevant) in tables 4.3 and 4.4. All results refer to $f_{\rm sky} = 0.5$ and $T_{\rm obs}^{\rm GW} = 15$yr.

	σ_{μ_0}	σ_{η_0}	σ_{Σ_0}	σ_{μ_0}	σ_{η_0}	σ_{Σ_0}
	darkGW×IM			**brightGW×IM**		
LENSING	10.46	25.46	1.06	16.38	40.61	2.06
CLUSTERING	0.18	1.10	0.62	0.19	1.23	0.68
L + C	0.09	0.20	0.02	0.03	0.09	0.03
	darkGW×IM×gal			**brightGW×IM×gal**		
LENSING	1.13	2.60	0.06	1.63	3.93	0.14
CLUSTERING	0.17	1.08	0.61	0.09	0.50	0.29
L + C	0.08	0.17	0.02	0.03	0.06	0.01

Table 4.4: Fisher estimated errors on the μ_0, η_0, Σ_0 parameters for different tracers and probes combinations. The parameters w_0, w_a are kept fixed.

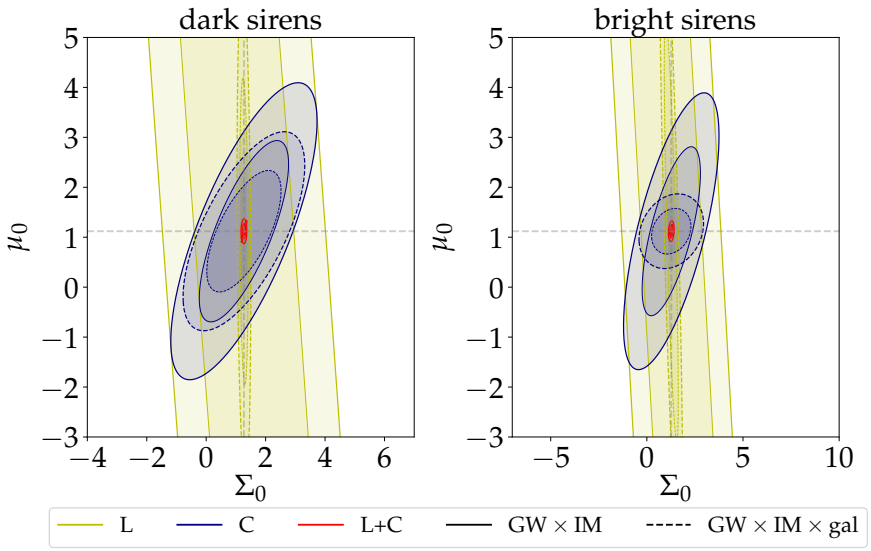

Figure 4.4: Contours for $\{\mu_0, \Sigma_0\}$ in the GW×IM (solid line) and GW×IM×gal (dashed line) cases, all probes considered (colors according to legend). Left panels refer to dark sirens (BHBH+BHNS), right panels refer to bright sirens (NSNS). w_0, w_a are among the Fisher parameters considered. $T_{\rm obs}^{\rm GW}$=15 yr and $f_{\rm sky} = 0.5$.

In figures 4.7, 4.8 we provide forecasts on $\{\mu_0, \Sigma_0\}$ for different values of $f_{\rm sky}$, fixing w_0, w_a. The same plots for the $\{\mu_0, \eta_0\}$ parameters are provided in appendix D (figures D.1, D.2, D.3, D.4). In light of these results, we can express the statements in the following.

Lensing-only case

Focusing on the Lensing-only case, we find that both bright and dark sirens cases are not good at constraining the parameters of interest, although some differences in the constraining power between the two cases can be found. Indeed, considering bright sources brings both advantages and disadvantages, with the resulting outcome depending on which of the two dominates. Specifically, the advantage of having an EM counterpart is enclosed in the presence of the MG function Ξ defined in section 4.4 (not present for dark sirens), which introduces a severely stronger dependence of the C_ℓs on the μ_0, η_0, Σ_0 parameters. On the other side, detectable bright sources cover a lower redshift range (since NSNS binaries are less massive than BHBH or BHNS they can be detected up to lower redshifts). This might give a disadvantage, both concerning the number of detected sources (i.e., worse shot noise) and the possibility to perform a less deep tomography (fewer redshift bins available, i.e., less information). Overall, bright sirens may give better/worse results with respect to the dark case depending on the balance between these two effects and on which probe we are considering.

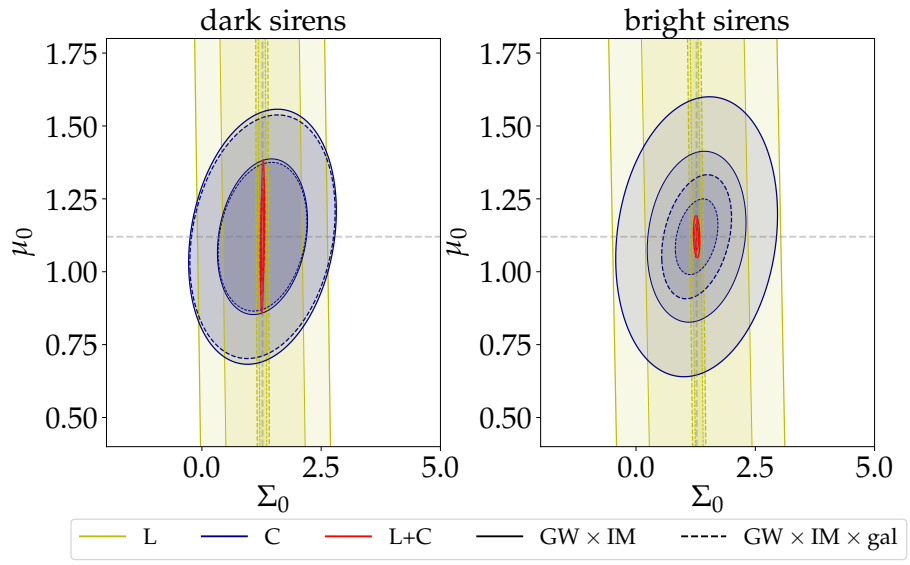

Figure 4.5: Contours for $\{\mu_0, \Sigma_0\}$ in the GW×IM (solid line) and GW×IM×gal (dashed line) cases, all probes considered (colors according to legend). Left panels refer to dark sirens (BHBH+BHNS), right panels refer to bright sirens (NSNS). w_0, w_a are fixed to fiducial values. $T_{\rm obs}^{\rm GW}$=15 yr and $f_{\rm sky} = 0.5$.

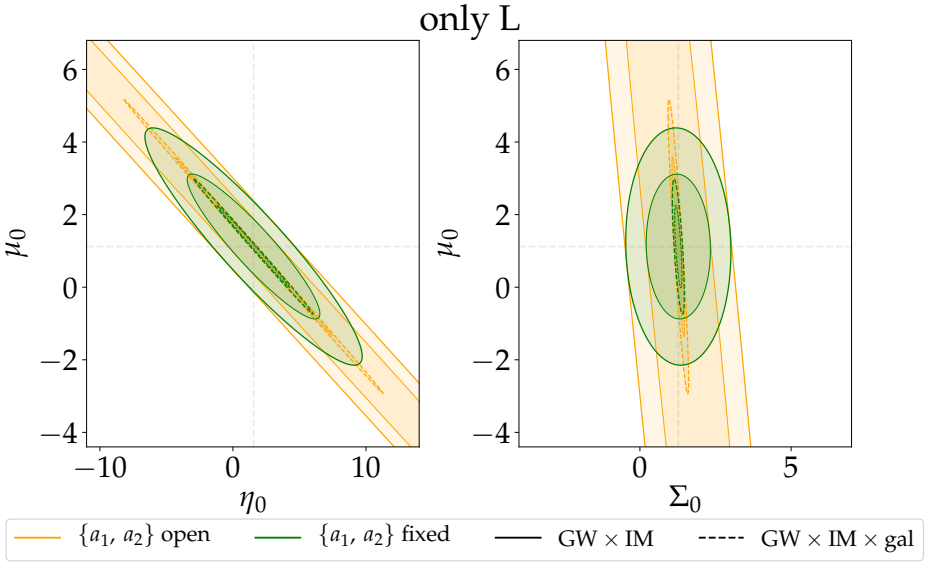

Figure 4.6: Contours for $\{\mu_0, \eta_0\}$ and (μ_0, Σ_0) in the GW×IM (solid line) and GW×IM×gal (dashed line) cases, for the only-L case. Comparison between forecasts fixing or opening the $\{a_1, a_2\}$ parameters describing the Ξ function according to equation (4.35). w_0, w_a are fixed to fiducial values. $T_{\rm obs}^{\rm GW}$=15 yr and $f_{\rm sky} = 0.5$.

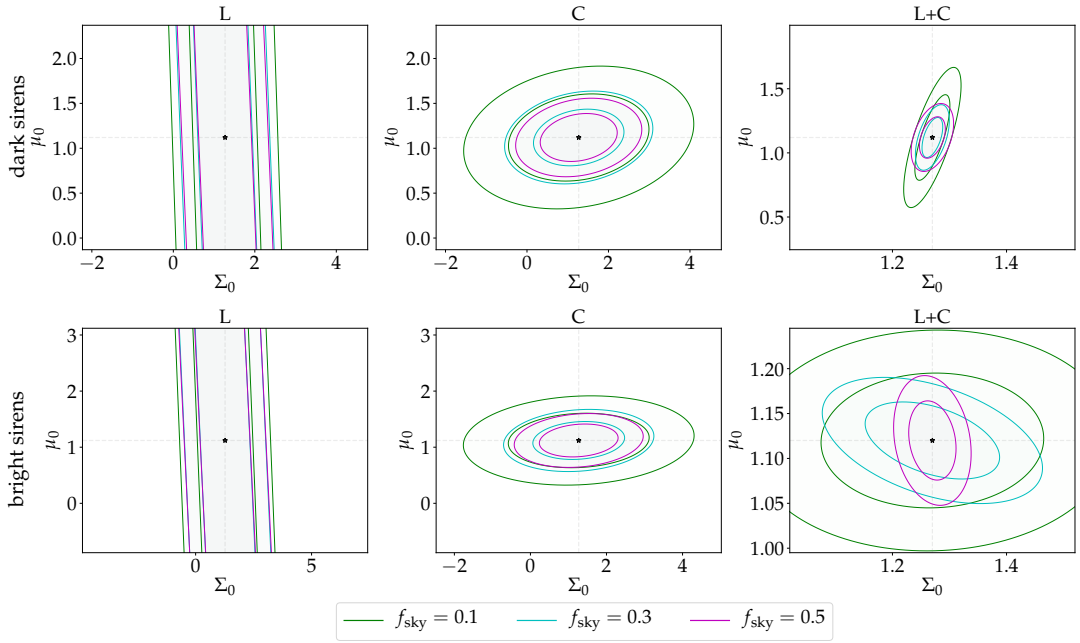

Figure 4.7: Contours for $\{\mu_0, \Sigma_0\}$ parameters for the GW×IM case, all probes considered (only Lensing: left panels; only Clustering: center panels; Lensing + Clustering: right panels), for dark (top panels) and bright (bottom panels) sirens and for different values of $f_{\rm sky}$ (colour-coded according to legend). w_0, w_a are fixed to fiducial values. $T_{\rm obs}^{\rm GW}$=15 yr.

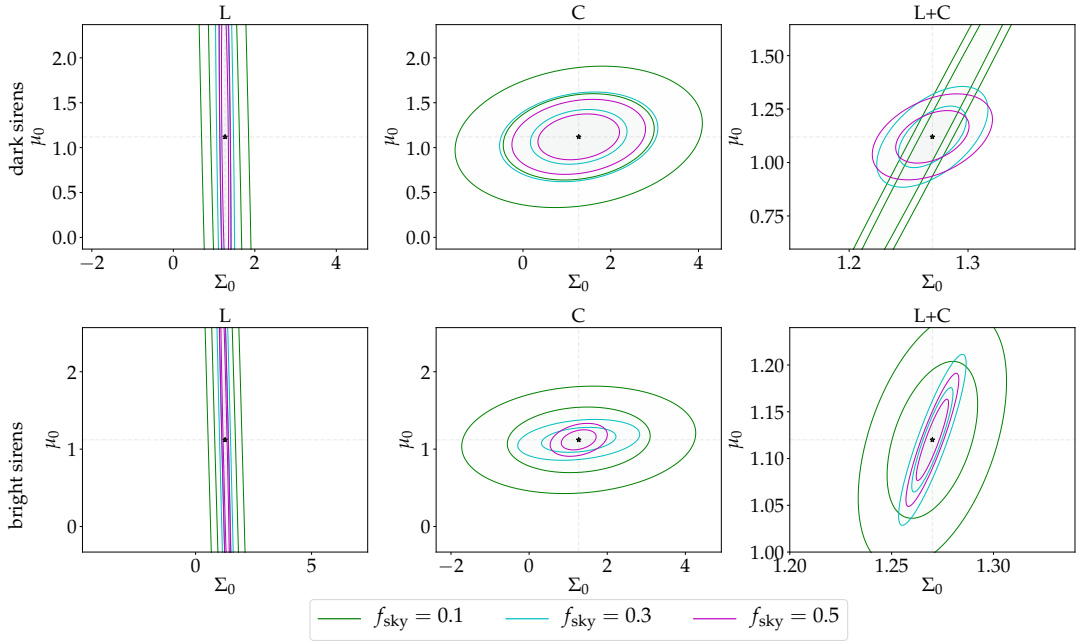

Figure 4.8: Contours for $\{\mu_0, \Sigma_0\}$ parameters for the GW×IM×gal case, all probes considered (only Lensing: left panels; only Clustering: center panels; Lensing + Clustering: right panels), for dark (top panels) and bright (bottom panels) sirens and for different values of $f_{\rm sky}$ (colour-coded according to legend). w_0, w_a are fixed to fiducial values. $T_{\rm obs}^{\rm GW}$=15 yr.

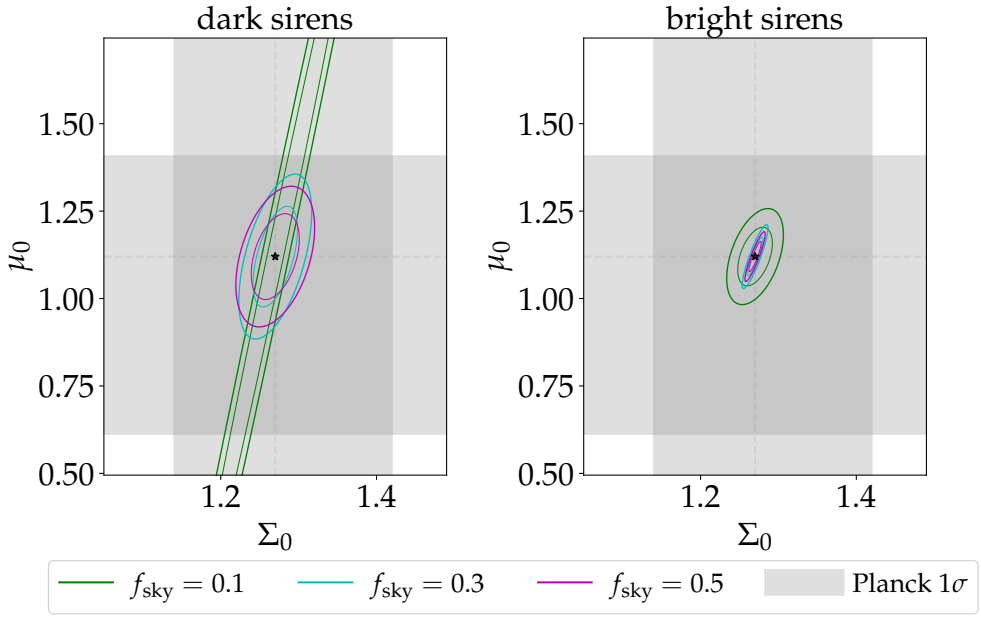

Figure 4.9: Contours for the most stringent constraints we find on $\{\mu_0, \Sigma_0\}$: GW×IM×gal, Lensing + Clustering case, for dark (left) and bright (right) sirens and for different values of $f_{\rm sky}$ (colour-coded according to legend). w_0, w_a are fixed to fiducial values. $T_{\rm obs}^{\rm GW}$=15 yr. The gray area shows $1\sigma = 68\%$ confidence regions from Planck TT,TE,EE+lowE without CMB lensing (see table 7 of Planck Collaboration et al. (2018)).

Generally, in the L-only case the advantages of considering bright sirens are not able to dominate on the downsides (or at least significantly), with constraints comparable between the two cases (see e.g., tables 4.3 and 4.4). This is even more evident in e.g., figures 4.4, 4.5, D.1, D.2: the L-only contour ellipses (in yellow) show an extremely wide extension in all dark sirens panels (left side), leaving especially μ_0 and η_0 barely constrained. Unfortunately, a similar trend can be found for bright sirens L-only ellipses (right panels of both figures). The same insight can be drawn from figures 4.7, 4.8, D.3, D.4.

Furthermore, we can see that adding galaxies in addition to the GW × IM cross-correlation significantly improves the results, especially in the dark sirens case: dashed lines (GW×IM×gal) in figures 4.4 and 4.5 tend to mark tighter ellipses than solid lines (GW×IM).

Overall, Lensing-only forecasts are non-competitive with Planck constraints Planck Collaboration et al. (2018), showing nonetheless the advantage of taking into account the information coming from a higher number of tracers (GW×IM×gal vs. GW×IM).

L+C case

Adding the angular Clustering probe to Lensing data (L+C case) significantly improves the results in any case considered (bright/dark sirens, with/without adding resolved galaxies), providing constraints tighter up to two orders of magnitude (see e.g., table 4.4). This shows that not only cross-correlating different tracers but especially combining together different probes is a remarkably powerful tool to exploit, that provides significant extra information. This is especially evident in figure 4.4: the C-only (in blue) and especially the L+C (in red) contours are firmly more constraining than the (yellow) L-only ones, often breaking down degeneracies between parameters.
The best results we obtain in the L+C case are very competitive with Planck results (Planck Collaboration et al. 2018), highlighting the power of cross-combining observables of different tracers and probes. Results concerning the Σ_0 parameter are especially promising. This is reasonable since Σ_0 is the parameter describing deviations from GR for Lensing effects, as explained in section 4.4. To highlight the competitiveness of our best constraints with those from Planck, in figure 4.9 we compare our L+C forecasts (GW×IM×gal case) with the 68% confidence regions from Planck TT,TE,EE+lowE (without CMB lensing, see table 7 of [127]). Planck results are compatible with ΛCDM and Planck data alone do not show a significant preference for beyond ΛCDM values of μ_0, η_0 and Σ_0: indeed, their results are less than 1σ away from the ΛCDM limit for μ_0 and η_0, and $\sim 2\sigma$ for Σ_0. Our best results are highly competitive and severely reduce Planck errors: assuming a Planck best fit as fiducial value our measurements show a mild preference for non-ΛCDM values of μ_0 and η_0 (respectively $\sim 4\sigma$ and $\sim 9\sigma$), and a clearly stronger preference for Σ_0 (at more than 20σ), since our lensing observable is strongly affected by it. This means that if experimental data will confirm beyond ΛCDM central values, we would be able to confirm a preference for MG models with a high confidence level.
Comparing the bright/dark sirens cases, we see no univocal pattern among the two (see e.g., red L+C contours in figures 4.4 and 4.5). This can be motivated by the explanation laid in the previous point: taking bright sirens has both pros (extra information contained in the Ξ parameter for Lensing) and cons (shallower tomography in both L and C). Given the addition of Clustering (which is independent of Ξ) we can not naturally expect a striking difference as for the L-only case, but a competition between these two opposite effects, with not clearly predictable outcomes. We also note that generally adding galaxies improves the constraining power, which is an expected outcome as more information is being fed to the pipeline (as for the L-only case).

Fixing $\{a_1, a_2\}$ ***parameters***

In section 4.4 we have introduced the $\Xi(z)$ function, which is parametrized by $\{a_1, a_2\}$ according to equation (4.35). In order to take into account possible uncertainties to the modeling of this function, we opted to allow $\{a_1, a_2\}$ to vary, introducing them among the Fisher parameters considered in the analysis (as described in section 4.4). Nonetheless, this inevitably introduces an extra source of uncertainty, disadvantaging predictions for the bright sources case and leading to forecasts in the Lensing-only case for bright sirens usually no better than those for dark sirens, as highlighted in the "Lensing-only case" subsection above. Nonetheless, one may wonder what the advantage of considering bright sources would be if the behaviour of $\Xi(z)$ was assumed fixed, getting rid of this extra source of uncertainty. Figure 4.6 provides constraints on μ_0, η_0, Σ_0 (for $f_{\rm sky} = 0.5$ and $T_{\rm obs}^{\rm GW} = 15$yr) for the Lensing-only case, comparing the cases of $\{a_1, a_2\}$ open and $\{a_1, a_2\}$ fixed to fiducial values (with w_0, w_a fixed). It shows a significant improvement in the constraining power of the experiments, with contour ellipses covering more reasonable ranges, highlighting a severe degradation in the constraining power due to the uncertainty on the modeling of the parameters describing $\Xi(z)$.

Indeed, Fisher estimated errors on $\{\mu_0, \eta_0, \Sigma_0\}$ when keeping $\{a_1, a_2\}$ fixed are the following: $\{1.32, 3.29, 0.70\}$ for the GW $\times$ IM case and $\{0.75, 1.80, 0.08\}$ when adding galaxies. When comparing these numerical values to those in the "LENSING" rows of table 4.4, we can see an improvement of up to one order of magnitude (for the GW $\times$ IM case).

These results show that if the behaviour of $\Xi(z)$ was to be known, being able to detect an EM counterpart would be of crucial importance for experiments based only on the Weak Lensing observable, allowing to constrain $\{\mu_0, \eta_0, \Sigma_0\}$ with good accuracy, and significantly better than a case in which only dark sirens would be available. Nonetheless, an approach taking into account the uncertainty on the modeling of $\Xi(z)$ is safer and more realistic, although provides more pessimistic forecasts.

$\{\mathbf{w_0}, \mathbf{w_a}\}$ ***effects***

Since we are studying theories with fixed background, it is natural to wonder about the impact of keeping the $\{w_0, w_a\}$ parameters fixed (results provided in table 4.4 and figures 4.5, D.2) or open, as extra Fisher parameters (table 4.3 and figures 4.4, D.1). When fixing w_0, w_a at their fiducial values results are in general either comparable or significantly more optimistic (up to a few factors unity), with smaller contour ellipses.

As one would expect, the higher number of free parameters usually leads to less tight constraints.

f_{sky} *effects*

Improving the surveyed area of the sky logically improves the constraining power, sometimes significantly. It can be seen in figures 4.7, 4.8, D.3, D.4 that the contours related to higher values of f_{sky} (in magenta) are tighter than those for low $f_{sky} = 0.1$ values (in green), sometimes reducing parameters degeneracies. This is valid for all considered probes: L, C and L+C (left, middle and right panels). We also report, not shown explicitly, a very mild dependence on the values of $T_{\rm obs}^{\rm GW}$, showing that in this framework the GW shot noise does not provide the bulk of the weight to the error budget.

Role of the EM counterpart for bright sirens

As described over the course of this manuscript, the bright sirens case relies on the assumption that NSNS mergers are associated with an EM counterpart. This is an optimistic starting point, which is why we accompany these results to the BHBH+BHNS dark case. For completeness (although not explicitly reported here for the sake of brevity) we have also computed forecasts labelling all GW sources (BHBH, BHNS and NSNS mergers) as dark sirens. We found that results are generally comparable to the BHBH+BHNS dark case up to a few percentages. For this reason, results in this latter case can also be seen as a proxy for forecasts in a scenario characterized by a complete lack of EM counterparts.

Impact of ℓ_{max} for bright sirens

Throughout this section, we have provided results with a choice of $\ell_{\rm max} = 300$ for detected bright sirens. As described in section 4.3.1, we are allowed to push our angular resolution limit beyond the intrinsic instrument limitation thanks to the detectability of EM counterparts. Nonetheless, we explored a set-up with an $\ell_{\rm max} = 100$ even for bright sirens. This way, we are testing the extreme case in which EM counterparts would not be exploited for improving the angular resolution. Forecasts obtained this way are less optimistic than the $\ell_{\rm max} = 300$ ones, with relative differences from just a few percentages (mainly for the Lensing-only case) up to a factor ~ 5 for the Clustering-only and L+C cases. Nonetheless, we note that this would not lead to orders of magnitude of difference among the forecasts, providing us fairly robust results to the specific $\ell_{\rm max}$ choice.

4.6 Summary

Cross-correlations between different tracers of the LSS and different observable probes can richly enhance the amount of physical information that can be extracted by present and forthcoming experiments. In this chapter we considered three different tracers: *(i)* resolved GW signals from compact object mergers as observed by ET, both assuming the detection of EM counterparts (for NSNS, bright sirens) or not (for BHBH and BHNS, dark sirens); *(ii)* the Intensity Mapping of the neutral hydrogen distribution as observed by the SKA-Mid survey; *(iii)* resolved radio-galaxies as mapped by SKAO. This allows us to correlate and compare both GW and EM signals, testing the possible imprints of beyond-GR behaviours, as these two observables are supposed to respond in the same way to matter perturbations effects such as lensing. For this reason, the primary observational probe we took into account is the weak lensing power spectrum, both in auto and cross-tracers correlation. In order to gauge the effects of combining together different probes, we also introduced the angular clustering power spectra and their L×C cross-term. We performed a Fisher matrix analysis in order to test a late-time parametrization scenario, forecasting the constraining power on the MG parameters $\{\mu_0, \eta_0, \Sigma_0\}$.

Our findings show that combining together different observational probes has a strikingly positive effect on the constraining power, with an improvement of up to an order of magnitude and results which are even competitive with constraints from Planck. We also find that, generally, cross-correlating together more tracers provides better constraints, as the combination of more information from different sources is more powerful than auto-correlation only experiments.

In addition, we also show that when considering probes that describe physical effects that would be different between GW and EM sources (i.e., Lensing), the detection of an EM counterpart might be of crucial importance, allowing us to actively test the presence of different behaviours between these two observables and confirm or rule out GR alternatives to the description of gravity.

This chapter extends the efforts of the scientific community in the field of multi-tracing and multi-probes Astrophysics and Cosmology, showing that in an era rich in surveys and data (both from the present time and near-future experiments) the interconnection of different sources is able to yield results and constraints which are significantly more powerful than auto-correlation or single-probe results.

5 Conclusions

5.1 Summary of the thesis

Works and results presented in this thesis cover a wide array of topics and applications, but all share the same common challenge: exploring the cross-correlation signal of GWs with other LSS luminous tracers in order to gauge and quantify the scientific potential, the advantages and the perks of the multi-tracing approach for Cosmology and Astrophysics. This chapter provides an organized summary of the main results presented in here.

In chapter 2, following Scelfo et al. (2020), we have presented an investigation of the cross-correlation signal of GWs and galaxies as an observational probe, potentially to test astrophysical models.
On the luminous tracer side, we considered actively star-forming galaxies without relying on any specific catalog: we characterized galaxies on the basis of the observationally established SFRFs at different redshifts, which are available thanks to high redshift far-IR/sub-mm surveys. We took into account galaxies with different star-formation activities, by forecasting results for the following SFR cuts: $\psi \geq 10,\, 100,\, 300\, M_{\odot}/\mathrm{yr}$. This allowed us to understand which contribution to the cross-correlation signal is provided by which type of galaxies (i.e., with which star formation activities).
On the GW side, we considered resolved events originated from any type of COs mergers in the stellar mass range (BHBH, BHNS, NSNS) and detected by the forthcoming

Einstein Telescope. These events were modeled starting from the same galaxy distributions. In addition, we used a refined modeling of the COs merging rates (based on Boco et al. (2019)) in which every single galaxy was linked to a metallicity distribution through a chemical evolution model. This prescription is then necessarily convolved with the sensitivity curve of the ET.
The first part of chapter 2 aimed at forecasting the detectability of the cross-correlation signal of the aforementioned tracers by means of a Signal-to-Noise ratio S/N. The adopted observable was the number counts angular power spectrum C_ℓ, by taking into account all lensing and GR-related contributions to the number counts fluctuations. We performed both a tomographic analysis, dividing our observation redshift range in several bins, and a non-tomographic one.
We have showed that various configurations would be able to provide a S/N above unity, leading to a clear signal. Nonetheless, scenarios with distant redshift bins or with a low number of sources (i.e., with a dominant shot noise contribution) would not be able to provide such clean signal. Anyways, when computing a total cumulative S/N we obtained fairly optimistic results, proving indeed that we would be able to detect a useful signal.
Finally, we explored the feasibility of testing different astrophysical scenarios with this type of cross-correlations. In particular, we presented a proof-of-concept scenario in which we compared, by means of a $\Delta\chi^2$ statistics, a case in which the COs merging efficiency presents a metallicity dependence versus a benchmark framework in which this dependence is neglected. We saw that with the appropriate configurations, in terms of total number of detected sources, this metallicity dependency feature could be distinguished by the benchmark scenario.
To sum up, in chapter 2 we have set the basis for a refined treatment of the GW and LSS tracers based on astrophysical detailed models and for a possible exploitability of the GW$\times$LSS C_ℓs observables to explore astrophysical scenarios.

In chapter 3, following Scelfo et al. (2022a), we have investigated for the first time, to our knowledge, the cross-correlation of GWs with the 21 cm line. We have considered resolved BHBH mergers as detected by ET and the IM of the neutral hydrogen distribution as detected by SKA-Mid. The observable taken into account consisted again in the angular power spectra C_ℓs, comprehensive of all lensing and GR contributions. Regarding the IM case, we have adapted the resolved number counts case to the unresolved one. The most powerful advantage of performing tomographic analyses with IM is given by the fact that the redshift information provided by such experiments is

highly refined, allowing very refined tomography, with finely sliced redshift bins. In that chapter we explored three different fields of application of GW×IM, ranging from Astrophysics to Cosmology. They are summarized in the following.
(i) Firstly, we focused on the calibration of the statistical redshift distribution of GWs events from BHBH mergers. We exploited the valuable redshift information on the HI distribution to better constrain the GW distribution in a statistical way. This effort revealed to be fairly optimistic at lower redshifts, whereas it is not as effective (at least for the configurations we explored) at higher redshifts.
(ii) Secondly, as an example of cosmology investigation with GW×IM, we explored the possibility of testing DE models by constraining the w_0, w_a parameters with GW×IM cross-correlations. We found that constraints obtained this way are not highly competitive with IM only experiments; nonetheless cross-correlations are well known in alleviating systematics limitations, so that they can still provide an alternative way to test such scenarios.
(iii) Thirdly, we focused our attention on the nature of the merging BBHs detected through GWs, specifically trying to understand wether the imprint of a population of PBHs would be detectable through GW×IM. Following Raccanelli et al. (2016b); Scelfo et al. (2018), where such analyses were performed with GWs and resolved galaxies, we relied on the idea that different scenarios (stellar or primordial) are expected to trace the underlying LSS in different ways. Consequently, GWs would be characterized by different values of their bias, which is the parameter we tried to constrain. Results showed that within a reasonable amount of observation time the effects of a PBHs population would be detectable, even for percentages of primordial-over-stellar BH mergers as low as $\sim 20\%$.
Overall, we showed that even a new cross-correlation observable such as that of GW×IM, has a large potential of applicability in both the astrophysics sector and the cosmology one.

In chapter 4, following Scelfo et al. (2022b), we kept exploring fields of applicability of the cross-correlation between GWs and other EM LSS tracers. In that chapter we focused our attention on the theories of gravity beyond GR, investigating the possibility to detect imprints of MG theories through GW×EM cross-correlations.
Indeed, we relied on the idea that, in a GR framework, GW and EM waves are expected to behave in the same way when crossing matter perturbations between the emitting source and the observing instrument. Any evidence of a different behaviour between the two types of way could be interpreted as a signature of beyond GR physics.

The luminous tracers considered in that chapter are both resolved radio galaxies (as observed by the SKAO) and the IM of the neutral hydrogen (with SKA-Mid). Regarding the GW side, we considered all types of COs mergers detected by ET, with the addition of a distinctive feature: the possibility of detecting an EM counterpart. NSNS mergers were then assumed as bright sirens (i.e., an EM counterpart is also detected), whereas BHBH and BHNS as dark. This allowed us to test the importance of detecting an EM counterpart along the GW emission.
The considered observable probes for this work were the following: the weak lensing angular power spectrum (where the main manifestation of the different behaviours of light and GW should in principle be seen), the angular clustering power spectrum and their cross term L×C. A tomographic Fisher analysis was performed, considering either GW×IM and GW×IM×gal cross-correlations, and either the single probes (L and C) or their overall combination (L+C). Furthermore, we explored configurations in which the background parameters w_0 and w_a were kept either fixed or open.
We aimed at constraining the MG $\{\mu_0, \eta_0, \Sigma_0\}$ parameters, and found that although L-only constrains are hardly competitive, combining together different probes and more tracers can provide substantially better results, competitive even with Planck. On top of this, we shed light on the advantages that an EM counterpart observation would bring for those probes which describe physical behaviours in a different way depending on whether GW or light would be involved (i.e., Lensing).

5.2 Future perspectives

This section sketches a few ideas and views I have about possible perspectives to either improve and make the investigations presented in this thesis more competitive, or about potential scientific paths to explore, connected to these ones.

Firstly, we know that the Fisher matrix approach has the great advantage of providing forecasts in a quick but still reliable way. Nonetheless, it may be interesting to compare Fisher results with those obtained with other approaches, namely Markov-Chains Monte-Carlo (MCMC, Gilks et al. (1995)), for further investigations. This can provide more reliability on the forecasts retrieved and potentially shed better light on degeneracies or other phenomena that might be lost with Fisher analyses.

Secondly, all chapter presented here have shown, in different ways, the importance of the study of the bias parameter of resolved GW events. This can be a fundamental

ingredient for either a better modeling and characterization of synthetic data in order to build forecasts for astrophysical models (as in e.g., chapter 2) or to investigate the nature of merging BBHs (astrophysical or primordial, as in chapter 3). Consequently, one channel in which I personally believe the efforts of the scientific community could be focused is definitely this one.

Furthermore, chapter 4 has showed the power of combining together not just two, but even three tracers in multi-tracing analysis, and even considering more than one probe. I believe that this way should be explored even more since, in cases in which the signal vividly dominates over the noise, the constraining gain is significant. For example, I believe that adding CMB to the pipeline of most of the applications presented in this thesis could give a significant contribution, as not only it is an extra observable, but mainly because it relies on much different physical processes than those of EM waves emitting observables in the local universe (resolved galaxies or IM by SKAO) and, especially, GWs.

On top of this, a very significant improvement to results shown in chapter 4 can be provided by modeling a full NL matter power spectrum (necessary brick for building up the C_ℓ) for the MG frameworks under study. Indeed, although GWs resolution is a limiting factor in determining the maximum multipole ℓ_{max} achievable, when an EM counterpart is available this limit is shifted to much higher values, with the condition of being able to model such C_ℓs up to those scales. This would provide a much higher amount of data to analyze for forecasts and would shrink the Fisher estimated errors on the parameters of study. For example, Casas et al. (2022) have reached higher multipoles with a NL power spectra in a similar work (although not considering GWs events, which are instead crucial for the analysis presented in chapter 4) by means of a the parameterized post-Friedmann (PPF) framework presented by Hu & Sawicki (2007), which claims to allow reaching smaller scales. This or other approaches would be a powerful way to improve constraints set in chapter 4.

Morover, it would be of great interest to keep investigating the GW×LSS cross-correlations including also unresolved GWs events. Several authors have already opened this path, studying the Stochastic Gravitational Waves Background (SGWB) accurate modeling (see e.g., Bertacca et al. (2020); Bellomo et al. (2022)) and its cross-correlations with other tracers, such as the CMB (see e.g., Capurri et al. (2022)). An

accurate modeling of this observable and its relationships with other ones is of fundamental importance for the disentanglement between an astrophysical component of the SGWB (due to unresolved COs merger events) and a cosmological one, shedding light on early universe physics and cosmological theories, other than astrophysical ones.

To conclude, this thesis extends the efforts of the scientific community in the field of multi-tracing Astrophysics and Cosmology. This era and the nearby future are and will be characterized by a richness of surveys and data. For this reason, the interconnection of different sources, often with a completely different physical nature or origin (as for GWs and light) can definitely be expected to open new scientific paths and yield results and constraints which can be significantly more powerful than auto-correlation experiments, or just simply provide alternative ways to test physical theories. My aim in writing this thesis is to justify these statements, by means of my scientific original research and results. I am optimistic and confident that any scientist having read up to this point, if not already involved in multi-tracing works, will now have the curiosity to explore such, or will simply just recognize how powerful this scientific path can be and all the promising potential hidden in there.

Appendices

A

Relativistic number counts for angular power spectra

This appendix provides the full expression for the relativistic number counts effects written in equation (1.65):

$$
\begin{aligned}
\Delta_\ell^{\rm den}(k,z) &= b_X \delta(k,\tau_z) j_\ell, \\
\Delta_\ell^{\rm vel}(k,z) &= \frac{k}{\mathcal{H}} j_\ell'' V(k,\tau_z) + \left[(f_X^{\rm evo} - 3)\frac{\mathcal{H}}{k} j_\ell + \left(\frac{\mathcal{H}'}{\mathcal{H}^2} + \frac{2-5s_X}{r(z)\mathcal{H}} + 5s_X - f_X^{\rm evo} \right) j_\ell' \right] V(k,\tau_z), \\
\Delta_\ell^{\rm len}(k,z) &= \ell(\ell+1)\frac{2-5s_X}{2} \int_0^{r(z)} dr \frac{r(z)-r}{r(z)r} \left[\Phi(k,\tau_z) + \Psi(k,\tau_z) \right] j_\ell(kr), \\
\Delta_\ell^{\rm gr}(k,z) &= \Bigg[\left(\frac{\mathcal{H}'}{\mathcal{H}^2} + \frac{2-5s_X}{r(z)\mathcal{H}} + 5s_X - f_X^{\rm evo} + 1 \right) \Psi(k,\tau_z) + (-2 + 5s_X)\, \Phi(k,\tau_z), \\
&\quad + \mathcal{H}^{-1} \Phi'(k,\tau_z) \Bigg] j_\ell, \\
&\quad + \int_0^{r(z)} dr \frac{2-5s_X}{r(z)} \left[\Phi(k,\tau) + \Psi(k,\tau) \right] j_\ell(kr), \\
&\quad + \int_0^{r(z)} dr \left(\frac{\mathcal{H}'}{\mathcal{H}^2} + \frac{2-5s_X}{r(z)\mathcal{H}} + 5s_X - f_X^{\rm evo} \right)_{r(z)} \left[\Phi'(k,\tau) + \Psi'(k,\tau) \right] j_\ell(kr).
\end{aligned}
\tag{A.1}
$$

The meaning of the physical quantities written above is the following: b_X is the bias parameter, s_X is the magnification bias parameter, $f_X^{\rm evo}$ is the evolution bias parameter, r is the conformal distance on the light cone, $\tau = \tau_0 - r$ is the conformal time, $\tau_z =$

$\tau_0 - r(z)$, j_ℓ, $j'_\ell = \frac{dj_\ell}{dy}$, $j''_\ell = \frac{d^2 j_\ell}{dy^2}$ are the Bessel functions and their derivatives (evaluated at $y = kr(z)$ if not explicitly stated), $\mathcal{H}$ is the conformal Hubble parameter, the prime symbol $'$ stands for derivatives with respect to conformal time, δ is the density contrast in the comoving gauge, V is the peculiar velocity, Φ and Ψ are Bardeen potentials.

B

GW×IM - Astrophysical vs. primordial BBHs: "early" primordial scenario as fiducial

For completeness, in this appendix we extend results presented in chapter 3 (based on Scelfo et al. (2022a)) and show that the optimistic results of section 3.6, regarding the possibility of determining the progenitors of merging BBHs, could be obtained also when considering a primordial scenario as fiducial model, aiming at distinguishing it from an alternative astrophysical case.

We consider here the "early" primordial scenario and assume the redshift evolution of the merger rate described by Raidal et al. (2019), which is an extension to the model by Ali-Haïmoud et al. (2017). As done for the astrophysical merger rate, we re-normalize it to the value of 30 $\mathrm{Gpc}^{-3}\mathrm{yr}^{-1}$, in agreement with local LIGO/Virgo observations. In fact, suppression effects to the merger rate could in principle shift it to agree with experimental values (Raidal et al. (2019)). We stress that due to the big uncertainties of both the PBHs merger rate and suppression effects, the state of the art in this field is still in full development.

Given the large uncertainties in the PBH modeling, we assume here a magnification bias with a value of $s_{\mathrm{GW}}^{\mathrm{PBH}} = 0.0$, since almost all sources in the $\mathcal{O}(10M_{\odot})$ mass range would be detected by the ET in our redshift interval (see e.g., figure 3 of Scelfo et al. (2018)) and a slightly more precise determination of this quantity would be possible only by fixing quantities accompanied by huge uncertainties (mass distribution, suppression

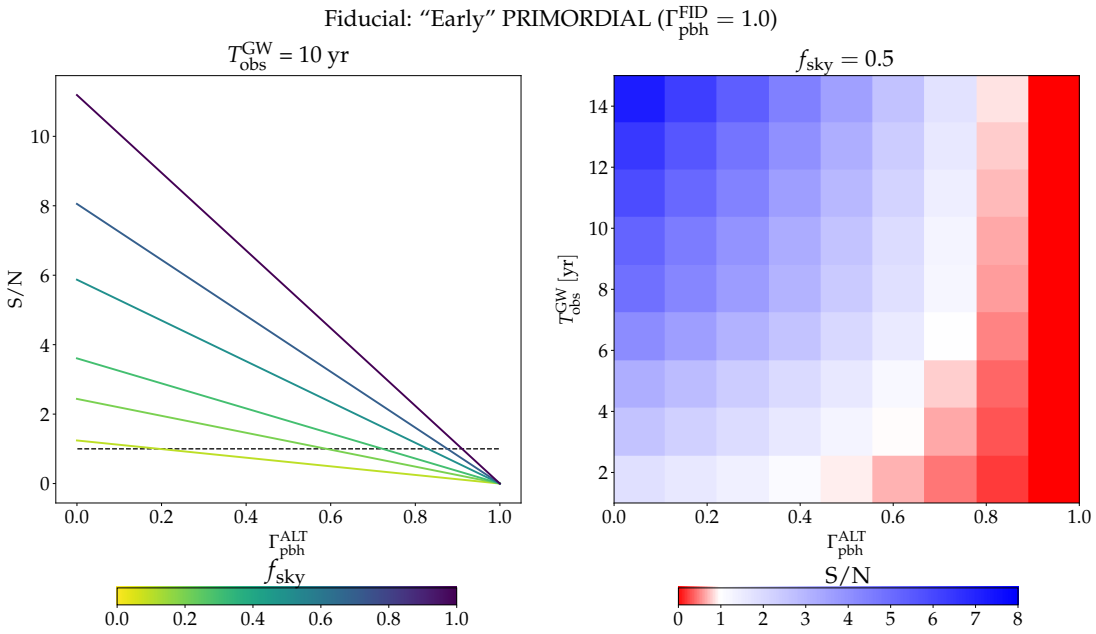

Figure B.1: S/N ratios for distinguishing the Fiducial scenario from the Alternative, for different values of $T_{\rm obs}^{\rm GW}$ (from 1 yr to 15 yr), $f_{\rm sky}$ (from 0.1 to 1.0) and $\Gamma_{\rm pbh}^{\rm ALT}$ (from 0.0 to 1.0). "Early" primordial model assumed as Fiducial. Models with different $\Gamma_{\rm pbh}^{\rm ALT}$ assumed as Alternative. The colorbar of the right-side plots is normalized to white at $S/N = 1$.

model, etc.). We provide in figure 3.5 the specifics assumed for this scenario, comparing them for completeness with those of the "late" primordial case (redshift distribution following prescriptions by Bird et al. (2016)).

As figure B.1 shows, high values of the SNR would be reached even for relatively low values of $f_{\rm sky}$ and $T_{\rm obs}^{\rm GW}$, in analogy with results from figure 3.6, in which the astrophysical scenario is instead assumed as fiducial.

C

Lyman-α forest constraints on Primordial Black Holes

This appendix is based on the following manuscript:
R. Murgia, G. Scelfo, M. Viel, A. Raccanelli
Lyman-α Forest Constraints on Primordial Black Holes as Dark Matter
Phys. Rev. Lett. 123 (2019) 7, 071102, `arXiv:1903.10509`

C.1 Overview and motivation

Primordial Black Holes (PBHs) formed in the early universe could constitute part of the dark matter. For an overview on PBHs and a possible method to detect the imprints of the existence of a PBHs population through GW×IM cross-correlations we address the reader to chapter 3 (section 3.6).
Another suitable method for constraining the mass and abundance of PBHs is offered by the Lyman-α forest, which is the main manifestation of the Intergalactic Medium (IGM). Such observable represents indeed a very powerful tool for tracing the DM distribution at (sub-)galactic scales (see, e.g., Viel et al. (2002, 2005, 2013)). Indeed, Poisson fluctuations in the PBHs number density impact on the linear matter power spectrum by inducing a small scale power enhancement which departs from the standard cold dark matter prediction. In this appendix, we present new limits on the PBH mass and abundance, through a comprehensive analysis of the high resolution, high redshift Lyman-α forest data by means of hydrodynamic simulations.

Almost two decades ago, by using Lyman-α forest data, Afshordi et al. (2003) set an upper limit of few $10^4 M_\odot$ on PBH masses, in the simple case in which all DM is made by PBHs with the same mass. In this appendix, we update and improve such limit, by using the highest resolution Lyman-α forest data set up-to-date (Viel et al. (2013)), and a new set of high resolution hydrodynamic simulations that allow a more precise modelling of the full 1D flux power. Furthermore, we generalize our results to different PBH fractions with respect to the total DM amount, and to non-monochromatic mass distributions.

This appendix is organized as follows: in section C.2 we discuss the impact on the matter power spectrum due to the existence of PBHs; in section C.3 we extend the discussion to non-monochromatic PBH mass distributions; in section C.4 we present the data set and the methods that we adopted for our analyses; in section C.5 we report and discuss the results that we have obtained; in section C.6 we wrap the discussion up.

C.2 Poisson noise and impact on the matter power spectrum

Stellar-mass PBHs would cause observable effects on the matter power spectrum; due to discreetness, a small-scale plateau in the linear power spectrum is induced by a Poisson noise contribution (Mészáros 1975; Afshordi et al. 2003; Gong & Kitajima 2017; Carr & Silk 2018).

If PBHs are characterized by a Monochromatic Mass Distribution (MMD), they are parameterized by their mass, $M_{\rm PBH}$, and abundance, so that the fraction parameter $f_{\rm PBH} \equiv \Omega_{\rm PBH}/\Omega_{\rm DM} = 1$ where all DM is made of PBHs.

If PBHs are randomly distributed, their number follows a Poisson distribution, and each wavenumber k is associated to an overdensity $\delta_{\rm PBH}(k)$, due to Poisson noise. The PBH contribution to the power spectrum is thus defined as

$$P_{\rm PBH}(k) = \langle |\delta_{\rm PBH}(k)|^2 \rangle = \frac{1}{n_{\rm PBH}}\,, \tag{C.1}$$

where $n_{\rm PBH}$ is the comoving PBH number density , i.e.

$$n_{\rm PBH} = \frac{\Omega_{\rm DM}\rho_{\rm cr} f_{\rm PBH}}{M_{\rm PBH}}, \tag{C.2}$$

with $\rho_{\rm cr}$ being the critical density of the universe. Since $n_{\rm PBH}$ is a k-independent quantity, $P_{\rm PBH}$ is scale-invariant.

One can interpret the PBH overdensity as an isocurvature perturbation (Afshordi et al. 2003; Gong & Kitajima 2017). Hence, the total power spectrum can be written as:

$$P_{\rm CDM}(k,z) = D^2(z)\left(T^2_{\rm ad}(k)P_{\rm ad} + T^2_{\rm iso}(k)P_{\rm iso}\right) , \tag{C.3}$$

where $D(z)$ is the growth factor, $P_{\rm iso}$ is the isocurvature power spectrum, and $P_{\rm ad} \propto A_s k^{n_s}$ is the primordial adiabatic power spectrum. $T_{\rm ad}$ and $T_{\rm iso}$ are the adiabatic and isocurvature transfer functions, respectively. The PBH linear power spectrum is thus defined by:

$$P_{\rm iso} = f^2_{\rm PBH} P_{\rm PBH} = \frac{2\pi^2}{k^3} A_{\rm iso} \left(\frac{k}{k_*}\right)^{n_{\rm iso}-1} , \tag{C.4}$$

where we set the pivot scale $k_* = 0.05/\mathrm{Mpc}$, and the primordial isocurvature tilt $n_{\rm iso} = 4$ in order to ensure the scale-invariance. Since the adiabatic power spectrum evolves as k^{-3} at large k, the isocurvature contribution is expected to become important only at the scales probed by Lyman-α forest; $A_{\rm iso}$ sets the amplitude of the isocurvature modes, depending on the PBH mass considered; we can then express the isocurvature-to-adiabatic amplitude ratio:

$$f_{\rm iso} = \sqrt{\frac{A_{\rm iso}}{A_s}} = \sqrt{\frac{k_*^3 f^2_{\rm PBH}}{2\pi^2 n_{\rm PBH}} \frac{1}{A_{\rm s}}} = \sqrt{\frac{k_*^3 M_{\rm PBH} f_{\rm PBH}}{2\pi^2 \Omega_{\rm CDM}\rho_{\rm cr}} \frac{1}{A_{\rm s}}} , \tag{C.5}$$

where the last equality holds only for MMDs. Different combinations of PBH mass and abundance correspond to the same isocurvature-to-adiabatic amplitude ratio if the quantity $f_{\rm PBH}M_{\rm PBH}$ is the same. In our framework, the effect on the linear matter power spectrum due to the presence of isocurvature modes consists of a power enhancement with respect to the standard ΛCDM spectrum, in the form of a small-scale plateau.
In figure C.1 we provide the relative differences with respect to a pure ΛCDM scenario for the 3D linear and non-linear matter power spectra, at redshift $z = 5$, for ΛPBH models with $M_{\rm PBH} = \{10^2, 10^3\}M_\odot$, assuming $f_{\rm PBH} = 1$. We also show the 1D flux power spectra, which are the Lyman-α forest observables, associated to the same ΛPBH models. The gray shaded area refers to the scales covered by our Lyman-α data set, obtained from MIKE/HIRES spectrographs. The non-linear power spectra have been extracted from the snapshots of cosmological simulations, thus they include both the linear contribution (encoded in the initial conditions) and, on top of that, the effects of the non-linear evolution computed by the numerical simulation itself. The PBH contribution is thereby included in the initial conditions, whereas during the non-linear evolution both the isocurvature and adiabatic DM modes are treated as cold and collisionless (see section C.4 for further details). It can be easily seen how non-linearities in the 3D matter power spectrum wash out the differences induced by the

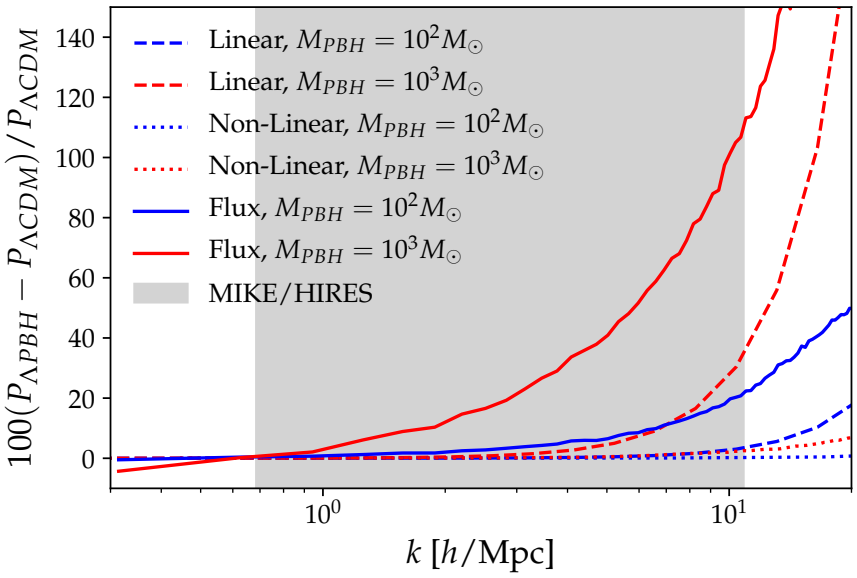

Figure C.1: Relative difference, at redshift $z = 5$, between ΛCDM and ΛPBH scenarios for the linear matter (*dashed*), non-linear matter (*dotted*) and 1D flux (*solid*) power spectra. Blue/red colors correspond to $M_{\rm PBH} = \{10^2, 10^3\}\ M_\odot$, respectively, for a monochromatic scenario with $f_{\rm PBH} = 1$. The gray shaded area refers to the scales covered by Lyman-α forest data.

presence of PBHs. On the other hand, the 1D flux spectra are a much more effective observable to probe the small-scale power.

The Lyman-α forest observable is the 1D flux power spectrum, which, being a projection of 3D non-linear matter power spectrum, is an ideal tracer for the small-scale DM distribution along our lines of sight. In figure C.2 we show the 1D flux power for the ΛCDM model, together with the spectra corresponding to different values of $M_{\rm PBH}$. Symbols refer to MIKE/HIRES data. To exhibit the variations in the flux power induced by different IGM thermal histories, we also show, as grey dashed areas, the impact of different IGM temperature evolutions.

C.3 Extended Mass Distributions

The PBH formation is, in the most standard case, due to large perturbations in the primordial power spectrum; while the exact details of the peak required to form PBH and how this is linked to the real-space overdensities are still unclear (Kalaja et al. 2019), PBHs could have an extended mass function. Moreover, a non-monochromatic mass distribution would be created by different merger and accretion history of each PBH. General methods to convert MMD constraints to limits on Extended Mass Dis-

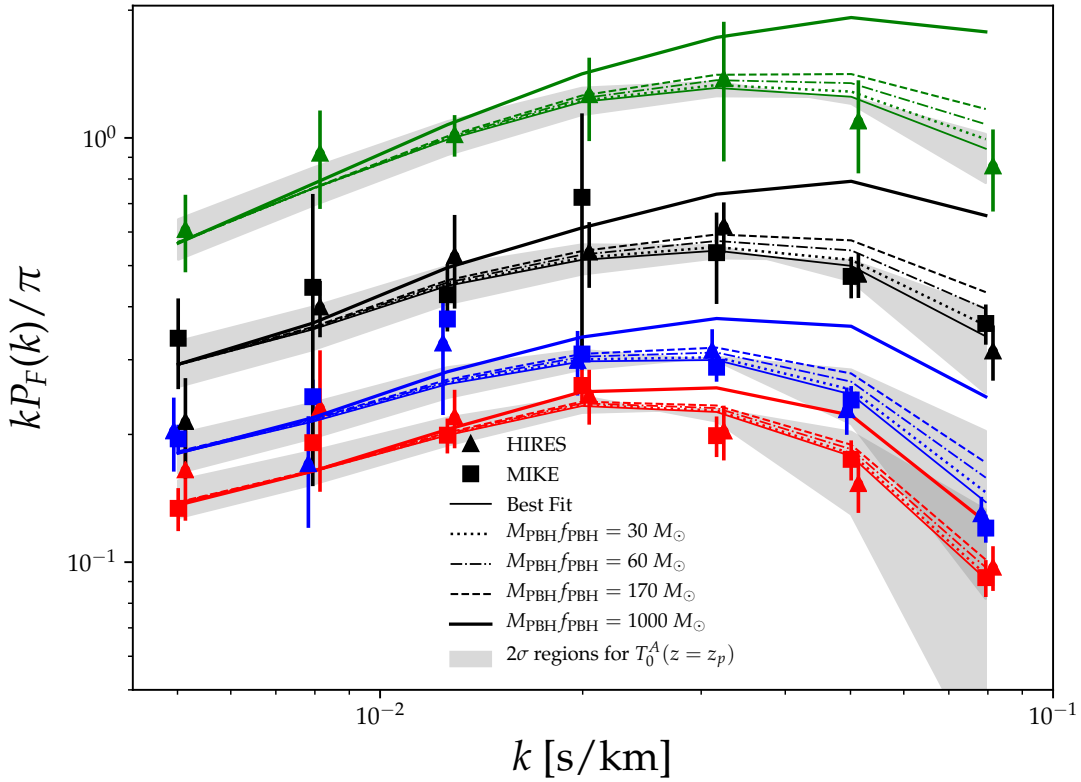

Figure C.2: 1D flux spectra for ΛCDM and ΛPBH, for different PBH masses. Symbols are data from MIKE/HIRES, lines are obtained by interpolating in the $(M_{\rm PBH} f_{\rm PBH})$-space defined by our simulations; while the best fit is technically for $M_{\rm PBH} \neq 0$, it is indistinguishable from the ΛCDM case. Red, blue, black and green indicate $z = 4.2, 4.6, 5.0, 5.4$, respectively. The grey dashed areas represent regions sampled by flux power spectra corresponding to values for T_0^A spanning its marginalized 2σ interval.

tributions (EMDs) have been developed by Carr et al. (2017); Bellomo et al. (2018). The extension to EMDs of the observable considered here arises naturally from the second equality in Equation (C.5), by directly taking the PBH number density corresponding to a given EMD. Consider EMDs in the form:

$$\frac{dn_{\rm PBH}}{d\ln M_{\rm PBH}} = f_{\rm PBH}\rho_{\rm DM}\frac{d\Phi_{\rm PBH}}{dM_{\rm PBH}}\,, \tag{C.6}$$

where the function $d\Phi_{\rm PBH}/dM_{\rm PBH}$ describes the EMD shape, and $\rho_{\rm DM} = \Omega_{\rm DM}\rho_{\rm cr}$. Given an EMD, one can define the so-called Equivalent Mass $M_{\rm eq}$, which is the mass of a MMD providing the same observational effect.
The conversion is given by:

$$f_{\rm PBH}^2\left[\frac{\Omega_{\rm DM}\rho_{\rm cr}f_{\rm PBH}}{M_{\rm eq}}\right]^{-1} = \frac{f_{\rm PBH}^2}{n_{\rm PBH}} = f_{\rm PBH}^2\left[\int\frac{dn_{\rm PBH}}{dM_{\rm PBH}}dM_{\rm PBH}\right]^{-1} \tag{C.7}$$

where we assume that the PBH abundances are the same for both the MMD and EMD cases. We finally have:

$$M_{\rm eq} = \left[\int\frac{1}{M_{\rm PBH}}\frac{d\Phi}{dM_{\rm PBH}}dM_{\rm PBH}\right]^{-1}. \tag{C.8}$$

We consider two popular EMDs: *Lognormal* and *Powerlaw*.
The *Lognormal* EMD (Dolgov & Silk 1993) is defined by

$$\frac{d\Phi_{\rm PBH}}{dM_{\rm PBH}} = \frac{\exp\left\{-\frac{\ln^2(M_{\rm PBH}/\mu)}{2\sigma^2}\right\}}{\sqrt{2\pi}\sigma M_{\rm PBH}}\,, \tag{C.9}$$

where σ and μ are the standard deviation and mean of the PBH mass, respectively. Such function describes, e.g., the scenario of PBHs forming from a smooth symmetric peak in the inflationary power spectrum (Green 2016; Kannike et al. 2017).
The *Powerlaw* EMD, corresponding to PBHs formed from collapsing cosmic strings or scale-invariant density fluctuations (Carr 1975), is given by

$$\frac{d\Phi_{\rm PBH}}{dM_{\rm PBH}} = \frac{\mathcal{N}_{\rm PL}}{M_{\rm PBH}^{1-\tilde{\gamma}}}\Theta(M_{\rm PBH}-M_{\rm min})\Theta(M_{\rm max}-M_{\rm PBH})\,, \tag{C.10}$$

characterized by an exponent $\tilde{\gamma}\in(-1,+1)$, a mass interval $(M_{\rm min}, M_{\rm max})$, and a normalization factor $\mathcal{N}_{\rm PL}$; Θ is the Heaviside step function.

C.4 Data set and Methods

To extract limits on the PBH abundance from the Lyman-α forest, we adapted the method proposed in Murgia et al. (2018). We built a new grid of hydrodynamic simulations in terms of the properties of PBHs, corresponding to initial linear power spectra featuring a small-scale plateau. Beside that, our analyses rely on a pre-computed multidimensional grid of hydrodynamic simulations, associated to several values of the astrophysical and cosmological parameters affecting the Lyman-α flux power spectrum. Simulations have been performed with `GADGET-III`, a modified version of the public code `GADGET-II` (Springel et al. 2001; Springel 2005). Initial conditions have been produced with `2LPTic` (Crocce et al. 2006), at $z = 199$, with input linear power spectra for the ΛPBH models obtained by turning on the isocurvature mode in `CLASS` (Blas et al. 2011b).

Our reference model simulation (Murgia et al. 2018; Iršič et al. 2017) has a box length of $20/h$ comoving Mpc with 2×768^3 gas and CDM particles in a flat ΛCDM universe with cosmological parameters as in Ade et al. (2016b).

For the cosmological parameters to be varied, we sample different values of σ_8, i.e., the normalization of the linear power spectrum, and $n_{\rm eff}$, the slope of the power spectrum evaluated at the scale probed by the Lyman-α forest ($k_\alpha = 0.009$ s/km) (Seljak et al. 2006; McDonald et al. 2006; Arinyo-i Prats et al. 2015). We included five different simulations for both σ_8 ($[0.754, 0.904]$) and $n_{\rm eff}$ ($[-2.3474, -2.2674]$). Additionally, we included simulations corresponding to different values for the instantaneous reionization redshift, i.e., $z_{\rm reio} = \{7, 9, 15\}$.

Regarding the astrophysical parameters, we modeled the IGM thermal history with amplitude T_0 and slope γ of its temperature-density relation, parameterized as $T = T_0(1 + \delta_{\rm IGM})^{\gamma-1}$, with $\delta_{\rm IGM}$ being the IGM overdensity (Hui & Gnedin 1997). We use simulations with temperatures at mean density $T_0(z = 4.2) = \{6000, 9200, 12600\}$ K, evolving with redshift, and a set of three values for the slope of the temperature-density relation, $\gamma(z = 4.2) = \{0.88, 1.24, 1.47\}$. The redshift evolution of both T_0 and γ are parameterized as power laws, such that $T_0(z) = T_0^A[(1 + z)/(1 + z_p)]^{T_0^S}$ and $\gamma(z) = \gamma^A[(1 + z)/(1 + z_p)]^{\gamma^S}$, where the pivot redshift z_p is the redshift at which most of the Lyman-α forest pixels are coming from ($z_p = 4.5$). The reference thermal history is defined by $T_0(z = 4.2) = 9200$ and $\gamma(z = 4.2) = 1.47$ (Bolton et al. 2017).

Furthermore, we considered the effect of ultraviolet (UV) fluctuations of the ionizing background, controlled by the parameter $f_{\rm UV}$. Its template is built from three simulations with $f_{\rm UV} = \{0, 0.5, 1\}$, where $f_{\rm UV} = 0$ corresponds to a spatially uniform UV

background (Iršič et al. 2017). We also included 9 grid points obtained by rescaling the mean Lyman-α flux $\bar{F}(z)$, namely $\{0.6, 0.7, 0.8, 0.9, 1.0, 1.1, 1.2, 1.3, 1.4\} \times \bar{F}_{\rm REF}$, with reference values given by SDSS-III/BOSS measurements (Palanque-Delabrouille et al. 2013). We also considered 8 additional values, obtained by rescaling the optical depth $\tau = -\ln \bar{F}$, i.e. $\{0.6, 0.7, 0.8, 0.9, 1.1, 1.2, 1.3, 1.4\} \times \tau_{\rm REF}$.

Concerning the PBH properties, we extracted the flux power spectra from 12 hydrodynamic simulations (512^3 particles; 20 comoving Mpc/h box length) corresponding to the following PBH mass and fraction products: $\log(M_{\rm PBH} f_{\rm PBH}) = \{1.0, 1.5, 2.0, 2.2, 2.3, 2.4, 2.5, 2.6, 2.7, 3.0, 3.5, 4.0\}$. For this set of simulations, astrophysical and cosmological parameters have been fixed to their reference values, and the equivalent ΛCDM flux power was also determined.

We use an advanced interpolation method, the *Ordinary Kriging* method (Webster & Oliver 2007), particularly suitable to deal with the sparse, non-regular grid defined by our simulations. Such method basically consists in predicting the value of the flux power at a given point by computing a weighted average of all its known values, with weights inversely proportional to the distance from the considered point. The interpolation is in terms of ratios between the flux power spectra of the ΛPBH models and the reference ΛCDM one. We first interpolate in the astrophysical and cosmological parameter space for the ΛCDM case, then correct all the $(M_{\rm PBH} f_{\rm PBH})$-grid points accordingly, and finally interpolate in the $(M_{\rm PBH} f_{\rm PBH})$-space. This procedure relies on the assumption that the corrections due to non-reference astrophysical or cosmological parameters are universal, so that we can apply the same corrections computed for the ΛCDM case to the ΛPBH models as well.

Our datasets are the MIKE and HIRES/KECK samples of quasar spectra, at $z = \{4.2, 4.6, 5.0, 5.4\}$, in 10 k-bins in the range $[0.001 - 0.08]$ s/km, with spectral resolution of 13.6 and 6.7 s/km (Viel et al. 2013). We consider only measurements at $k > 0.005$ s/km, to avoid systematic uncertainties due to continuum fitting. Moreover, we did not use MIKE highest redshift bin. We thus have a total of 49 (k, z) data-points.

C.5 Results and Discussion

We obtain our results by maximising a Gaussian likelihood with a Monte Carlo Markov Chain (MCMC) approach, using the publicly available MCMC sampler `emcee` (Foreman-Mackey et al. 2013). We adopted Gaussian priors on the mean fluxes $\bar{F}(z)$, centered on their reference values, with standard deviation $\sigma = 0.04$ (Iršič et al. 2017), and on σ_8 and $n_{\rm eff}$, centered on their Planck values (Ade et al. 2016b), with $\sigma = 0.05$,

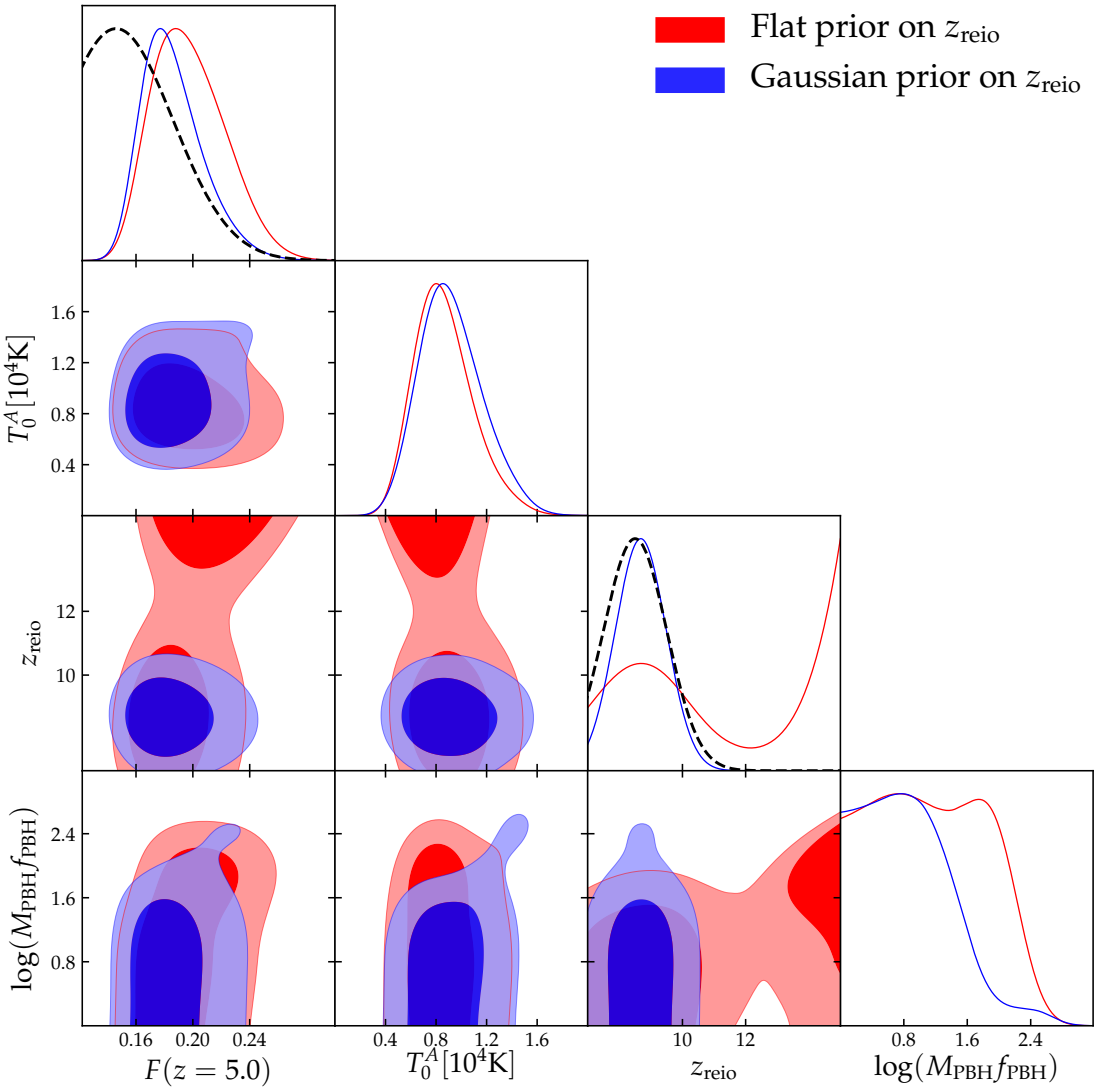

Figure C.3: 1 and 2σ contour plots for some of the parameters of our analyses, for the two different prior choices on $z_{\rm reio}$. The values for $M_{\rm PBH}$ are expressed in units of $M_\odot$. The dashed lines correspond to the Gaussian priors that we used for some of our analyses.

	Flat prior on $z_{\rm reio}$		**Gaussian prior on $z_{\rm reio}$**	
Parameter	**(2σ)**	**Best Fit**	**(2σ)**	**Best Fit**
$\bar{F}(z=4.2)$	[0.35, 0.41]	0.37	[0.35, 0.41]	0.37
$\bar{F}(z=4.6)$	[0.26, 0.34]	0.28	[0.27, 0.34]	0.28
$\bar{F}(z=5.0)$	[0.15, 0.25]	0.20	[0.15, 0.23]	0.16
$\bar{F}(z=5.4)$	[0.03, 0.12]	0.08	[0.04, 0.11]	0.05
T_0^A [10^4 K]	[0.44, 1.36]	0.72	[0.46, 1.44]	0.84
T_0^S	[-5.00, 3.34]	-4.47	[-5.00, 3.35]	-4.53
γ^A	[1.21, 1.60]	1.51	[1.19, 1.61]	1.44
γ^S	[-2.43, 1.30]	-1.76	[-2.25, 1.51]	0.46
σ_8	[0.72, 0.91]	0.79	[0.72, 0.91]	0.81
$z_{\rm reio}$	[7.00, 15.00]	14.19	[7.12, 10.25]	9.07
$n_{\rm eff}$	[-2.40, -2.22]	-2.30	[-2.41, -2.22]	-2.33
$f_{\rm UV}$	[0.00, 1.00]	0.02	[0.00, 1.00]	0.03
$\log(f_{\rm PBH}M_{\rm PBH})$	¡ 2.24	1.96	¡ 1.78	0.34
χ^2/d.o.f.		32/42		33/43

Table C.1: 2σ limits and best fit values for the parameters of our analyses, for the two different prior choices on $z_{\rm reio}$ adopted. Values for $M_{\rm PBH}$ are expressed in units of $M_\odot$.

since the latter two parameters, whereas well constrained by CMB data, are poorly constrained by Lyman-α data alone (Murgia et al. 2018). We adopt logarithmic priors on $f_{\rm PBH}M_{\rm PBH}$ (but our results are not affected by this choice). Concerning the IGM thermal history, we adopt flat priors on both T_0^A and T_0^S, in the ranges $[0,2]\cdot 10^4$ K and $[-5,5]$, respectively. When the corresponding $T_0(z)$ are determined, they can assume values not enclosed by our template of simulations. When this occurs, the corresponding values of the flux power spectra are linearly extrapolated. Regarding γ^S and γ^A, we impose flat priors on the corresponding $\gamma(z)$ (in the interval $[1,1.7]$). The priors on $z_{\rm reio}$ and $f_{\rm UV}$ are flat within the boundaries defined by our grid of simulations.

Let us firstly focus on the simple case of PBHs featuring a MMD. In table C.1 we report the marginalized 2σ constraints, in the case of a MMD, and the best fit values for all the parameters considered in our analyses. The first two columns refer to the case in which a flat prior is applied to the reionization redshift.

The limit on the PBH abundance under the MMD assumption corresponds to:

$$f_{\rm PBH}M_{\rm PBH} \lesssim 170\ M_\odot\ (2\sigma), \tag{C.11}$$

However, both Planck and Boera et al. (2018) favour $z_{\rm reio}\sim 8.5$, so we repeated our analysis with a Gaussian prior centered around $z_{\rm reio}=8.5$, with $\sigma=1.0$. The results obtained under such assumption are shown in the last two columns of table C.1, and

in this case we have:

$$f_{\rm PBH} M_{\rm PBH} \lesssim 60\ M_\odot\ (2\sigma)\,. \tag{C.12}$$

Where all DM is made by PBHs ($f_{\rm PBH} = 1$), these constraints can be interpreted as absolute limits on the PBH mass. On the other hand, such bounds weaken linearly for smaller PBH abundances ($0.05 < f_{\rm PBH} < 1$). The lower limit on $f_{\rm PBH}$ is given by the fact that, for the monochromatic case, at $z = 199$, i.e. the redshift of the initial conditions of our simulations, if $f_{\rm PBH}$ is smaller, the Poisson effect is subdominant with respect to the so-called *seed effect*, the treatment of which goes beyond our purposes.
The degeneracy between $z_{\rm reio}$ and the PBH mass can be understood as follows: a higher reionization redshift corresponds to a more effective filtering scale, and thus to a power suppression compensated by larger values of the PBH mass. The fact that the degeneracies are much more prominent for this parameter is telling us that the increase of power at small scales is a distinctive feature whose effect is more likely to be degenerate with a different gas filtering scale.
In figure C.3 we show the 1 and 2σ contours for some of the parameters of our analyses, for both prior choices on $z_{\rm reio}$. The degeneracy between the amplitude of the IGM temperature $T_0^A(z = z_p)$ and the PBH mass derives from the opposite effects on the flux power spectra due to the increase of the two parameters. A hotter IGM implies a small-scale power suppression which is balanced by increasing $M_{\rm PBH} f_{\rm PBH}$. Slightly larger values for the mean fluxes $\bar{F}(z)$ are also required for accommodating the power enhancement induced by relatively large values of the PBH mass. The dashed lines represent the Gaussian priors imposed on $\bar{F}(z = 5)$ and $z_{\rm reio}$, with the latter referring to the blue plots. Note that our MCMC analyses favour higher values for $\bar{F}(z = 5)$ (still in agreement with its prior distribution), allowing in turn a larger power enhancement due to PBHs. This is a further hint of the conservativity of the constraints presented in this work.
In order to test the stability of our results, we also performed an analysis with flat priors both on σ_8 and $n_{\rm eff}$. Under these assumptions, the constraint (using a Gaussian prior for $z_{\rm reio}$) on $f_{\rm PBH} M_{\rm PBH}$ is mildly weakened, up to 100 $M_\odot$. However, the largest values for the PBH mass are allowed only in combination with extremely low values for $n_{\rm eff}$, allowed in turn by our data set due to its poor constraining power on such parameter. As we have already stated, this is the main reason to impose a (still conservative) Gaussian prior motivated by CMB measurements on $n_{\rm eff}$.
In figure C.4 we report the plot with the constraints on the DM fraction in PBHs, in the monochromatic case, updated to the time of publication of Murgia et al. (2019). The "LIGO window" between $\sim 20-80 M_\odot$ initially suggested in Bird et al. (2016) has been

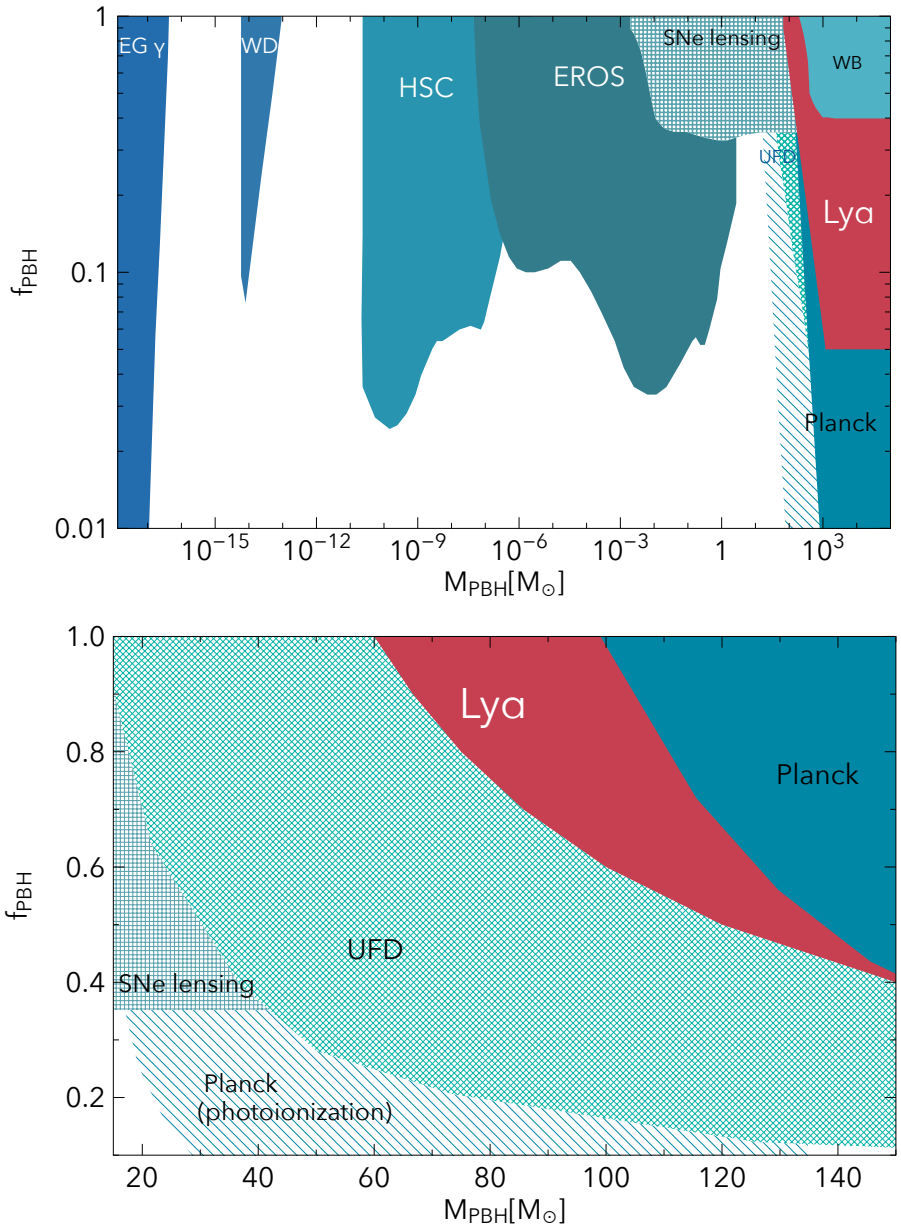

Figure C.4: Experimental constraints on the PBH abundance for MMDs (from Bartolo et al. (2019); Zumalacarregui & Seljak (2018); Ali-Haïmoud & Kamionkowski (2017); Carr et al. (2010)), in shades of blue, while in red are limits from this work. Patterned areas show limits that are the most dependent on astrophysical assumptions Carr et al. (2016b). The bottom panel is zoomed in the LIGO mass range.

probed and tentatively closed by constraints from Ultra-Faint Dwarf galaxies (Brandt 2016) and Supernovæ lensing (Zumalacarregui & Seljak 2018); these constraints have been questioned because of astrophysics uncertainties (e.g., Li et al. (2017); Carr et al. (2016b) [1]): we show them in a patterned area. In this work we robustly close the higher mass part of that remaining window. There remains however, an interesting possibility in the very low mass range, $\lesssim 10^{-10} M_\odot$ (Pi et al. 2018; Bartolo et al. 2019). By defining an equivalent mass $M_{\rm eq}$ one can convert the limits for the MMD case to bounds on the parameters of a given EMD. In figure C.5 we provide such bounds, similarly to what was shown in figure 3 of Carr et al. (2017) for other observational constraints. In other words, each of the panels maps the limits on MMDs peaked at $M_{\rm eq}$ to constraints on EMDs. The left panel shows the *Powerlaw* EMD, with $\tilde{\gamma} = 0$, focusing on the following mass range: $M_{\rm min},\ M_{\rm max} \in [10^{-2}, 10^{7}]\ M_\odot$. In the right panel we show the *Lognormal* EMD, scanning the parameter space defined by $\mu \in [10^{-2}, 10^{7}]\ M_\odot$, and $\sigma \in [0, 5]$. The two black lines correspond to the contraints quoted above, i.e. $M_{\rm eq} = 60\, M_\odot$ (*solid*), and $M_{\rm eq} = 170\, M_\odot$ (*dashed*). The blue regions are admitted by our analyses, while the red areas ruled out. All our analyses are based on the straightforward assumption that the PBH number density $n_{\rm PBH}$ is fixed during the cosmic time investigated by our simulations, i.e. from $z = 199$ to $z = 4.2$, which indeed corresponds to epochs when PBHs do not form anymore. However, the possibility that PBHs can fully evaporate during such time interval would alter our conclusions, since in that case $n_{\rm PBH}$ would vary with time. Nevertheless, from $z = 199$ to now, only PBHs with masses smaller than $\mathcal{O}(10^{-18})\ M_\odot$ might completely evaporate (Hawking (1974)). For this reason, such value has to lie below the PBH mass ranges investigated in this work. We have thus set $10^{-18}\ M_\odot$ as lower limit for the integral in Equation (C.8), and $10^{7}\ M_\odot$ as upper limit.

C.6 Summary

In this work we have presented new bounds on the DM fraction in PBHs, using an extensive analysis of high-redshift Lyman-α forest data, improving over previous similar analyses in three different ways: 1) we used the high-resolution MIKE/HIRES data, exploring better the high-redshift range where primordial differences are more prominent; 2) we relied on very accurate high-resolution hydrodynamic simulations which expands over a thermal history suggested by data; 3) we used the full shape of the 1D flux power rather than a single amplitude parameter.

[1] See also Primordial versus Astrophysical Origin of Black Holes – CERN workshop

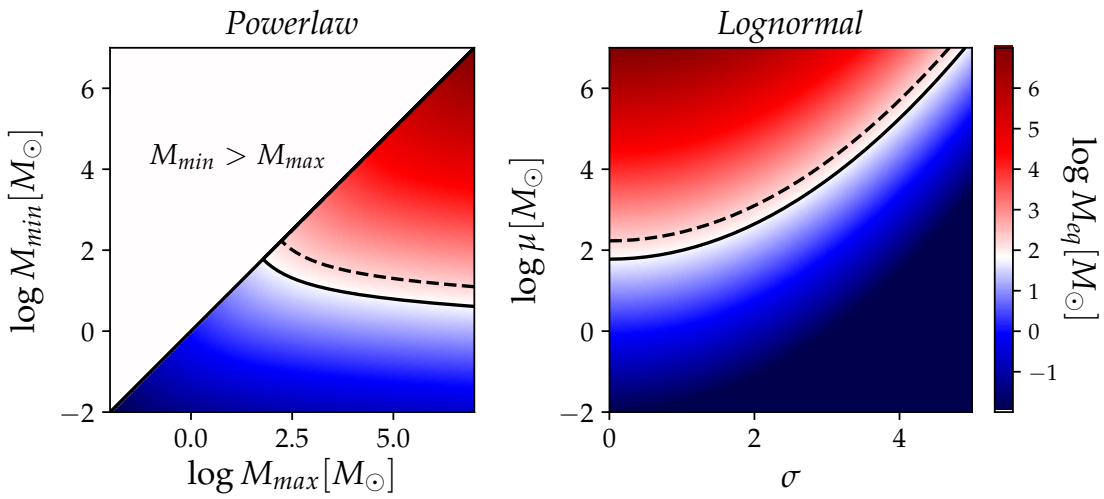

Figure C.5: Equivalent Mass $M_{\rm eq}$ for EMDs. *Left:* *Powerlaw* with $M_{\rm min}$, $M_{\rm max} \in [10^{-2}, 10^{7}]\ M_\odot$, and $\tilde{\gamma} = 0$. *Right:* *Lognormal* with $\mu \in [10^{-2}, 10^{7}]\ M_\odot$, $\sigma \in [0, 5]$. Solid lines are $M_{\rm eq} = 60\ M_\odot$, dashed lines refer to $M_{\rm eq} = 170$.

Our results improve previous constraints by roughly 2 orders of magnitude; furthermore, we have generalized our results to non-monochromatic PBH mass distributions, and ruled out a large part of the parameter space for two of the most popular EMDs: *Powerlaw* and *Lognormal*.

In the near future, it is expected that a larger number of high-redshift, high-resolution and signal-to-noise quasar spectra collected with the ESPRESSO spectrograph (Pepe et al. 2013) or at the E-ELT could allow to achieve tighter constraints. Another relevant aspect would be an accurate modeling of the heating and ionization due to accretion effects around the PBHs, to quantify how and if they could impact on the (much larger) scales of the Lyman-α forest.

The accumulation of limits on the PBHs as DM model in the mass range probed by LIGO seems to suggest that the hypothesis of $30 M_\odot$ PBHs being the DM is less and less likely to be true. It has however become clear that these studies brought a plethora of astrophysical information, and even the exclusion of certain PBH mass ranges will bring information on some of the processes happening in the very early Universe.

D

GW×EM - Constraints on $\{\mu_0, \eta_0\}$: plots

In this appendix we provide contours plots on the constraints on the $\{\mu_0, \eta_0\}$ parameters from Scelfo et al. (2022b). Comments on the results are embedded in the main text (chapter 4).

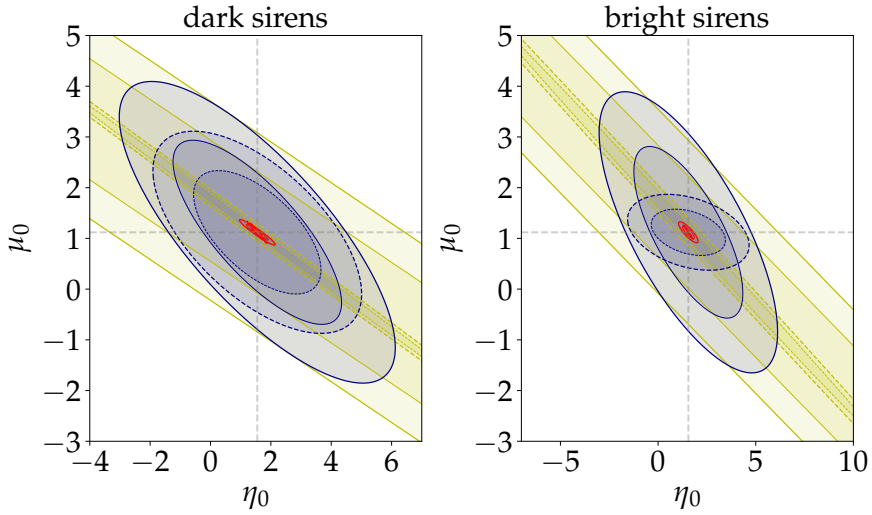

Figure D.1: Contours for $\{\mu_0, \eta_0\}$ in the GW×IM (solid line) and GW×IM×gal (dashed line) cases, all probes considered (colors according to legend). Left panels refer to dark sirens (BHBH+BHNS), right panels refer to bright sirens (NSNS). w_0, w_a are among the Fisher parameters considered. $T_{\rm obs}^{\rm GW}$=15 yr and $f_{\rm sky} = 0.5$.

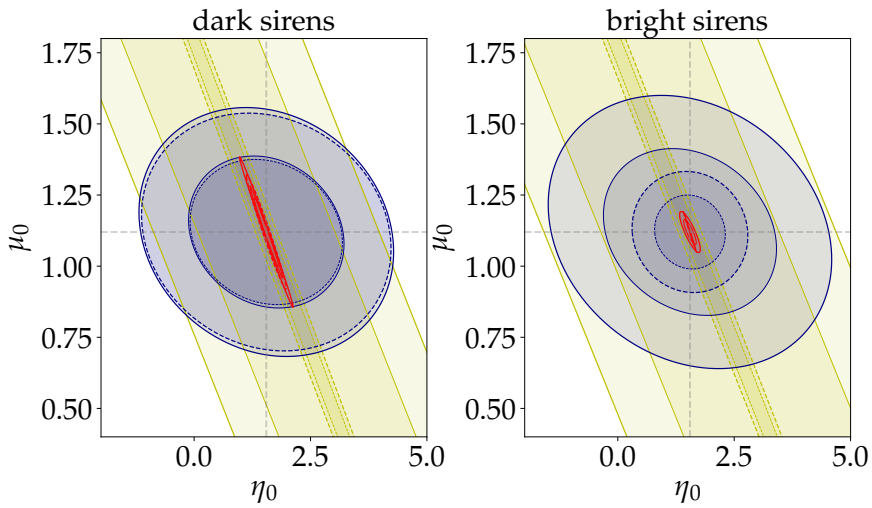

Figure D.2: Contours for $\{\mu_0, \eta_0\}$ in the GW×IM (solid line) and GW×IM×gal (dashed line) cases, all probes considered (colors according to legend). Left panels refer to dark sirens (BHBH+BHNS), right panels refer to bright sirens (NSNS). w_0, w_a are fixed to fiducial values. $T_{\rm obs}^{\rm GW}$=15 yr and $f_{\rm sky} = 0.5$.

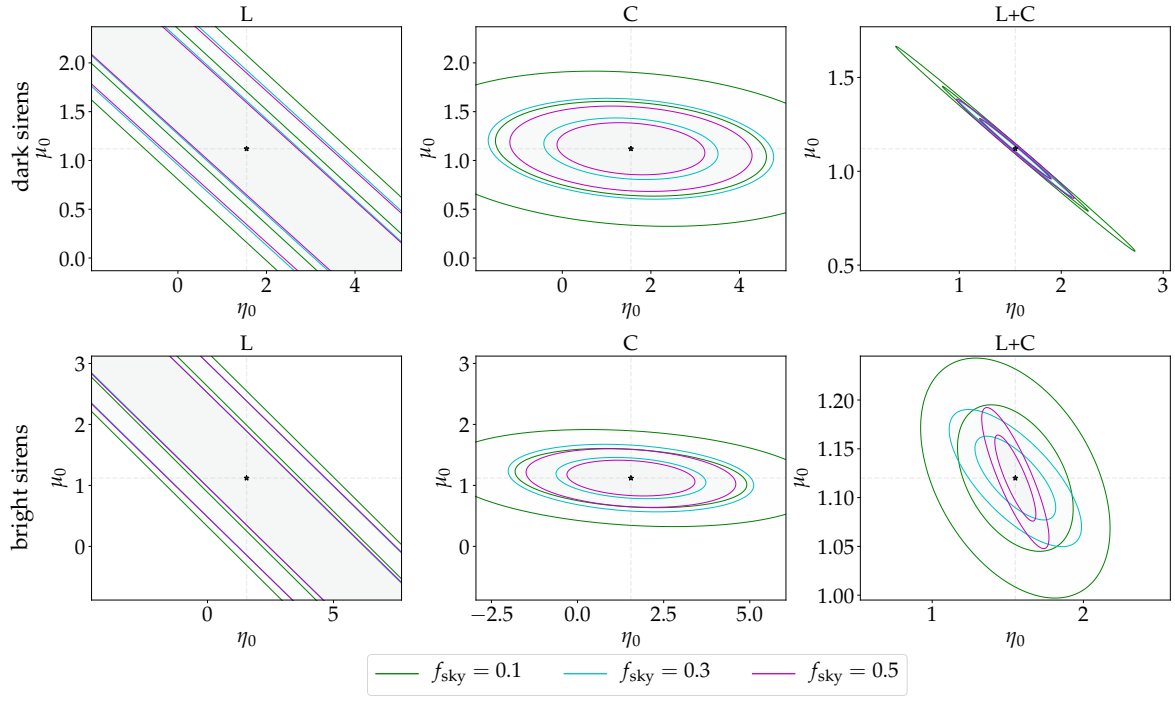

Figure D.3: Contours for $\{\mu_0, \eta_0\}$ parameters for the GW×IM case, all probes considered (only Lensing: left panels; only Clustering: center panels; Lensing + Clustering: right panels), for dark (top panels) and bright (bottom panels) sirens and for different values of $f_{\rm sky}$ (colour-coded according to legend). w_0, w_a are fixed to fiducial values. $T_{\rm obs}^{\rm GW}$=15 yr.

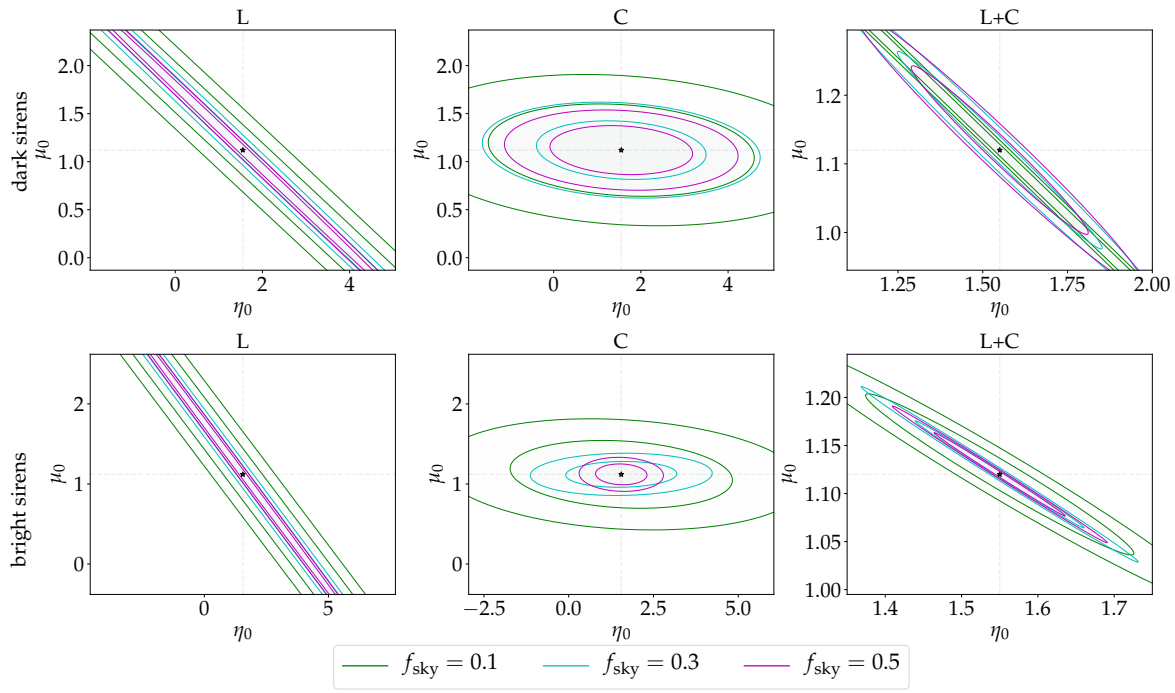

Figure D.4: Contours for $\{\mu_0, \eta_0\}$ parameters for the GW×IM×gal case, all probes considered (only Lensing: left panels; only Clustering: center panels; Lensing + Clustering: right panels), for dark (top panels) and bright (bottom panels) sirens and for different values of $f_{\rm sky}$ (colour-coded according to legend). w_0, w_a are fixed to fiducial values. $T_{\rm obs}^{\rm GW}$=15 yr.

Bibliography

Abbott, B. P. et al. 2009, Reports on Progress in Physics, 72, 076901

Abbott, B. P. et al. 2016a, Phys. Rev. Lett., 116, 131103

Abbott, B. P. et al. 2016b, Phys. Rev. Lett., 116, 061102

Abbott, B. P. et al. 2016c, Phys. Rev. Lett., 116, 241102

Abbott, B. P. et al. 2019a, Phys. Rev. X, 9, 031040

Abbott, R. et al. 2021, Phys. Rev. X, 11, 021053

Abbott, T., Aguena, M., Alarcon, A., et al. 2022, arXiv preprint arXiv:2207.05766

Abbott, T. M. C. et al. 2019b, Phys. Rev. D, 99, 123505

Accadia, T. et al. 2012, Journal of Instrumentation, 7, P03012

Adamek, J., Byrnes, C. T., Gosenca, M., & Hotchkiss, S. 2019, Phys. Rev. D, 100, 023506

Ade, P. A., Aghanim, N., Arnaud, M., et al. 2016a, Astronomy & Astrophysics, 594, A14

Ade, P. A. R. et al. 2016b, Astron.Astrophys., 594, A13

Adshead, P., Afshordi, N., Dimastrogiovanni, E., et al. 2021, Phys. Rev. D, 103, 023532

Afshordi, N., McDonald, P., & Spergel, D. N. 2003, ApJ, 594, L71

Aghanim, N., Akrami, Y., Ashdown, M., et al. 2020, Astronomy & Astrophysics, 641, A6

Ali-Haïmoud, Y. & Kamionkowski, M. 2017, Phys. Rev. D, 95, 043534

Ali-Haïmoud, Y., Kovetz, E. D., & Kamionkowski, M. 2017, Phys. Rev. D, 96, 123523

Alonso, D., Bellini, E., Hale, C., Jarvis, M. J., & Schwarz, D. J. 2021, Monthly Notices of the Royal Astronomical Society, 502, 876

Alonso, D., Bull, P., Ferreira, P. G., & Santos, M. G. 2014, Monthly Notices of the Royal Astronomical Society, 447, 400

Alonso, D., Cusin, G., Ferreira, P. G., & Pitrou, C. 2020, Phys. Rev. D, 102, 023002

Alonso, D. & Ferreira, P. G. 2015a, Phys. Rev. D, 92, 063525

Alonso, D. & Ferreira, P. G. 2015b, Phys. Rev. D, 92, 063525

Alonso, D., Ferreira, P. G., Jarvis, M. J., & Moodley, K. 2017, Phys. Rev. D, 96, 043515

Amendola, L., Kunz, M., & Sapone, D. 2008, JCAP, 04, 013

Anderson, C. J., Luciw, N. J., Li, Y. C., et al. 2018, Monthly Notices of the Royal Astronomical Society, 476, 3382

Andrews, B. H. & Martini, P. 2013, The Astrophysical Journal, 765, 140

Arinyo-i Prats, A., Miralda-Escude, J., Viel, M., & Cen, R. 2015, JCAP, 1512, 017

Arrigoni, M., Trager, S. C., Somerville, R. S., & Gibson, B. K. 2010, Monthly Notices of the Royal Astronomical Society, 402, 173

Artale, M. C., Mapelli, M., Giacobbo, N., et al. 2019, Monthly Notices of the Royal Astronomical Society, 487, 1675

Aso, Y. et al. 2013, Phys. Rev. D, 88, 043007

Assassi, V., Simonović, M., & Zaldarriaga, M. 2017, Journal of Cosmology and Astroparticle Physics, 2017, 054

Audley, H. et al. 2017

Aversa, R., Lapi, A., de Zotti, G., Shankar, F., & Danese, L. 2015, The Astrophysical Journal, 810, 74

Bacon, D. J., Battye, R. A., Bull, P., et al. 2020, Publications of the Astronomical Society of Australia, 37, e007

Baker, T. & Harrison, I. 2021, Journal of Cosmology and Astroparticle Physics, 2021, 068

Balaudo, A., Garoffolo, A., Martinelli, M., Mukherjee, S., & Silvestri, A. 2022, arXiv preprint arXiv:2210.06398

Bandura, K. et al. 2014, in Society of Photo-Optical Instrumentation Engineers (SPIE) Conference Series, Vol. 9145, Ground-based and Airborne Telescopes V, ed. L. M. Stepp, R. Gilmozzi, & H. J. Hall, 914522

Bardeen, J. M., Bond, J., Kaiser, N., & Szalay, A. 1986, The Astrophysical Journal, 304, 15

Bartelmann, M. & Schneider, P. 2001, Physics Reports, 340, 291

Bartolo, N., De Luca, V., Franciolini, G., et al. 2019, Phys. Rev. D, 99, 103521

Battye, R. et al. 2016, arXiv e-prints, arXiv:1610.06826

Battye, R. A., Browne, I. W. A., Dickinson, C., et al. 2013, Monthly Notices of the Royal Astronomical Society, 434, 1239

Belczynski, K., Dominik, M., Bulik, T., et al. 2010, The Astrophysical Journal Letters, 715, L138

Belgacem, E. et al. 2019, JCAP, 07, 024

Bellomo, N., Bernal, J. L., Raccanelli, A., & Verde, L. 2018, JCAP, 2018, 004

Bellomo, N., Bernal, J. L., Scelfo, G., Raccanelli, A., & Verde, L. 2020, Journal of Cosmology and Astroparticle Physics, 2020, 016

Bellomo, N., Bertacca, D., Jenkins, A. C., et al. 2022, Journal of Cosmology and Astroparticle Physics, 2022, 030

Benjamin, J., Van Waerbeke, L., Ménard, B., & Kilbinger, M. 2010, Monthly Notices of the Royal Astronomical Society, 408, 1168

Bennett, C. L., Larson, D., Weiland, J. L., & Hinshaw, G. 2014, The Astrophysical Journal, 794, 135

Benson, A. J., Cole, S., Frenk, C. S., Baugh, C. M., & Lacey, C. G. 2000, Monthly Notices of the Royal Astronomical Society, 311, 793

Bera, S., Rana, D., More, S., & Bose, S. 2020, The Astrophysical Journal, 902, 79

Berezin, V., Kuzmin, V., & Tkachev, I. 1983, Physics Letters B, 120, 91

Bernal, J. & Kovetz, E. 2022, arXiv preprint arXiv:2206.15377

Bernal, J. L., Bellomo, N., Raccanelli, A., & Verde, L. 2020, Journal of Cosmology and Astroparticle Physics, 2020, 017

Bernardeau, F., Colombi, S., Gaztañaga, E., & Scoccimarro, R. 2002, Physics Reports, 367, 1

Bertacca, D., Maartens, R., Raccanelli, A., & Clarkson, C. 2012a, Journal of Cosmology and Astroparticle Physics, 2012, 025

Bertacca, D., Maartens, R., Raccanelli, A., & Clarkson, C. 2012b, Journal of Cosmology and Astroparticle Physics, 2012, 025

Bertacca, D., Raccanelli, A., Bartolo, N., & Matarrese, S. 2018, Physics of the Dark Universe, 20, 32

Bertacca, D., Ricciardone, A., Bellomo, N., et al. 2020, Physical Review D, 101, 103513

Berti, M., Spinelli, M., & Viel, M. 2022, arXiv preprint arXiv:2209.07595

Bertschinger, E. 2006, Astrophys. J., 648, 797

Betoule, M., Kessler, R., Guy, J., et al. 2014, Astronomy & Astrophysics, 568, A22

Bianchini, F. & Lapi, A. 2014, IAU Symp., 306, 202

Bianchini, F. et al. 2015, Astrophys. J., 802, 64

Bianchini, F. et al. 2016, Astrophys. J., 825, 24

Bird, S., Cholis, I., Muñoz, J. B., et al. 2016, Phys. Rev. Lett., 116, 201301

Blake, C., Carter, P., & Koda, J. 2018, Monthly Notices of the Royal Astronomical Society, 479, 5168

Blas, D., Lesgourgues, J., & Tram, T. 2011a, Journal of Cosmology and Astroparticle Physics, 2011, 034

Blas, D., Lesgourgues, J., & Tram, T. 2011b, JCAP, 1107, 034

Boco, L., Lapi, A., & Danese, L. 2020, The Astrophysical Journal, 891, 94

Boco, L., Lapi, A., Goswami, S., et al. 2019, The Astrophysical Journal, 881, 157

Boera, E., Becker, G. D., Bolton, J. S., & Nasir, F. 2018, 1809.06980

Bolton, J. S., Puchwein, E., Sijacki, D., et al. 2017, MNRAS, 464, 897

Bonaldi, A., Bonato, M., Galluzzi, V., et al. 2018, Monthly Notices of the Royal Astronomical Society, 482, 2

Bonaldi, A., Harrison, I., Camera, S., & Brown, M. L. 2016, Monthly Notices of the Royal Astronomical Society, 463, 3686

Bonvin, C. & Durrer, R. 2011, Phys. Rev. D, 84, 063505

Bouwens, R. J., Illingworth, G. D., Oesch, P. A., et al. 2015, The Astrophysical Journal, 803, 34

Boylan-Kolchin, M., Springel, V., White, S. D., Jenkins, A., & Lemson, G. 2009, Monthly Notices of the Royal Astronomical Society, 398, 1150

Braglia, M. & Kuroyanagi, S. 2021, Phys. Rev. D, 104, 123547

Brandt, T. D. 2016, ApJ Letters, 824, L31

Braun, R., Bourke, T. L., Green, J. A., Keane, E., & Wagg, J. 2015, in Advancing Astrophysics with the Square Kilometre Array, Vol. 215, SISSA Medialab, 174

Brax, P. 2021, Screening Mechanisms

Bull, P., Ferreira, P. G., Patel, P., & Santos, M. G. 2015, The Astrophysical Journal, 803, 21

Byrnes, C. T., Cole, P. S., & Patil, S. P. 2019, Journal of Cosmology and Astroparticle Physics, 2019, 028

Byrnes, C. T., Copeland, E. J., & Green, A. M. 2012, Phys. Rev. D, 86, 043512

Cañas Herrera, G., Contigiani, O., & Vardanyan, V. 2020, Phys. Rev. D, 102, 043513

Calore, F., Cuoco, A., Regimbau, T., Sachdev, S., & Serpico, P. D. 2020, Physical Review Research, 2, 023314

Calzetti, D., Armus, L., Bohlin, R. C., et al. 2000, The Astrophysical Journal, 533, 682

Camera, S., Harrison, I., Bonaldi, A., & Brown, M. L. 2016, Monthly Notices of the Royal Astronomical Society, 464, 4747

Camera, S. & Nishizawa, A. 2013, Phys. Rev. Lett., 110, 151103

Cañas-Herrera, G., Contigiani, O., & Vardanyan, V. 2021, 918, 20

Cao, L., Lu, Y., & Zhao, Y. 2018, Monthly Notices of the Royal Astronomical Society, 474, 4997

Capurri, G., Lapi, A., & Baccigalupi, C. 2022, Universe, 8

Carr, B., Kühnel, F., & Sandstad, M. 2016a, Phys. Rev. D, 94, 083504

Carr, B., Kühnel, F., & Sandstad, M. 2016b, Phys. Rev. D, 94, 083504

Carr, B. & Kühnel, F. 2020, Annual Review of Nuclear and Particle Science, 70, 355

Carr, B., Raidal, M., Tenkanen, T., Vaskonen, V., & Veermäe, H. 2017, Phys. Rev. D, 96, 023514

Carr, B. & Silk, J. 2018, MNRAS, 478, 3756

Carr, B. J. 1975, The Astrophysical Journal, 201, 1

Carr, B. J. & Hawking, S. W. 1974, Monthly Notices of the Royal Astronomical Society, 168, 399

Carr, B. J., Kohri, K., Sendouda, Y., & Yokoyama, J. 2010, Phys. Rev. D, 81, 104019

Carucci, I. P., Irfan, M. O., & Bobin, J. 2020, Monthly Notices of the Royal Astronomical Society, 499, 304

Casas, S., Carucci, I. P., Pettorino, V., Camera, S., & Martinelli, M. 2022, arXiv preprint arXiv:2210.05705

Casas, S., Kunz, M., Martinelli, M., & Pettorino, V. 2017, Phys. Dark Univ., 18, 73

Castorina, E. & Villaescusa-Navarro, F. 2017, Monthly Notices of the Royal Astronomical Society, 471, 1788

Chabrier, G. 2003, The Astrophysical Journal Letters, 586, L133

Challinor, A. & Lewis, A. 2011a, Phys. Rev. D, 84, 043516

Challinor, A. & Lewis, A. 2011b, Phys. Rev. D, 84, 043516

Chang, T.-C., Pen, U.-L., Bandura, K., & Peterson, J. B. 2010, Nature, 466, 463

Choi, A., Heymans, C., Blake, C., et al. 2016, Monthly Notices of the Royal Astronomical Society, 463, 3737

Chruslinska, M., Belczynski, K., Klencki, J., & Benacquista, M. 2018, Monthly Notices of the Royal Astronomical Society, 474, 2937

Chruslinska, M., Nelemans, G., & Belczynski, K. 2019, Monthly Notices of the Royal Astronomical Society, 482, 5012

Cigarrán Díaz, C. & Mukherjee, S. 2022, Monthly Notices of the Royal Astronomical Society, 511, 2782

Clesse, S. & García-Bellido, J. 2017, Physics of the Dark Universe, 15, 142

Cole, P. S. & Byrnes, C. T. 2018, Journal of Cosmology and Astroparticle Physics, 2018, 019

Congedo, G. & Taylor, A. 2019, Phys. Rev. D, 99, 083526

Coppin, K. E. K., Geach, J. E., Almaini, O., et al. 2015, Monthly Notices of the Royal Astronomical Society, 446, 1293

Crawford, M. & Schramm, D. N. 1982, Nature, 298, 538

Crighton, N. H. M., Murphy, M. T., Prochaska, J. X., et al. 2015, Monthly Notices of the Royal Astronomical Society, 452, 217

Crocce, M., Pueblas, S., & Scoccimarro, R. 2006, MNRAS, 373, 369

Cunnington, S., Harrison, I., Pourtsidou, A., & Bacon, D. 2018, Monthly Notices of the Royal Astronomical Society, 482, 3341

Cunnington, S., Irfan, M. O., Carucci, I. P., Pourtsidou, A., & Bobin, J. 2021, Monthly Notices of the Royal Astronomical Society, 504, 208

Cutler, C. & Holz, D. E. 2009, Phys. Rev. D, 80, 104009

Dai, L., Kamionkowski, M., & Jeong, D. 2012, Phys. Rev. D, 86, 125013

Das, S. et al. 2018, in Society of Photo-Optical Instrumentation Engineers (SPIE) Conference Series, Vol. 10708, Millimeter, Submillimeter, and Far-Infrared Detectors and Instrumentation for Astronomy IX, ed. J. Zmuidzinas & J.-R. Gao, 1070836

de la Rosa, I. G., La Barbera, F., Ferreras, I., et al. 2016, Monthly Notices of the Royal Astronomical Society, 457, 1916

De Luca, V., Franciolini, G., & Riotto, A. 2021, Phys. Rev. Lett., 126, 041303

de Mink, S. E. & Belczynski, K. 2015, The Astrophysical Journal, 814, 58

de Mink, S. E., Langer, N., Izzard, R. G., Sana, H., & de Koter, A. 2013, The Astrophysical Journal, 764, 166

Dekel, A. & Lahav, O. 1999, The Astrophysical Journal, 520, 24

Desjacques, V., Jeong, D., & Schmidt, F. 2018, Physics Reports, 733, 1

Dewdney, P. E., Hall, P. J., Schilizzi, R. T., & Lazio, T. J. L. W. 2009, Proceedings of the IEEE, 97, 1482

Di Dio, E., Montanari, F., Lesgourgues, J., & Durrer, R. 2013, Journal of Cosmology and Astroparticle Physics, 2013, 044

Dolgov, A. & Silk, J. 1993, Phys. Rev. D, 47, 4244

Dominik, M., Belczynski, K., Fryer, C., et al. 2012, The Astrophysical Journal, 759, 52

Dominik, M., Belczynski, K., Fryer, C., et al. 2013, The Astrophysical Journal, 779, 72

Dominik, M., Berti, E., O'Shaughnessy, R., et al. 2015, The Astrophysical Journal, 806, 263

Dunlop, J. S., McLure, R. J., Biggs, A. D., et al. 2017, Monthly Notices of the Royal Astronomical Society, 466, 861

Efstathiou, A., Rowan-Robinson, M., & Siebenmorgen, R. 2000, Monthly Notices of the Royal Astronomical Society, 313, 734

Elbert, O. D., Bullock, J. S., & Kaplinghat, M. 2018, Monthly Notices of the Royal Astronomical Society, 473, 1186

Euclid Collaboration, Blanchard, A., Camera, S., et al. 2019, arXiv e-prints, arXiv:1910.09273

Fairhurst, S. 2014, Journal of Physics: Conference Series, 484, 012007

Fang, K., Banerjee, A., Charles, E., & Omori, Y. 2020, The Astrophysical Journal, 894, 112

Fisher, K. B., Scharf, C. A., & Lahav, O. 1994, Monthly Notices of the Royal Astronomical Society, 266, 219

Flanagan, E. E. & Hughes, S. A. 1998, Physical Review D, 57, 4535

Foreman-Mackey, D., Hogg, D. W., Lang, D., & Goodman, J. 2013, PASP, 125, 306

Fudamoto, Y., Oesch, P. A., Schinnerer, E., et al. 2017, Monthly Notices of the Royal Astronomical Society, 472, 483

Furlanetto, S. R., Oh, S. P., & Briggs, F. H. 2006, Physics reports, 433, 181

Gallazzi, A., Bell, E. F., Zibetti, S., Brinchmann, J., & Kelson, D. D. 2014, The Astrophysical Journal, 788, 72

García-Bellido, J., Linde, A., & Wands, D. 1996, Phys. Rev. D, 54, 6040

Gardner, J. P. et al. 2006, Space Science Reviews, 123, 485

Garoffolo, A., Raveri, M., Silvestri, A., et al. 2021, Phys. Rev. D, 103, 083506

Gebhardt, H. S. G. & Jeong, D. 2018, Physical Review D, 97, 023504

Giacobbo, N. & Mapelli, M. 2018, Monthly Notices of the Royal Astronomical Society, 480, 2011

Gilks, W., Richardson, S., & Spiegelhalter, D. 1995, Markov Chain Monte Carlo in Practice, Chapman & Hall/CRC Interdisciplinary Statistics (Taylor & Francis)

Giudice, G. F., McCullough, M., & You, T. 2021, Journal of High Energy Physics, 2021, 1

Gong, J.-O. & Kitajima, N. 2017, JCAP, 1708, 017

Gow, A. D., Byrnes, C. T., & Hall, A. 2022, Phys. Rev. D, 105, 023503

Green, A. M. 2016, Phys. Rev. D, 94, 063530

Green, A. M. & Kavanagh, B. J. 2021, Journal of Physics G: Nuclear and Particle Physics, 48, 043001

Gruppioni, C., Calura, F., Pozzi, F., et al. 2015, Monthly Notices of the Royal Astronomical Society, 451, 3419

Gruppioni, C. & Pozzi, F. 2019, Monthly Notices of the Royal Astronomical Society, 483, 1993

Gruppioni, C., Pozzi, F., Rodighiero, G., et al. 2013, Monthly Notices of the Royal Astronomical Society, 432, 23

Hall, A., Bonvin, C., & Challinor, A. 2013, Phys. Rev. D, 87, 064026

Hartle, J. B. 2003, AAPT

Hawking, S. 1971, Monthly Notices of the Royal Astronomical Society, 152, 75

Hawking, S. 1989, Physics Letters B, 231, 237

Hawking, S. W. 1974, Nature, 248, 30

Heavens, A. F. & Taylor, A. N. 1995, Monthly Notices of the Royal Astronomical Society, 275, 483

Heisenberg, L., Bartelmann, M., Brandenberger, R., & Refregier, A. 2018, Phys. Rev. D, 98, 123502

Hirata, C. M., Ho, S., Padmanabhan, N., Seljak, U., & Bahcall, N. A. 2008, Physical Review D, 78, 043520

Ho, S., Hirata, C., Padmanabhan, N., Seljak, U., & Bahcall, N. 2008, Physical Review D, 78, 043519

Hoekstra, H. & Jain, B. 2008, Annual Review of Nuclear and Particle Science, 58, 99

Hojjati, A., Pogosian, L., & Zhao, G.-B. 2011, JCAP, 08, 005

Hu, W. & Sawicki, I. 2007, Phys. Rev. D, 76, 104043

Hu, W., Wang, X., Wu, F., et al. 2020, Monthly Notices of the Royal Astronomical Society, 493, 5854

Hubble, E. 1929, Proceedings of the National Academy of Science, 15, 168

Hui, L. & Gnedin, N. Y. 1997, MNRAS, 292, 27

Inomata, K., McDonough, E., & Hu, W. 2021, arXiv preprint arXiv:2104.03972

Ipser, J. & Sikivie, P. 1984, Phys. Rev. D, 30, 712

Iršič, V. et al. 2017, Phys. Rev. D, 96, 023522

Ishak, M. 2019, Living Rev. Rel., 22, 1

Ivanov, P. 1998, Phys. Rev. D, 57, 7145

Ivanov, P., Naselsky, P., & Novikov, I. 1994, Phys. Rev. D, 50, 7173

Ivezić, Ž. et al. 2019, The Astrophysical Journal, 873, 111

Jain, B., Scranton, R., & Sheth, R. K. 2003, Monthly Notices of the Royal Astronomical Society, 345, 62

Jeong, D., Schmidt, F., & Hirata, C. M. 2012, Phys. Rev. D, 85, 023504

Joachimi, B., Mandelbaum, R., Abdalla, F. B., & Bridle, S. L. 2011, Astronomy & Astrophysics, 527, A26

Johnson, A., Blake, C., Amon, A., Erben, T., et al. 2016, Monthly Notices of the Royal Astronomical Society, 465, 4118

Joyce, A., Jain, B., Khoury, J., & Trodden, M. 2015, Phys. Rept., 568, 1

Kaiser, N. 1984, The Astrophysical Journal, 284, L9

Kalaja, A., Bellomo, N., Bartolo, N., et al. 2019, Journal of Cosmology and Astroparticle Physics, 2019, 031

Kannike, K., Marzola, L., Raidal, M., & Veermäe, H. 2017, JCAP, 2017, 020

Kilbinger, M., Heymans, C., Asgari, M., et al. 2017, Monthly Notices of the Royal Astronomical Society, 472, 2126

Klimenko, S., Vedovato, G., Drago, & others. 2011, Physical Review D, 83, 102001

Kovetz, E. D., Cholis, I., Breysse, P. C., & Kamionkowski, M. 2017a, Physical Review D, 95, 103010

Kovetz, E. D., Raccanelli, A., & Rahman, M. 2017b, Monthly Notices of the Royal Astronomical Society, 468, 3650

Kovetz, E. D., Viero, M. P., Lidz, A., et al. 2017c, arXiv preprint arXiv:1709.09066

La, D. & Steinhardt, P. J. 1989, Physics Letters B, 220, 375

Laguna, P., Larson, S. L., Spergel, D., & Yunes, N. 2010, The Astrophysical Journal, 715, L12

Lahav, O., Fisher, K., Hoffman, Y., Scharf, C., & Zaroubi, S. 1993, arXiv preprint astro-ph/9311059

Lamberts, A., Garrison-Kimmel, S., Clausen, D. R., & Hopkins, P. F. 2016, Monthly Notices of the Royal Astronomical Society, 463, L31

Lamberts, A., Garrison-Kimmel, S., Hopkins, P. F., et al. 2018, Monthly Notices of the Royal Astronomical Society, 480, 2704

Lapi, A. & Cavaliere, A. 2011, The Astrophysical Journal, 743, 127

Lapi, A. & Danese, L. 2014, JCAP, 2014, 044

Lapi, A., González-Nuevo, J., Fan, L., et al. 2011, The Astrophysical Journal, 742, 24

Lapi, A., Pantoni, L., Boco, L., & Danese, L. 2020, arXiv e-prints, arXiv:2006.01643

Lapi, A., Raimundo, S., Aversa, R., et al. 2014, The Astrophysical Journal, 782, 69

Lapi, A., Shankar, F., Mao, J., et al. 2006, The Astrophysical Journal, 650, 42

Lee, S. et al. 2021, Mon. Not. Roy. Astron. Soc., 509, 4982

Lewis, A., Challinor, A., & Lasenby, A. 2000, Astrophys. J., 538, 473

Li, S.-S., Mao, S., Zhao, Y., & Lu, Y. 2018, Monthly Notices of the Royal Astronomical Society, 476, 2220

Li, T., Simon, J. D., Drlica-Wagner, A., et al. 2017, The Astrophysical Journal, 838, 8

Libanore, S., Artale, M., Karagiannis, D., et al. 2022, 2022, 003

Libanore, S., Artale, M. C., Karagiannis, D., et al. 2021, Journal of Cosmology and Astroparticle Physics, 2021, 035

Littenberg, T. B. & Cornish, N. J. 2010, Phys. Rev. D, 82, 103007

Liu, A. & Shaw, J. R. 2020, Publications of the Astronomical Society of the Pacific, 132, 062001

Liu, D., Daddi, E., Dickinson, M., et al. 2018, The Astrophysical Journal, 853, 172

Loeb, A. & Zaldarriaga, M. 2004, Phys. Rev. Lett., 92, 211301

Maartens, R., Abdalla, F. B., Jarvis, M., & Santos, M. G. 2015, Cosmology with the SKA – overview

Magnelli, B., Popesso, P., Berta, S., et al. 2013, A&A, 553, A132

Mancuso, C., Lapi, A., Shi, J., et al. 2016, The Astrophysical Journal, 823, 128

Mapelli, M. & Giacobbo, N. 2018, Monthly Notices of the Royal Astronomical Society, 479, 4391

Mapelli, M., Giacobbo, N., Ripamonti, E., & Spera, M. 2017, Monthly Notices of the Royal Astronomical Society, 472, 2422

Marrone, D. P., Spilker, J. S., Hayward, C. C., et al. 2018, Nature, 553, 51

Martin, A. M., Papastergis, E., Giovanelli, R., et al. 2010, The Astrophysical Journal, 723, 1359

Martínez, H. J., Merchán, M. E., Valotto, C. A., & Lambas, D. G. 1999, The Astrophysical Journal, 514, 558

Masui, K. W., Switzer, E. R., Banavar, N., et al. 2013, The Astrophysical Journal Letters, 763, L20

Matarrese, S., Coles, P., Lucchin, F., & Moscardini, L. 1997, Monthly Notices of the Royal Astronomical Society, 286, 115

Matshawule, S. D., Spinelli, M., Santos, M. G., & Ngobese, S. 2021, Monthly Notices of the Royal Astronomical Society, 506, 5075

Matsubara, T. 2000, The Astrophysical Journal, 535, 1

Matthews, D. J. & Newman, J. A. 2010, The Astrophysical Journal, 721, 456

McDonald, P. et al. 2006, Astrophys. J. Suppl., 163, 80

McQuinn, M. & White, M. 2013, Monthly Notices of the Royal Astronomical Society, 433, 2857

Ménard, B., Scranton, R., Schmidt, S., et al. 2013, arXiv preprint arXiv:1303.4722

Mészáros, P. 1975, Astronomy and Astrophysics, 38, 5

Meurer, G. R., Heckman, T. M., & Calzetti, D. 1999, The Astrophysical Journal, 521, 64

Mo, H. J. & White, S. D. M. 1996, Monthly Notices of the Royal Astronomical Society, 282, 347

Moore, C. J., Cole, R. H., & Berry, C. P. L. 2015, Classical and Quantum Gravity, 32, 015014

Morales, M. F. & Wyithe, J. S. B. 2010, Annual review of astronomy and astrophysics, 48, 127

Motohashi, H. & Hu, W. 2017, Phys. Rev. D, 96, 063503

Mpetha, C. T., Congedo, G., & Taylor, A. 2022, arXiv preprint arXiv:2208.05959

Muñoz, J. B., Kovetz, E. D., Dai, L., & Kamionkowski, M. 2016, Phys. Rev. Lett., 117, 091301

Mukherjee, S., Krolewski, A., Wandelt, B. D., & Silk, J. 2022, arXiv preprint arXiv:2203.03643

Mukherjee, S. & Silk, J. 2021, Monthly Notices of the Royal Astronomical Society, 506, 3977

Mukherjee, S., Wandelt, B. D., Nissanke, S. M., & Silvestri, A. 2021a, Physical Review D, 103, 043520

Mukherjee, S., Wandelt, B. D., & Silk, J. 2020a, Phys. Rev. D, 101, 103509

Mukherjee, S., Wandelt, B. D., & Silk, J. 2020b, Monthly Notices of the Royal Astronomical Society, 494, 1956

Mukherjee, S., Wandelt, B. D., & Silk, J. 2021b, Monthly Notices of the Royal Astronomical Society, 502, 1136

Muñoz, J. B., Kovetz, E. D., Raccanelli, A., Kamionkowski, M., & Silk, J. 2017, Journal of Cosmology and Astroparticle Physics, 2017, 032

Murgia, R., Iršič, V., & Viel, M. 2018, Phys. Rev. D, 98, 083540

Murgia, R., Scelfo, G., Viel, M., & Raccanelli, A. 2019, Phys. Rev. Lett., 123, 071102

Musco, I. 2019, Phys. Rev. D, 100, 123524

Musco, I., De Luca, V., Franciolini, G., & Riotto, A. 2021, Phys. Rev. D, 103, 063538

Musco, I., Miller, J. C., & Rezzolla, L. 2005, Classical and Quantum Gravity, 22, 1405

Namikawa, T., Nishizawa, A., & Taruya, A. 2016, Physical review letters, 116, 121302

Neijssel, C. J., Vigna-Gómez, A., Stevenson, S., et al. 2019, Monthly Notices of the Royal Astronomical Society, 490, 3740

Newburgh, L. B. et al. 2016, in Society of Photo-Optical Instrumentation Engineers (SPIE) Conference Series, Vol. 9906, Ground-based and Airborne Telescopes VI, ed. H. J. Hall, R. Gilmozzi, & H. K. Marshall, 99065X

Newman, J. A. 2008, The Astrophysical Journal, 684, 88

Ng, K. K. Y., Vitale, S., Farr, W. M., & Rodriguez, C. L. 2021, The Astrophysical Journal Letters, 913, L5

Nolta, M. R., Wright, E., Page, L., et al. 2004, The Astrophysical Journal, 608, 10

Norris, R. P. et al. 2011, Publications of the Astronomical Society of Australia, 28, 215

Novak, M., Smolčić, V., Delhaize, J., et al. 2017, Astronomy & Astrophysics, 602, A5

Oguri, M. 2016, Physical Review D, 93, 083511

Onodera, M., Carollo, C. M., Lilly, S., Renzini, A., et al. 2016, The Astrophysical Journal, 822, 42

O'Shaughnessy, R., Bellovary, J. M., Brooks, A., et al. 2017, Monthly Notices of the Royal Astronomical Society, 464, 2831

O'Shaughnessy, R., Kalogera, V., & Belczynski, K. 2010, The Astrophysical Journal, 716, 615

Paech, K., Hamaus, N., Hoyle, B., et al. 2017, Monthly Notices of the Royal Astronomical Society, 470, 2566

Palanque-Delabrouille, N., Yèche, Christophe, Borde, Arnaud, et al. 2013, A&A, 559, A85

Pantoni, L., Lapi, A., Massardi, M., Goswami, S., & Danese, L. 2019, The Astrophysical Journal, 880, 129

Pápai, P. & Szapudi, I. 2008, Monthly Notices of the Royal Astronomical Society, 389, 292

Peacock, J. A. & Smith, R. E. 2000, Monthly Notices of the Royal Astronomical Society, 318, 1144

Peebles, P. 1973, The Astrophysical Journal, 185, 413

Peebles, P. 1980, Research supported by the National Science Foundation. Princeton, N. J., Princeton University Press, 1980. 435 p

Pepe, F., Cristiani, S., Rebolo, R., et al. 2013, The Messenger, 153

Pi, S., li Zhang, Y., Huang, Q.-G., & Sasaki, M. 2018, Journal of Cosmology and Astroparticle Physics, 2018, 042

Planck Collaboration, Ade, P. A. R., Aghanim, N., et al. 2016, A&A, 594, A13

Planck Collaboration, Aghanim, N., Akrami, Y., et al. 2018, arXiv e-prints, arXiv:1807.06209

Pogosian, L., Raveri, M., Koyama, K., et al. 2021, arXiv preprint arXiv:2107.12992

Pogosian, L. & Silvestri, A. 2008, Phys. Rev. D, 77, 023503, [Erratum: Phys.Rev.D 81, 049901 (2010)]

Pogosian, L. & Silvestri, A. 2016, Phys. Rev. D, 94, 104014

Polnarev, A. & Zembowicz, R. 1991, Phys. Rev. D, 43, 1106

Pourtsidou, A. 2016, Monthly Notices of the Royal Astronomical Society, 461, 1457

Pourtsidou, A., Bacon, D., & Crittenden, R. 2017, Monthly Notices of the Royal Astronomical Society, 470, 4251

Pourtsidou, A., Bacon, D., Crittenden, R., & Metcalf, R. B. 2016, Monthly Notices of the Royal Astronomical Society, 459, 863

Pourtsidou, A. & Metcalf, R. B. 2014, Monthly Notices of the Royal Astronomical Society: Letters, 439, L36

Pourtsidou, A. & Metcalf, R. B. 2015, Monthly Notices of the Royal Astronomical Society, 448, 2368

Pozzo, W. D. 2014, Journal of Physics: Conference Series, 484, 012030

Pritchard, J. & Loeb, A. 2011, arXiv preprint arXiv:1109.6012

Pullen, A. R., Chang, T.-C., Doré, O., & Lidz, A. 2013, The Astrophysical Journal, 768, 15

Raccanelli, A. 2017, Monthly Notices of the Royal Astronomical Society, 469, 656

Raccanelli, A., Bertacca, D., Pietrobon, D., et al. 2013, Monthly Notices of the Royal Astronomical Society, 436, 89

Raccanelli, A., Bonaldi, A., Negrello, M., et al. 2008, Monthly Notices of the Royal Astronomical Society, 386, 2161

Raccanelli, A., Kovetz, E., Dai, L., & Kamionkowski, M. 2016a, Phys. Rev. D, 93, 083512

Raccanelli, A., Kovetz, E. D., Bird, S., Cholis, I., & Muñoz, J. B. 2016b, Phys. Rev. D, 94, 023516

Raccanelli, A., Samushia, L., & Percival, W. J. 2010, Monthly Notices of the Royal Astronomical Society, 409, 1525

Rahman, M., Ménard, B., & Scranton, R. 2016, Monthly Notices of the Royal Astronomical Society, 457, 3912

Raidal, M., Spethmann, C., Vaskonen, V., & Veermäe, H. 2019, Journal of Cosmology and Astroparticle Physics, 2019, 018

Raveri, M., Pogosian, L., Koyama, K., et al. 2021, arXiv preprint arXiv:2107.12990

Reddy, N. A., Kriek, M., Shapley, A. E., et al. 2015, The Astrophysical Journal, 806, 259

Regos, E. & Szalay, A. S. 1989, The Astrophysical Journal, 345, 627

Reitze, D., Adhikari, R. X., Ballmer, S., et al. 2019, arXiv preprint arXiv:1907.04833

Ricciardone, A., Dall'Armi, L. V., Bartolo, N., et al. 2021, Phys. Rev. Lett., 127, 271301

Riechers, D. A., Leung, T. K. D., Ivison, R. J., et al. 2017, The Astrophysical Journal, 850, 1

Ross, A. J., Beutler, F., Chuang, C.-H., et al. 2017, MNRAS, 464, 1168

Rowan-Robinson, M., Oliver, S., Wang, L., et al. 2016, Monthly Notices of the Royal Astronomical Society, 461, 1100

Safarzadeh, M., Berger, E., Ng, K. K., et al. 2019, The Astrophysical Journal Letters, 878, L13

Santos, M. G., Bull, P., Alonso, D., et al. 2015, arXiv preprint arXiv:1501.03989

Santos, M. G., Cluver, M., Hilton, M., et al. 2017, arXiv preprint arXiv:1709.06099

Sasaki, M., Suyama, T., Tanaka, T., & Yokoyama, S. 2018, Classical and Quantum Gravity, 35, 063001

Sathyaprakash, B. et al. 2012a, Classical and Quantum Gravity, 29, 124013

Sathyaprakash, B. et al. 2012b, Classical and Quantum Gravity, 29, 124013

Sato-Polito, G., Kovetz, E. D., & Kamionkowski, M. 2019, Phys. Rev. D, 100, 063521

Scelfo, G., Bellomo, N., Raccanelli, A., Matarrese, S., & Verde, L. 2018, JCAP, 2018, 039

Scelfo, G., Boco, L., Lapi, A., & Viel, M. 2020, Journal of Cosmology and Astroparticle Physics, 2020, 045

Scelfo, G., Spinelli, M., Raccanelli, A., et al. 2022a, Journal of Cosmology and Astroparticle Physics, 2022, 004

Scelfo, G., Berti, M., Silvestri, A., & Viel, M. 2022b, arXiv preprint arXiv:2210.02460

Scharf, C., Hoffman, Y., Lahav, O., & Lynden-Bell, D. 1992, Monthly Notices of the Royal Astronomical Society, 256, 229

Schmidt, S. J., Ménard, B., Scranton, R., Morrison, C., & McBride, C. K. 2013a, Monthly Notices of the Royal Astronomical Society, 431, 3307

Schmidt, S. J., Ménard, B., Scranton, R., Morrison, C., & McBride, C. K. 2013b, Monthly Notices of the Royal Astronomical Society, 431, 3307

Schutz, B. F. 1986, Nature, 323, 310

Scottez, V., Mellier, Y., Granett, B. R., Moutard, et al. 2016, Monthly Notices of the Royal Astronomical Society, 462, 1683

Seljak, U., Slosar, A., & McDonald, P. 2006, JCAP, 0610, 014

Sheth, R. K., Mo, H. J., & Tormen, G. 2001, Monthly Notices of the Royal Astronomical Society, 323, 1

Silva, L., Granato, G. L., Bressan, A., & Danese, L. 1998, The Astrophysical Journal, 509, 103

Silvestri, A. & Trodden, M. 2009, Rept. Prog. Phys., 72, 096901

Soares, P. S., Watkinson, C. A., Cunnington, S., & Pourtsidou, A. 2021, arXiv e-prints, arXiv:2105.12665

Spera, M. & Mapelli, M. 2017, Monthly Notices of the Royal Astronomical Society, 470, 4739

Spera, M., Mapelli, M., & Bressan, A. 2015, Monthly Notices of the Royal Astronomical Society, 451, 4086

Spera, M., Mapelli, M., Giacobbo, N., et al. 2019, Monthly Notices of the Royal Astronomical Society, 485, 889

Spinelli, M., Carucci, I. P., Cunnington, S., et al. 2021, arXiv e-prints, arXiv:2107.10814

Spinelli, M., Zoldan, A., De Lucia, G., Xie, L., & Viel, M. 2020, Monthly Notices of the Royal Astronomical Society, 493, 5434

Spolaor, M., Kobayashi, C., Forbes, D. A., Couch, W. J., & Hau, G. K. T. 2010, Monthly Notices of the Royal Astronomical Society, 408, 272

Sprenger, T., Archidiacono, M., Brinckmann, T., Clesse, S., & Lesgourgues, J. 2019, Journal of Cosmology and Astroparticle Physics, 2019, 047

Springel, V. 2005, MNRAS, 364, 1105

Springel, V., Yoshida, N., & White, S. D. M. 2001, New Astron., 6, 79

Switzer, E. R., Masui, K. W., Bandura, K., et al. 2013, Monthly Notices of the Royal Astronomical Society: Letters, 434, L46

Szalay, A. S., Matsubara, T., & Landy, S. D. 1998, The Astrophysical Journal, 498, L1

Takahashi, R. 2006, The Astrophysical Journal, 644, 80

Taruya, A., Saga, S., Breton, M.-A., Rasera, Y., & Fujita, T. 2019, Monthly Notices of the Royal Astronomical Society, 491, 4162

Tasinato, G., Garoffolo, A., Bertacca, D., & Matarrese, S. 2021, JCAP, 06, 050

Taylor, S. R. & Gair, J. R. 2012, Physical Review D, 86, 023502

Turner, E. L., Ostriker, J. P., & Gott, III, J. R. 1984, Astrophysical Journal, 284, 1

van Daalen, M. P. & White, M. 2018, Monthly Notices of the Royal Astronomical Society, 476, 4649

Viel, M., Becker, G. D., Bolton, J. S., & Haehnelt, M. G. 2013, Phys. Rev. D, 88, 043502

Viel, M., Lesgourgues, J., Haehnelt, M. G., Matarrese, S., & Riotto, A. 2005, Phys. Rev. D, 71, 1

Viel, M., Matarrese, S., Mo, H. J., Haehnelt, M. G., & Theuns, T. 2002, MNRAS, 329, 848

Villaescusa-Navarro, F., Genel, S., Castorina, E., et al. 2018, The Astrophysical Journal, 866, 135

Villaescusa-Navarro, F., Viel, M., Datta, K. K., & Choudhury, T. R. 2014, Journal of Cosmology and Astroparticle Physics, 2014, 050

Wang, J., Santos, M. G., Bull, P., et al. 2020, arXiv preprint arXiv:2011.13789

Webster, R. & Oliver, M. A. 2007, Geostatistics for environmental scientists (John Wiley & Sons)

Weinberg, S. 2008, Cosmology (Oxford University Press)

Wichoski, U. F., MacGibbon, J. H., & Brandenberger, R. H. 1998, Physics Reports, 307, 191

Wilman, R., Miller, L., Jarvis, M., et al. 2008, Monthly Notices of the Royal Astronomical Society, 388, 1335

Wolz, L., Blake, C., & Wyithe, J. S. B. 2017, Monthly Notices of the Royal Astronomical Society, 470, 3220

Wolz, L., Murray, S. G., Blake, C., & Wyithe, J. S. 2018, Monthly Notices of the Royal Astronomical Society, 484, 1007

Wolz, L., Pourtsidou, A., Masui, K. W., et al. 2021, arXiv preprint arXiv:2102.04946

Wolz, L., Tonini, C., Blake, C., & Wyithe, J. S. B. 2016, Monthly Notices of the Royal Astronomical Society, 458, 3399

Wootten, A. & Thompson, A. R. 2009, Proceedings of the IEEE, 97, 1463

Yang, X., Mo, H. J., van den Bosch, F. C., et al. 2005, Monthly Notices of the Royal Astronomical Society, 362, 711

Yoo, J. & Desjacques, V. 2013, Phys. Rev. D, 88, 023502

Young, S., Musco, I., & Byrnes, C. T. 2019, Journal of Cosmology and Astroparticle Physics, 2019, 012

Zahid, H. J., Kashino, D., Silverman, J. D., et al. 2014, The Astrophysical Journal, 792, 75

Zavala, J. A., Montaña, A., Hughes, D. H., et al. 2018, Nature Astronomy, 2, 56

Zhang, P., Liguori, M., Bean, R., & Dodelson, S. 2007, Phys. Rev. Lett., 99, 141302

Zhao, G.-B., Pogosian, L., Silvestri, A., & Zylberberg, J. 2009, Phys. Rev. D, 79, 083513

Zucca, A., Pogosian, L., Silvestri, A., & Zhao, G.-B. 2019, JCAP, 05, 001

Zumalacarregui, M. & Seljak, U. 2018, Phys. Rev. Lett., 121, 141101